INTERNATIONAL DOCTORAL
SCHOOL OF THE USC

Elisabet
Galiana Baldó

PhD Thesis

PIGE Cross Sections in ^{35,37}Cl and EnsarRoot Developments in Applied Gamma Spectroscopy

Santiago de Compostela, 2023

Doctoral Programme in Nuclear and Particles Physics

TESIS DE DOCTORADO

PIGE CROSS SECTIONS IN ^{35,37}Cl AND ENSARROOT DEVELOPMENTS IN APPLIED GAMMA SPECTROSCOPY

Elisabet Galiana Baldó

ESCUELA DE DOCTORADO INTERNACIONAL DE LA UNIVERSIDAD DE SANTIAGO DE COMPOSTELA

PROGRAMA DE DOCTORADO EN FÍSICA NUCLEAR Y DE PARTÍCULAS

SANTIAGO DE COMPOSTELA
AÑO 2023

USC
UNIVERSIDADE
DE SANTIAGO
DE COMPOSTELA

AUTORIZACIÓN DEL DIRECTOR/TUTOR DE LA TESIS

D. **Héctor Álvarez-Pol**.

En condición de: **Director y Tutor**.

Título de la Tesis: **PIGE cross sections in ^{35,37}Cl and EnsarRoot developments in applied gamma spectroscopy**.

INFORMA:

Que la presente tesis, se corresponde con el trabajo realizado por Dña. Elisabet Galiana Baldó, bajo mi dirección/tutorización, y autorizo su presentación, considerando que reúne los requisitos exigidos en el Reglamento de Estudios de Doctorado de la USC, y que como director/tutor de esta no incurre en las causas de abstención establecidas en la Ley 40/2015.

Santiago de Compostela, ... de ... de 2023

Fdo. Héctor Álvarez-Pol

AUTORIZACIÓN DEL DIRECTOR DE LA TESIS

D. **Daniel Galaviz Redondo**.

En condición de: **Director**.

Título de la Tesis: **PIGE cross sections in ^{35,37}Cl and EnsarRoot developments in applied gamma spectroscopy**.

INFORMA:

Que la presente tesis, se corresponde con el trabajo realizado por Dña. Elisabet Galiana Baldó, bajo mi dirección, y autorizo su presentación, considerando que reúne los requisitos exigidos en el Reglamento de Estudios de Doctorado de la USC, y que como director de esta no incurre en las causas de abstención establecidas en la Ley 40/2015.

Santiago de Compostela, ... de ... de 2023

Fdo. Daniel Galaviz Redondo

USC
UNIVERSIDADE
DE SANTIAGO
DE COMPOSTELA

I am among those who think that science has great beauty. A scientist in his laboratory is not only a technician: he is also a child placed before natural phenomena which impress him like a fairy tale.

Marie Curie, physicist, 1867-1934

This work is dedicated to all scientists and discoverer women who preceded me for having the bravery, the courage and the strength to lead the way, because the leader is not who fights to be the first but the first to fight...

Some day the anvil, tired of being anvil, will become hammer.

Mikhail Bakunin, anarchist, 1814-1876

And to the forgotten, who create the history from the bottom up.

USC
UNIVERSIDADE DE SANTIAGO DE COMPOSTELA

USC
UNIVERSIDADE
DE SANTIAGO
DE COMPOSTELA

Acknowledgments

Ante todo quería expresar mi total gratitud a mis dos tutores Héctor y Dani, ya que sin su apoyo, tiempo, dedicación y sabiduría esta tesis no estaría entre nuestras manos. Me habéis brindado una oportunidad única y extraordinaria, y es la de ver con mis propios ojos y calcular con mis propias manos como surge la física. Gracias por la confianza que me habéis dipositado, por respetar mis sugerencias e ideas y por ser comprensivos en todo momento. Y lo más importante de todo, gracias porque habéis sido un gran ejemplo como personas.

Quería también agradecer a Pablo su infinita paciencia mientras me explicaba los entresijos de EnsarRoot y más de una vez tenía que utilizar el comando *kill* porque mi ordenador no reaccionaba, y por responder a mis innumerables preguntas con otras preguntas y buen humor!

Pam, gracias por ayudarme en todo momento y enseñarme a maniobrar en el laboratorio con bata blanca y todo! Porque no solo aprendía física sino que me contabas fenómenos interesantísimos de biología y me dabas consejos de vida, la verdad que echo de menos nuestras charlas...

A Luis y a Sandra por querer colaborar y ver con ilusión los experimentos de radiación de fondo, el artículo está en camino...

A Lola por apoyarme siempre y ser un gran ejemplo como profesional.

Gracias a los equipos de personas de la USC, del LIP i del CTN/IST que de un modo u otro me han prestado su ayuda, sus consejos y con los cuales he compartido buenos momentos.

Visto en perspectiva creo que durante estos años me he rodeado de personas excelentes y siempre os recordaré con mucho cariño, de hecho, ya me asalta la *morriña e saudade* cada vez que oigo hablar en vuestro idioma...

USC
UNIVERSIDADE DE SANTIAGO DE COMPOSTELA

Però aquest treball va començar molt abans, quan vaig començar a somiar i ningú em va dir que existien fronteres...

El meu profund agraïment per a dues persones extraordinàries, especials i carismàtiques, Evaristo i Lydia, els meus pares, per estar sempre al meu costat en totes les meves decisions, tan bones com roïnes, per ensenyar-me a no rendir-me davant de l'adversitat, per fer desaparéixer la paraula culpa del diccionari i acceptar la responsabilitat, per ensenyar-me que la diferència és meravellosa, per no seguir el camí i perdre's en la jungla, per anar a buscar la tempesta...

I a la meva iaia amb molt d'amor... per ajudar-me a créixer com a persona.

A la meva nova família castellarenca per cuidar-me, per la vostra estima i comprensió durant aquests últims anys, perquè m'he sentit com a casa...

A totes les meves amistats, de la terreta, del nord, de Portugal i de la montanya! per estar amb mi en la distància, per donar-me tants ànims i fer-me riure per oblidar-ho tot... encara que ens veiem a la llarga vos porte al meu cor.

A *La Linterna de Diógenes* per donar-me consciència de classe, un programa radiofònic que m'ha acompanyat durant tots aquestos anys per aeroports, busos i trens...

I en especial per Adrià, el meu company d'aventures en aquest meravellós viatge que és la vida... per ensenyar-me a gaudir-la i compartir moments únics que no oblidaré mai. Gràcies per donar-me la mà quan la necessite i estimar totes les meves peculiaritats...

Amb molta estima, gràcies!

And my gratitude to you dear reader if you have reached the last page without falling asleep... that means that you find it, at least, a little bit interesting, my only hope is to have contributed with a pebble to the science castle, but... *if you are already dreaming, good night!*

USC
UNIVERSIDADE DE SANTIAGO DE COMPOSTELA

USC
UNIVERSIDADE
DE SANTIAGO
DE COMPOSTELA

Abstract

Gamma spectroscopy plays an important role in many fields, from material and biological analysis up to state-of-the-art research. It studies gamma radiations and their interactions with matter. This analytical technique is based on the measurement of the energy and the quantification of the intensity of each gamma ray. One of the main advantages is that it allows a simultaneous identification of photopeaks coming from distincts radioactive sources. This identification is feasible thanks to the uniqueness of gamma energies of each nucleus. Moreover, the high precision of this technique makes possible to study relevant properties of nuclei.

The present thesis is centered on gamma spectroscopy studies using germanium semiconductor detectors with similar characteristics. In particular, two different lines of research were addressed. On one hand, we investigated gamma emissions coming from low energy proton interactions on the two stable isotopes of chlorine, ^{35}Cl and ^{37}Cl, via elastic scattering and (p,α) and (p,n) channels. These studies were carried out with the aim of measuring for the first time gamma yields and differential cross sections. The measurements were done at CTN/IST facility using PIGE technique, one of the most widely used IBA methods. In order to carry on this experiment, we produced natural chlorine targets using vacuum thermal deposition technique at the Target Laboratory of FCiências. Afterwards, the target characteristics were analysed using the RBS method.

The other branch of research of this work is the study of environmental gamma radiation. We have studied the natural sources of radiation by measuring the environmental background at three enclaves with diverse mineral soil compositions. These locations were placed in facilities at the west part of Iberian Peninsula: at CTN/IST, at UBI installations and at USC laboratory. These monitorizations were undertaken during long periods of time and have allowed us to analyse and quantify potassium, uranium and thorium radioactive sources and understand their patterns over time.

All the previous investigations were framed inside the EnsarRoot program. It is an object oriented software that accommodates simulations, re-

USC
UNIVERSIDADE DE SANTIAGO DE COMPOSTELA

constructions and real data analysis within the same framework. An important part of this work was the development of EnsarRoot base code in order to implement the previous investigations. Diverse elements as experimental setups and gamma source generators have been simulated. A great asset of this framework is that all data regarding its origin could be analysed and treated with the same tools and routines avoiding additional bias. As a result, measured data have been evaluated and benchmarked against simulated data and these results were useful to address some unknown variables and draw conclusions.

USC
UNIVERSIDADE
DE SANTIAGO
DE COMPOSTELA

USC
UNIVERSIDADE
DE SANTIAGO
DE COMPOSTELA

Contents

Abstract **X**

Contents **XIII**

1 INTRODUCTION **1**

2 OBJECTIVES **4**
2.1 Motivation of the PIGE Study 4
2.1.1 Outline 6
2.1.2 Chlorine: Physical and Chemical Properties 7
2.1.3 General Review of Available PIGE Cross Sections . . . 8
2.1.3.1 ^{35}Cl(p,p'γ)^{35}Cl reaction 8
2.1.3.2 ^{35}Cl(p,$\alpha\gamma$)^{32}S reaction 10
2.1.3.3 ^{37}Cl(p,p'γ)^{37}Cl and ^{37}Cl(p,nγ)^{37}Ar reactions . 10
2.1.3.4 ^{37}Cl(p,$\alpha\gamma$)^{34}S reaction 11
2.2 Motivation of the Environmental Gamma Study 12
2.2.1 Outline 13
2.2.2 General Review of Available Data in Literature 14
2.2.2.1 Studies of Environmental Background 14
2.2.2.2 Studies of Environmental Radiation Simulations 16

3 METHODOLOGY: THEORETICAL SECTION **18**
3.1 PIGE Technique 18
3.1.1 IBA Techniques 18
3.1.1.1 Rutherford Backscattering Spectrometry (RBS) 20
3.1.1.2 Particle Induced Gamma-Ray Emission (PIGE) 28
3.2 Environmental Radiation 39
3.2.1 Radioactivity of the Nucleus 39
3.2.2 The Decay Equation 39
3.2.3 Individual Decay Chains 40

USC UNIVERSIDADE DE SANTIAGO DE COMPOSTELA

3.2.4 Radioactive Chains: Bateman Equations 42
3.2.5 Natural Sources of Radiation 44
3.2.5.1 Terrestrial Radiation 45
3.2.5.2 Anthropogenic Radioactivity in Nature 52

4 METHODOLOGY: EXPERIMENTAL SECTION 56
4.1 EnsarRoot Framework 56
4.1.1 EnsarRoot Description 57
4.1.1.1 Detector Constructor 58
4.1.1.2 Event Generators 61
4.1.1.3 Analytical Tasks 61
4.2 EnsarRoot Developments 62
4.2.1 EnsarRoot Experimental Setups 63
4.2.1.1 The CTN/IST Setup 63
4.2.1.2 The Universidade da Beira Interior Setup . . 64
4.2.2 EnsarRoot Generators 65
4.2.2.1 Environmental Radiation EnsarGenerators . . 65
4.3 PIGE Experimental Procedures: Target Production 67
4.3.1 Vacuum Thermal Deposition 68
4.3.2 Target Production 69
4.4 PIGE Experimental Procedures at CTN/IST Installations . . 74
4.4.1 Installations of the Experimental Setups 74
4.4.1.1 Van der Graaff Accelerator 74
4.4.1.2 Tandem Accelerator 76
4.4.2 RBS Experiment 82
4.4.3 PIGE Experiment 82
4.4.3.1 Detector Efficiency Definition 83
4.4.3.2 Efficiency Calibration of the HPGe Detector . 85
4.4.3.3 Resolution of the HPGe Detector 88
4.4.3.4 Calibration of the HPGe Detector 89
4.5 Environmental Radiation Experimental Procedures 91
4.5.1 CTN/IST Environmental Radiation Measurements . . 91
4.5.2 UBI Environmental Radiation Measurement 93
4.5.3 USC Environmental Radiation Measurements 94

5 RESULTS 97
5.1 PIGE Experimental Results 97
5.1.1 RBS Target Data Analysis 97
5.1.2 PIGE Data Analysis and Discussion of Results 100
5.1.2.1 RBS Data Analysis from the PIGE Experiment 103
5.1.2.2 HPGe Data Analysis 107

USC UNIVERSIDADE DE SANTIAGO DE COMPOSTELA

5.1.2.3 Cross Section Measurements 113
5.2 Environmental Radiation Experimental Results 121
5.2.1 Data Analysis 121
5.2.1.1 Environmental Radiation Comparison 122
5.2.2 Environmental Radiation Simulations 132
5.2.2.1 CTN/IST Data Simulation 132
5.2.2.2 UBI Data Simulation 141

6 CONCLUSIONS **147**

Resumen **151**

Resumo **166**

Glossary **180**

Appendix **183**

Bibliography **239**

List of Figures **257**

List of Tables **269**

USC UNIVERSIDADE DE SANTIAGO DE COMPOSTELA

USC
UNIVERSIDADE
DE SANTIAGO
DE COMPOSTELA

Chapter 1

INTRODUCTION

The science that study the interactions between gamma rays and matter is known as gamma spectroscopy (from the ancient Greek *skopéō* "to observe" and the Latin *spectrum* "appearance, image"). It measures the energy and quantifies the intensity of each gamma ray identifying its origin whenever is possible. Gamma rays were discovered in 1900 by Paul Villard when he was studying the radiation emitted by radium salts [1]. However, they were named "gamma" by Ernest Rutherford, following the same nomenclature, because they were more energetic than alpha and beta particles. The first quantitative analysis where the wavelength of gamma radiation was determined was carried out some years later in 1914 also by E. Rutherford and Edward Andrade in a diffraction experiment [2].

In nature there are many gamma emitters making spectroscopy technique widely used in a large variety of fields, such as, geology, analysis of biological samples, environmental radiation monitoring, radiopharmaceuticals, material analysis, nuclear research, etc. The widespread use of this technique started in the 1950s when the first portable detectors were developed and could be easily manageable outside the laboratory [3]. These first detectors were inorganic scintillators made of thallium activated sodium iodide, NaI(Tl), which still is one of the most used materials for gamma ray detection. The other type of device employed is semiconductor detectors such as germanium detectors [4].

In the present work two research lines based on gamma spectroscopy were addressed. On one side, diverse nuclear reactions were studied interpreting and quantifying the outcoming gamma rays. This technique is called Particle Induced Gamma ray Emission (PIGE) and is a non-destructive method used to study samples with low atomic number [5, 6]. In particular, there were studied low energy cross sections and gamma yields of proton induced reactions on natural chlorine. The two stable isotopes of chlorine have not

USC
UNIVERSIDADE DE SANTIAGO DE COMPOSTELA

been previously investigated in depth and one of the aims of the present work was to fill these gaps of knowledge. In order to carry out these measurements chlorine targets were produced and characterized using Rutherford Backscattering Spectrometry (RBS) technique.

The other field of study was environmental gamma radiation. Natural radioactive sources are present in our daily life in materials, water and air, for this reason, a good knowledge of their nature and behaviour is of great importance [7]. Natural radioactivity has been measured at diverse locations in the west region of Iberian Peninsula for long periods of time. These monitorizations have allowed us to analyse and quantify radioactive sources and understand their patterns over time.

These investigations have been supported by the EnsarRoot program [8, 9, 10]. It is an object oriented software framework for simulation as well as for reconstruction and data analysis. It has a similar structure and functionalities as other analysis codes used for several experiments mainly at GSI/FAIR installations, like the R3BRoot program [11]. In order to implement these studies we have expanded its base code to simulate the experimental setups and to reconstruct gamma emissions. Afterwards, we have benchmarked simulated and measured data. A great asset of this framework is that both data could be analysed and treated with the same tools and routines avoiding additional bias.

During the reading of this work we have to bear in mind that each chapter is divided in two in order to cover both lines of investigation, having EnsarRoot as a common framework and conducting wire. Moreover, the environmental background study has been useful in the data analysis of the PIGE study; thus, they are mutually interrelated.

The present work is organized as follows: in the Chapter 2 there is a general overview of each investigation including their motivations and objectives to achieve, as well as a general review of the published literature and available data. The theoretical foundations of both lines of research are explained in Chapter 3. In the following Chapter 4 there is detailed the experimental methodology: the EnsarRoot program, its internal design and operation and the developed code; secondly the chlorine target production; then all PIGE experimental procedures at CTN/IST installations including the description of the facility, the RBS and the PIGE experiments and the last part of this chapter is centered on the environmental radiation experimental procedures. In Chapter 5 the experimental results are presented, firstly the RBS and PIGE discussion is shown and then the environmental radiation study. And finally, the conclusions of the presented dissertation along with the prospects of future work are discussed in Chapter 6.

USC UNIVERSIDADE DE SANTIAGO DE COMPOSTELA

USC
UNIVERSIDADE
DE SANTIAGO
DE COMPOSTELA

Chapter 2

OBJECTIVES

In the present chapter the motivations and objectives behind the two areas of research are presented. Moreover, at the end of each section there is a general review of the literature data and publications.

2.1 Motivation of the PIGE Study

One of the main goals of the PIGE study is to measure low energy cross sections and gamma yields from proton induced nuclear reactions of the two stable chlorine isotopes. These investigations are of great interest in diverse disciplines:

- **PIGE lack of reference data:** Low energy gamma spectroscopy is one of the most widely used IBA (Ion Beam Analysis) techniques because of its sensitivity to elements with low atomic number. However, there is a transition region around Z $\sim$ 18 between gamma ray and X-ray spectroscopy, where the number of the PIGE studies previously done decreases dramatically. In the case under examination, in particular ^{35}Cl isotope, there are three academic works done in the mid-80s where the only information available are gamma yields at some particular energies [12, 13, 14]. The ^{37}Cl isotope is practically under the same circumstances [12, 13, 15]. These reference data are available in the IBANDL (Ion Beam Analysis Nuclear Data Library) web page. In recent years special effort has been carried out by the IAEA (International Atomic Energy Agency) organization [16] in order to standardize and systematize PIGE studies, to obtain reliable data [6]. Therefore, the aim of this work is to rectify this lack of information by performing an exhaustive study following the guidelines recommended by the IAEA.

USC UNIVERSIDADE DE SANTIAGO DE COMPOSTELA

- **Astrophysical importance:** Chlorine isotopes are produced as secondary products in the explosive oxygen-burning phase of the CNO-cycle. This cycle is one of the two paths of hydrogen burning and allows the creation of heavier elements beyond He and lower than Fe [17]. This burning phase occurs, for example, inside massive stars that provide the required density and temperature. The final isotopical abundances of each element are determined by the competition between proton, alpha and neutron induced reactions and their inverses. In the case of ^{37}Cl, the most important creation reaction is ^{37}Ar(n,p)^{37}Cl, which is the inverse of ^{37}Cl(p,n)^{37}Ar, and the destruction reaction is ^{37}Cl(p,γ)^{38}Ar, which in turn is one mode of production of ^{38}Ar. The knowledge of all these reactions are the input of the nucleosynthesis network equations that describe the abundance of an specific isotope by summing all possible decay and production rates. Therefore, the study of proton induced cross sections is fundamental in order to describe the nucleosynthesis evolution in this mass region [15]. From the nuclear structure standpoint, these reactions are of particular interest since the ^{37}Cl nucleus has a closed shell of 20 neutrons.

  In regard to ^{35}Cl isotope, it contributes to the SCl hydrogen burning cycle, which predominates in the rp-process at lower temperatures [18]. Figure 2.1 shows the flow chart of the process. The cycle starts from an ^{32}S even-even nucleus, which after consecutive proton captures and beta decays is transformed into a ^{35}Cl nucleus, finally a (p,α) reaction closes the cycle arriving to the initial ^{32}S nucleus. This last transition is produced because the Q-value of the (p,α) reaction is lower than the (p,γ) threshold. The leakage ratio between (p,γ)/(p,α), or in other words, the competition between (p,γ) and (p,α), determines the number of nucleus bypassing into a heavier cycle (see Figure 1 of [18]). Consequently, a good experimental determination of all these processes is essential [17, 18].

As we have explained before, in order to conduct these studies we used a strong analytical and simulation tool called EnsarRoot [10, 19, 20]. This framework has been further expanded to include gamma ray generators to reproduce the previously mentioned reactions. Geant4 has been used to recreate the simulated setup in order to obtain the detector and geometrical efficiences, two indispensable parameters for the calculus of proton induced cross sections. Owing to the foregoing, data simulations are generated under the same geometrical conditions and equally treated as real data and both could be used by the same analytical procedures. This code development is a part of the objective of this thesis.

USC UNIVERSIDADE DE SANTIAGO DE COMPOSTELA

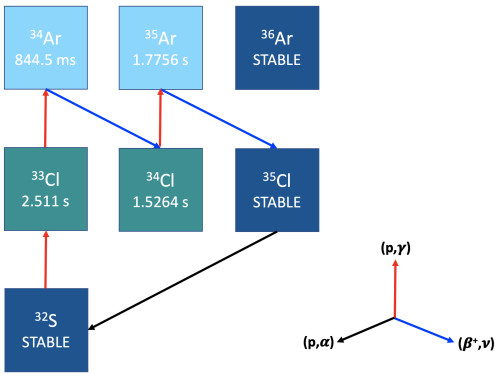

Figure 2.1: SCl cycle diagram. There are represented three types of processes: (p,α) is the black arrow, (p,γ) is the red arrow and (β^+,ν) is the blue arrow. The cycle starts from an even-even nucleus (^{32}S) with two successive proton captures up to ^{34}Ar, then a beta-decay leads to ^{34}Cl, a proton capture reaches ^{35}Ar, a further beta-decay brings down until ^{35}Cl and the closing reaction via (p,α) arrives to the initial ^{32}S nucleus.

Finally, the last purpose of the present work was the production of a chlorine target in order to go ahead with the PIGE experiment. This target had to comply with some requirements as to be self supported, thickness lower than 10 μm/cm^2 (to be considered a thin target) and to have a substantial amount of chlorine to obtain reasonable statistics.

2.1.1 Outline

The three main objectives of this part of the work were:

1. Determination of cross sections and gamma yields measurements for various reactions in ^{35}Cl and ^{37}Cl isotopes induced by low energy protons from the CTN/IST Tandem accelerator.

2. EnsarRoot code development to incorporate the entire PIGE experiment, starting from gamma rays generators, setup simulation to subroutines for data analysis.

3. The development of a technique in order to produce chlorine targets in the Target Laboratory of FCUL/LIP installations [21, 22] via vacuum deposition.

The steps to achieve these goals were:

USC UNIVERSIDADE DE SANTIAGO DE COMPOSTELA

- Chlorine target production in the Target Laboratory of FCiências and its posterior characterization by RBS technique at the Van der Graaff laboratory of CTN/IST [23].

- PIGE experiment: measurement of chlorine samples at CTN/IST Tandem accelerator.

- Gamma spectroscopy analysis of proton induced chlorine reactions.

- Implementation and simulations of the PIGE experiment within EnsarRoot.

- Cross sections calculations.

2.1.2 Chlorine: Physical and Chemical Properties

Chlorine was discovered by Carl-Wilhelm Scheele in 1774 [24], although until 1810 was not proved that it was an element. More concretely, it is the seventeenth element, the second of the halogen group (salt-forming). It was named *chloros* (green in greek) after its greenish-yellow color.

Physical Properties:

Under standard conditions[1] it is a dense gas made of Cl_2^- molecules with a density of 3,214 g/l, although it has never been found freely. Its melting and boiling points are -101,5°C and -34,04°C. To date there are known 24 isotopes ranging from ^{52}Cl [25] to ^{28}Cl and reported in NNDC [26], two of whom are stable: ^{35}Cl and ^{37}Cl with relative abundances of 0,7576(10) and 0,2424(10), respectively [27]. Most of the radioactive isotopes have small half-lifes except ^{36}Cl that has a half-life of $3,01(2) \times 10^5$ years [26]. As we have mentioned before, ^{37}Cl has a closed shell in the number of neutrons.

Chemical Properties:

Chlorine has the second highest electronegativity of all elements with a 3,16 on Pauling scale and, also, a high ionization energy of 12,97 keV [27], due to the smallness of the nuclear radius: 175 pm in the Van der Waals scale [28]. As a result, it is a very active element because it combines with all elements except in the case of noble gases. Sometimes, they combine explosively as in the formation of hydrogen chloride (HCl). Moreover, chlorine forms negative ions easily because it has the highest electron affinity of all elements with 3,617 eV [29], as a result, it is a strong oxidizing agent.

[1] Temperature of 25 °C and pressure of 1,01 bar.

USC UNIVERSIDADE DE SANTIAGO DE COMPOSTELA

In nature, it is commonly found in the Earth's crust and in seawater. It is the 20th most abundant element on earth with 145 mg/kg and it represents the 2 % of seawater as sodium chlorine (19,4 g/l) [30]. The most probable compounds are sodium chlorine (NaCl), also known as common salt, carnallite ($Cl_3H_{12}KMgO_6$) and sylvite (KCl) [28]. Electrolysis is the most conventional method of obtaining it [28].

Chlorine has been used for centuries for different purposes. Historically, it has been used as a food seasoning and food preservation. A curious fact is that tree frog skin contains chlorine compound, mortal in large doses and used as a painkiller in small quantities. Recently, it is employed also to kill bacteria that cause disease in water as in public water, swimming pools, etc. as well as to bleach products. Furthermore, the radioactive isotope ^{36}Cl is a useful tool in diverse investigations thanks to its long half life, for instance, it is used for geochronology (determining the geology and hydrology age) because some ^{36}Cl has a cosmogenic origin. Another interesting application is as a tracer in studies that investigate how seawater damages metals [31].

2.1.3 General Review of Available PIGE Cross Sections

In this section, a general review on the available data on chlorine proton induced reactions is presented aiming to list lacks and requirements on the reported data in the literature. Special attention is being given to the IBANDL PIGE database [32], because it is the reference site for PIGE technique. This investigation conducted our studies to fill the gaps in knowledge.

2.1.3.1 ^{35}Cl(p,p'γ)^{35}Cl reaction

Gamma emissions from ^{35}Cl(p,p'γ)^{35}Cl reaction have been studied by Kiss *et al.* [12] and Anttila *et al.* [13] in 1981 and Räisänen *et al.* [14] in 1987. All these analyses reported gamma yields normalized by stereoradian and charge, but no cross sections were provided.

In particular, Kiss *et al.* [12] studied gamma emissions from the first and second excited states, at 1219,3(2) and 1763,13(10) keV, respectively, at three specific proton beam energies 2,4, 3,1 and 3,8 MeV. The measurements were done with a Ge(Li) detector placed at an angle of 55° w.r.t. the beam direction and the beam was obtained from a 5 MV Van de Graaff accelerator of the Institute of Nuclear Research in Debrecen. The target used was a pellet of a non-specified chemical compound. This work was an extension of Anttila *et al.* [13] that investigates chlorine gamma emissions at 1, 1,7 and 2,4 MeV bombardement energies. The setup arrangements were a Ge(Li)

USC UNIVERSIDADE DE SANTIAGO DE COMPOSTELA

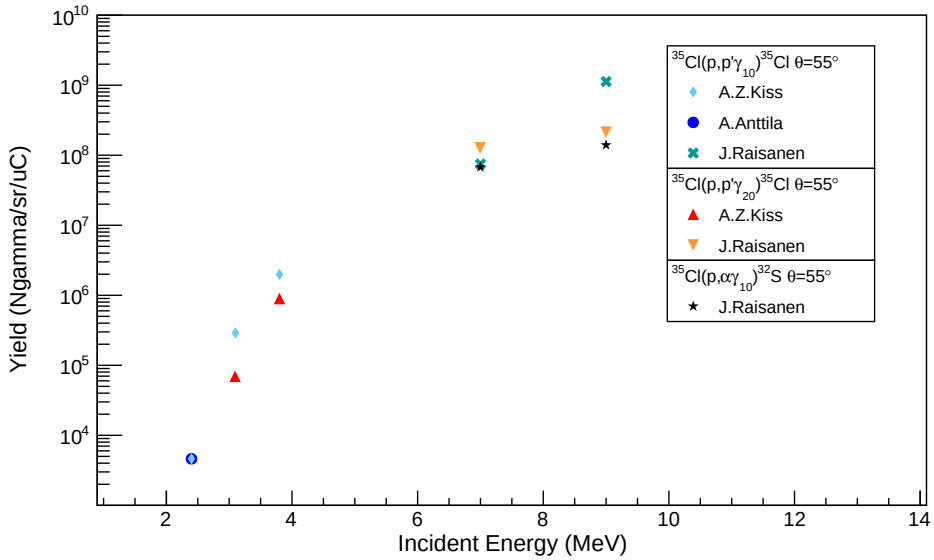

Figure 2.2: Diverse gamma ray yields of ^{35}Cl proton induced reactions. In the first legend there are represented in blue shades the gamma yields of the ^{35}Cl first excited state at 1219,3 keV from the reaction ^{35}Cl(p,p'γ)^{35}Cl determined by Kiss *et al.* [12], Anttila *et al.* [13] and Räisänen *et al.* [14]. In the second legend, there are represented in red shades the gamma yields of the ^{35}Cl second excited state at 1763,04 keV from the reaction ^{35}Cl(p,p'γ)^{35}Cl measured by Kiss *et al.* and Räisänen *et al.*. In the last legend, it is displayed the yield of 2230,49 keV peak from the ^{35}Cl(p,$\alpha\gamma$)^{32}S reaction studied by Räisänen *et al.*.

detector placed at 55° relative to the beam and the accelerator was a 2,5 MV Van der Graff located at the Helsinki University. The only information about the target was its thickness of 1 mm and diameter of 6 mm. In this case, they reported yields from more gammas: 670, 1219, 1642, 1970, 2127, 2168 and 2208 keV, though, only 1219 corresponds to (p,p'γ) reaction and it is only observed at the highest proton energy.

The last study of this reaction that appears at IBANDL [32] is Räisänen *et al.* [14]. They measured thick target gamma yields at two high impinging energies of 7 and 9 MeV. The Ge(Li) detector was situated at 55° w.r.t. the beam line and the proton beam was obtained from a 5 MV Tandem accelerator EGP-10-11 of the University of Helsinki laboratory. The targets utilized were NaCl and PbCl pellets of 1 mm thickness and 6 mm diameter. The yields reported were from gamma at 1219, 1763, 2230 and 3163 keV energies.

Spectra emitted from the ^{35}Cl first excited states and reported by these

USC UNIVERSIDADE DE SANTIAGO DE COMPOSTELA

three works are displayed in blue and red shades in Figure 2.2.

2.1.3.2 ^{35}Cl(p,$\alpha\gamma$)^{32}S reaction

The only gamma examined of (p,$\alpha\gamma$) reaction has an energy of 2230,49(15) keV and it was analyzed by Räisänen *et al.* [14]. It is coming from ^{32}S first excited state. As in the previous cases, the only accessible data are gamma yields at 7 and 9 MeV proton energies and they are displayed in black crosses in Figure 2.2.

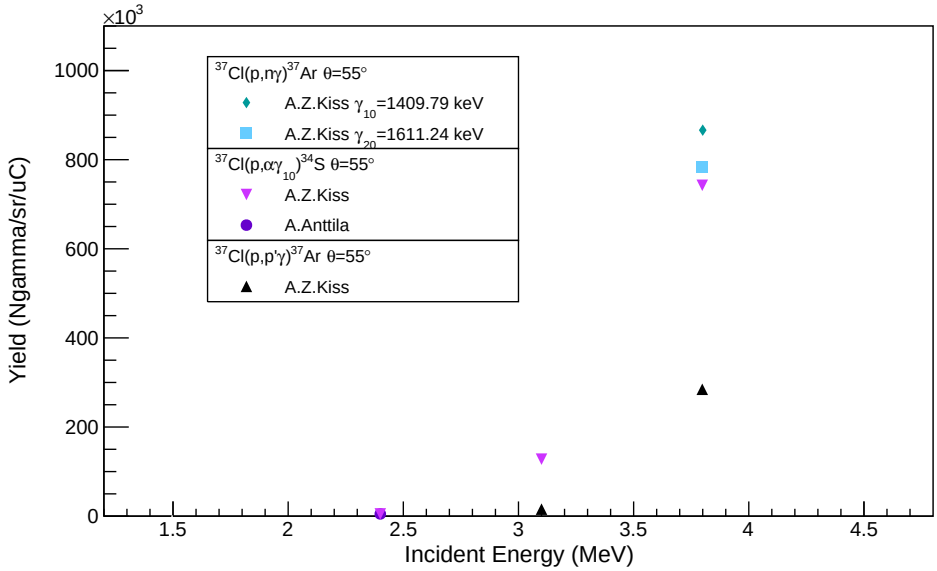

Figure 2.3: Diverse gamma ray yields of ^{37}Cl proton induced reactions. In the first legend there are represented in blue shades the gamma yields of the first and second excited states at 1409,79 keV and 1611,24 keV energies from the neutron channel ^{37}Cl(p,nγ)^{37}Ar measured by Kiss *et al.* [12]. In the second legend, there are represented the gamma ray spectra of 2127,499 keV line from the ^{37}Cl(p,$\alpha\gamma$)^{34}S reaction determined by Kiss *et al.* and Anttila *et al.* [13]. In the last legend, it is displayed the yield of 1726,4 keV peak from the ^{37}Cl(p,p'γ)^{37}Cl reaction studied by Kiss *et al.*.

2.1.3.3 ^{37}Cl(p,p'γ)^{37}Cl and ^{37}Cl(p,nγ)^{37}Ar reactions

In the previous mentioned work, Kiss *et al.* [12] also investigated the 1726,4(2) keV gamma yield of the first ^{37}Cl excited state by using the same procedure at 3,1 and 3,8 MeV proton incident energies. It is displayed in black in Figure

USC UNIVERSIDADE DE SANTIAGO DE COMPOSTELA

2.3. In the same paper, the neutron channel is investigated as it opens at relatively low energies. The gamma yields from the first ^{37}Ar excited states at 1409,79(7) and 1611,24(5) keV are shown in blue markers in the same Figure 2.3.

2.1.3.4 ^{37}Cl(p,$\alpha\gamma$)^{34}S reaction

Finally, the alpha channel of the ^{37}Cl isotope has been studied by Kiss *et al.* [12] and Anttila *et al.* [13] at three diverse energies and the gamma yields of 2127,499(20) keV peak are provided (purple markers in Figure 2.3). Moreover, Weber *et al.* studied this reaction in [15] over the range 1,25-2,15 MeV by bombarding $BaCl_2$ enriched to 98,2 % in ^{37}Cl targets with protons from the University of Melbourne 5U Pelletron accelerator. In this work two targets were used: one with a thickness of 64 keV for 1 MeV protons and the second around a quarter of the thickness of the previous one. The gamma rays were detected by Ge(Li) detectors of different sizes located at an angle of 55° w.r.t. the beam direction. The cross section measured in this last study is plotted in Figure 2.4 and its associated error is 12 %. It is noteworthy to mention that this is the only available cross section on which we will be able to compare our results.

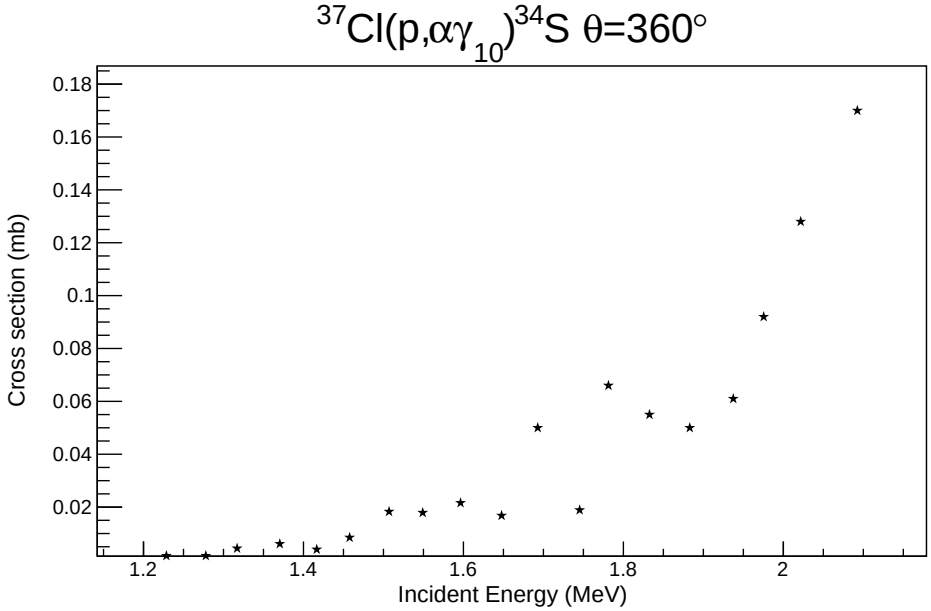

Figure 2.4: Cross Section of 2127,499 keV gamma ray from the ^{37}Cl(p,$\alpha\gamma$)^{34}S reaction measured by Weber *et al.* [15] over the range 1,25-2,15 MeV with an associated error of 12 %.

USC UNIVERSIDADE DE SANTIAGO DE COMPOSTELA

2.2 Motivation of the Environmental Gamma Study

The other line of investigation of the present thesis is the study of natural sources of radiation by measuring environmental background at different locations. Moreover, these gamma sources and environments have been recreated artificially inside the EnsarRoot framework. These studies will have a great impact at diverse branches of knowledge:

- **Lack of long term background spectrometry studies:** Although many efforts have been carried out in order to measure natural radiation [7, 33, 34, 35], it has been found a deficiency of background monitorization studies from gamma spectrometry approximation, especially, in the western part of the Iberian peninsula. Moreover, no temporal analysis of radioactive sources separately has been found, i.e., individual studies about the three series and the potassium decay.

- **Lack of background simulation studies:** Diverse simulation studies about the ^{137}Cs dispersion [36, 37], cosmic rays [38], Mondane laboratory background [39] among others have been published. However, no studies have been found that analyse natural radiation by simulating its emission and its mechanism of detection, and posteriorly comparing it with gathered data.

- **Environmental background study for PIGE experiment:** PIGE spectra is a sum of the environmental gamma radiation and the gamma yield coming from the nuclear reactions of the experiment, therefore, a good understanding of the CTN/IST laboratory natural background was required for PIGE data analysis. In addition, photopeaks from the background have been used to calibrate the HPGe detector at higher energies than the usual photopeaks of calibration sources. As a result, the two lines of investigations of the present thesis are complementary because background studies are used to interpret PIGE gamma data.

- **Radiation Health Effects:** Natural ionising radiation and artificial radioactivity are the two main contributors to the exposure of the human population. These radiations are able to damage the DNA of the living cells because they have enough energy to ionize matter. Although it is not a linear phenomena [40], continuous exposure to environmental radiation has long term health effects as increases the cancer risk [41]. Moreover, high levels of radiation causes irreparable health damage as skin burns or acute radiation syndrome [42]. In consequence,

USC UNIVERSIDADE DE SANTIAGO DE COMPOSTELA

environmental radioactivity monitoring and its analysis has become an important subject for national competent authorities, scientific community and population.

As we have mentioned before, the EnsarRoot framework is the key tool to conduct these studies. This framework has been further expanded to include gamma ray generators to reproduce gamma emissions from the natural occurring decays, in addition to the setups used to measure background radiation have been recreated in simulations. Moreover, simulated data and measured data have been equally analysed using the same subroutines and analytical environment. These improvements on the code could be used in the future for similar background studies carried out in the same installations or be used in comparable experiments. Furthermore, due to the fact that EnsarRoot is an open code, it can be modified and adapted by different users to other experiments not related to the ones conducted in this work.

2.2.1 Outline

The two main objectives of this part of the work are:

1. The temporal study of natural radiation at three different locations on the west of Iberian Peninsula which have diverse subsoil compositions and its posterior gamma spectroscopy analysis in order to compare them and find out pattern variations over time.

2. EnsarRoot code development to simulate environmental background. Gamma ray generators have been included to recreate natural radioactive chains and the potassium decay, as well as setup simulations. The previous measurements were also useful to benchmark the validity of these simulations at different environments.

The steps to achieve these goals were:

- EnsarRoot code implementation of the gamma rays generators which simulates the natural ionizing radiation. The development of the code incorporates the uranium, actinium and thorium radioactive chains, as well as the decay of ^{40}K.

- Environmental background measurements at three locations characterized by different types of soil using germanium semiconductor detectors with similar shapes and sizes. The two portuguese sites were CTN/IST (Lisbon) and Universidade da Beira Interior (Covilha) [43]. In Spain

USC UNIVERSIDADE DE SANTIAGO DE COMPOSTELA

the chosen site was the University of Santiago the Compostela [44, 45]. Measurements were done at the same sampling interval of 30 minutes in order to observe temporal variability.

- Gamma spectroscopy analysis of the previously measured environmental background. All radioactive series and potassium decay were analysed and monitorized. In addition, a time dependent analysis was carried out to study daily and hour variations.

- Simulation of the natural radiation formerly measured (including the three radioactive chains, potassium decay and cosmic rays showers) and the simulation of the setups where data was gathered. Subsequently, a benchmark between simulated and measured data was performed.

2.2.2 General Review of Available Data in Literature

2.2.2.1 Studies of Environmental Background

Diverse researches have been conducted over the past decades in order to map natural radiation at global and continental scale, especially since the Chernobyl accident, the IAEA organism and the European Commission [46] encouraged institutions to monitor environmental background and its eventual increase [7, 34].

Following these recommendations, the Consejo de Seguridad Nuclear (CSN) [47] and ENUSA [48] entity in Spain developed MARNA project since 1991 in order to map environmental radiation along the territory [34]. They surveyed 250 000 sites measuring gamma radiation at 1 m from the ground.

The most recent study carried out by the European Commission, under way for more than 10 years and published in 2019, is the European Atlas of Natural Radiation [7]. It is a large collection of environmental radiation maps of European Union member states together with general background information. This project also includes maps of concentrations of naturally occurring radionuclides, such as uranium, thorium and potassium in rocks. Moreover, diverse geochemical studies such as GEMAS [49], a study of grazing soils radioactivity around Europe, can be found in literature.

More concretely, in our region of interest, the terrestrial gamma dose rate was displayed in The Radiometric Map of Continental Portugal [35], and it is available for the general public at [50]. It was a long-term survey of 733 201 measurements acquired since 1950. It was intended to provide support for mineral and geothermic sources prospecting, geological mapping and risk studies. Also in Portugal, they compiled large-scale geochemical data

USC UNIVERSIDADE DE SANTIAGO DE COMPOSTELA

from literature sources to produce a geochemical database and investigate its usability [51].

The inconvenience of using the previously provided data is the large scale of the mapping (see, for example, Plate 4: European Terrestrial Gamma Dose Rate Map of [7] or the 1:500 000 map scale in [35]) in comparison to the installations where the background is measured at an experiment. As a result, the data from these studies can not be extrapolated.

At more local level, there are a large number of studies that investigate radioactivity along the portuguese territory: in the vicinities of mines [52], radionuclides from past uranium mining in rivers [53], estimation of the radon production rate in granite rocks [54], and even studies about the radioactivity detected in Lisbon after the Fukushima accident [55].

In the central part of Portugal, close to the Universidade da Beira Interior laboratory where we gathered environmental data, a study monitorized indoor radon levels and simultaneously measured diverse physical environmental variables as temperature, pressure, humidity, rainfall, and tides, in order to observe any influence in radon fluctuations [56]. It was found that radon exhibits daily variability but not an obvious long-term trend, these oscillations are found to be linked with outdoor temperature variations (although this correlation is complex and not linear) and a weak relation with outdoor relative humidity.

Near the same portuguese region, another research [57] studied the temporal variability of radon in a remediated tailing of uranium ore processing. They observed complex temporal structures on radon concentrations, as a strong asymmetric diurnal variability, and no influence of the environmental conditions.

Other local studies measured radon concentrations in the north-west of Spain (where we performed some measurements) [58, 59]. The former measured indoor radon concentrations in the Santiago de Compostela area; the research revealed a direct correlation between the indoor radon concentration and the outdoor temperature, although no other dependences could be established with other physical constraints such as barometric pressure, wind direction, humidity, etc. In the second study, an extensive radon measurement was carried out at secondary schools in the largest radon-prone area in the Iberian Peninsula; radon concentrations were analysed in order to ensure health conditions, and its seasonal variations were monitorized in some selected schools, although no significant correlations were established.

In general, some studies report direct correlations between radon levels and precipitation [60, 61], atmospheric pressure fluctuations [62, 63], soil surface [64], seismic events [61, 64] and general meteorological variations [65]; others claim that these dependences are not well established [66, 67]. Indeed

USC UNIVERSIDADE DE SANTIAGO DE COMPOSTELA

in the vast majority, if not all cases, they coincide with radon concentration fluctuations exhibit complex patterns depending on multiple factors such as geographical characteristics, meteorological conditions, ventilation rates of indoor measurements, among others. Consequently, this research subject is still under investigation and debate.

Although many studies have been found about radon monitoring and how external factors influence radon emanation and diffusion, no gamma spectroscopic studies of the radioactive series separately or the potassium decay near the vicinity of the installations used in this thesis have been found.

2.2.2.2 Studies of Environmental Radiation Simulations

Many studies about natural radiation simulations have been published in recent years. They investigate a wide variety of aspects using distinct simulation tools. In this subsection some interesting works are presented.

The study of ionizing radiation coming from building materials, as well as natural radiation, is crucial for low background physics experiments as the ones conducted in the Modane underground laboratory [68]. In a study [39], they simulated gamma ray background induced by the typical radioactive sources along with the radioactive contamination of the construction materials of diverse parts of the setup as shieldings or the detector holder. Monte Carlo simulations were done using GEANT4 software package. This research is the most comparable to the work carried out in the present thesis due to the fact that they used the same type of detector, a gamma-ray spectrometer, and similar simulation tools.

In another research with similar conditions [69], they maximize the sensitivity of an HPGe spectrometer in the case of low-energy and low-activity radionuclides. They use a Monte Carlo simulation to determine the optimum material and thickness of the germanium detector to be used in environmental radiation measurements.

Gamma background measurements were carried out at high mountain altitude in the Basic Environmental Observatory Moussala with the purpose of measuring dose rates [70]. At those altitudes cosmic radiation is an important fraction, therefore, they simulated this contribution using a Monte Carlo simulation tool called CORSIKA 6.52 and FLUKA. Also at the same observatory, there is another study where cosmic rays experimental data is compared with Monte Carlo simulations using a numerical model [38].

Moreover, diverse works have been found where the Fukushima radiation is studied after the nuclear incident. In [71] they simulate outdoor ambient dose at three suburban sites near the power station. On the other hand,

USC UNIVERSIDADE DE SANTIAGO DE COMPOSTELA

some research are centered in the ^{137}Cs dispersion in the world ocean [36] and the reproduction of the ^{137}Cs atmospheric dispersion at large-scale [37].

As it has been seen, many studies about the simulations of natural or artificial ionizing radiation have been found, although they have been aimed to solve practical reasons, such as efficiencies or dose rates, not aiming to investigate environmental radiation itself. To our knowledge, there is no gamma spectroscopy analysis of natural background using simulated radiations as a benchmarking.

USC
UNIVERSIDADE DE SANTIAGO DE COMPOSTELA

Chapter 3

METHODOLOGY: THEORETICAL SECTION

3.1 PIGE Technique

3.1.1 IBA Techniques

The progressive development and enhancement of nuclear facilities in the first half of the twentieth century led to the birth of analytical techniques Ion Beam Analysis (IBA). Among the first Nuclear Reaction Analysis (NRA) that appeared in the decade of 1950 we count Particle Induced Gamma-ray Emission (PIGE) and Rutherford Backscattering Spectrometry (RBS). In the following decade, the development of semiconductor detectors and the upgrading of accelerators allowed the expansion of this field around the world. One of the most used IBA techniques, Particle Induced X-ray Emission (PIXE) was employed for the first time in 1970.

IBA techniques are based on the detection of the products originated by the interaction of an ion beam with the atoms of a sample through nuclear or atomic reactions [72]. The ion beam is generally composed of light ions, as protons, deuterons or alpha particles, with energies in the MeV range. The particles detected, which can be either photons or ions, are emitted during the irradiation and their energy and angular distributions characterize the atoms in the target. The delayed emissions, due to neutron activation for example, are not included in this group.

They comprise a wide definition due to each technique greatly differ from each other. Therefore, the study of a sample could be performed at different levels: elemental, isotopic, depth, spatial, etc. This versatility makes the application of them to diverse fields possible.

The main IBA techniques and their principle of detections are briefly pre-

USC UNIVERSIDADE DE SANTIAGO DE COMPOSTELA

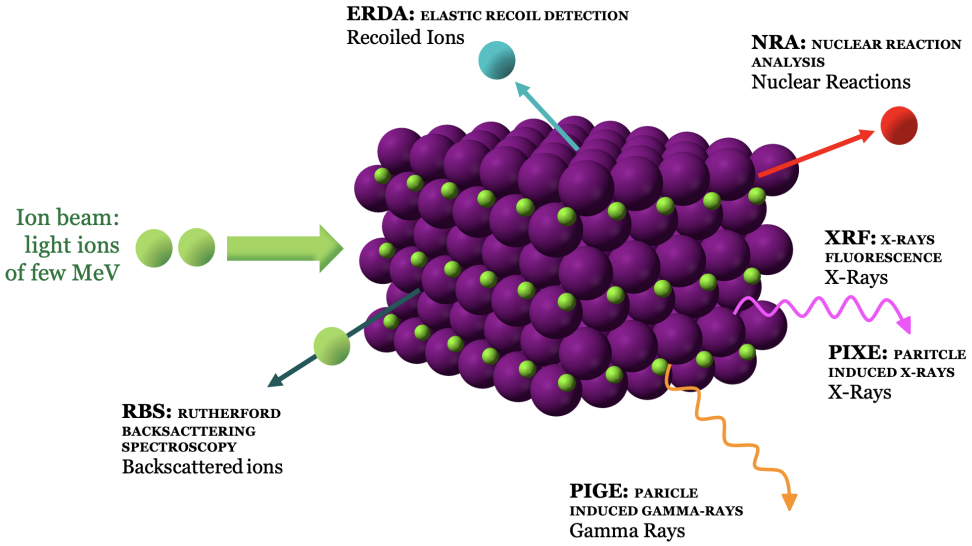

Figure 3.1: Scheme of diverse IBA techniques. On the left the incoming beam is represented by green particles, in the central part, the sample under analysis is placed (purple particles) and surrounding it there are different techniques: ERDA (which measures elastcially-recoild ions depicted by blue particles), NRA (which measures the outcoming particles of a nuclear reaction and these are depicted by red particles), XRF and PIXE (which measure X-rays depicted by pink photons), PIGE (which measures gamma rays depicted by orange photons), and RBS (which measures backscattered ions depicted by green particles).

sented below [5]. In Figure 3.1 there is a scheme of the different techniques.

- Particle Induced X-ray Emission (PIXE): detection of X-rays emitted by the atoms, and X-rays Fluorescense (XRF) measures the secondary X-ray (fluorescent) from the atoms when they have been excited by the previous emission of a primary X-ray induced by the beam ion. Both involve an electromagnetic interaction between the ion beam and the electrons in the atoms.

- Rutherford Backscattering Spectrometry (RBS): detection of incoming ions that have been backscattered by the electromagnetic interaction (Coulomb repulsion).

- Elastic Recoil Detection Analysis (ERDA): detection of incoming ions that have been elastically scattered by the electromagnetic interaction (Coulomb repulsion).

USC UNIVERSIDADE DE SANTIAGO DE COMPOSTELA

- Nuclear Reaction Analysis (NRA): based on the detection of the emitted particles produced after a nuclear interaction.
- Particle Induced Gamma-ray Emission (PIGE): detection of gamma rays emitted after the induced nuclear reaction.

In this thesis two IBA techniques have been used: RBS and PIGE, and they will be explained in more detail in the following sections. It's worth to mention that RBS and ERDA rely on the same detection principle, however, they have different setup configurations: the detector in ERDA is placed in front and in RBS aback. In some cases, during one single irradiation different techniques can be carried out simultaneously. This is of a great advantage because some of them are complementary and more information about the sample could be obtained. Moreover, due to the fact that they are multielemental, diverse chemical elements are analysed together.

These techniques are widely used because they are generally non-destructive for most materials, usually mineral and metallic samples, although, samples more sensitive and delicate, such as organic, could suffere some damage induced by the impinging beam [73]. Some observed alterations are: change of visual appearance, loss of water (dehydration), break of chemical bonds (radiolysis), among others. In anticipation, all the sensitive targets are treated with low beam intensities (0,1 nA) during short time intervals (100 s). The samples do not need to be treated beforehand, they can be operated directly [73].

On the other hand, these techniques have some limitations. It is only possible to study the near-surface of the sample (between 10 and 20 μm) and the bulk of the sample is only accessible by disposal alteration [73]. Another drawback is that they do not provide any information about the chemical state of the material's elements. In addition, for some insulating materials the charge collection during the irradiation and the electrical charging could be problematic.

3.1.1.1 Rutherford Backscattering Spectrometry (RBS)

Rutherford Backscattering are head-on collisions at low energies between two nuclei where the lightest and incoming one is scattered backwards[1]. It is named after its discoverer E. Rutherford, who performed the famous gold foil experiment in 1911 and, afterwards, theorized that in the central part of the atom (nucleus) all the positive charge was placed [74]. These reactions

[1]This only happens if the beam nucleus is lighter than the target nucleus. Otherwise, if it is heavier, the beam particles are scattered forwards.

USC UNIVERSIDADE DE SANTIAGO DE COMPOSTELA

are dominated by the electromagnetic interaction because their energies do not allow them to come closer to induce nuclear reactions.

Rutherford Backscattering Spectrometry is an IBA technique based on this type of reactions [5, 72]. The experimental method consists on a positively charged light ion beam, usually alpha particles, which is deflected after hitting a sample at large angles (beyond 150°) by the repulsive electrostatic fields created by the positive charge of the sample's nuclei.

To ensure that only pure Rutherford scattering occurs, the beam energy (E_1) must be lower than the Coulomb barrier,

$$E_1 < \left(\frac{e^2}{4\pi\varepsilon_0}\right)\frac{Z_1 Z_2}{1,4(A_1^{1/3}+A_2^{1/3})}, \tag{3.1}$$

avoiding, thus, any nuclear reaction. Moreover, the projectile energy should be high enough (over MeV) to neglect the screening effect created by the electrons which, at large impact parameters, reduce the positive effective charge of the nucleus. As a result, the suitable energetic window for alpha particles is comprised between 1 and 3 MeV. In the previous equation, the subindex 1 represents the impinging ion while the subindex 2 denotes the target nucleus, Z and A are the respective atomic number and atomic mass number, e is the electron charge and ε_0 is the vacuum permittivity.

The probability of an ion being scattered by the target nucleus in the Laboratory Reference System is expressed by the Rutherford scattering cross section formula (Eq. 3.2). It should be noted that this is a differential scattering cross section meaning that this probability is expressed only for a particular angle. Experimentally talking, this will be the scattering that you receive in your detector as a signal at the angle that is placed [5].

$$\left(\frac{d\sigma}{d\Omega}\right)_{lab} = \left(\frac{Z_1 Z_2 e^2}{8\pi\varepsilon_0 E_1}\right)^2 \cdot \frac{1}{\sin^4\theta} \cdot \frac{\left[M_2\cos\theta + (M_2^2 - M_1^2\sin^2\theta)^{1/2}\right]^2}{M_2 \times (M_2^2 - M_1^2\sin^2\theta)^{1/2}}. \tag{3.2}$$

In the previous equation θ is the backscattering angle in the same Laboratory Reference System. The fact that in most experiments the mass difference between projectile and target nuclei is large ($M_2 \gg M_1$) makes the below approximation the most employed:

$$\left(\frac{d\sigma}{d\Omega}\right)_{lab} = \left(\frac{Z_1 Z_2 e^2}{16\pi\varepsilon_0 E_1}\right)^2 \frac{1}{\sin^4(\theta/2)}. \tag{3.3}$$

USC UNIVERSIDADE DE SANTIAGO DE COMPOSTELA

This probability is proportional to the square of the atomic numbers (Z_1 and Z_2) and inversely proportional to the square of the beam energy (E_1). Moreover, Rutherford scattering increases for forward angles going as $1/\sin^4(\theta/2)$.

Some deviations from the Rutherford formula could appear in certain regions in the form of resonant structures or smooth variations. These enhanced cross sections do not obey Rutherford law and are called non-Rutherford scattering cross sections. This happens when the nuclear interaction between the projectile and the target nuclei becomes significant due to the fact that the distance of closest approach between the projectile and the sample nucleus (d) is comparable to the nuclear size (see the scheme of Figure 3.2). This can occur when: the incident energy (E_1) is higher than the Coulomb barrier and the scattering angle (θ) is high. In the case of alpha particles, this structures are important (> 5 % than the Rutherford cross-section) at angles between 160° and 180° when [5]

$$E_1(\text{MeV}) > 0,25\ Z_2 + 0,4, \tag{3.4}$$

and for protons at

$$E_1(\text{MeV}) > 0,12\ Z_2 - 0,5. \tag{3.5}$$

There are diverse databases of non-Rutherford scattering cross sections included, in addition, in some computer simulation codes [75, 76].

There is another situation when the cross section of the reaction does not correspond to the Rutherford equation. Under certain circumstances such as, low beam energies (E_1), low scattering angles (θ) and high atomic number (Z_2), the electron cloud shields the effective positive charge of the nucleus. In this case, the Rutherford scattering cross section must be multiplied by a shielding factor $F(E, \theta)$ [5].

This technique allows a multielemental analysis, although it can also lead to a technique limitation since no light elements can be detected on heavy substrates because signals overlap. Another constraint that arises from the formulas is the impossibility of an isotope differentiation due to they depend on the atomic number (Z_2) which is equal for all isotopes. As all IBA techniques, RBS is a nondestructive method.

The excellent knowledge acquired of the Rutherford cross sections of various elements over the years allows to calculate the exact quantities of the elements in a sample by only applying conservation laws. Moreover, these calculations do not require standards to determine these quantities.

USC UNIVERSIDADE DE SANTIAGO DE COMPOSTELA

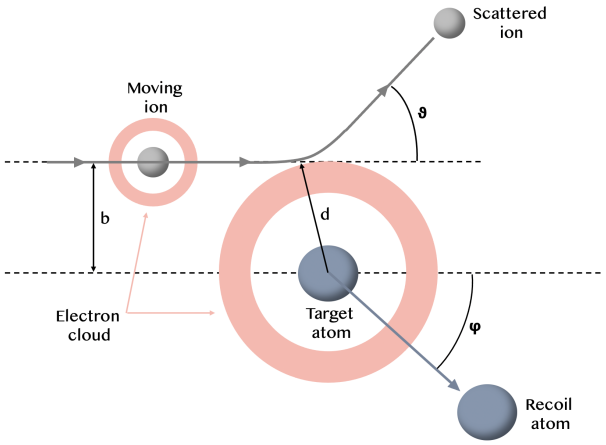

Figure 3.2: Schematic view of an interaction between an impinging ion and an atom of the target in the Laboratory Reference System where different parameters are featured: impact parameter (b), distance of closest approach (d), backscattering angle (θ) and recoiling angle (φ).

Kinematics and Scattering Fundamentals

The kinematics of RBS basic reaction is presented in Figure 3.3 with X(a,a)X notation. The projectile a, with a mass M_1 and an initial velocity v_1 and energy E_1, suffers the Coulomb repulsion induced by the target atom X which is at rest in the Laboratory Reference System. The incident ion is backscattered by an angle θ drawing an hyperbolic trajectory and the atom is recoiled with an angle φ. This type of collisions is explained by classical mechanics. The dynamic parameters of a typical scattering reaction are featured in Figure 3.2. The initial distance between the ion and atom centres perpendicular to the ion trajectory is the so-called impact parameter b and is related with the others parameters as [5],

$$b = \frac{Z_1 Z_2 e^2 \cot(\theta/2)}{4\pi\epsilon_0 M_1 v_1^2}. \tag{3.6}$$

The distance of closest approach d is determined by the initial energy and the already described impact parameter. It is defined as,

$$d = \frac{Z_1 Z_2 e^2}{4\pi\epsilon_0} \frac{1}{E_1}. \tag{3.7}$$

The previous two equations are interrelated as,

$$b = \frac{d}{2} \cot(\theta/2). \tag{3.8}$$

USC UNIVERSIDADE DE SANTIAGO DE COMPOSTELA

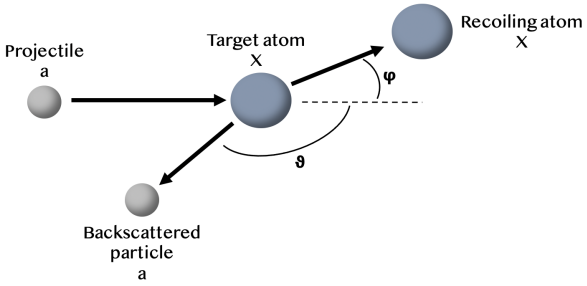

Figure 3.3: Principle of the RBS technique: Beam of low-mass ions of 1-3 MeV is made to impinge on the atom's sample which recoils with an angle φ and the particles scattered through angle θ are detected by a particle detector. The scheme is represented in the Laboratory Reference System.

For backscattering collisions the projectile and the target must be so close that the distance of closest approach is the K-shell radius of the target atom, although the Coulomb barrier is not surmounted, otherwise, nuclear reactions appear. This is the reason for not considering the screening effect created by electrons in the dynamic, even if Figure 3.2 the electron cloud is represented as a red area wrapping the nuclei. On the contrary, when the impact parameter is very large, the energy transferred is almost negligible and the scattering angle small, hence, the projectile is deflected in the forward direction.

In the case the target atom mass is smaller than the projectile mass, the impinging particle is sent always forward. As a result, in such an experiment, the detector is placed in front of the sample and not in the back position. Otherwise, there is no sensitivity because no projectiles coming from that element are detected.

Kinematic Factor

The Kinematic factor is the quantity that indicates the energy transferred from the impinging projectile to the target atom [5]. Therefore, it is defined as the ratio between the incident particle energy and the final scattered particle energy (E_{1f}), following the same notation,

$$K = \frac{E_1}{E_{1f}}. \tag{3.9}$$

After some algebra, and considering the conservation of energy and momentum, it can be expressed only in terms of masses and scattering angle as

USC UNIVERSIDADE DE SANTIAGO DE COMPOSTELA

[5],

$$K = \left[\frac{(M_2^2 - M_1^2 \sin^2\theta)^{1/2} + M_1 \cos\theta}{M_1 + M_2} \right]^2 . \tag{3.10}$$

So, the Kinematic factor is independent of the initial and final particle energies. This is of great advantage because this parameter allows to identify the unknown elements present in a sample. If we consider two extreme cases, when the particle is backscattered to $\theta = 180°$ and forward scattered to $\theta = 0°$ and a redefinition of the masses $x = M_1/M_2$ is included:

$$K\ (\theta = 180°) \ = \left(\frac{M_2 - M_1}{M_2 + M_1} \right)^2 = \left(\frac{1-x}{1+x} \right)^2 , \tag{3.11}$$

$$K\ (\theta = 0°) \ = \left(\frac{M_2 - M_1}{M_2 + M_1} \right) = \left(\frac{1-x}{1+x} \right). \tag{3.12}$$

It is concluded that, for the same ion beam and sample, the energy transferred in the backward direction is the square of the energy transferred to the particles in the forward direction. Moreover, taking the same projectile beam (M_1) for elements with higher mass (M_2) the energy transferred would be larger.

Energy Loss, Stopping Power, Straggling and Range

When an incident beam enters into the target material, different processes occur until reaching the target atom. Along these processes the impinging particle loses energy, hence, the scattering produced in the surface is more energetic than one in greater depths. This energy is called energy loss, and the energy loss per unit path length is the stopping power of the material for a particular ion beam and energy. It depends on one side on the charge and velocity (energy) of the projectile, and on the other side, on the elements and density of the sample material. A typical stopping power for an alpha particle of 2 MeV is in the range of 100 to 800 eV/nm.

There are two possible interactions between the bombarding ions and the atoms of the material: inelastic collisions with the atomic electrons and elastic collisions with the nucleus. In the IBA range of energies (1-3 MeV/u) the energy loss is mainly due to collisions with electrons inducing excitation and ionization of the sample atoms.

The Bethe formula gives the mean rate of stopping power for a particular charged particle,

USC UNIVERSIDADE DE SANTIAGO DE COMPOSTELA

$$-\frac{dE}{dx} = \left(\frac{e^2}{4\pi\varepsilon_0}\right)^2 \cdot \frac{4\pi Z_1^2}{m_e v_1^2} \cdot \frac{\mathcal{N}_A Z_2}{A} \cdot \left(ln\frac{2m_e v_1^2}{I}\right), \tag{3.13}$$

where m_e is the electron mass, $\mathcal{N}_A$ is the Avogadro number, A the atomic weight of the target and the symbol I is the mean excitation energy. Particularly important is the fact that the energy loss does not depend on the ion beam mass, as a result, the stopping power is the same for protons, deuterons, etc. In general, it is proportional to the electronic density of the material. In the "high energy" regime (above 100 keV for alpha and 25 keV for protons) the stopping power is proportional to $Z_1^2 Z_2/E$ ratio, as a result, dE/dx decreases as the energy beam increases. Moreover, the Z_1^2 dependence makes that the energy loss of alpha's will be four times bigger than for protons. There are some useful programs such as SRIM [77] or LISE [78] that estimate this value for different material's composition.

The spread of energy loss (dispersion) is called energy straggling and it is caused by statistical fluctuations in the energy loss. This quantity is the average over all interactions occurred along the beam trajectory that fluctuate in number and type (quantity of energy transferred).

As inelastic collisions with the electrons domain, the energy straggling increases with the atomic number since the number of electrons present in the sample also augments. It causes a spread in the FWHM of the ion inicial energy that limits the energy resolution of the beam, resulting in a limit in the depth and mass resolution. Furthermore, the energy straggling increases with depth due to more collisions are given.

Another parameter that describe the projectile dynamics is the range (distance) travelled into an specific material until it stops,

$$R = \int_0^{E_1} \frac{dE}{S(E)}, \tag{3.14}$$

where $S(E) = -(dE/dx)$ is the stopping power.

Thin and Thick Targets

Figure 3.4 shows the different possible beam trajectories across a thin and a thick target and the energy loss in each case. They are described by three angles: α is the angle between the target normal and the direction of the incident beam (incident angle), β is the angle between the the target normal and the scattered particle (exit angle), and θ is the subtraction between 180° and β angle (scattering angle), the three of them are always considered positive.

USC UNIVERSIDADE DE SANTIAGO DE COMPOSTELA

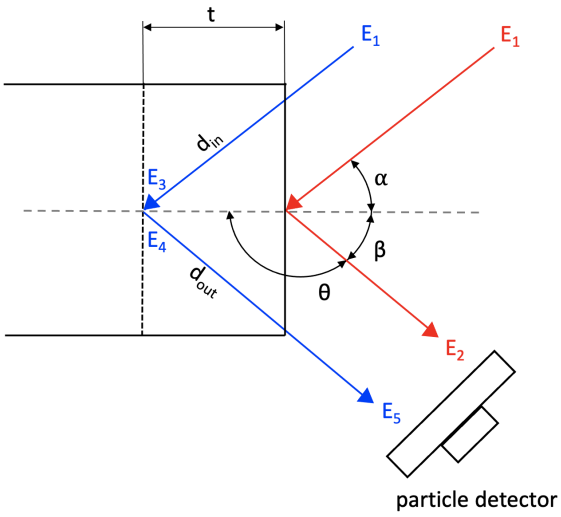

Figure 3.4: Schematic diagram to illustrate scattering trajectories and energy losses for a thin target (red) and for a thick target (blue), where α is the incident angle, β the exit angle and θ the scattering angle.

In the first case (red line), a thin target is considered and the backscattered energy is

$$E_2 = KE_1, \tag{3.15}$$

which is the same as the detected energy.

In the second case (blue line), a thick target is considered. The ingoing and outgoing paths at depth t are

$$d_{\text{in}} = \frac{t}{\cos\alpha}, \qquad \text{and} \qquad d_{\text{out}} = \frac{t}{\cos\beta}.$$

At the entrance of the surface the energy of the beam is the same, E_1, and the energy at depth t just before the scattering is

$$E_3 = E_1 - \int_0^{t/\cos\alpha} \frac{dE}{dx}dx \simeq E_1 - \frac{t}{\cos\alpha}\left[\frac{dE}{dx}\right]_{E=E_1}, \tag{3.16}$$

at depth t, just after the scattering the particle energy is

$$E_4 = KE_3, \tag{3.17}$$

and finally the particle energy after leaving the surface (detected energy) is

USC UNIVERSIDADE DE SANTIAGO DE COMPOSTELA

$$E_5 = KE_3 - \int_0^{t/\cos\beta} \frac{dE}{dx} dx \simeq K\left[E_1 - \frac{t}{\cos\alpha}\left[\frac{dE}{dx}\right]_{E=E_{01}}\right] - \frac{t}{\cos\beta}\left[\frac{dE}{dx}\right]_{E=KE_1}. \tag{3.18}$$

The energy loss in the target is the difference between the energy of an ion scattered on the surface and an ion scattered from an atom at depth t,

$$\Delta E = E_2 - E_5 \simeq \left[K\frac{1}{\cos\alpha}\left[\frac{dE}{dx}\right]_{E=E_1} + \frac{1}{\cos\beta}\left[\frac{dE}{dx}\right]_{E=KE_1}\right] t. \tag{3.19}$$

In the case of normal incidence the incident angle is $\alpha = 0$ and the previous equations change accordingly.

The average over all possible ion trajectories through the target is considered in the previously defined stopping power (Eq. 3.13). Therefore, these two magnitudes where the energy is dissipated are related as,

$$\frac{\Delta E}{\Delta t} \simeq \left.\frac{-dE}{dx}\right|_{E=E_1-\Delta E/2}, \tag{3.20}$$

this is, the fraction of the energy loss (ΔE) and the average path length (Δt) is a good approximation to the stopping power $-dE/dx$ at an average energy of $E = E_1 - \Delta E/2$.

3.1.1.2 Particle Induced Gamma-Ray Emission (PIGE)

Light ion beams, as proton, deuteron or alpha-particles, in the MeV energy range are capable of surmounting the Coulomb barrier of the lightest target elements and approach to a distance of the order of the nuclear radius. As a result, a compound nucleus in a highly excited state is created and, sometimes, charged particles are emitted. Consecutively, this remaining nucleus de-excites by the emission of gamma rays. The detection of these gamma rays is the principle of PIGE technique and the detection of the emergent particles is called NRA. These interactions are dominated by low-energy nuclear forces. The most important reactions than can occur are: scatterings as (p,p'γ), (α,α'γ) or (d,d'γ) and nuclear reactions (p,γ), (p,$\alpha\gamma$), (p,nγ), etc.

Therefore, the basic principle of PIGE is the measurement of gamma yields coming from the target and the sample's elements are characterized by determining the energies of these gammas. Moreover, due to each particular nucleus has its own energy levels depending on the number of nucleons and their dispositions, an isotopic differentiation is possible considering each

USC UNIVERSIDADE DE SANTIAGO DE COMPOSTELA

nucleus has its own gamma pattern. Sometimes, the aforementioned gamma emissions are also called prompt emissions because they take place during the irradiation (< 1 s).

As we have just stated, PIGE is based on nuclear reactions happening when the ion beam surpass nucleus repulsion and this only happens when the Coulomb barrier is weak[2], this is, when the sample elements are Z<20. The good part is that elements with Z<16 correspond to 95 % of the Earth crust. This fact is of great convenience because most materials could be studied under PIGE technique. On the other hand, this feature is also a technique limitation due to all elements with Z>20 are inaccessible. On the contrary, PIXE technique only is used with elements with Z>20, when the X-rays are strong enough to be detected (more energetic). For these reasons, many times in literature PIXE and PIGE techniques are seen as complementary methods because both cover the whole nuclear chart.

In order to detect one element in a sample using PIGE technique its cross section must be large enough to induce nuclear reactions. The cross section also depends on the energy of the impinging beam. As a result, the sensitivity of PIGE is not constant for a particular nucleus and beam. In comparison to PIXE cross sections, they are some orders of magnitude smaller.

Kinematics of PIGE Nuclear Reaction

The following Eq. 3.21 represents the nuclear reaction occurring during the process and Figure 3.5 shows its dynamic. The incident particle "a" with a mass M_1 impinges on the target nucleus "X" of mass M_2 and the formation of a compound nucleus occurs, such as "X+a". This intermediate nucleus labeled as X^* splits into the recoil nucleus "Y" with a mass M_4 and into a smaller particle "b" with a mass M_3. Finally, if the recoil nucleus has remained in an excited state it de-excites emitting gamma cascades represented as "nγ" in the equation. The angles φ and θ represent the angle formed by the "Y" nucleus and the "b" particle with respect to the beam direction.

$$\mathrm{X} + \mathrm{a} \rightarrow \mathrm{X}^* \rightarrow \mathrm{Y} + \mathrm{b} + \mathrm{n}\gamma. \tag{3.21}$$

The Q-value of the reaction is, therefore,

$$Q = E_3 + E_4 - E_1 - E_2, \tag{3.22}$$

where E_3, E_4, are the kinetic energies of the products (E_4 still includes the gamma energy E_γ) and E_1, E_2 the kinetic energies of the inicial corpuscles.

[2]Indeed, elements which can be analyzed are those whose atomic number are comprised in 3<Z<20.

USC UNIVERSIDADE DE SANTIAGO DE COMPOSTELA

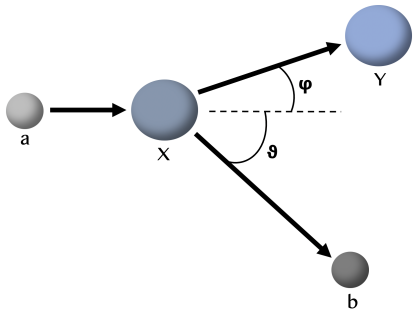

Figure 3.5: Schematic representation of a nuclear reaction dynamics in the Laboratory Reference System.

Considering all dynamics in the Laboratory Reference System the kinetic energy $E_2 = 0$ due to the target nucleus is at rest. In exothermic nuclear reactions ($Q > 0$) each particle of the beam carrying an energy E_1 could generate a nuclear reaction. On the contrary, endothermic reactions ($Q < 0$) requires a minimum energy $E_1 > E_{threshold}$ to start the reaction.

From the previous equation we know that the total energy is $E_T = E_1 + E_2 + Q = E_3 + E_4$. Applying energy and momentum conservation laws, we obtain that the ratio between the smallest product and the total energy is [5],

$$\frac{E_3}{E_T} = B\left[\cos\theta \pm \left(\frac{D}{B} - \sin^2\theta\right)^{1/2}\right]^2, \tag{3.23}$$

and the ratio between the recoil nucleus and the total energy is,

$$\frac{E_4}{E_T} = A\left[\cos\phi \pm \left(\frac{C}{A} - \sin^2\phi\right)^{1/2}\right]^2, \tag{3.24}$$

where some constants have been redefined as:

$$\begin{aligned}
A &= \frac{M_1 M_4}{(M_1+M_2)(M_3+M_4)}\frac{E_1}{E_T}, \\
B &= \frac{M_1 M_3}{(M_1+M_2)(M_3+M_4)}\frac{E_1}{E_T}, \\
C &= \frac{M_2 M_3}{(M_1+M_2)(M_3+M_4)}\left(1+\frac{M_1 Q}{M_2 E_T}\right), \\
D &= \frac{M_2 M_4}{(M_1+M_2)(M_3+M_4)}\left(1+\frac{M_1 Q}{M_2 E_T}\right).
\end{aligned}$$

USC UNIVERSIDADE DE SANTIAGO DE COMPOSTELA

The previous expressions have a non-relativistic treatment, due to mass energies are in the range of GeV while these interactions are in the order of few MeV.

At this point, it is worth to discuss the Coulomb barrier due to its importance. As we have defined before, it is the repulsive nuclear force created between the impinging particle and the target nucleus. On the contrary of RBS reactions, the kinetic energy of the incident particle E_1 must be higher than this force to undergo nuclear reactions, which is over 1 MeV in these type of processes (see Eq. 3.1) [5].

Although less probable, when the energy of the incident ion is smaller than this potential barrier, under-barrier reactions are also feasible thanks to quantum mechanics effects. One example would be (p,p'γ) reactions, studied in this thesis, where the incident ion and the sample's nucleus interchange energies through Coulomb interaction leaving the nucleus in an excited state which de-excited to ground state emitting gamma rays. Above the Coulomb barrier, lots of channels open and the number rises as energy increases.

Depth Profiling

Gamma rays do not lose energy when passing through matter, they are only attenuated in intensity or, in other words, they do not provide information about the depth from which they have been created. Therefore, the PIGE method is not capable of measure profile concentrations as NRA does measuring the energy loss of the outcoming particles.

In spite of that, a strong resonance in the cross section could be used to perform depth profiling analysis with greater resolution than other IBA methods [6]. Hereafter it is explained in further detail. At certain energies, there are resonances in the cross section of the reaction more outstanding and narrow than in the non-resonant regions. Setting the beam energy at these certain energies a strong resonance is induced on the surface of the sample and by increasing the energy of the beam this resonance would start to move through the material. The energy beam is increased sequentially above the resonance energy to compensate the ion energy loss while penetrating the material. A depth profile would be obtained when plotting the gamma yield from the reaction versus the beam energy loss. This method allows an isotopical discernment as the cross sections change on every isotope. If the lightest elements are under analysis inverse kinematics with heavier beams, such as ^{15}N for ^{1}H target, are used [79, 80]. Particularly important is the hydrogen depth profiling to study hydrogen in materials because most techniques can not do it [81]. Figure 3.6 shows visually this depth profiling

USC UNIVERSIDADE DE SANTIAGO DE COMPOSTELA

method [6].

The beam energy loss is defined as the difference between the energy of the impinging particles and the energy of the resonance and it can be converted into atoms/cm^2 or to nm. In consequence, this energy loss gives information about the depth in every step. This conversion could be done if the composition of the sample is already known because it uses the density of the material and the stopping power of the beam in that material. Surprisingly, the detector resolution does not affect the depth resolution, it is only determined by the width of the resonance (usually in the order of nm). Although, in an experiment there are other factors that should be taken into account as the beam energy resolution and the Doppler broadening.

The profile of the concentration is calculated as the integral over the beam energy resolution, the beam energy straggling and the resonance width. This calculation could also be performed by ERYA (Emitted Radiation Yield Analysis) code [82, 83]. This program is a software application specialized in PIGE analysis.

Thin and Thick Targets

PIGE analysis could be done by two distinct approaches which highly differ with each other depending on the target thicknesses. Targets with thickness below 10 μm are considered thin, on the contrary, thick targets have several 10 μm.

The crucial point which makes the difference, is when using thick targets the ion beam is stopped inside the sample, meaning that the impinging particles cover the full range of energies from the initial beam energy to zero. As a result, the entire cross section up to the initial energy plays an important role in the production of the gamma yield. In the case of thin targets, impinging particles pass through the target and the collisions between the hitting particle and the nucleus happen at almost the same initial beam energy, as a result, the cross section of the reaction is at that determined energy. For this reason, when a cross section is under study in an experiment, thin targets are indispensable. An illustration of a thin target spectra from proton induced reactions on chlorine measured in the present work is displayed in Figure 5.2.

USC UNIVERSIDADE DE SANTIAGO DE COMPOSTELA

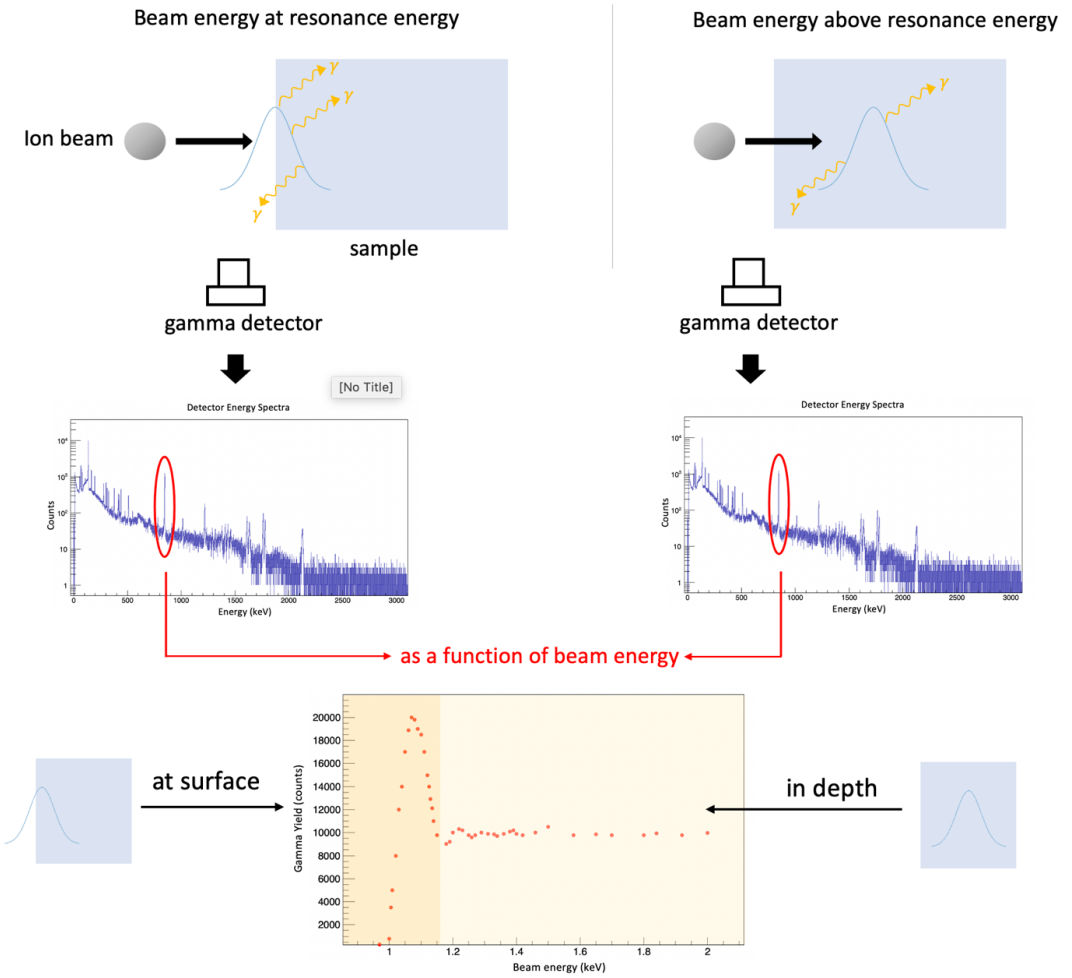

Figure 3.6: PIGE Depth Profiling Scheme from IAEA TECDOC Series [6]. It is despicted the scanning of the sample in depth by increasing the energy of the beam and how this produces the movement of the resonance. The material region where the resonance has already passed lies on a low cross section domain emitting quite few gammas. On the left of the figure, it is displayed the resonance on the surface while on the right the resonance has traveled through the material. In the middle, there are plots of the PIGE spectra obtained by gamma measurement and highlighted in red the peak chosen of a certain reaction. On the bottom, it is represented the gamma ray spectra of the previous specific gamma as a function of the beam energy.

USC
UNIVERSIDADE DE SANTIAGO DE COMPOSTELA

Doppler Broadening

There are some particular cases where gamma rays are emitted in movement and the Doppler effect appears. In any decay, due to the momentum conservation, the nucleus and the particle are propelled in opposite directions. After the process, the nucleus remains in an excited state until it de-excites emitting gamma cascades. If excited state lifetimes are inferior than the time of flight of the recoiling nucleus in that material, the transition is short, and gamma radiation is emitted while the nucleus is still in movement. This shift is a light movement inside the solid lattice of the target and it is determined by the recoil velocity of the nucleus and the stopping power of that nucleus in the material. In fact, in [84] has been found that velocities for kinetic energies lower than 100 keV do not contribute significantly to Doppler broadening. Summarizing, there are three points to fulfill aiming to observe Doppler effect in gamma rays [85]:

1. De-excitation of the recoiling nucleus while moving;

2. High speed of the decaying nucleus (high kinetic energy);

3. Transition must have a short lifetime (much less than nanoseconds).

The result of this effect is not a shift in the energy peak, rather than a broadening in the gamma line leading to a square contour peak. This spread in the peak's shape can be calculated to the first order, by the approximation

$$\Delta E = E_\gamma(1 + \beta cos\theta), \tag{3.25}$$

where ΔE is the energy spread, E_γ is the gamma ray energy, β is the fraction between the recoil velocity and the speed of light and θ is the angle created between the velocity of the emitting nucleus and the detector. The maximum energy spread can be as high as $2\beta E_\gamma$.

Doppler broadening can complicate the study of spectra, leading to miscalculations of the photopeak areas or misidentifications of peaks (because of overlapping). Moreover, the resolution function calculated via calibration sources or known photopeaks does not apply in these cases.

An example of the Doppler effect and how it is treated within the EnsarRoot framework is in [86]. It shows the broadening of two photopeaks from ^{19}F(p,$\alpha\gamma$)^{16}O reaction and the comparison between the measured data and the simulated data which includes the kinematics of the reaction.

USC UNIVERSIDADE DE SANTIAGO DE COMPOSTELA

Gamma Ray Yields of Thin and Thick Targets

As discussed before, the analysis of thin and thick targets differ; the gamma yield emitted in each case is different. In this section both situations are studied.

Gamma yields are deduced from the definition of the differential cross section (Eq. 11.14 of [87]):

$$\frac{d\sigma}{d\Omega} = \frac{Y(\theta,\phi)}{4\pi N_b N_i}. \tag{3.26}$$

Accordingly, when N_b incident beam particles with an energy E_1 interact to a number of isotopes (phosphorescent nucleus) of a thin layer with an areal density N_i, the differential gamma yield emitted by the isotope i and measured by a detector with an absolute efficiency of $\varepsilon_{abs}(E_\gamma)$ is given by

$$Y_{thin}(E_1,\theta) = 4\pi\varepsilon_{abs}(E_\gamma)N_b N_i \frac{d\sigma}{d\Omega}, \tag{3.27}$$

where $d\sigma/d\Omega$ is the differential cross section for the emission of a particular γ-ray at E_1 proton energy. Note that either yields of the former equations depend on the energy beam and on θ,ϕ angles because particles often are emitted anisotropically following an angular distribution [87], though for notation reasons sometimes ϕ angle is omitted. Moreover, while $Y(\theta,\phi)$ represents the emitted yield, $Y_{thin}(E_1,\theta)$ represents the yield after being detected. This previous equation could only be applied for thin targets because it considers a puntual energy (the beam energy loss is around few keV in this target thickness and therefore negligible).

On the other hand, when it comes to a thick target, the gradual loss of energy through the material, from E_1 to 0 when the hitting particles are at rest, is taken into account. Considering an homogenous sample, the previous equation becomes

$$Y_{thick}(E_1,\theta) = 4\pi\varepsilon_{abs}(E_\gamma)N_b f_m f_i \frac{\mathcal{N}_A}{A}\int_0^{E_1}\frac{1}{S_m(E)}\frac{d\sigma}{d\Omega}dE, \tag{3.28}$$

where f_m is the relevant element mass fraction, f_i the isotopic abundance, A the atomic mass, the Avogadro number is denoted as $\mathcal{N}_A$ and $S_m(E)$ is the mass stopping power[3] at energy E. The mass stopping power could be converted into linear stopping power by applying the factor

[3]The mass stopping power $S_m(E)$ is the stopping power divided by the density of the material.

USC UNIVERSIDADE DE SANTIAGO DE COMPOSTELA

$$\frac{N_i}{\rho} = \frac{f_m f_i \mathcal{N}_A}{A}. \tag{3.29}$$

Furthermore, if the mass fraction does vary along the depth of the sample,

$$Y_{thick}(E_1, \theta) = 4\pi\varepsilon_{abs}(E_\gamma) N_b f_i \frac{\mathcal{N}_A}{A} \int_0^{E_1} \frac{f_m(E)}{S_m(E)} \frac{d\sigma}{d\Omega} dE. \tag{3.30}$$

Finally, beam particle could have an energy distribution $F_{\bar{E}}(E)$ where $\bar{E}$ is the mean proton energy,

$$Y_{thick}(E_1, \theta) = 4\pi\varepsilon_{abs}(E_\gamma) N_b f_i \frac{\mathcal{N}_A}{A} \int_0^{E_1} \frac{f_m(\bar{E})}{S_m(\bar{E})} \left[\int_0^{\text{inf}} F_{\bar{E}}(E) \frac{d\sigma}{d\Omega} dE \right] d\bar{E}. \tag{3.31}$$

Thin Target Cross Section Determination

The cross section determination varies depending on the experimental conditions, such as, the use of standard samples, target thickness, backscattered particles measurement, etc. Therefore, we are going to concentrate on the PIGE methodology applied in this thesis.

The number of collected charge (incident particles) induces uncertainties in the measurement, thus, in order to avoid them, a simultaneous measurement is carried out: on one side, the number of gamma emissions are detected and, on the other side, the number of backscattered particles are also measured. This means that two IBA techniques (PIGE and RBS) are executed in parallel. Afterwards, both data analysis will be combined to work out the cross section of each reaction. In addition, this particular method does not need of an standard sample as a result, an standardless analysis is performed.

The detected radiation yield for a thin target is expressed in Eq. 3.27. This is a general expression suitable for non-resonance and resonance regions that are wide compared with the target energy thickness, or in other words, the cross section is constant in the energy interval between the energy beam and the energy beam minus the energy loss in the target.

In regard to the number of ions elastically scattered by a nucleus of j-species and detected by a particle detector placed at an angle ω w.r.t. the beam direction,

$$Y_j(E_1, \omega) = 4\pi\varepsilon_p N_b N_j \left(\frac{d\sigma}{d\Omega} \right)^j_{Ruth}, \tag{3.32}$$

USC UNIVERSIDADE DE SANTIAGO DE COMPOSTELA

where ε_p is the particle detector absolute efficiency, N_b is, as before, the number of incident particles with an energy E_1, N_j the number of j-nuclei in the target per surface unit and $(\frac{d\sigma}{d\Omega})^j_{Ruth}$ is the Rutherford cross section of j-element.

Combining the previous equations 3.27 and 3.32 into one, we obtain the differential cross section for a thin target as a function of the two measured yields and other parameters,

$$\left(\frac{d\sigma}{d\Omega}\right)_{\gamma}(E_1,\theta) = \frac{\varepsilon_p}{r\varepsilon_{abs}} \cdot \frac{Y_{thin}(E_1,\theta)}{Y_j(E_1,\omega)} \cdot \left(\frac{d\sigma}{d\Omega}\right)^j_{Ruth}, \tag{3.33}$$

where the stoichiometric factor r has been introduced and it is defined as $r = N_i/N_j$. As we can observe, this expression is independent of the beam charge collection and does not need any data from a standard sample.

Detection Limits

The sensitivity of PIGE technique depends on many factors: sample composition and experimental conditions. For this reason, it is difficult to establish general detection limits. In some works, this sensitivity has been delimited inside a wide range: from 10 to 100 ppm [88]. A list of sensitivities for diverse utilisations can be found in [89, 90].

Chemical composition of the target determines the nuclear reactions taking place and those with large cross section values maximise PIGE sensitivity, making the peak-to-background differentiation easier. In addition, isotopical abundances increase or decrease the detection probabilities.

On the other hand, the background of the spectra has diverse origins: environmental radiation and ion bombardment. This last one, in turn, has two contributors: the Bremsstrahlung coming from the accelerator line and the Compton effect created by all gamma rays measured (peaks from the ion-target interaction and from the interaction of the beam with the surrounding materials, such as, collimators, slits, magnets, etc.). The Compton contribution strongly depends on the experimental conditions, such as the shape and size of the detector active volume or the detector shielding. Regarding the natural radiation induced background, it depends mainly on the shielding system which, in many cases, is a fixed parameter of the setup that can not be modified. As a result, the understanding of the laboratory environmental radiation beforehand can improve the sensitivity of the analytical technique [91].

Detection limits in an experiment could be estimated by using ERYA code [82, 83] to convert yield into concentrations and taking into account all

USC UNIVERSIDADE DE SANTIAGO DE COMPOSTELA

background contributions just mentioned [92].

Aplications of PIGE

There is a large quantity of analytical works using this technique in a wide variety of fields. Due to this method covers the bulk of elements present on Earth which have Z<16, a significant number of materials could be object of study. Basically, these studies determine elemental compositions and depth profilings of samples. Many of these samples are valuable objects for their antiquity and uniqueness, therefore, it is of great importance its non-destructive feature along with the non-requirement of sample treatment. Another asset is the usage of PIGE along other IBA techniques like PIXE, NRA, ERDA and RBS. All previous specifications make PIGE a really versatile method with a wide range of applications, diverse cases are cited below just as exemplifications.

- **Material Analysis.** Two important applications are the measurements of chlorine in industrial oil samples [93] and of borosilicate in insulator materials [94].

- **Medical Samples.** One of the most common studies is the fluorine determination in bones of dead humans and animal organisms through $^{19}F(p,p'\gamma)^{19}F$ reaction [95], as well as, in teeth dentin [96].

- **Archaeological Objects and Cultural Heritage Objects.** Their compositions are of primordial interest for archaeology in order to study materials employed in some historical periods, resolve the utility of artifacts and even determine the origin of a piece. There are studies on indian ceramics [97], on glasses from a post-Roman settlement [98], on Leonardo da Vinci paintings such as the "Madonna dei fusi" [99], etc.

- **Aerosol Samples.** Air composition measurements are less frequent. In [100] study, the air pollution was analysed in a region near Florence where there are located numerous ceramic and glass factories. On another paper, a measurement of the air quality was carried out in four italian cities and they combined PIGE and PIXE techniques [101].

- **Geochemical and Geological Samples like Minerals, Soils and Rocks.** The current technique is used in many geological investigations to determine geological processes such as: nitrogen determination in micas rocks [102], to study igneous and metamorphic charnockitic rocks by determining the concentrations of fluorine and phosphorus [103] or

USC UNIVERSIDADE DE SANTIAGO DE COMPOSTELA

even to establish correlations between the colour zoning in northern Mozambique and the elements forming the mineral tourmaline [104].

- **Scientific Investigations.** There are diverse studies to determine cross sections of different elements at low energies such as the analysis of ^{19}F(p,$\alpha\gamma$)^{16}O reaction in [86] or the ^{7}Li(p,p'γ)^{7}Li reaction in [105].

3.2 Environmental Radiation

3.2.1 Radioactivity of the Nucleus

Radioactivity is a natural process where an atomic nucleus emits one or several types of particles, transmuting itself (decaying) by one or more decaying modes. Sometimes, it is followed by a de-excitation of the daughter nucleus to a lower energy level emitting gamma rays. The most frequent decays are α, β^+ and β^-, but electron capture or spontaneous fission are also feasible, as well as other more exotic decays (as proton emission). Around 40 elements of the Earth crust have this property. The other natural radioactive source are the radionuclides created by collisions with cosmic rays. Alternatively, 2500 artificial nuclei have been created on purpose by particle accelerators. In this section, the fundamentals of the decaying process are presented and, afterwards, a detailed description of radioactive sources in nature is shown.

3.2.2 The Decay Equation

The activity of a radioactive sample is the number of atoms which decay per unit of time [4, 106]:

$$A = -\frac{dN}{dt} = \lambda N, \tag{3.34}$$

and it is proportional to the number of atoms present in the sample (N) and the decay constant (λ). This last parameter expresses the decay probability of a nucleus per unit of time and has units of reciprocal time (e.g. s^{-1}). The amount of radionuclides in a source is expressed in Becquerels (rate of disintegration per second) in the IS units, although traditionally it was expressed in Curies (1 Ci=$3,7 \times 10^{10}$ decays/s) which is the activity of 1 gram of radium. From the previous expression, the decay law is deduced:

$$N = N_0 e^{-\lambda t}, \tag{3.35}$$

which is the same law the activity follows:

USC UNIVERSIDADE DE SANTIAGO DE COMPOSTELA

$$A = A_0 e^{-\lambda t}, \tag{3.36}$$

where N_0 and A_0 are the number of radionuclides and its activity at $t = 0$.

Therefore, the number of decays expected in the interval dt would be $\langle dN \rangle = \lambda N dt$ which should be considered as a mean. Previous equations follow a Poisson probability distribution with the same mean $\mu = \lambda N dt$:

$$P(n;\mu) = \frac{e^{-\mu}}{n!}\mu^n, \tag{3.37}$$

where n denotes the number of decays in a dt time interval.

The reciprocal of the decay constant is the mean lifetime (τ) and represents the average time which an atom can be expected to exist before its nucleus decays:

$$\tau = \frac{1}{\lambda}. \tag{3.38}$$

It is more convenient and meaningful to use the radionuclide half-life ($t_{1/2}$) that is the time during which the number of atoms decreases to half its original value $N = N_0/2$. Applying this condition to Eq. 3.35 we obtain:

$$t_{1/2} = \frac{\ln 2}{\lambda} = 0,693 \cdot \tau, \tag{3.39}$$

which is also the time during the activity decreases by half. Under these circumstances, a sample with N_0 radionuclides with a half-life of $t_{1/2}$, when k semiperiods have been passed, $N_0/2^k$ radionuclides will remain unchanged.

Moreover, the activity of a sample with mass M and atomic weight A' could be calculated by

$$A = \lambda M \frac{\mathcal{N}_A}{A'}, \tag{3.40}$$

where $\mathcal{N}_A$ is the Avogadro number already defined.

3.2.3 Individual Decay Chains

Within the same type of decay there are different cases of decaying depending on the characteristics of the decay parameters, such as the relative half-life between the parent and the daughter nucleus or the number of daughters produced in the process. In all cases, the total activity in the system would be the sum of the parent and daughter activities.

Firstly, we are going to consider the simplest case when one radionuclide (the parent) decays into another radionuclide (the daughter) as $N_1 \rightarrow N_2 + x$,

USC UNIVERSIDADE DE SANTIAGO DE COMPOSTELA

being x the emitted particle, N_2 stable and N_1 is a fixed inicial quantity (it is not constantly generated). The number of nuclides varies following these laws:

$$N_1 = N_0 e^{-\lambda_1 t}, \tag{3.41}$$
$$N_2 = N_0 \left(1 - e^{-\lambda_1 t}\right), \tag{3.42}$$

where λ_1 is the decay constant of the father nucleus and they satisfy instantly $N_1 + N_2 = N_0$. The parent radionuclide will continue decaying until its disappearance when $N_2 = N_0$.

Another case would be when the parent nucleus has two or more final states (decaying modes). Consider two different decaying modes going to two stable nuclei, N_{2a} and N_{2b} emitting in the process x and y particles, respectively.

$$\begin{aligned} N_1 &\rightarrow N_{2a} + x \\ &\rightarrow N_{2b} + y \end{aligned}$$

In this case, the partial half-life or more useful the partial decay constant are introduced, as λ_a and λ_b:

$$-\frac{dN}{dt} = -\left(\frac{dN}{dt}\right)_a - \left(\frac{dN}{dt}\right)_b, \tag{3.43}$$
$$N\lambda_t = N\left(\lambda_a + \lambda_b\right),$$

where the total decay constant is the sum of the partial decay constants $\lambda_t = \lambda_a + \lambda_b$. The partial decay constants give information about the proportion of each partial decay mode. Therefore, the number of each nucleus during the process at any time t would be:

$$N_1 = N_0 e^{-\lambda_t t}, \tag{3.44}$$
$$N_{2a} = N_0(\lambda_a/\lambda_t)\left(1 - e^{-\lambda_t t}\right), \tag{3.45}$$
$$N_{2b} = N_0(\lambda_b/\lambda_t)\left(1 - e^{-\lambda_t t}\right). \tag{3.46}$$

The cocients $BR(a) = \lambda_a/\lambda_t$ and $BR(b) = \lambda_b/\lambda_t$ called Branching Ratios are the fractions of nuclei decaying by an individual decay mode with respect to the total number of nuclei. A radionuclide with various decay modes is very common, for example, ^{226}Ac has three decay modes [26]:

USC UNIVERSIDADE DE SANTIAGO DE COMPOSTELA

$$
\begin{aligned}
^{226}_{89}Ac &\rightarrow {}^{226}_{90}Th + e^- + \overline{\nu}_e; \quad \lambda_\beta = 0,83\lambda_t; \quad t_{1/2,\beta} = 35,39\,\text{h} \\
^{226}_{89}Ac &\rightarrow {}^{222}_{87}Fr + \alpha; \quad \lambda_\alpha = 6 \times 10^{-5}\lambda_t; \quad t_{1/2,\alpha} = 55,87\,\text{y} \\
^{226}_{89}Ac + e^- &\rightarrow {}^{226}_{88}Ra + \nu_e; \quad \lambda_e = 0,17\lambda_t; \quad t_{1/2,e} = 172,76\,\text{h}
\end{aligned}
$$

where the decaying constant $\lambda_t = 6,6 \times 10^{-6}$ s^{-1} is the sum of the partial decaying constants, λ_i. Despite the different half-life of each branch, the ^{226}Ac disappears according to the total half-life $t_{1/2} = 29,37(12)$ h [26], as shown in Eq. 3.44.

In general, the decay parameters for a radionuclide going to a one or various stables states could be expressed as:

$$\lambda = \sum_i \lambda_i, \tag{3.47}$$

$$\frac{1}{t_{1/2}} = \sum_i \frac{1}{t_{1/2,i}}. \tag{3.48}$$

3.2.4 Radioactive Chains: Bateman Equations

A more complex case is when one radionuclide decays into another nucleus, which is also unstable. If these decays are followed for more radionuclides a radioactive series (also called decay chain) is formed. The successive decays of daughter's nuclei do not stop until a stable nucleus is reached. In these cases, the rate of change of the number of daughter atoms must be the difference between the rate of growth from the parent and the rate of decay of the daughter. Consider the simplest case with only three elements $N_1 \rightarrow N_2 \rightarrow N_3$ being N_3 the stable element. The equations of the radioactive chain when initially only the parent nucleus is present in the sample, this is $N_2(t=0) = N_3(t=0) = 0$, are [106]:

$$\frac{dN_1}{dt} = -\lambda_1 N_1, \tag{3.49}$$

$$\frac{dN_2}{dt} = \lambda_1 N_1 - \lambda_2 N_2, \tag{3.50}$$

$$\frac{dN_3}{dt} = \lambda_2 N_2. \tag{3.51}$$

Solving these linear differential equations we obtain the number of nuclei as a function of time t:

USC UNIVERSIDADE DE SANTIAGO DE COMPOSTELA

$$N_1 = N_0 e^{-\lambda_1 t}, \tag{3.52}$$

$$N_2 = N_0 \frac{\lambda_1}{\lambda_2 - \lambda_1}\Big(e^{-\lambda_1 t} - e^{-\lambda_2 t}\Big), \tag{3.53}$$

$$N_3 = N_0 \left\{1 + \frac{1}{\lambda_2 - \lambda_1}\Big(\lambda_1 e^{-\lambda_2 t} - \lambda_2 e^{-\lambda_1 t}\Big)\right\}, \tag{3.54}$$

where we have followed the same notation. Bearing in mind that $A = \lambda N$, we can rewrite the previous equations in terms of activity as:

$$A_1 = A_0 e^{-\lambda_1 t}, \tag{3.55}$$

$$A_2 = A_0 \frac{\lambda_2}{\lambda_2 - \lambda_1}\Big(e^{-\lambda_1 t} - e^{-\lambda_2 t}\Big). \tag{3.56}$$

Evidently, $A_3 = 0$, due to the nucleus is stable. If there were some daughter atoms initially present in the sample (N_{20} nuclei with an activity of A_{20}) a second term is included in Eq. 3.53 and 3.56 to take into account the growths of daughter's number of nuclei and activity:

$$N_2 = N_0 \frac{\lambda_1}{\lambda_2 - \lambda_1}\left(e^{-\lambda_1 t} - e^{-\lambda_2 t}\right) + N_{20} e^{-\lambda_2 t}, \tag{3.57}$$

$$A_2 = A_0 \frac{\lambda_2}{\lambda_2 - \lambda_1}\left(e^{-\lambda_1 t} - e^{-\lambda_2 t}\right) + A_{20} e^{-\lambda_2 t}. \tag{3.58}$$

Three diverse situations can be distinguishable depending upon whether parent half-life is greater or lesser than daughter half-life, or equivalently, the decay constants:

- Transient equilibrium $\lambda_2 > \lambda_1$: daughter decay probability is greater than of the parent nucleus, as a result, the quotient of activities A_2/A_1 slowly grows up without reaching an stable point.

- Secular equilibrium $\lambda_2 >> \lambda_1$: when the daughter decay probability is much greater than of the parent nucleus or, in other words, when the half-life of the parent nuclide is very long compared to that of the daughter. The quotient $A_2/A_1 \approx 1$ means that the daughter activity equals parent activity, even though the number of parent nuclei is much bigger. This ratio remains unchanged endlessly.

USC UNIVERSIDADE DE SANTIAGO DE COMPOSTELA

- No equilibrium $\lambda_2 < \lambda_1$: if the daughter half-life is greater than the parent half-life, the parent nuclei decay rapidly while daughter atoms decay following the exponential law at their own rate. As a result, no equilibrium is established.

In general terms, it could be generalized as $1 \rightarrow 2 \rightarrow 3... \rightarrow k$ and Eq. 3.34 for each element in the chain would be:

$$\frac{dN_i}{dt} = \lambda_{i-1} N_{i-1}(t) - \lambda_i N_i(t). \tag{3.59}$$

Assuming there is chemical separation between all elements in the sample, this is, $N_i(0) = 0$ for $i > 1$ and $N_i = N_0$ for the first element of the series, the activity for the n-element of the chain will follow Bateman equations [87, 106]:

$$A_n = N_0 \sum_{i=1}^{n} c_i e^{-\lambda_i t} \tag{3.60}$$

$$= N_0 \Big(c_1 e^{-\lambda_1 t} + c_2 e^{-\lambda_2 t} + ... + c_n e^{-\lambda_n t} \Big), \tag{3.61}$$

where

$$c_m = \frac{\prod_{i=1}^{n} \lambda_i}{\prod_{i=1}^{n} (\lambda_i - \lambda_m)} \tag{3.62}$$

$$= \frac{\lambda_1 \lambda_2 \lambda_3 ... \lambda_n}{(\lambda_1 - \lambda_m)(\lambda_2 - \lambda_m)...(\lambda_n - \lambda_m)}, \tag{3.63}$$

where in the lower product we omit the term $i = m$.

The number of nuclei for the n-element at any time t will be N_n, whereas previous equations accomplish that $A_n = \lambda_n N_n$.

In order to reach secular equilibrium the condition $\lambda_1 N_1 = \lambda_2 N_2 = ... = \lambda_n N_n$ must be satisfied. An example of this type of chain would be natural radioactive series which are explained below.

3.2.5 Natural Sources of Radiation

Natural ionising radiation on the Earth is emitted by a variety of sources: terrestrial, which, in turn, can be primordial (existing since the origin of the heavier elements) or secondary (derived from radioactive decay of the primordials) and cosmogenic, created by cosmic radiation and its interaction

USC UNIVERSIDADE DE SANTIAGO DE COMPOSTELA

with matter. On the other hand, there is artificial radiation introduced into nature by humans using modern techniques, which is also referred as anthropogenic.

Humans and other life forms are exposed to these ionising radiations, via three different ways: external, essentially from radionuclides and its decay products present in rocks, soils and cosmic rays; internal, from ingestion of food and drinking water (with trace amounts of different radionuclides); and inhalation of dust particles containing uranium decay products (namely radon and its decay products). These exposures are unavoidable and, in some rates, can cause health damage on living organisms, for instance, the second cause in lung human cancer is the inhaled radon [41]. Therefore, the topic of natural radiation is of great significance to the scientific community, population and national authorities. The later have invested in the creation of a common legislation to establish standards and regulations. Furthermore, special effort has been made on the monitoring of environmental radiation and on the creation of radiometric maps over the territory as The European Atlas of Natural Radiation [7]. It is a collection of maps displaying the levels of radioactivity caused by different natural sources in Europe.

From the scientific point of view, natural radiation interferes in the data acquisition of many experiments. In our field, gamma spectrometry, there is a large number of mutual spectral interferences between many nuclides in the decay series of uranium or thorium and the gamma yield coming from the experiment. This overlapping, sometimes, makes the differentiation impossible, as a consequence, some detectors have been yielded with thick shielding walls of iron and lead.

Once the general idea of natural ionising radiation has been presented, a deeper insight about each radioactive source is shown.

3.2.5.1 Terrestrial Radiation

As we have just mentioned, terrestrial radiation is gamma radiation from terrestrial sources, including primordial and secondary nuclides.

The primordial radionuclides that now exist on Earth have half-lifes at least comparable to the age of the Universe (around $13,8 \times 10^9$ years [107]). They are classified in non-series and series depending on the decay pathway. The main radioactive source in non-series group is the ^{40}K potassium isotope with a half-life of $1,248(3) \times 10^9$ years [26] (Figure 3.7). On the other hand, there are the following series, three of them headed by unstable nuclei with half-lifes greater than 10^8 years [26]:

- The thorium series with ^{232}Th (half-life of $14,0(1) \times 10^9$ years).

USC UNIVERSIDADE DE SANTIAGO DE COMPOSTELA

- The uranium series with ^{238}U (half-life of $4,468(3) \times 10^9$ years).
- The actinium series with ^{235}U (half-life of $7,038(5) \times 10^8$ years).
- The neptunium series with ^{237}Np (half-life of $2,144(7) \times 10^6$ years).

There are only four radioactive chains since the disintegration of the parent nucleus is through alpha decay therefore, the mass number of the members may be expressed as four times an integer (n) plus the remainder for that series. As a result, the thorium series is also named as 4n series, the neptunium series, 4n + 1; the uranium series, 4n + 2; and the actinium series, 4n + 3.

Primordial radionuclides with half-lifes of less than 10^8 years have become undetectable on Earth after about 30 half-lifes since their creation, bearing in mind that the age of Earth is around $4,5 \times 10^9$ years [108]. This is the case of the neptunium series, originated with ^{241}Pu, an isotope with a very short half-life of 14 years. The series name comes from the longest lived nucleus heavier than bismuth, ^{237}Np, which is considered as the parent species. The only isotope from this chain still existing today is the almost stable ^{209}Bi with a half-life of $2,01 \times 10^{19}$ years. The other members of the chain can only be produced artificially by nuclear reactions. Finally, primordial radionuclides with half-lifes greater than 10^{10} years have decayed very little up to the present time.

Origin and Spreading

There exist different sources where the terrestrial radiation comes from, although, to be precise, practically all natural materials contain radioactive nuclei, but in such low concentrations that they can be detected only by very sensitive analysis. The composition and structure of the sub-surface (rocks and soil) has a strong influence on the local level of natural background radiation, along with other conditions such as altitude and climate. Therefore, looking at the geology of a territory, natural radioactivity can be predicted at large-scale. For instance, fewer radionuclides have been found in young and mobile unconsolidated sediments (clay or sand) present in the northern and northwestern Europe than in some magmatic or metamorphic rocks found in, for example, Bohemian Massif (Central Europe) or Iberian Massif (Spain) [7, 109]. As a result, materials derived from these volcanic rocks contain large amounts of radioactivity. Migration of these radionuclides occurs naturally in different pathways: terrestrial, aquatic and atmospheric contributing to their dispersion [7, 109].

USC UNIVERSIDADE DE SANTIAGO DE COMPOSTELA

Uranium Series

Uranium element with Z=92 was discovered by Klaproth in 1879, who named it after the newly discovered planet Uranus [110]. Natural uranium consists of three isotopes: ^{234}U, the progenitor of the actinium series ^{235}U and the parent isotope of the uranium series ^{238}U. Their relative abundances are $0,0054(5)$ %, $0,7204(6)$ % and $99,2742(10)$ %, respectively [26]. On average, the entire Earth's crust contains 8070400 tonnes of uranium metal [111]. Of course, local concentrations in large granitic or volcanic rocks gather major quantities up to 50 ppm.

The uranium chain is a complex radioactive decay series which emits alpha, beta and gamma radiation until a stable isotope of lead is produced, in this case ^{206}Pb. In Figure 3.8 there are represented all nuclear transitions and ramifications occurred through it. In this diagram, we can observe that the half-life of all daughter nucleus are at least four orders of magnitude smaller than the half-life of ^{238}U. This means that in an undisturbed environment every daughter radionuclide must be in secular equilibrium with its series' parent. Consequently, the activity of the progenitor is equal to the activity of any daughter and, as the main radionuclides in the chain are fourteen, the total activity of an ore will be fourteen times of the parent or of any individual radionuclides. If the source is treated in any way, i.e. disturbed, the overall chain equilibrium would be broken. This last case is of great importance as we are going to see in the next Subsection 3.2.5.1. In respect to gamma ray spectrometry, not all nuclides in this series emit gamma radiation, and of those, only five can be measured with ease (highlighted in gray in Figure 3.8).

Radon Dynamics and Natural Disturbance of Uranium Decay Series

One particular descendant of the uranium chain is radon, a colourless, odourless and radioactive noble gas, which can be found in nature in three isotopes: ^{219}Rn, ^{220}Rn and ^{222}Rn. It is usually trapped within a solid sample or mineral grains, however, part of it escapes through material fractures or pore-space (emanation) and migrates to the atmosphere. As a result, the secular equilibrium between the post-radon nuclides and pre-radon nuclides of a series disappears and alters the total activity of the sample. This loss of radon will cause disequilibrium between members of all decay chains, however, not in the same degree, as the half-lifes of each radon isotope plays an important role.

USC UNIVERSIDADE DE SANTIAGO DE COMPOSTELA

One of the most important forms of disruption of the uranium decay series corresponds to this radon migration [7]. In this chain, when ^{226}Ra decays by alpha emission, it transmutes to its decay product ^{222}Rn with a half-life of 3,8 days [26]. After the decay, there is ample time of days when the gas can move freely before the subsequent decays occur and the stable nucleus ^{206}Pb is reached. Although the other two radioactive series have also radon as a decay product, the half-lifes of ^{219}Rn, in the actinium series, and ^{220}Rn, in the thorium series, are very short, the order of seconds, and even if radon escapes equilibrium is re-established within minutes. Therefore, the half-lifes of the radon are key in the equilibrium between nuclei in the chain.

This migrative process is so significant that radon ^{222}Rn is the largest contributor to the dose population due to natural radiation [33, 42]. The main risk is not the gas itself because after the decay it does not emit any radiation, though its short-lived decay products, which are alpha and gamma emitters. These radionucleus are again in a solid state and they attach to aerosol particles, thus, increasing the chance of inhalation. If any of these nuclei is trapped by lung, the tissues surrounding it would be irradiated until the stable nucleus of lead is reached.

Actinium Series

Actinium radioactive chain begins with one of the unstable uranium isotopes: the ^{235}U [112]. Even this isotope represents only a small fraction of the total uranium amount, their activities are comparable $A_{^{235}\mathrm{U}} = 0,046 \times A_{^{238}\mathrm{U}}$ (considering a natural material under normal circumstances) [4]. Therefore, under these conditions, the ^{235}U/^{238}U ratio would be fixed and all nuclides among them in equilibrium. This is of capital importance because actinium series could be rarely measured, hence, assuming this equilibrium and knowing the quantity of any decay product of uranium series the activity of the actinium chain could be determined. This procedure has been applied in Section 5.2 in order to estimate the environmental actinium radioactivity.

The difficulty of its measurement resides in the total gamma yield smallness and the overlapping between gamma rays of distinct background radionucleus. Within this series, only the parent nucleus can be measured with relative ease, although ^{227}Th, ^{223}Ra and ^{219}Rn can be also measured but with more troublesome. The major gamma ray at 185,72 keV coming from ^{235}U should be treated to eliminate the contribution of the peak emitted almost at the same energy by ^{226}Ra at 185,99 keV. Any of these measurements can provide useful information about the uranium quantity present in a sample or give insight into the disruption of the decay series.

USC UNIVERSIDADE DE SANTIAGO DE COMPOSTELA

Actinium chain, shown in Figure 3.9, involves beta and alpha decays distributed in different minor decay branches, nevertheless, the number of main decays is eleven. Consequently, the total activity of the series is eleven times of any radionucleus activity due to secular equilibrium condition. As in all chains, lead is the final stable product, in the current case ^{207}Pb. Natural uranium is present in all geological materials in usual proportions to a greater or lesser extent. In contrast, enriched uranium is a manmade type of uranium in which ^{235}U percentage has been increased. It is used due to its fissibility with thermal neutrons as a fuel for nuclear power, military nuclear weapons, naval propulsion and for research reactors in lower amounts.

Thorium Decay Series

Thorium was first discovered in 1828 by the mineralogist Esmark in a thorite sample ($ThSiO_4$) and later in time, identified as an element with Z=90 by the chemist Berzelius, who named it after the god of thunder Thor in Norse mythology [113]. Natural thorium occurs almost with 100 % isotopic abundance through ^{232}Th, one of the longest-lived isotopes ($1,41\times10^{10}$ years) and parent nucleus of the radioactive thorium series [112].

Thorium chain is shown in Figure 3.10. Diverse beta and alpha decays are required to transform the original parent nucleus into the stable species ^{208}Pb. Practically in the end of the chain an important ramification occurs: ^{212}Bi decays 34,94 % via alpha decay into ^{208}Tl and 64,06 % via beta decay into ^{212}Po, as a result, when the total activity of the series is calculated we have to take into account that the thallium activity would be a 0,35 the activity of any upper radionucleus, as well as, polonium activity should be reduced by its equivalent factor. Both branches end in the same isotope of lead ^{208}Pb. As in the others series, these assumptions could be made because the overall chain is considered in secular equilibrium, due to the huge difference between the parent and daughters half-lifes.

In nature, thorium is more common than uranium, about 3 to 4 times, with an Earth's crust content of 6 to 10 g/t [114]. It is present in igneous rocks, such as granites, some sedimentary rocks and, in small quantities, in biological materials. The amount of thorium in the sea water is less than $0,5\times10^{-3}$ g/m^3, which is lower than uranium, because of its low solubility [7].

Potassium Decay

USC UNIVERSIDADE DE SANTIAGO DE COMPOSTELA

The seventh most abundant element in nature is potassium [115]. It is

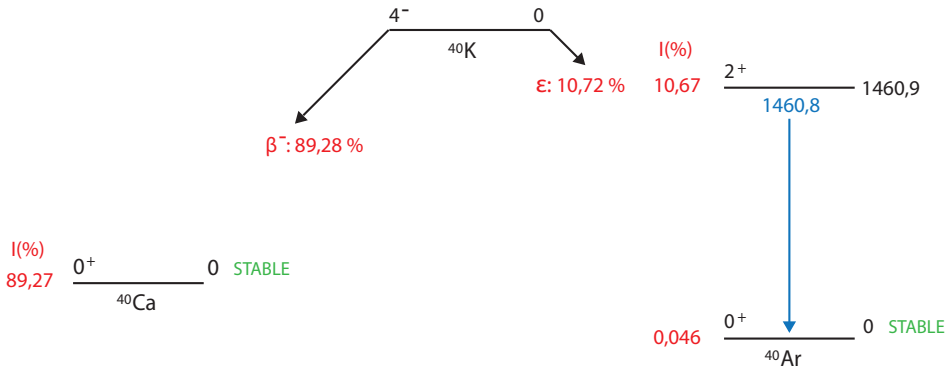

Figure 3.7: Potassium decay of the unstable ^{40}K isotope [26]. It decays 89,28 % via beta-minus to ^{40}Ca and 10,72 % via electron capture to ^{40}Ar which, in turn, de-excites emitting a gamma ray of 1460,8 keV.

composed by two stable isotopes, ^{39}K and ^{41}K, and a radioactive isotope ^{40}K with just an abundance of $0,01170(10)$ % [26]. The unstable nucleus decays naturally following two branches: $89,28$ % decays via beta-minus to ^{40}Ca ground state with no gamma emissions and the other $10,72$ % suffers electron capture and it transmutes into ^{40}Ar noble gas. In this last decay, a gamma of 1460,820(5) keV is emitted by the de-excitation of the daughter nucleus. Figure 3.7 shows these two processes.

The dating method K-Ar uses the just mentioned electron capture decay. The measurement of the ^{40}K/^{40}Ar ratio gives direct information about the mineral's age, due to the half-life of potassium radioisotope is the same order of magnitude as the age of the Earth [116].

Potassium is a widespread element accumulated mostly in the Earth's upper crust and the highest concentrations have been found in magmatic and metamorphic rocks [7]. Moreover, potassium is mobile in the biological and geological environment, in fact, it is the largest internal source of natural radioactivity in animals and humans, even greater than ^{14}C.

From a gamma spectrometry point of view, the ^{40}K photopeak is very evident in background spectra. Usually it comes from building materials (clay and rocks), wood furniture and even living organisms from the vicinity. Therefore, it is almost impossible to elude its contribution. In any gamma yield, the particular shape of 1460,8 keV peak with its long Compton continuum appears restricting severely the detection limits at low energies [4]. As a result, in many experiments a peak-to-background correction is needed.

USC UNIVERSIDADE DE SANTIAGO DE COMPOSTELA

Cosmic Radiation

In 1911 the physicist V. Hess discovered cosmic rays by a series of measurements of atmospheric radiation with the aid of air balloons [117]. Cosmic radiation is a natural and extra-terrestrial source of high-energy particles.

The largest component is cosmogenic radionuclides: 70 % protons; 20 % α-particles; 1,7 % carbon, nitrogen and oxygen ions; 0,7 % lithium, beryllium and boron ions; and the 0,6 % remaining are ions of Z >10. Electromagnetic radiation and electrons also conform cosmic radiation. The former covers a wide range in the electromagnetic spectrum, from gamma rays to radiation in the radiofrequency region, being the X-ray domain the most intense [112].

The origin of nearly all of them is extra-galactic with very high energies up to about 3×10^{11} GeV. This extend group can be divided in two: the ones with lower energy that come from the center of the Milky Way Galaxy and the most energetic which presumably emerge from external sources outside of our galaxy, as exploding super novae or colliding galaxies. Although, some particles originate within the solar system, specifically from Sun bursts, and they are easily recognizable by their temporal correlations with the solar activity. This last group is composed primarily of protons with energies below 1 GeV because it is part of the solar material that has been ejected in a solar eruption.

The flux of primary cosmic particles hitting the Earth is about 1000 $m^{-2}s^{-1}$ [118]. When they traverse the atmosphere, they are annihilated because of the collisions with suspended corpuscles creating a vast number of massive new particles. The kinetic energy of primary cosmic rays is converted after the annihilation process into large rest masses. These reaction products are known as secondary cosmic radiation and the main component is, by large, pions [112]. While traveling downwards, they suffer different events, such as decay, head-on collisions, bremsstrahlung, etc. increasing the number of particles of the cascade. Each type of primary particle creates a characteristic pattern. Indeed, we are only capable of measure atmospheric showers that arrive to the ground using large detector arrays and from which we extract the information of all physical processes that occurred during the journey. In general, only a small portion of the initial amount is detected. Besides, there are fluctuations in the number of cosmic rays reaching the earth surface, essentially due to the altitude and latitude.

In particular, free pions are unstable particles with very short life-times and suffer decay via muons and muon neutrinos for charged pions and via gamma rays for neutral pions. As a result, the main component that strikes the earth is high energy muons, also known as hard component, which almost do not interact with atomic nuclei, allowing a high penetration through ma-

USC UNIVERSIDADE DE SANTIAGO DE COMPOSTELA

terials. The other cosmic ray component which does not interact with matter are neutrinos with a flux around 10^{11} $m^{-2}s^{-1}$. The low energetic component which contributes to the environmental background measurable by gamma spectroscopy contains photons, electrons and positrons. This component, regarded as well as soft component, comes from direct ionizations in the atmosphere and represents around 10 %. Furthermore, there is a low rate of about 2 or 3 ion pairs per $cm^{-2}s^{-1}$.

It is worth to mention, that cosmic radiation induces spallation reactions creating a large number of nucleons, protons and neutrons, which recombine with the atmospheric nuclei (O_2, N_2, Ar, etc.) resulting in the production of radioactive nuclei. The production rates are extremely low and constant, 2500 $m^{-2}s^{-1}$ for ^{3}H, 300 $m^{-2}s^{-1}$ for ^{10}Be and 22000 $m^{-2}s^{-1}$ for ^{14}C. These nuclei are introduced in the biological chain directly by inhalation or brought to terrestrial reservoirs by rain water. Thanks to these influxes, radioactive methods of analysis could be used, such as radiocarbon dating for dead biological materials which uses ^{14}C [119, 120].

3.2.5.2 Anthropogenic Radioactivity in Nature

As stated, natural occurring materials are the main sources of environmental radiation, however, some anthropogenic activities have increased the natural values of radioactivity. There is a large variety of anthropogenic radioactive sources, so we are just going to mention the most outstanding.

Substantial releases of radioactive material were made by nuclear weapons, nuclear power accidents and nuclear satellites scorched [112]. Fission products and actinides have been released by nuclear weapon detonations and nuclear weapon tests whereas nuclear catastrophes released mainly ^{131}I and ^{137}Cs radionuclides. Its effects can be distinguishable in two zones: near and far field. Near field contribution is produced when radioactive material dissolves into the atmosphere and is precipitated by rain, afterwards, this fallout could cause many radioactive contamination problems to the biota. Far from the vicinity of the release, radionuclides spread out and mix with natural activity, although, from a global standpoint, these injections into the atmosphere are practically negligible.

USC UNIVERSIDADE DE SANTIAGO DE COMPOSTELA

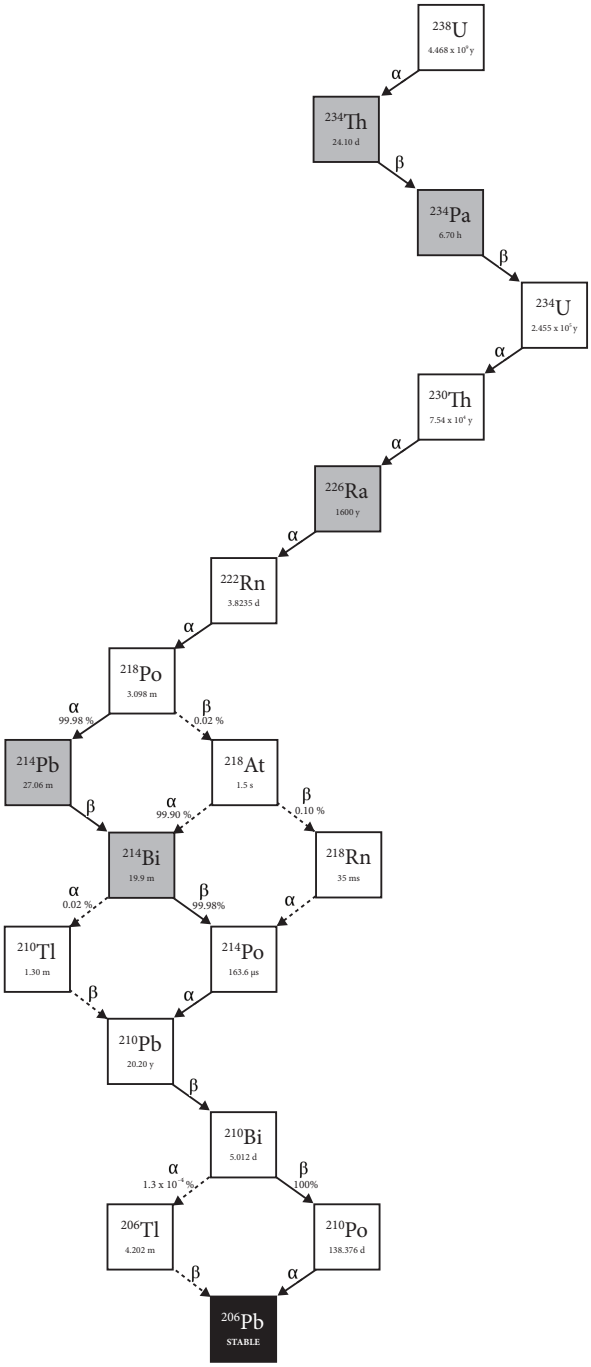

Figure 3.8: Uranium radioactive series [26]. It represents the successive decays from the parent nucleus ^{238}U until the stable nucleus ^{206}Pb is reached (black square). The easiest nuclei to detect by gamma spectroscopy, because of their outstanding photopeaks, are highlighted in grey (considering a small-sized germanium detector).

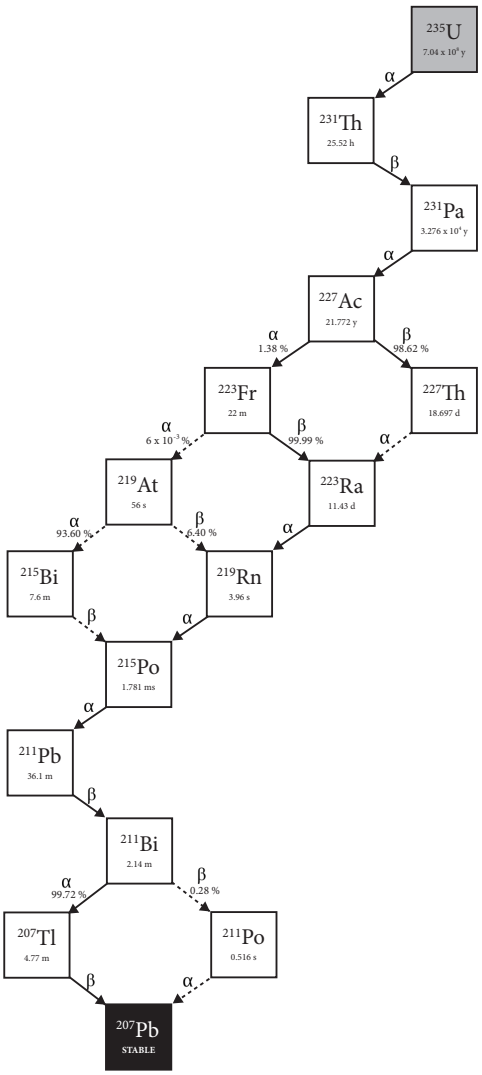

Figure 3.9: Actinium radioactive series [26]. It represents the successive decays from the parent nucleus ^{235}U until the stable nucleus ^{207}Pb is reached (black square). The easiest nuclei to detect by gamma spectroscopy, because of their outstanding photopeaks, are filled in grey (considering a small-sized germanium detector).

USC UNIVERSIDADE DE SANTIAGO DE COMPOSTELA

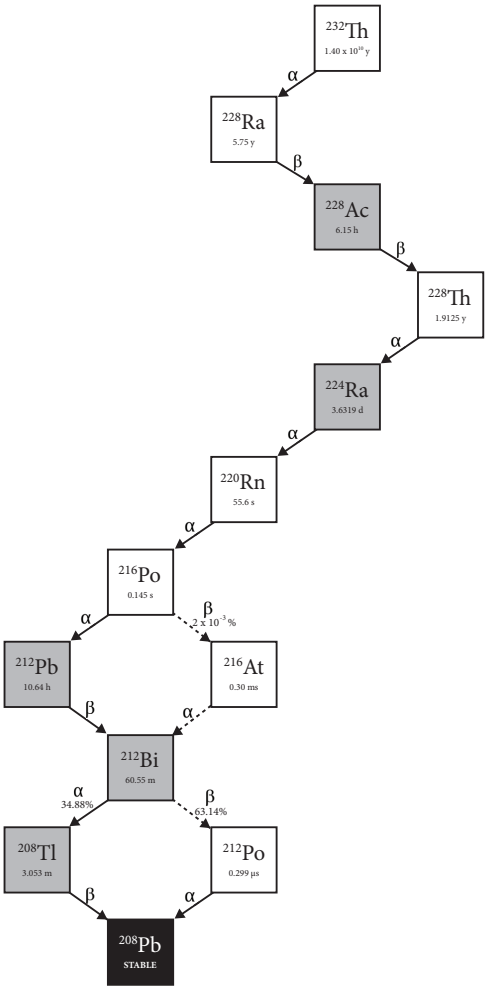

Figure 3.10: Thorium radioactive series [26]. It represents the successive decays from the parent nucleus ^{232}Th until the stable nucleus ^{208}Pb is reached (black square). The easiest nuclei to detect by gamma spectroscopy, because of their outstanding photopeaks, are highlighted in grey (considering a small-sized germanium detector).

USC
UNIVERSIDADE DE SANTIAGO DE COMPOSTELA

Chapter 4

METHODOLOGY: EXPERIMENTAL SECTION

4.1 EnsarRoot Framework

Computer simulation is the representation of a physical system or process over time by using a computer model designed after them. With the aim of imitate the behaviour of the original system, this model is composed by the mathematical equations of the physical laws that follow the process and, on the whole, it conforms the computer program. The outcome of the model takes the form of data or graphical images. In essence, a computer simulation is a mathematical description of a real system, decoded in a computer. Generally, this description is a simplification or an approximation of the original system in order to not complicate the model in terms of running time or user friendliness.

In order to verify the reliability of a model, when it is possible, the output of the simulation is compared against real data and, by reiterating this process and changing some variables, the divergences between the simulation and the data could be minimized. Moreover, the majority of the computer models require some real data inputs to run. Computer simulations could also be seen as the bridge that connects theory and experiment.

Over the years, computational modeling have become an essential tool of ongoing research in almost every field of activity: climatology, biology, chemistry, social science, economics, health care, architecture, entertainment, etc. The great advantage of computer simulations is its versatility and its scalability, and, in consequence, it replaces traditional methodologies where they are unfeasible, such as in the study of a nuclear blast, or ineffective, as in the study of an astrophysical event.

USC
UNIVERSIDADE DE SANTIAGO DE COMPOSTELA

Furthermore, philosophers of science were the first to open the debate on how computer simulations, among other new technologies, were changing the scientific practices and even considering it a new form of experimentation [121, 122, 123].

In a historical perspective, Buffon used an early version of the Monte Carlo method in the famous "needle-throwing" experiment in 1777 [124], afterwards, it was corrected by Laplace and nowadays is known as Buffon-Laplace needle problem [125, 126]. A century later, the first manual simulation was carried out by William Sealy Gosset [125, 127]. He published an statistical analysis called Student′s t-distribution where he used data from the Arthur Guiness, Son & Co. brewery. It reviewed an industrial-engineering problem in the field of industrial process control.

The computer era was born in the middle of 1940s with the construction of the first general-purpose electronic computer ENIAC [125, 128]. This event launched simulations towards new technologies domain. Stanislaw Ulam, John von Neumann, and others combined Monte Carlo method and electronic computers to solve the complex problem of neutron behavior in the design of the hydrogen bomb after WWII [129]. It is generally considered the first computer simulation.

In the second half of the twentieth century, with the remarkable success of the first application, the modelling technique soon became popular and found many applications in the business and industry. Moreover, new technologies developed for military purposes found a way out as a problem-solving tool in many areas. However, there was still a long way to go before the current status, needing many skilled people, user's group conferences as SHARE [130], high-level computer languages as FORTRAN (FORMula TRANslator) [131, 132], and other advances included in the bibliography [125, 128].

The present thesis is centered on a recently developed program called EnsarRoot [8, 9, 10] and it is further described in the following sections. Moreover, the new classes created and the code implementations done for the present work are detailed.

4.1.1 EnsarRoot Description

EnsarRoot framework was developed within the activities of ENSAR Joint Research Activity SiNuRSE (Simulations for Nuclear Reactions and Structure in Europe) and expanded in SATNuRSE (Simulations and Analysis Tools for Nuclear Reactions and Structure in Europe) [133], the second phase of the ENSAR project (ENSAR2) with the aim of providing a common framework for diverse small-medium size experiments. It holds different experimental setups as the CALIFA calorimeter test setup, TRASGO RPCs for cosmic

USC UNIVERSIDADE DE SANTIAGO DE COMPOSTELA

detection, and other small-size projects. Furthermore, there are available standard detectors as HPGe or NaI, which can be used and reconditioned for simulations of new experimental setups. This framework was designed to provide a flexible and a manageable open code to grant accessibility for developers, in addition, to reinforce synergies and share knowledge between different experiments within the ENSAR2 project. A significant advantage of this framework is the possibility to analyse experimental and simulated data using the same analytical tasks. Treating both type of data equally avoids additional bias and simplifies the development process.

Figure 4.1 shows schematically the main components of the EnsarRoot framework and the bounds between them. It can be noted that it is splitted into three blocks, in descending order: the codes and libraries, the base part called FairRoot [134, 135] and the specific code for describing the particular setup.

EnsarRoot requires the installation of FairRoot and the software compilation FairSoft [136]. FairRoot structure is displayed in the central part of Figure 4.1 and its own base classes are inherited by experimental codes. Specifically, FairRoot delivers, on one hand, classes that lead to the simulation and reconstruction executions, and, on the other hand, classes for the creation of detectors, event generators, analysis tasks and magnetic field definition. In the upper part of Figure 4.1 appears the toolkit used for the simulation of particles through matter Geant4 and it includes tracking, geometry, physics models and hits functionalities [137, 138, 139, 140]. ROOT [141] is used as the general framework for statistical analysis, graphical representations and geometry management, in addition, the VMC included in ROOT is the interface with the Monte Carlo of Geant4.

As we can observe in Figure 4.2, EnsarRoot has inherited three FairRoot group of classes: Detectors, Event Generators and Tasks. It is worth to mention, that each of them is independent, i.e. they act as a single unit, so, could be modified without affecting the others. The interaction between them is stablished only while the simulation is running. This flexibility is of great advantage because the user can test on the fly (without re-compiling the code) different detector configurations or several event generators for the same geometry, among other things. In order to achieve this adjustability, many settings are configurable at run time by input parameters or files. In the following sections, these three components are explained in detail.

4.1.1.1 Detector Constructor

As we have mentioned before, inside EnsarRoot there are classes specially designed to construct detectors including the reproduction of their character-

USC UNIVERSIDADE DE SANTIAGO DE COMPOSTELA

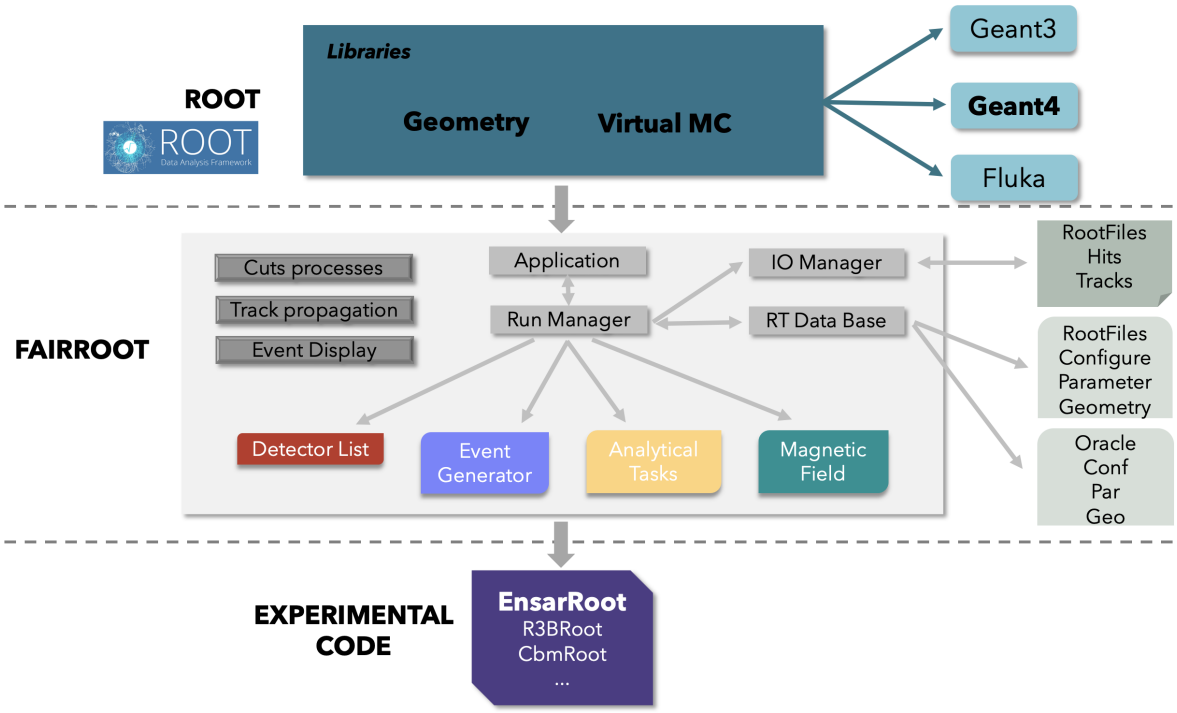

Figure 4.1: Schematic view of the FairSoft/FairRoot interdependences and their relation to diverse experimental codes; EnsarRoot among them. In the upper part of the scheme, some required system packages needed to construct a complete building environment to compile the FairSoft/FairRoot source code are displayed. In the central part, the FairRoot structure is shown. It contains diverse interrelated components linked by arrows and its own base constituents (Detector List, Event Generator, Analytical Tasks and Magnetic Field) which will be inherited by specific experimental codes, in the lower part of the diagram.

istics as well as its physical response. In Figure 4.2 there is a list of detectors already simulated inside the code, such as HPGe, NaI, and the CALIFA calorimeter which is a complex detector based on scintillation crystals [142]. In general, a detector is represented in the code by distinct parts: a physical representation, instructions to collect information when particle tracks cross the active volume, the detector response representation (to know the response to the passing of the particles) and other classes for the storage of the information.

The representation of the detector (simulated geometry) generally has active (detecting material) and inactive parts (shielding, connectors, etc.). Within the geometry interface, these geometries are built and saved in ROOT files. The developer tries to detach different parts of the geometry setup: the

USC UNIVERSIDADE DE SANTIAGO DE COMPOSTELA

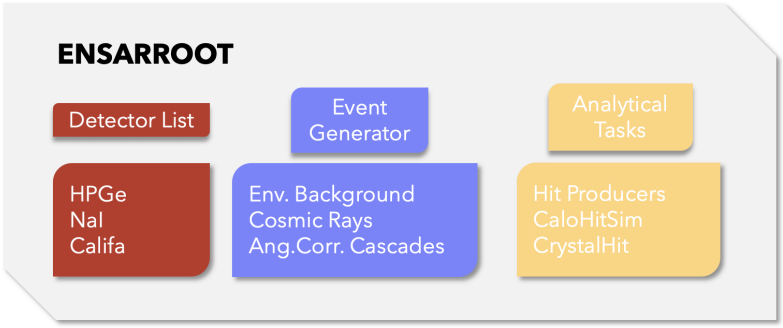

Figure 4.2: EnsarRoot scheme with the inherited components from FairRoot code: Detector List, Event Generator and Analytical Tasks. Underneath these categories some specific classes inside EnsarRoot are listed.

reaction chamber, the target, or other elements, from the detector itself, in order to mantain the individuality of each component. At run time, the geometry files are included in the steering macro and loaded in the simulation. As a result, convenient and significant changes could be done easily in the experimental setup. When the simulation has finished, the whole geometry is saved in the parameter set. These parameters could be read by the Event Viewer, a tool inherited from FairRoot, to visualize the geometry created in 3D (see, for example, Figures in Section 4.2). It is particularly useful in some cases when the user needs to check the orientation or position of the geometrical components. It has integrated some functions to facilitate the visualization as 3-axes plotting, plane cuts, rotations, etc. Another important feature that is shown is the MC track information.

At the same time, each type of detector has its own definition class where the detector response is simulated. They reproduce the behaviour of every detector based on their specific principle of detection: charge collector, time of flight, etc. A particle tracking is also done by Geant4 in case the particle interact with other materials different from the active parts.

Finally, there are classes to store the information from a simulation, or from any task, into data objects. They are the ROOT outputs of the entire simulation. Generally, there are three data levels: Point, Raw and Hit. Point level data gathers all the information from the MC engine that tracks the particles through the detectors (each step of the track generates an entry in this data category). Raw data level, on the contrary, merges information from the previous level and generates an output similar to a real detector (digitization). Afterwards, if this data passes through analytical tasks a new data stage is reached: Hit Data Level. This is a general explanation; details

USC UNIVERSIDADE DE SANTIAGO DE COMPOSTELA

on the output and procedures for each detector differ. Moreover, any of these data classes can be inactivated (data objects not saved) when they are not required making the simulation lighter in memory.

4.1.1.2 Event Generators

The function of a generator is to emit particles or nuclei in a certain direction, initial position and energy. These parameters are determined by the user or originated by default from an interaction vertex in case of reactions, decays... The user settings can be modified in the steering macro, and, particle interactions are dictated by physics lists. An specific generator emits, for instance, cosmic ray showers that includes high energetic particles as muons, protons, pions, etc. from top to bottom direction. Various generators are already defined inside the program and can be used in any simulation. As we mentioned before, the Event Generators operate independently from the other framework components. An important remark is that the simulation is done event by event: in one event the generator emits a certain number of particles, they propagate through matter and generate the detector response (if there is any). This is not a feature of EnsarRoot itself, but how a nuclear and particle physics Monte Carlo code as Geant4 works. In the following Section 4.2.2 the characteristics of diverse generators developed for this thesis are explained.

4.1.1.3 Analytical Tasks

EnsarRoot provides the tasks and the facilities to access to the simulated data and performs an event by event analysis, concretely, each type of detector has defined specific analytical tools. An important remark is that these analytical tasks can be applied on equal footing on simulated and real data as they have a similar data structure. This approach provides great advantages: it avoids bias and systematic uncertainties, and the same code is used for all data regardless of its origin. The simplicity and flexibility of these analytical tools lead to a complex analysis to obtain manageable physical observables. In addition, successive tasks could be implemented expanding the code in a convenient way.

Figure 4.3 shows sequential steps that data undergoes in a simulation session (upper part) and in a real data analysis (bottom part). The simulation process starts by considering one or several generators, who define the properties (type of particle, momentum, position) of the primary particles, which are labelled together in a structure called *event*. Afterwards, Virtual MC transports these particles one by one using an specific transport engine

USC UNIVERSIDADE DE SANTIAGO DE COMPOSTELA

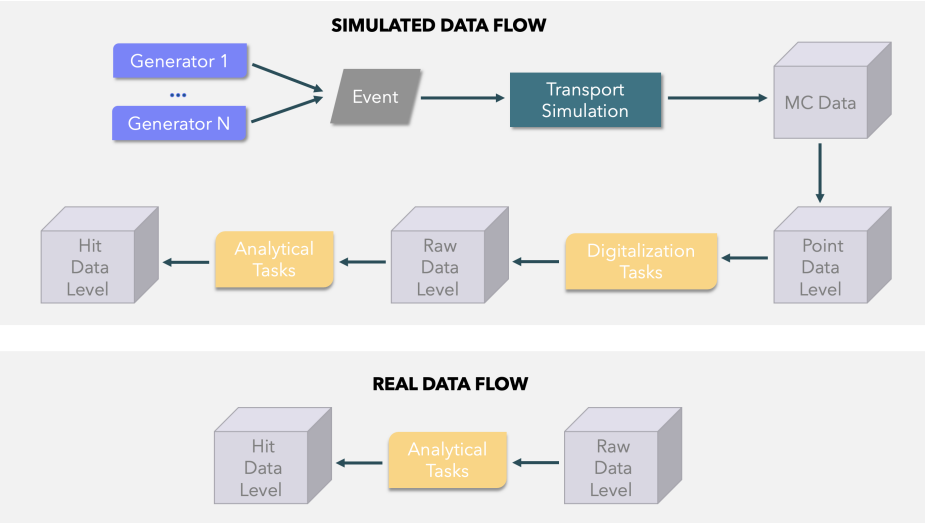

Figure 4.3: EnsarRoot data flow. In the upper part, the simulated data flow is shown, while in the bottom part, the real data flow is displayed.

through the matter of the experimental setup. If the particles deposit energy in the sensitive detector volume, a collection of points is generated in the ProcessEvent function of the detector. At this stage, Point Data level is completed. This data undergoes a digitalization process to convert it into the next data stage: Raw Data Level. Subsequently, this data is treated by diverse reconstruction mechanisms until Hit Data level is generated. On the other hand, measured data coming from the detector is already at Raw Data Level, therefore, only analytical tasks are applied until Hit Data Level is created. Eventually, we have obtained the same type of data via two different routes. For the analytical tools they are indistinguishable (unless you go back to previous data levels) and, in consequence, treated on equal basis.

4.2 EnsarRoot Developments

In order to expand the EnsarRoot program some developments on the basic code were carried out following the aims of the two investigation lines of this thesis. On the one hand, we simulated the experimental setups where PIGE data and environmental radiation were measured, and on the other hand, distinct particle generators have been created to reproduce the nuclear processes under study. Moreover, to analyse the gathered data diverse codes and subroutines have been developed although they are used as independent macros in the data analysis and do not appear in this section.

USC UNIVERSIDADE DE SANTIAGO DE COMPOSTELA

4.2.1 EnsarRoot Experimental Setups

4.2.1.1 The CTN/IST Setup

The standard setup dedicated to PIGE studies of the CTN/IST PIGE Line was simulated within the EnsarRoot framework as an integral setup. As it is described in Section 4.4.1, it includes two main components: an HPGe semiconductor detector situated at 130° in polar angle in a system with Z direction along the beam line and a reaction chamber placed at the end of the PIGE line. This reaction chamber has been taken as the central position (origin) of the simulated setup. Silicon detectors which are inside the reaction chamber have not been developed in this simulated setup because no data analysis was required within EnsarRoot, and, moreover, their interference in the HPGe response function is marginal, as they occupy a small volume and their possible contribution was limited.

The HPGe detector simulation includes different active and inactive layers in order to recreate particle energy loss through all materials. The active part made of germanium material is the major portion of the detector and it has an empty central part where the dewar is connected. Besides, the germanium wrapping contains diverse layers such as steel, lithium and aluminium which conform the detector inactive part. These distinct parts are visible on the left side of Figure 4.4. The detector is cylindrical with dimensions 7,01 cm length and 8,07 cm of diameter. As we can observe in Figure 4.5 the detector is placed half inside a lateral wall of the reaction chamber. The chamber is also cylindrical and it is a 25 cm high by 19 cm in diameter. It is made of steel and its central part is filled with vacuum, while the surroundings of both volumes are filled with air, aiming to recreate setup conditions.

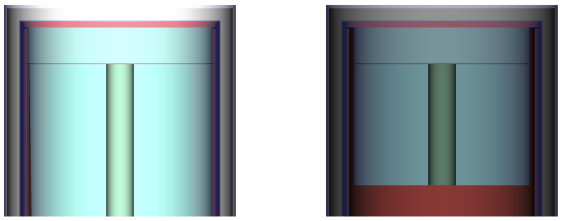

Figure 4.4: Simulation of HPGe detectors, side view. Layers of diverse materials are distinguishable by different colors with the active volume in blue. At left, it is displayed the CTN/IST HPGe detector while, at right, it is exposed the HPGe of the Universidade da Beira Interior laboratory which has 24 % less active volume.

The present recreated setup has been used in two simulations: for the analysis of proton induced chlorine reactions using PIGE technique and for the CTN/IST environmental background simulations, namely the two

USC UNIVERSIDADE DE SANTIAGO DE COMPOSTELA

branches of this work. For this last study, an additional volume of earthy materials has been added to the setup in order to reproduce real background conditions.

As we have explained in Section 3.2.5, radioactive series cover predominantly low-to-intermediate energy range. As a result of this wide interval, the flux rate loss in matter between the highest and the lowest photopeak energy is not negligible. In fact, we experimentally observed photopeaks of lower energies were more attenuated before reaching the detector. After an extensive study benchmarking the laboratory environmental radiation and diverse simulations (where many elements of the setup where recreated and modified in order to observe changes in the simulated data), the present setup had to be adapted including a rectangular block of silicon under the detector to recreate earthy materials that gammas coming from the subsoil have to cross, partially or totally. The thickness of this added volume was calculated applying the attenuation of gamma radiation law (Eq. 2.16 of [4]) to two photopeaks from the thorium series at low energies (238,320(3) keV peak) and at high energies (2614,533(13) keV peak) [26]. As a result, we have incorporated a block of earth of 12,2 cm of thickness under the detector (Figure 4.6). This volume is not needed in PIGE experiments as the photons come from the center of the reaction chamber and they are not influenced by this volume.

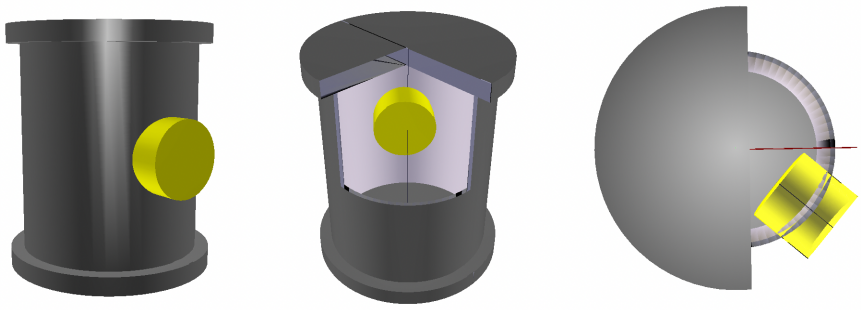

Figure 4.5: Diverse views of the CTN/IST setup design in the event viewer of the EnsarRoot simulation. It includes a reaction chamber (grey volume) and an HPGe detector (yellow volume).

4.2.1.2 The Universidade da Beira Interior Setup

In the present case, we have reproduced the setup of Universidade da Beira Interior laboratory that has as a single component: an HPGe cylindrical detector with similar shape and size as in the previous simulation. This detector

USC UNIVERSIDADE DE SANTIAGO DE COMPOSTELA

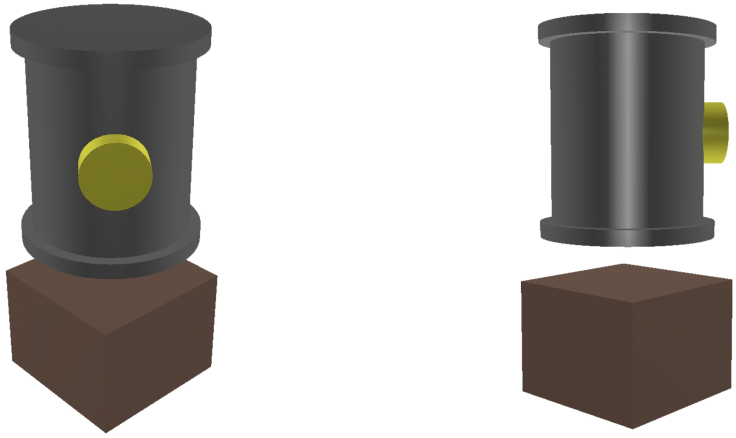

Figure 4.6: Frontal and lateral views of the CTN/IST setup with an earth block design in the event viewer of the EnsarRoot simulation. It includes a reaction chamber (grey volume), an HPGe detector (yellow volume) and a block of earth (brown volume).

includes the same inactive layers, although has a smaller active volume, representing around 76 % of the CTN/IST HPGe detector. The comparision of these two germanium detectors is showed in Figure 4.4. As this simulation was dedicated to natural radiation studies, where the moderation of the background source is needed, we had to include a silicon block under the detector in order to recreate laboratory ground conditions. The thickness of this added volume is 7 cm and it was calculated following the same procedure as in the previous case.

4.2.2 EnsarRoot Generators

As was mentioned, diverse particle generators have been developed to fulfill the experimental simulation requirements and to expand EnsarRoot code. In this section they are introduced and their functionalities explained.

4.2.2.1 Environmental Radiation EnsarGenerators

In order to reproduce all decays and de-excitations spontaneously occurring in nature, different generators have been developed. Natural background coming from earth materials includes the three radioactive chains of uranium, thorium and actinium and the potassium decay (see Section 3.2.5). For each nuclear decay an individual generator was recreated and it includes the decay of the parent nucleus and the de-excitation of its daughter. On account of

USC UNIVERSIDADE DE SANTIAGO DE COMPOSTELA

being centred on gamma spectroscopy, these generators only emit gamma radiation and not α-particles or electrons.

Potassium Decay EnsarGenerator

Figure 3.7 illustrates the decay of ^{40}K going to ^{40}Ca via β^- and to a ^{40}Ar via electron capture. In the first decay, there is no gamma emission because the transition goes from ground to ground state. In the second decay, if the parent nucleus lands on the 2^+ excited state of the daughter nucleus, a posterior de-excitation occurs and a gamma of 1460,820(5) keV is emitted.

The potassium generator reproduces all these processes emitting the corresponding gamma distributions. It works in two steps: the first one simulates the decay of the parent nucleus accordingly to the decay probabilities and it lands into one of the two daughter nuclei, secondly, it reproduces the de-excitation of the ^{40}Ar nucleus until the ground state is reached also following the intensities of each transition. The decay information used in this generator is displayed in Table 4.1. We can observe that in order to include the probabilities that NNDC database provides, we had to convert them in a decimal fraction (I_{decay}), in this case, the conversion is straightforward but in nucleus with 29 energy levels and a large amount of gamma emissions, such as ^{214}Po of the uranium chain, the calculus is more complex (see Appendix A). The user can control the number of decays produced in a run, as well as the origin (x, y, and z coordinates) and the direction of the gammas emitted (spherical angles).

Table 4.1: Decay of ^{40}K. Energy units are expressed in keV and the probabilities for each transition are indicated in decimal fraction. The nuclear data is extracted from NNDC [26].

Parent Nucleus	**Parent $T_{1/2}$**	**Decay Mode**	**Daughter Nucleus**	**I_{decay}**	**Initial Daughter State E_i**
^{40}K	1,248×10^9(3) y	ε : 10,72(11) %	^{40}Ar	0,004 0,995	**g.s.** 1460,849(5)
^{40}K	1,248×10^9(3) y	β^- : 89,28(11) %	^{40}Ca	1	**g.s.**

USC UNIVERSIDADE DE SANTIAGO DE COMPOSTELA

Radioactive Series EnsarGenerators

This set of generators includes all radioactive processes of the natural series that have gamma emissions coming from transitions with probabilities higher than 1 % as they are the only visible photopeaks in the spectra of the HPGe detector (employed in background measurements). The minor branches have also been excluded, for example, the ^{223}Fr alpha decay to the daughter nucleus ^{219}At which has a probability of 0,006 % (actinium chain). Figures 3.8, 3.9, and 3.10 represent the successive decays of each radioactive chain.

Particularly, an individual generator recreates the decaying process and emits all gammas of the daughter de-excitation according to the relative intensities of each gamma line. It works just like the previous Potassium Decay: in the first stage the decay of the nucleus is reproduced and in the second step the de-excitation of the daughter occurs, although in this case the emission of gamma cascades do not cease until the ground state is reached, this means that this secondary process is a loop structure. The user has the same power of management as in the previous generator and can control the number of decays, the origin, and the direction of the particles. When all simulations of the same radioactive chain are gathered we obtain the signal of this series where all the gammas of the family appear.

Appendix A, B and C show the tables with the decaying probabilities, energy levels, particle energies and intensities included in all these classes. To be consistent, every generator is based on the information provided by the Table of Radioactive Isotopes from The Lund/LBNL Nuclear Data Search [143] and on the NNDC database [26].

Further code developments of EnsarRoot program are explained in Appendix D. In particular, there was developed one generator that reproduces gamma cascades with angular correlations and the CALIFA Testing Experiment setup simulation. There are also code developments related to the CALIFA calorimeter based on the R3BRoot program in the Appendix E.

4.3 PIGE Experimental Procedures: Target Production

Targety is the method of target preparation and gathers diverse disciplines such as physics, chemistry and technical [144]. Moreover, manual skills and previous knowledge of vacuum technology, etc. are also desirable. In nuclear research, a target is, by definition, the sample at rest in the Laboratory

USC UNIVERSIDADE DE SANTIAGO DE COMPOSTELA

Reference System where the beam impinges. As a consequence, target characteristics and quality are of major importance for the experimental results.

Historically, the first target used in a nuclear reaction experiment was a thin metal foil by H. Geiger and E. Marsden in 1909, manufactured for the observation of scattered alpha particles [145], since then, targety has been evolving and adapting to fulfill research requisites.

Nowadays, there is a large variety of targets. Physically, they can have diverse shapes, dimensions, thicknesses and be in a solid, liquid or gaseous state. Chemically, they can have an elemental composition, be a compound or even have been produced with unstable isotopes [146]. Moreover, they can be self-supporting or on a backing. All these features are dictated by experimental requirements, for example, high beam intensities need stable samples with good mechanical strength. In general, target size depends on the projectile: diameters of 1 cm are used for lighter beams with 2-3 mm spot and diameters from 1 to 2 cm are used for heavy ion beams. Target thickness, on the other hand, ranges from 1 $\mu g/cm^2$ up to 10-20 mg/cm^2 for nuclear experiments and hundreds of mg/cm^2 for medical applications. In order to make all these types of samples, diverse production techniques have been developed, although for a specific target there are different methods of producing it.

In order to study chlorine reactions using PIGE technique a chlorine target for lighter beams was needed. Moreover, cross section measurements required it to be as thin as possible and with a great quantity of chlorine to obtain good statistics. The process of target preparation employed in this work is explained in detail in the present section. Further information, publications and international conferences are held by the International Nuclear Targets Development Society (INTDS) [144].

4.3.1 Vacuum Thermal Deposition

Vacuum thermal deposition is one target production technique based on evaporation-condensation inside high vacuum. It consists in the heating of the source material until it evaporates and condensates on a substrate situated above the evaporated source. The high vacuum inside the chamber facilitates the evaporation of the material due to the melting point diminishes. It can be heated by diverse procedures: electrospraying, ion beam sputtering, levitation heating and melting, electron beam gun, electron bombardment and, the one used in this work, resistant heating [147].

In general, this method provides an homogenous material distribution along the substrate, although the thickness varies along it: the substrate sides have less material (they are thinner) than targets extracted from the central

USC UNIVERSIDADE DE SANTIAGO DE COMPOSTELA

part, just above the vapour source. This is caused because the distance to the source is not equal neither is the area defined to receive the material. This feature could be seen as an advantage since targets of diverse thicknesses are produced in the same evaporation. The main drawback is the large quantity of material loss as a consequence of the low efficiency collection. Vacuum deposition can produce relatively thin targets in the $\mu g/cm^2$ range up to mg/cm^2 and they can be self-supporting or be condensated on a backing.

4.3.2 Target Production

The production of silver chloride target was carried out via vacuum thermal deposition in the Target Laboratory in the Faculdade de Ciências da Universidade de Lisboa [21] and Laboratório de Instrumentação e Física Experimental de Partículas [22] (FCUL/LIP). This laboratory setup consists of a vacuum chamber (Figure 4.7) with two electrodes (Figure 4.8) controlated by an electronic module; two vacuum systems: one primary pump that lowers the atmospheric pressure to $\sim 1 \times 10^{-1}$ mbar and a turbo pump that makes a high vacuum of $\sim 1 \times 10^{-7}$ mbar. In addition, a chiller is installed to cool down the whole setup. The vacuum chamber is mechanically activated by a compressed air system.

Figure 4.7: Vacuum chamber of the Target Laboratory at FCUL/LIP [21, 22].

The first step of target production was the preparation of diverse glass substrates. The substrates were cleaned by using propan-2-ol and dried using compressed air (in order to avoid paper fluffs or other external agents on the

USC UNIVERSIDADE DE SANTIAGO DE COMPOSTELA

Figure 4.8: View of the inside vacuum chamber. On the left picture there are two boats (one loaded with silver) connected to two electrodes. On the right picture, a boat loaded with silver chloride is shown.

surface). Afterwards, they were coated with a thin film of release agent. Special attention should be driven into the coating thickness if the layer was too thin, the evaporated material was not released at the moment of fishing[1], on the contrary, when the coating layer was too thick the targets broke at the moment of releasing them, as we can observe in Figure 4.9 where some cracked targets appear.

The initial material to evaporate was silver, since it was the backing of silver chloride targets. A small quantity of natural silver (305,4 mg) was placed inside a boat of which only 154,5 mg was evaporated. This boat was connected from both sides to two electrodes through which the current passed (the left picture of Figure 4.8 shows two boats connected to the current and one of them is loaded with Ag small balls). During the evaporation, which took a few minutes, a small quantity of material was deposited on the bottom of the glass substrates. Figure 4.10 shows the interior view of the chamber just after a silver evaporation, we can observe the substrates with condensated silver placed on the target support just above the evaporating source. Thereafter, these silver layers were released from the substrates using distilled water in order to dissolve the release agent (Figure 4.9). These targets were manually fished from the water into target holders.

Once backings were created, they were placed again inside the vacuum chamber where a second evaporation was performed. In this case, the boat was loaded with 233 mg of natural AgCl (see the right photo of Figure 4.8), from which only 159 mg was evaporated. During the whole process

[1]Fishing refers to the action of capture a target floating on the surface water by using a target holder and forceps.

USC UNIVERSIDADE DE SANTIAGO DE COMPOSTELA

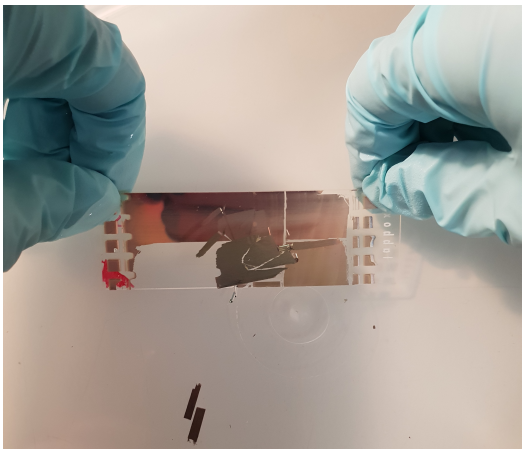

Figure 4.9: Manual work of releasing targets from the substrate on distilled water. Some targets break at the moment of release due to an excess of release agent.

the majority of targets broke or cracked (at the moment of fishing, because pressure changes, etc.). The remaining targets extracted without damage from this last stage were ready to be used (in Figure 4.11 diverse finalized targets are shown). They had a diameter around 1 cm and their thicknesses were still unknown at that point.

The source material in both evaporations were placed inside tantalum boats, which were previously heated in order to release surface impurities. In the course of evaporation, when the current was passing through the electrodes, either boats were also heated and their color changed to a bright glowing orange (Figure 4.12). In fact, by using this visual sign we checked if the evaporation was carrying on successfully[2]. Both evaporations were performed in dark conditions to have a good view of the chamber interior and because silver chloride darkens on exposure to light (see Figure 4.11). Afterwards, targets were kept in special conditions: inside a glass drying vessel to avoid hygroscopicity and most of the time in the dark.

Since it was the first time in our laboratory that this type of targets was manufactured, diverse combinations and tests were done until the desirable result was obtained. Note that to perform both evaporations at the same stage (this means, without opening the vacuum chamber and fishing the silver backings) was also possible, although, the thin layers of the condensated material were glued on top of the glass substrates and it was impossible to remove them. The same inconvenience arose when we tried to make silver chloride targets self-supporting. On the other hand, different materials as

[2]The vacuum chamber has a small glass window on the lateral side.

USC UNIVERSIDADE DE SANTIAGO DE COMPOSTELA

Figure 4.10: View of the inside chamber after the silver evaporation. In the middle of the cavity there are two crucibles for resistant heating and on top of it there is placed the target support with substrates.

a backing have been considered, one of the most being used is aluminium. However, in [148, 149] it was observed that silver chloride reacts with the aluminium foil during irradiation compromising its use as backing material for this particular type of targets. Other materials such as barium chloride were also considered for the target, although it was rejected for its high levels of toxicity. Finally, the combination of silver chloride on a silver backing was the most convenient in terms of budget and because silver targets have been produced successfully in the same laboratory. Another advantage of this election was that PIGE and RBS analysis simplify due to the fewer elements in the sample the less overlapping appears on the spectra.

USC UNIVERSIDADE DE SANTIAGO DE COMPOSTELA

Figure 4.11: Silver chloride targets mounted on a thin silver substrate produced in the framework of this thesis work. We can observe that chlorine targets are photosensitive due to its dark pinkish color (on the right), while the silver backing is not (on the left).

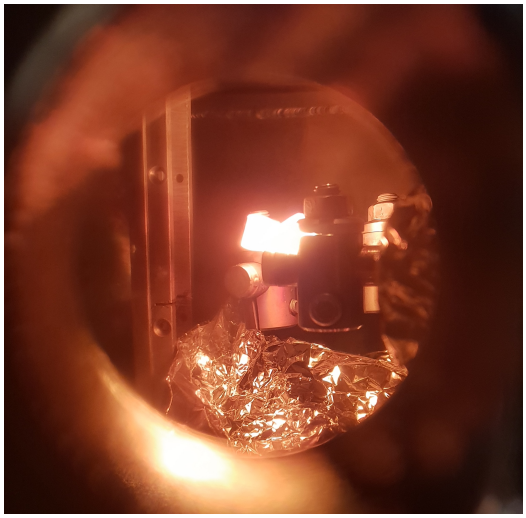

Figure 4.12: View of the inside vacuum chamber while the evaporation was taking place. In the middle of the picture a heated tantalum boat appears in bright orange.

USC
UNIVERSIDADE DE SANTIAGO DE COMPOSTELA

4.4 PIGE Experimental Procedures at CTN/IST Installations

4.4.1 Installations of the Experimental Setups

PIGE experiments, RBS experiments and environmental radiation measurements of the present thesis were carried out in the C^2TN laboratory [23]. It is located at the Campus Tecnológico e Nuclear (CTN) of the Instituto Superior Técnico (IST) [150] in Sacavém (Portugal). Along the work we refer to this facility as CTN/IST to shorten the name. It is an outstanding research center in the fields of advanced materials, cultural heritage, radioactivity, Earth systems, radiation protection and radiopharmaceutical sciences. The laboratories, equipment and infrastructures are operated by scientists, technicians and students from research units from IST, although it is also open to external researchers. Figure 4.13 shows the ion beam laboratories where the accelerators that we have operated are located: on the left part it is the Van der Graaff accelerator (in green) and on the right side the Tandem accelerator (in yellow). In the following subsections the technical characteristics of both installations are explained in detail.

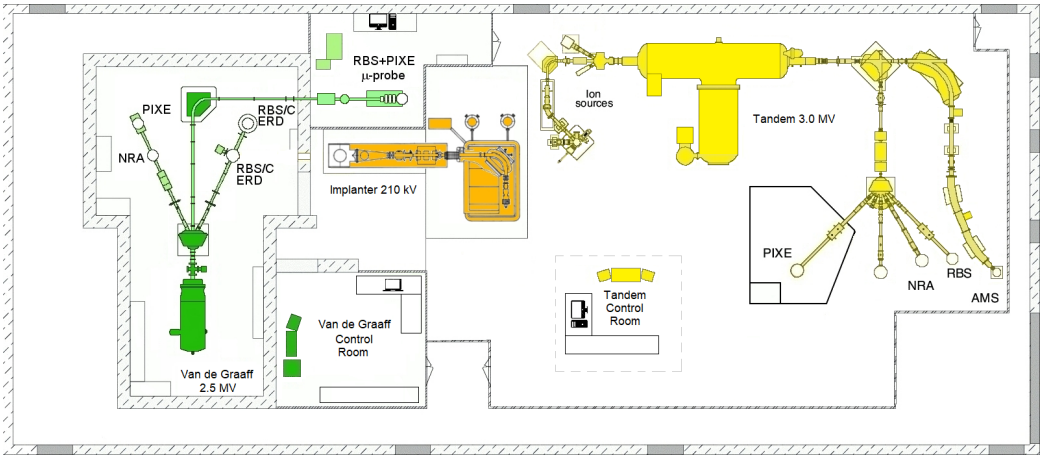

Figure 4.13: CTN/IST ion beam laboratories and their accelerator schemes. On the left, there is displayed the Van der Graaff accelerator (green), and on the right, there is shown the Tandem accelerator (yellow).

4.4.1.1 Van der Graaff Accelerator

The Van der Graaff accelerator is an horizontal electrostatic accelerator with a high voltage terminal up to 2,5 MV. It can accelerate positive ion beams

USC UNIVERSIDADE DE SANTIAGO DE COMPOSTELA

of H^+, $^2H^+$, $^3H^+$ and $^4He^+$. The resulting beam can have a maximum total kinetic energy of 2,5 MeV and currents of a few microamperes. As we can observe in the left side of Figure 4.13 there are three experimental beam lines with distinct associated IBA techniques: NRA and PIXE in the first two lines and the third line that we used RBS and ERDA techniques. There is a set of vacuum pumps located along the setup to keep the pressure inside the lines and reaction chambers around 2×10^{-6} mbar. The accelerator is controlled manually by the user, from switching on the ion source until the manipulation of the data coming out of the detector.

RBS Line

The track that follows an ion at the RBS Line starts in the ion source where the plasma is generated, then it is accelerated in the belt of the Van der Graaf and extracted by a high voltage source. An important stage is when the beam passes through the deflector electromagnet situated after the extraction phase because it guides the beam towards the desired line and it determines exactly the beam energy. By using the magnetic field value provided by this electromagnet the beam is calibrated. Along the trajectory the beam passes through diverse collimators that allow the measurement and tune the beam dispersion. The beam current is measured by a tantalum piece connected to an ampermeter (when the current in the tantalum is maximum the beam is collimated). In the last stage, the ion beam enters into the reaction chamber; its geometry is displayed in Figure 4.14. As we can observe, there are three PIPS ("Passivated Implanted Planar Silicon") semiconductor detectors placed at backward angles named RBS1, RBS2 and ERD. In Table 4.2 there are detailed the detector's features. Targets are placed inside the reaction chamber by using the goniometer shown in Figure 4.15.

Table 4.2: Technical characteristics of the RBS1, RBS2 and ERD detectors placed in the RBS Line.

Detector	**Angle (°)**	**Distance (mm)**	**Colimator (mm)**	**Solid Angle (msr)**
RBS1	+165	75,4	9,2	11,7
RBS2	−140	67,0	4,6	3,7
ERD	−165	75,4	9,2	11,7

USC UNIVERSIDADE DE SANTIAGO DE COMPOSTELA

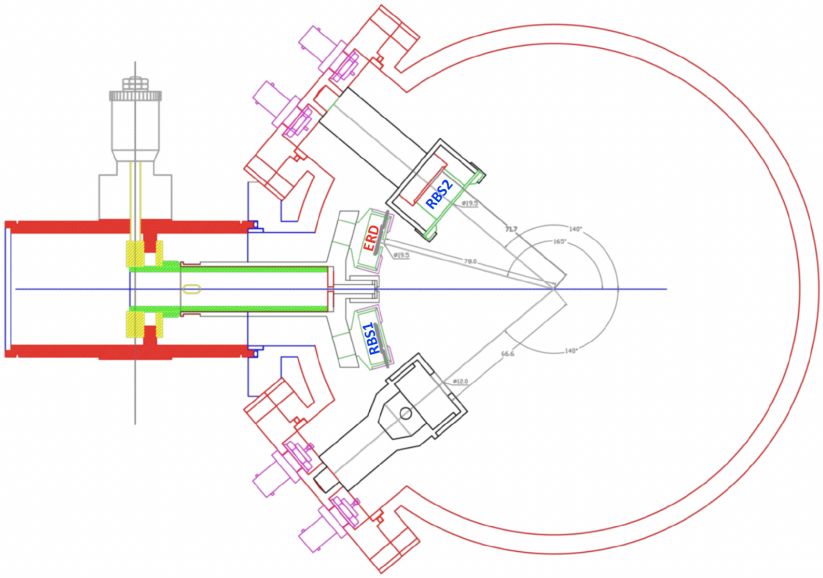

Figure 4.14: Reaction chamber geometry of the RBS Line. The three detectors RBS1, RBS2 and ERD are tagged in their respective positions. The angles with respect to the beam line are also indicated: RBS2 is placed at 140° and ERD and RBS1 are situated at 165° on oposite sides.

4.4.1.2 Tandem Accelerator

PIGE experiments were carried out at the CTN/IST Tandem installation (Figure 4.16). This setup is capable of accelerating H^+ ions up to 6 MeV by using an electrostatic Tandem accelerator of 3 MV. A detailed scheme of the entire setup is presented on the right side of the Figure 4.13. The line has different sections and in each stage the beam is treated until reaching the desirable conditions to carry out the experiment. As in the previous case, this accelerator is controlled manually by the user.

At the beginning of the line, a duoplasmatron source produces a negative ion beam (H^-) that is bended and focalized by a bending magnet and electrostatics lens, respectively, before entering into the accelerator.

In the first stage of the Tandem the negative ions are accelerated by a positive electric potential created by a high voltage supply Cockcroft-Walton of 3 MV. In the middle of the tank there is a stripper, an argon gas target that removes all the electrons of the beam. Once the ion beam is positive it is accelerated in a second phase by the same positive electric potential, but this time, due to charge repulsion. The total energy acquired by the particles is,

USC UNIVERSIDADE DE SANTIAGO DE COMPOSTELA

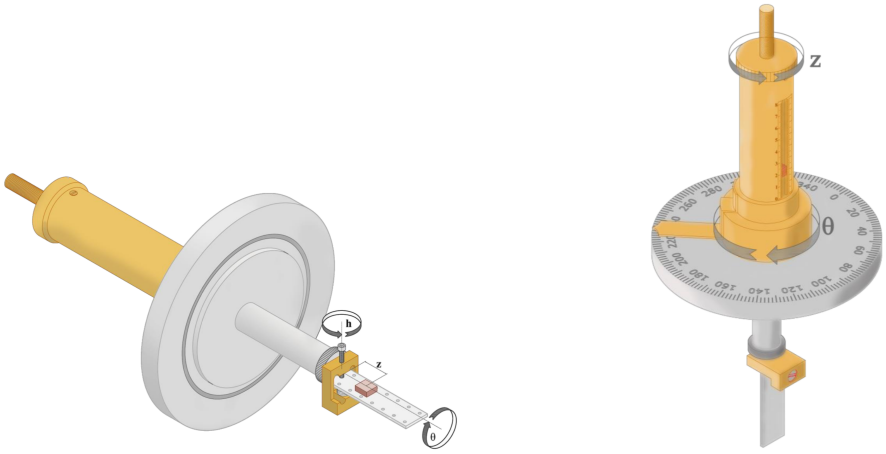

Figure 4.15: Goniometer of the RBS Line. On the left, the sample holder and the three adjustable parameters are shown: z represents the height, θ the inclination and h the screw that fixes the targets. On the right, there is a goniometer vertical sketch with the two manipulable parameters z and θ from outside (once the reaction chamber is closed).

$$E_{beam} = (1 + q)V, \tag{4.1}$$

where q corresponds to the final ion charge and V to the accelerator potential settled by the user. Although, this equation gives the calibration of the Tandem is a rough approximation and for the experiments another calibration formula more accurate is used.

Subsequently, the beam crosses three magnetic fields: the 90° analysing magnet which deflects the beam trajectory by 90°, the quadrupole that focalizes the beam and finally the switching magnet which redirects the beam trajectory towards the desired experimental line. In our case, the beam was redirected to the nuclear reaction line also known as PIGE Line (Figure 4.17). Along the line, the beam passes through diverse Faraday caps to measure the beam intensity and slides to reduce the beam diameter.

Before entering into the reaction chamber the beam is orientated by electrostatic deflectors and passes through a collimator just in the entrance of the chamber, which makes that the final beam spot would be 2 mm of diameter. The reaction chamber is shown in Figure 4.18. As we can observe, inside the chamber there is the entrance collimator on the top. In the opposite direction, the beam stopper that deter the ions once they have crossed the target, on the left creating an angle of 130° with respect to the beam direction there is the steel holder where the HPGe detector is placed and, lastly, on the bottom of the chamber there is a movable structure holding the particle detectors

USC UNIVERSIDADE DE SANTIAGO DE COMPOSTELA

Figure 4.16: Photography of the Tandem accelerator (blue) and its control room at CTN/IST.

MOVD and MOVE. The reaction chamber is electrically isolated (acting as a Faraday cup) in order to quantify the charge coming from the hitting ions and the secondary electrons emitted by the target (charge collection). The pressure inside the line is regulated by a series of vacuum pumps and in the reaction chamber the pressure reaches a minimum of $\sim 10^{-6}$ mbar.

Positioning the beam into the reaction chamber is not a straightforward task due to the fact that there are many elements intervening. Occasionally, a shift of 4 cm has been observed in either vertical and horizontal planes [151].

MOVE and MOVD Detectors

MOVE and MOVD[3] are Canberra PIPS detectors of an active area of 50 mm^2, effective thickness of 100 μm and a resolution sigma of 12 keV for 5486 keV alpha particles coming from a ^{241}Am radioactive source [151]. Each one is placed inside a teflon box which, in turn, is placed in a stainless steel box with 6 mm diameter aperture. They are placed in a movable arm at a fixed angle of 21° between them. This arm can move along θ_{lab} = 84-165° with an accuracy of 1° and, specifically, at an angle of 145° the distance between the target and the detectors' structure is 88(1) mm. Depending

[3]MOVE and MOVD are the acronyms of "MÓVil Esquerda" (movable left) and "MÓVil Direita" (movable right), indicating the position of each PIPS detector (left or right) viewed from above of the reaction chamber.

USC UNIVERSIDADE DE SANTIAGO DE COMPOSTELA

Figure 4.17: Nuclear reaction line of the Tandem accelerator at CTN/IST. On the left side the switching magnet is displayed. On the center diverse elements of the setup are shown: the HPGe with its cryostat, the reaction chamber and the turbo vacuum pump. In the lower part of the picture the neutron detector used for controlling neutron yields appears (it was only used in order to maintain safety conditions.)

on the experimental setup requirements, this angle could be modified by the user from outside the chamber. For this configuration the solid angle covered by each detector is $\Omega = 3,651(83)$ msrad [4]. These detectors are used for RBS and ERDA techniques because they detect charged particles as protons and alpha particles.

HPGe Detector

The gamma detector installed in the nuclear reaction line is a High Purity Germanium (HPGe) Radiation Detector GLP Series Planar fabricated by ORTEC [152]. It is composed of layers of diverse materials. The first aluminium wrapping has dimensions of 37,5 mm radius and 68,1 mm length and 10 mm thickness, then, there is a more internal aluminium wrapping of a thickness of 0,5 mm and between both layers there is a space of 4 mm of vacuum. In the central part of the detector, there is a 2 mm germanium

[4] Where it has been used $\Omega = \pi r^2/d^2$ formula valid only at long distances from [151].

USC UNIVERSIDADE DE SANTIAGO DE COMPOSTELA

inactive layer and the germanium active volume of 30 mm of radius and 60,6 mm length. The external layer plays an important role absorbing low energetic gammas, fact that has been observed in simulation by modifying their thickness. In order to maintain the active material in good conditions, all germanium semiconductor detectors require cryogenic cooling. The flowing liquid cryogen enters into the detector through an internal cavity in the middle of the germanium active part with dimensions of 4,5 mm radium and 49,1 mm length. As we have mentioned before, the detector is placed at 130° w.r.t. the beam line and, in principle, it was situated at 55,5 mm from the center of the reaction chamber, although this distance was not well known. The dead time of the detector is around 0,3 μs per event [151].

Target Positioning

To have a precise knowledge of the target position inside the reaction chamber is of major importance, due to the fact that it might lead to miscalculations on the detector efficiencies, solid angles, or, furthermore, at the time of the experiment if the target is not centered in the beam trajectory part of the target holder can be hit.

For these reasons the target (or targets) is placed in a regulated frame called goniometer similar to the one displayed in Figure 4.15. It can control the distance between the lid of the reaction chamber and the center of each target and the angular inclination with respect to the beam line. These two magnitudes could be modified at any time without opening the reaction chamber by rotating two wheels on the top of the frame (right sketch of Figure 4.15). Therefore, by placing the target in the target holder at a known distance z you can control the height at which the target is situated and the θ angle at which it is tilted (see left picture of Figure 4.15). Targets are fixed on the target holder securing the screw on the upper part (h symbol on the left picture of Figure 4.15).

USC UNIVERSIDADE DE SANTIAGO DE COMPOSTELA

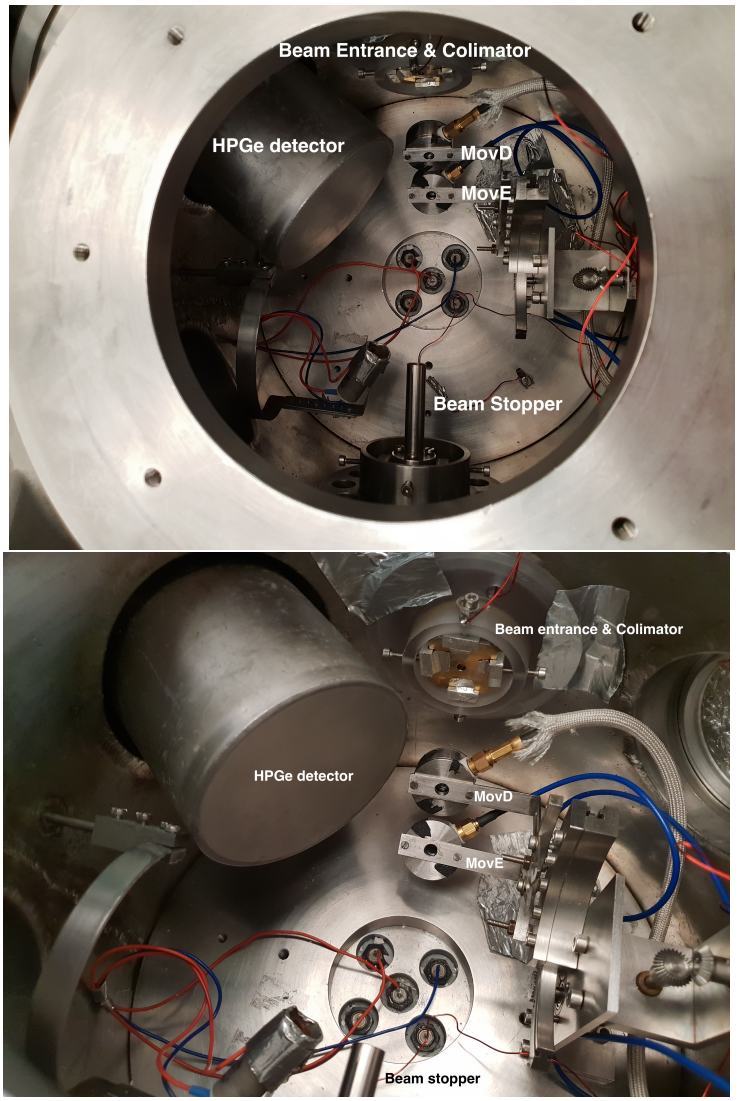

Figure 4.18: The interior of the reaction chamber of the nuclear reaction line. Diverse elements of the setup appear: HPGe detector, beam entrance, collimator, particle detectors MOVD and MOVE and the beam stopper on the opposite side of the entrance.

USC UNIVERSIDADE DE SANTIAGO DE COMPOSTELA

4.4.2 RBS Experiment

The RBS measurements were done at the RBS Line of the CTN/IST Van der Graaff in January 2020 with the aim of analysing the thickness and composition of the target used at the PIGE experiment. This information is of capital importance because it allows the transformation of gamma yields into cross sections (consult Section 5.1.2). The experiment consisted on backscattering measurements of alpha particles using RBS1 and RBS2 detectors. The $^4He^+$ ion beam was directed orthogonally to the target surface with a current of 15 nA and a beam spot around 2 mm in diameter. Each spectrum measured was normalized at 2 μC of collected charge.

Van der Graaff calibration was done using the magnetic field of the deflector electromagnet of the RBS Line at the beginning and at the end of each run and a calibrated excel that the Tandem working group provides to the user. Hence, the alpha energy was $E = 1999,96$ keV.

Diverse targets from different evaporations were studied in order to measure their thickness and compositions to choose the most suitable target for the PIGE experiment. The targets under analysis were placed in the middle of the reaction chamber by using the goniometer of Figure 4.15. The angles that formed the beam, the targets and the RBS1[5] detector were $\theta = 165°$, $\beta = 15°$ and $\alpha = 0°$ in accordance with IBM 1 geometry [153]. These angles were in-plane and the sum of all them give 180°. Afterwards, this data was analysed using the SIMNRA program [75] (see Section 5.1.1).

4.4.3 PIGE Experiment

The PIGE experiment was carried out entirely at the CTN/IST installations using the Tandem laboratory and the nuclear reaction line. It was performed during two rounds. The first part was carried out in July of 2019 and it was measured at beam energies between 2,6 and 3,2 MeV. The second part of the experiment done in January 2020 is an extension of the first one at higher and lower energies (from 2,4 to 2,6 and from 3,2 to 3,5 MeV) in order to determine yield evolutions. We did not measure at lower energies because chlorine gamma yields were not observable. These energetic intervals were inspectioned by fine steps of 4 keV, this means, steps of 2 kV in the Tandem accelerator, in case of the appearance of narrow resonances. In both experiments the intensity of the beam in the reaction chamber was oscillating between 50 and 150 nA depending on the momentary conditions (higher intensities were not desirable because they induce target damage). Installed in the setup, there is a current integrator which measures the current

[5]RBS1 particle detector is the one used for the target analysis.

USC UNIVERSIDADE DE SANTIAGO DE COMPOSTELA

collected in the reaction chamber and starts or stops the DAQ signal. This system was really useful because each spectrum had the same amount of collected charge, and therefore, they were directly comparable. In addition, we did some measurements by setting a double of charge collection to check if this system was working correctly.

The target used in both experiments was an AgCl thin target made at the Target laboratory (see Section 4.3). Due to the chlorine of the target was natural chlorine the gammas observed came from proton induced ^{35}Cl and ^{37}Cl reactions. The following elastic and inelastic nuclear reactions were observed and afterwards analysed:

$$^{35}\mathrm{Cl}(\mathrm{p},\mathrm{p}'\gamma)^{35}\mathrm{Cl}$$
$$^{35}\mathrm{Cl}(\mathrm{p},\alpha\gamma)^{32}\mathrm{S}$$
$$^{37}\mathrm{Cl}(\mathrm{p},\mathrm{p}'\gamma)^{37}\mathrm{Cl}$$
$$^{37}\mathrm{Cl}(\mathrm{p},\alpha\gamma)^{34}\mathrm{S}$$
$$^{37}\mathrm{Cl}(\mathrm{p},\mathrm{n}\gamma)^{37}\mathrm{Ar}$$

Special care had to be taken in the opening of the ^{37}Cl neutron channel[6], as to the Tandem accelerator and research lines are not shielded (the control panel is in the same room as the setup). As a result, during the experiment, another neutron detector was placed next to the reaction chamber and neutron emissions were regularly measured to not exceed standard radiation levels.

The target stability and composition remained equal during the two stages of the PIGE experiment and was verified by repeating some measurements at the same values of the proton energy beam.

During the experiment we had problems with the signal of the MOVE detector, as a result, the only useful data for the posterior analysis came from MOVD and HPGe detectors.

4.4.3.1 Detector Efficiency Definition

There is a crucial parameter to determine when gamma ray spectrometry analysis is used and it is the efficiency of the detector [3, 6]. It measures the quantity of electronic pulses that have been generated for a given number of gammas emitted by the source in all directions. The detector absolute

[6]The $^{37}\mathrm{Cl}(\mathrm{p},\mathrm{n}\gamma)^{37}\mathrm{Ar}$ reaction has a relative low Q value of -1596,22 keV while $^{35}\mathrm{Cl}(\mathrm{p},\mathrm{n}\gamma)^{35}\mathrm{Ar}$ has a higher Q of -6748,6 keV

USC UNIVERSIDADE DE SANTIAGO DE COMPOSTELA

efficiency (Eq. 4.2) is the product of two main contributions: the intrinsic and the geometric efficiencies, ε_{int} and ε_{geo} respectively. Due to both efficiencies are expressed as fractions, by definition, the absolute efficiency is lower than 1.

$$\varepsilon_{abs} = \varepsilon_{int} \cdot \varepsilon_{geo}. \tag{4.2}$$

The intrinsic efficiency is determined by the detector's characteristics, such as detector thickness and building materials (atomic number and density). It is defined as the number of particles recorded by the detector divided by the number of incident particles in the same interval, or, in other words, it measures the detection capability of the system for a particular radiation. It increases with higher density of the detector material active-part and it decreases as the particle energy increases. Moreover, the housing of the detector plays an important role in the detection process. It is designed to not allow the entering of external radiation and it has an entrance window facing towards the source to maximize the signal. Sometimes, attenuation layers are placed on top of this window.

On the other hand, the geometric efficiency directly depends on the setup geometrical configuration: detector volume and shape, distance between the source and the detector and their relative disposal. Any variation on these parameters modifies the solid angle covered by the detector, and, as a result, the geometric efficiency. For instance, if the source-to-detector distance increases the solid angle decreases and so the geometric efficiency. Hence, the geometric efficiency represents the ratio between the number of particles hitting the detector and the overall yield emitted by the source in all solid angle.

If the previous definition (Eq. 4.2), is expressed as a function of energy, it is called photopeak efficiency and it expresses the probability of producing a photopeak, i.e. a signal of a particular energy (Eq. 4.3) [3].

$$\varepsilon_{abs,i} = \frac{N_{\gamma,i}}{N_{tot,i}}, \tag{4.3}$$

where $N_{\gamma,i}$ is the number of gammas of a particular energy and $N_{tot,i}$ is the total number of gammas of the same energy emitted by the source.

It is worth to mention that the intrinsic efficiency of germanium detectors varies along its lifetime as a consequence of the material deterioration of the detector's active and inactive parts [154, 155, 156]. In [154] has been reported a change of 13 % in the absolute efficiency after 9 years of operation for gammas in the 200-1800 keV energy range while in [156] they observed an efficiency deviation between 10 and 12 %.

USC UNIVERSIDADE DE SANTIAGO DE COMPOSTELA

4.4.3.2 Efficiency Calibration of the HPGe Detector

The absolute efficiency of an HPGe detector is measured using calibrated gamma point sources, which emit diverse gammas that cover a wide energetic range [157, 158]. The ^{137}Cs, ^{60}Co, ^{152}Eu and ^{133}Ba sources are often used. They are placed exactly on the position of the target to take into account all geometrical characteristics. The time of measurement should be enough to have good statistics but not too large to avoid environmental background interferences.

In our experiment, we have employed ^{152}Eu radioactive source because it has energies ranging from 0,1 MeV up to 1,4 MeV shown in Table 4.3. As this nuclear decay has many gamma emissions, we have only considered the most probable ones with a Branching Ratio (BR) higher than 5 % [26, 159]. The activity of the source at the day of our measurement was,

$$A = 129354(625) \text{ Bq}. \tag{4.4}$$

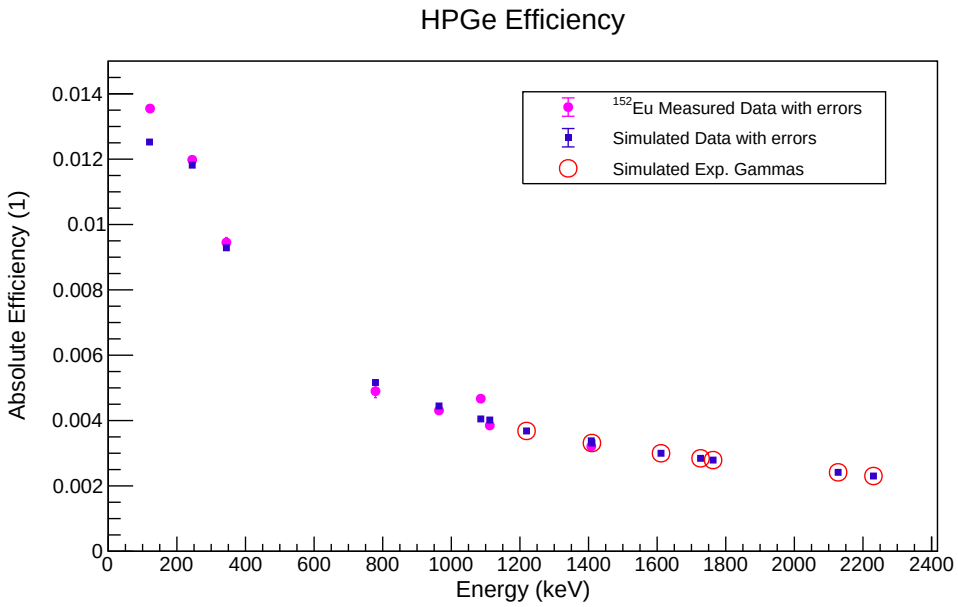

Figure 4.19: Measured (pink) and simulated (violet) photopeak efficiencies of the HPGe by using a ^{152}Eu radioactive source. There are also plotted the simulated efficiencies of the gammas under study in the PIGE experiment (they are highlighted with red circles). There is a point where two peaks almost overlap: the 1408,013 keV from the europium source and the 1409,79 keV from the ^{37}Ar de-excitation. The error bars are also plotted although in most cases are too small to be visible.

USC
UNIVERSIDADE DE SANTIAGO DE COMPOSTELA

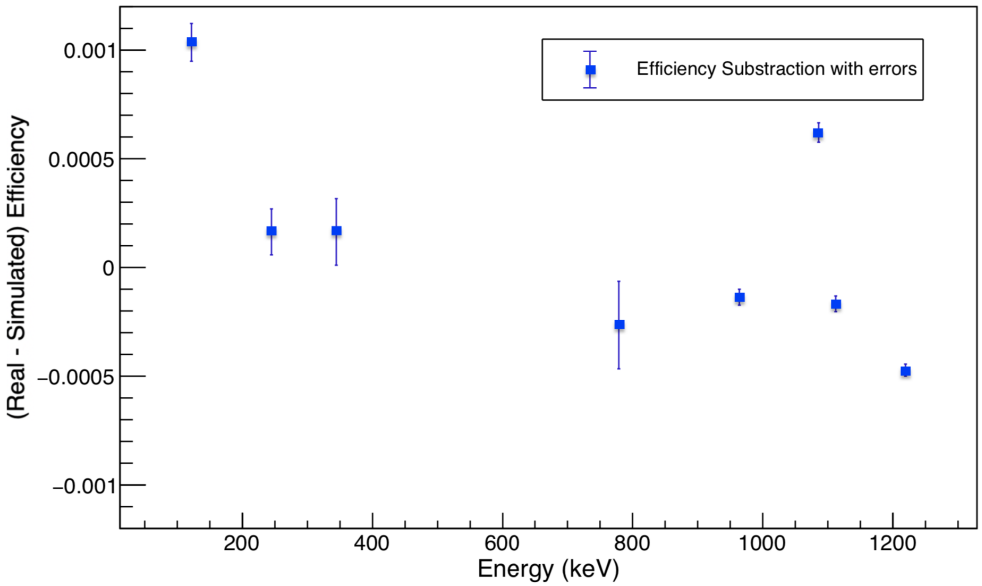

Figure 4.20: Differenced of HPGe photopeak efficiencies (measured minus simulated) from a ^{152}Eu radioactive source. Their error bars are also displayed.

The absolute efficiency for each gamma during a Δt time interval is calculated by using Eq. 4.3 and the relation between the number of emitted gammas, their branching ratios (BR_i) and the activity of the source (A) at the moment of measurement is,

$$N_{tot,i} = \Delta t \cdot A \cdot \mathrm{BR}_i, \tag{4.5}$$

combining both equations the photopeak efficiency results in,

$$\varepsilon_{abs,i} = \frac{N_{\gamma,i}}{\Delta t \cdot A \cdot \mathrm{BR}_i}. \tag{4.6}$$

In the next step, to obtain the efficiency calibration function each photopeak efficiency is plotted against its photopeak energy and these points could be fitted by diverse functions as [160] indicates.

Special care should be taken if the gammas under study are energetically far from the photopeak energies used in the fitting function, as it is our case. Following the recommendations of IAEA [6], we have calculated the simulated efficiency of the ^{152}Eu gammas by using the generators and the experimental setup simulation of EnsarRoot. Afterwards, the simulated efficiency is benchmarked against the real efficiency and, in case of a discrepancy between both, the simulation should be modified until their match.

USC UNIVERSIDADE DE SANTIAGO DE COMPOSTELA

Table 4.3: Gammas from ^{152}Eu decay with a BR> 5%. Data extracted from the NNDC database [26].

$\mathbf{E_\gamma}$ **(keV)**	**BR** (%)
121,7817(3)	28,58(6)
244,6974(8)	7,583(19)
344,2785(12)	26,5(4)
778,9045(24)	12,942(19)19
964,057(5)	14,605(21)
1085,68(11)	10,207(21)
1112,076(3)	13,644(21)
1408,013(3)	21,005(24)

In our experiment, the distance between the source and the entrance of the detector was not accurately known. In principle, it was thought that the detector was placed at 5,55 cm from the center of the reaction chamber, although, when we performed the simulations with this geometrical disposal we realized that the detector was closer. Finally, we determined that the distance between the entrance of the detector and the source position was 4,9 cm. Figure 4.19 shows the measured (pink) and the simulated (violet) efficiencies with their respective error bars. There are two regions easily distinguishable: from low energies up to 1 MeV the detector efficiency drops rapidly and from that point the decrease becomes steadier. In order to see the differences between them more clearly, in Figure 4.20 it is represented the subtraction of both efficiencies and it is appreciable their match, being the substraction rather close to zero.

This method is of great advantage because once the simulation is accordingly adjusted, the efficiency of any measured photopeak could be obtained with precision by calculating the simulated efficiency. Efficiencies from the gammas measured in the PIGE experiment (they are listed in Table 5.3) have been simulated and plotted along the previous efficiency points in Figure 4.19 (red circles).

The efficiency errors of the ^{152}Eu source have been calculated by error propagation. In Figure 4.21 there are plotted the uncertainties of each contribution expressed in percentages for each gamma of the radioactive source. The uncertainty of the source activity has been also considered in the calculations, although due to it is a constant in all gammas (it represents the 0,48 %) has not been included in the graph. The errors of the simulated

USC UNIVERSIDADE DE SANTIAGO DE COMPOSTELA

efficiencies are simply Poisson statistical errors. For a detailed discussion see Appendix F.

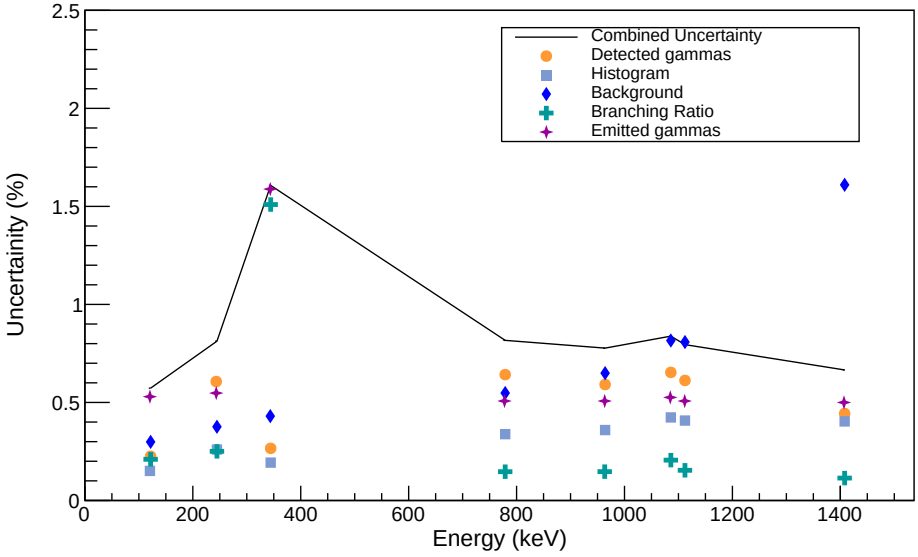

Figure 4.21: Main uncertainty components of the ^{152}Eu radioactive source efficiency. Black line represents the combined uncertainty of the radioactive source efficiency calculated by error propagation (see Appendix F). Orange points represent the photopeak error, a combination of the histogram error (light blue squares) and background errors (dark blue rhombus). Purple stars represent the error of all gammas emitted by the source during the measurement time interval, it also includes the error of the gamma branching ratio (teal crosses) and the error of the source activity that is not included here because it is a constant value of 0,48 %.

4.4.3.3 Resolution of the HPGe Detector

The resolution of the HPGe detector has been calculated at different energies using photopeaks from the laboratory environmental radiation (see Table 4.4) instead of using radioactive sources because some gammas of the background achieve higher energies than the gammas of the radioactive samples available in the laboratory at the time of the experiment.

With the purpose of reproducing the detector response along all energy range, the resolution function depending on energy was calculated. The following series of data points (Table 4.4) were fitted by the following resolution equation:

USC UNIVERSIDADE DE SANTIAGO DE COMPOSTELA

Table 4.4: Resolution of CTN/IST HPGe detector at different energies. The origin of the photopeaks is environmental radiation.

Source	**Nuclear Decay**	**E_γ (keV)**	**Resolution (%)**
Uranium series	^{214}Pb	351,932(2)	0,62(4)
Potassium decay	^{40}K	1460,849(5)	0,141(3)
Uranium series	^{214}Bi	1764,494(14)	0,134(10)
Thorium series	^{208}Tl	2614,533(13)	0,094(6)

$$R = \frac{A}{\sqrt{E}} + B. \tag{4.7}$$

The parameters of the fitting function were $A = 16,1(1,1)$ and $B = -0,25(4)$. The experimental points with their error bars (red) and the resolution function (red line) are displayed in Figure 4.24 along other detectors because this HPGe was also used in the environmental background study at the CTN/IST facility.

4.4.3.4 Calibration of the HPGe Detector

In the first stage of the experiment, the HPGe calibration was made using photopeaks of the radioactive background instead of using calibrated sources for diverse reasons. One important point is, as mentioned before, the wide energy range covered by natural gammas. Another reason to not use calibrated sources is that during the experiment you can do a new calibration as often as it is required without the necessity of placing a radioactive source near the detector. Finally, it is important to measure the radioactive background as many times as possible during the course of the experiment in case of appearance of photopeaks coming from material activation, because this may lead to a mismatching when the analysis is carried out.

In the second part of the experiment, once the environmental background was controlled, we decided to use either background photopeaks (to calibrate the high energy region) and ^{60}Co and ^{137}Cs calibrated sources. In Table 4.5 there are shown the photopeaks employed in the calibration at this second experimental stage. The calibration function obtained from a linear fit of these data sets of the second experimental stage is:

$$E = A \cdot Ch + B \tag{4.8}$$

USC UNIVERSIDADE DE SANTIAGO DE COMPOSTELA

where E represents the energy, Ch the channels and the parameters are $A = 0,38254(5)$ keV/channels and $B = -28,0(2)$ keV. This function is represented in Figure 4.22 (red line), as well as the experimental points (green markers).

Table 4.5: Experimental points from ^{60}Co and ^{137}Cs sources and two natural background photopeaks used for the calibration of the HPGe detector in the second experimental phase [26].

Source	**Nuclear Decay**	**E_γ (keV)**	**Channel (ch)**
Cesium Decay	^{137}Cs	661,657(3)	1803(3)
Cobalt Decay	^{60}Co	1173,228(3)	3140(4)
Cobalt Decay	^{60}Co	1332,501(5)	3557(4)
Potassium decay	^{40}K	1460,849(5)	3891(5)
Thorium series	^{208}Tl	2614,533(13)	6908(7)

USC UNIVERSIDADE DE SANTIAGO DE COMPOSTELA

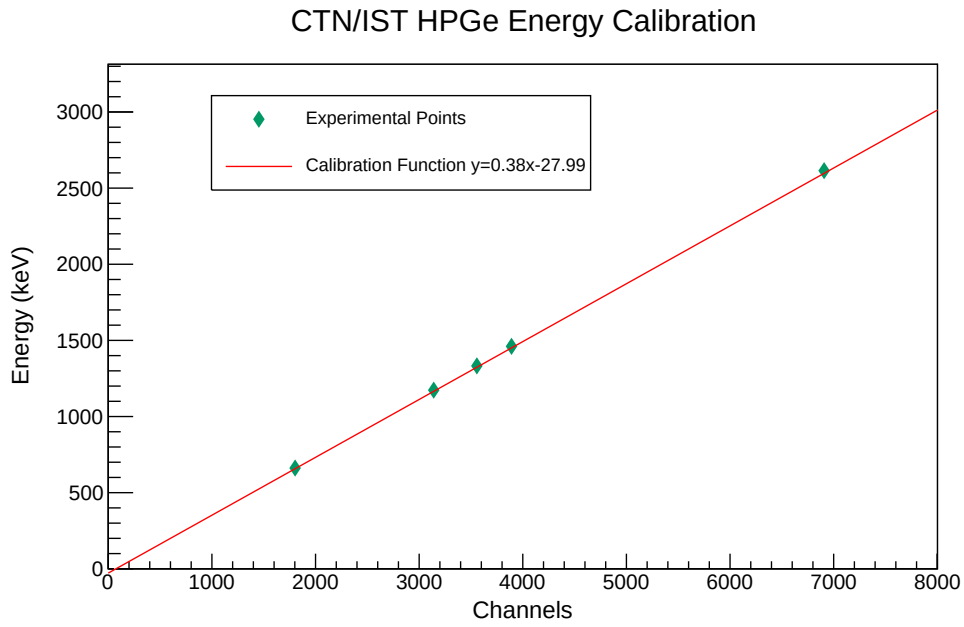

Figure 4.22: HPGe calibration function (red) and experimental points (green) of the second stage of the PIGE experiment.

4.5 Environmental Radiation Experimental Procedures

Long-term environmental gamma radiation measurements have been taken at three locations in the west part of the Iberian Peninsula along 2019 and 2021. These regions have different chemical soil compositions inducing to distinct radioactive backgrounds as we can observe in the European Annual Terrestrial Gamma Dose Map from the European Atlas of Natural Radiation [109]. In this section, all surveys are explained as well as the setups and their corresponding detectors.

4.5.1 CTN/IST Environmental Radiation Measurements

The first location where we have measured background radiation was in the laboratory of CTN/IST [23, 161] located in a near-shore marine environment. We have used the HPGe semiconductor detector of the PIGE line because its high resolution allows a clear identification and an easy distinction of most of the natural gammas. We used the HPGe default electronics, such as the 8192 MCA, and setup disposition, though in this case, the measurements were not stopped by the current integrator but by a time interval predefined. For this

USC UNIVERSIDADE DE SANTIAGO DE COMPOSTELA

reason, the HPGe configuration was changed every time the measurements were carried out.

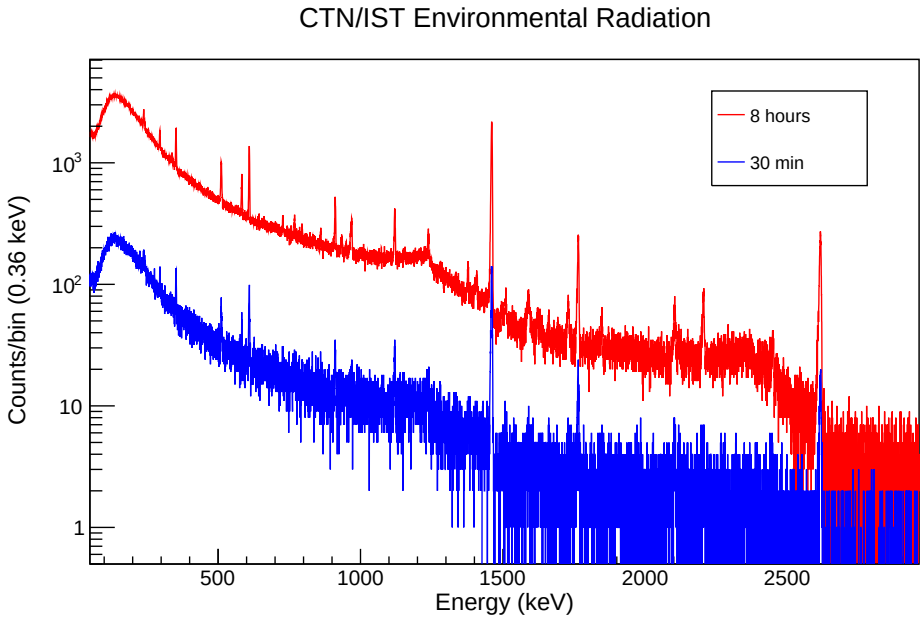

Figure 4.23: CTN/IST environmental radiation spectra. The blue line shows a spectrum measured in an interval of 30 min and the red line during a period of 8 hours.

The environmental measurements have been taken in the inactive periods of this detector, usually from 6 pm to 9 am and during the weekends, although we also have data from almost entire weeks. This data was measured during the firsts months of 2019 in periods of 30 min to allow a posterior detailed analysis over time. In Figure 4.23 two spectra are displayed: data measured during 30 minutes (blue line) and data gathered during 8 hours (red line). We could observe that the outstanding photopeaks correspond to the main gammas of the radioactive series, such as the 2614,533 keV from the uranium chain, along with the gamma emission of the potassium decay at 1460,8 keV with its characteristic Compton shape. At higher energies the only contribution is cosmic rays radiation.

Figure 4.24 shows a comparison between the resolutions of all detectors employed in the study of environmental radiation (Eq. 4.7). It is appropriate to compare all of them because they are germanium semiconductor detectors with analogous dimensions. The CTN/IST detector resolution and its function are highlighted in red.

USC UNIVERSIDADE DE SANTIAGO DE COMPOSTELA

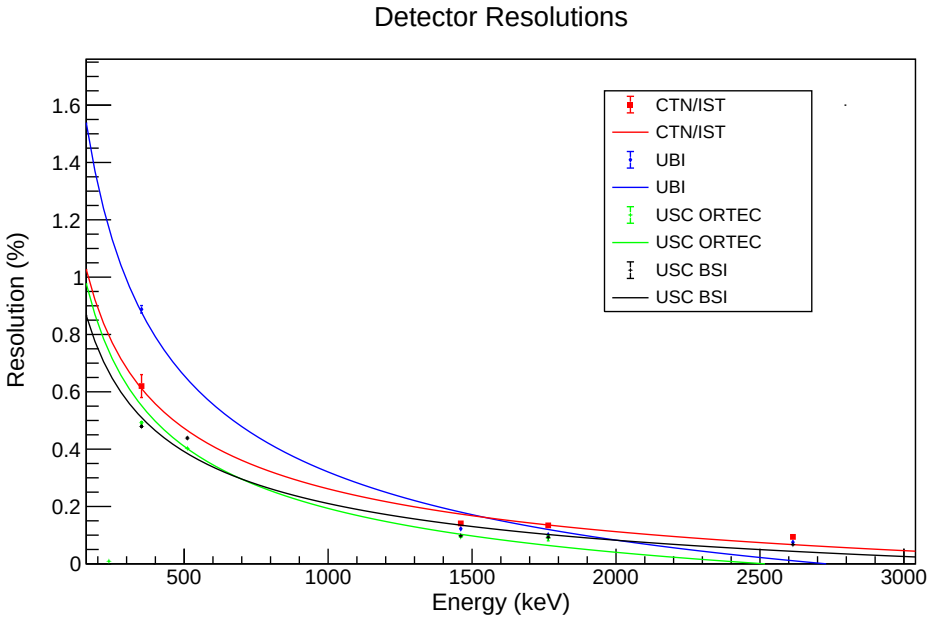

Figure 4.24: The resolution of all detectors used for the analysis of environmental radiation. It shows the resolution functions (Eq. 4.7) and the experimental points of the CTN/IST detector (red), Universidade da Beira Interior detector (blue), ORTEC of the USC (green) and BSI of the USC (black). The resolutions are plotted with their associated error bars, although some of them are too small to be visible.

4.5.2 UBI Environmental Radiation Measurement

The second site where data was collected was in the Laboratório de Estudos dos Efeitos da Exposição ao Radão of Universidade da Beira Interior (UBI) [43] in Covilhã a montanious environment in the central part of Portugal. In order to compare the diverse measurements of natural radiation we also used a germanium detector (GC 2518 Canberra) with a cylindrical shape and a similar size as the CTN/IST detector. At the time of the experiment the detector was placed in a vertical position. The electronic setup was also configured to start/stop the measurements over a prestablished period of time and the MCA had a total of 1024 channels. Following the same methodology as before, we measured natural gamma radiation in periods of 30 min during consecutive days in almost three weeks in February of 2019.

The detector resolution compared to the CTN/IST detector is worse (compare red and blue lines of Figure 4.24), because the response of the detector is limitated by the MCA used. A typical spectra of the UBI environmental radiation is plotted in Figure 5.21 (green line).

USC UNIVERSIDADE DE SANTIAGO DE COMPOSTELA

4.5.3 USC Environmental Radiation Measurements

The last locality where the environmental data was studied was in the Laboratorio de Análisis de Radiaciones at University of Santiago de Compostela (USC) in a valley city at the north-west of Spain [44, 45, 162]. The measurement was done during two entire weekends in January of 2021. As in the other studies, the detectors used were two HPGe with similar dimensions. More specifically, one detector was an HPGe GCD-50190 (BSI) and the other was an HPGe GMX50 (ORTEC). Their electronics were predefined with an energy range of 5-10000 keV and 5-2465 keV, respectively, and the number of channels was 16384 for both MCA. However, in this case, they were surrounded by lead walls of various cm of thickness. The purpose of this shielding is to avoid interferences between environmental background and data measurements made inside it, as this laboratory is dedicated to radiometric studies. Consequently, these measurements were done with the shielding's lap open to facilitate the entry of radiation. Although the air circulation was achieved, a proper environmental data analysis could not be done because many gamma radiations were absorbed by the lead walls. Instead, this data was helpful to understand cosmic rays showers.

In Figure 4.27 there are plotted the two data collections taken with these detectors along with a spectrum of CTN/IST background (black line) in order to have a reference. All of these measurements have been taken during the same time interval of 2 days. These detectors have different gains to cover distinct energetic ranges: ORTEC detector (red line) covers low energy range where the photopeaks from radioactive chains appear, on the contrary, BSI detector (blue line) embraces a wider range up to 12 MeV where in the high energy region cosmic rays are visible without the overlapping of other background contributions. We could observe that the amount of natural radiation in the CTN/IST facility is higher, however, it can not be concluded that the natural radiation there is higher than in the USC laboratory due to many gammas have been absorbed by the shielding.

The ORTEC and BSI detector resolutions are depicted in Figure 4.24. Their resolutions are slightly better than the CTN/IST detector, maybe because electronics is better than in the other measurements, i.e. the number of channels is much higher, or maybe due to the HPGe characteristics, age, etc.

USC UNIVERSIDADE DE SANTIAGO DE COMPOSTELA

Figure 4.25: Interior of the ORTEC detector with the shielding's lap open from the Laboratorio de Análisis de Radiaciones of the USC.

Figure 4.26: Setup of the ORTEC detector from the Laboratorio de Análisis de Radiaciones of the USC.

USC
UNIVERSIDADE DE SANTIAGO DE COMPOSTELA

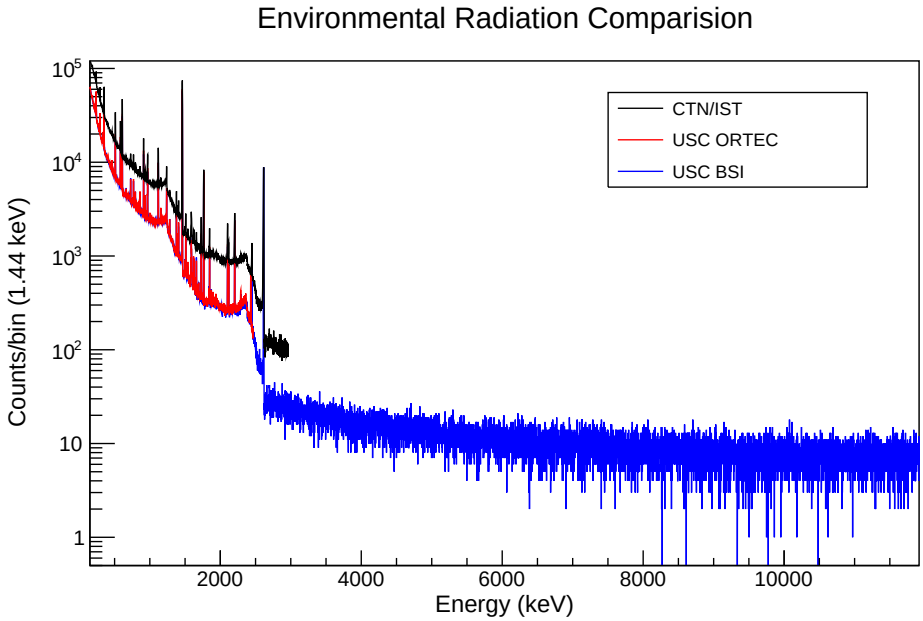

Figure 4.27: Environmental radiation spectra of the Laboratorio de Análisis de Radiaciones [44, 45, 162] measured during 2 days. The red line represents the ORTEC detector while the blue line illustrates the BSI detector. In order to compare natural radiation, a spectra of the CTN/IST laboratory measured during the same time interval has been also plotted.

USC UNIVERSIDADE DE SANTIAGO DE COMPOSTELA

Chapter 5

RESULTS

5.1 PIGE Experimental Results

5.1.1 RBS Target Data Analysis

RBS data from the target used at the PIGE experiment has been quantitatively evaluated by using the RBS simulation tool from the SIMNRA program [75, 153]. It is a versatil fitting code which simulates gamma ray yields and charged particle energy spectra for diverse IBA techniques.

Figure 5.1 shows the RBS spectrum of the chlorine target employed in the PIGE study. This spectrum was measured using the RBS1 particle detector and the backscattered particles are $^4He^+$. It shows the experimental data (red points) and the SIMNRA fit (blue line). This fit is done within the SIMNRA program overlapping diverse layers of materials and thickness and by trial and error the best arrangement is chosen. This spectrum is not calibrated in energy because it is not needed, the information extracted from it is the amount of material and deposition of layers. After the setup characteristics are provided as inputs, the program makes a rough approximation where each element should appear in the spectrum. As it was expected, a Cl peak appears (around channel 525) and at higher energies an Ag peak plus a plateau materializes (around channel 750). However, we can observe a third small peak on the right side of the spectrum (around channel 840) meaning that within the target there is another element with Z higher than silver (Z=47). It seems that at the moment of AgCl evaporation or at Ag evaporation a small amount of tantalum (Z=73) material of the boats containing the substances was also evaporated.

The final disposal of layers, their thickness and elemental composition that most fits RBS experimental data are displayed in Table 5.1. The first layer has a thickness of 800×10^{15} atoms/cm^2 with 100 % of Cl, the second

USC UNIVERSIDADE DE SANTIAGO DE COMPOSTELA

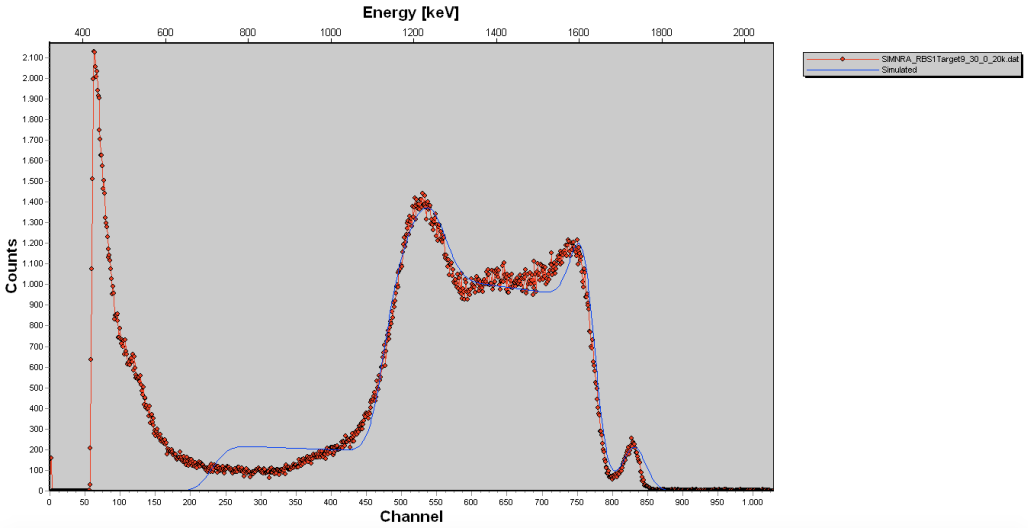

Figure 5.1: RBS chlorine target spectrum of the RBS1 detector at an angle of $\theta = 165°$, $\beta = 15°$ and $\alpha = 0°$ by using an $^4He^+$ ion beam. It is normalized at 20 μC of collected charge. The experimental points are indicated in red and the SIMNRA fit in blue.

layer has a thickness of 14×10^{15} atoms/cm^2 with 100 % of Ta, the third layer has a thickness of 190×10^{15} atoms/cm^2 with 97,5 % of Ag and 2,5 % of Ta and the fourth layer has a thickness of 3000×10^{15} atoms/cm^2 with 60 % of Cl and 40 % of Ag. We can also observe that during the evaporation a decomposition and diffusion of the molecules occurred because neither the distribution of layers nor the following stechiometric ratios were the expected ones. Table 5.2 shows the setup parameters introduced in the SIMNRA program to reproduce experimental conditions.

Using the elemental quantities in $\times 10^{15}$ atoms/cm^2 obtained in this fit and taking into account the isotopical abundances of natural chlorine from NIST Physical Reference Data [27], we could calculate the isotopical ratios between chlorine and natural silver:

$$\text{ratio}(^{35}\text{Cl/Ag}) = 1,42(3),$$
$$\text{ratio}(^{37}\text{Cl/Ag}) = 0,455(9).$$

Ratios uncertainties have been calculated using a visual estimation of the fit and considering that ratios follow square function distributions[1].

[1]The uncertainty of an square function with a width of x is, by definition, $x/\sqrt{12}$.

USC UNIVERSIDADE DE SANTIAGO DE COMPOSTELA

Table 5.1: Layers and their parameters introduced in the SIMNRA program to reproduce the RBS chlorine target spectrum.

Layers	**Thickness** ($\times 10^{15}$ **atoms/cm**^{2})	**Element**	**Percentage** (%)
Layer 1	800	Cl	100
Layer 2	14	Ta	100
Layer 3	190	Ag	97,5
		Ta	2,5
Layer 4	3000	Cl	60
		Ag	40

Table 5.2: Experimental setup parameters introduced in the SIMNRA program.

Setup parameters	
Detector resolution	60 keV
Energy spread of incident beam	20 keV
Particles×sr	$6,5 \times 10^{10}$
Incident angle	$\alpha = 0°$
Exit angle	$\beta = 15°$
Scattering angle	$\theta = 165°$

USC UNIVERSIDADE DE SANTIAGO DE COMPOSTELA

Furthermore, by using the physics calculator of the LISE program [78] and introducing the parameters of the SIMNRA fit the target thickness is estimated to be around 0,825 μm (considering all layers) with an error of 2 %[2]. In addition, LISE program has also been used to calculate the energy loss of the proton beam in the target which is the main component of the proton energy error.

5.1.2 PIGE Data Analysis and Discussion of Results

After many discrepancies within PIGE scientific literature were found, IAEA organism proposed an interlaboratory exercise: the measurement of a specific reaction following the same methodology detailed in Section 3 of [6] aiming to compare the outcoming data. As far as possible, we have followed this methodology in order to minimize variances and reduce uncertainties. The procedure employed in this work and the results obtained are explained in the following.

As discussed in Theory Section 3.1.1.2, to avoid uncertainties associated with beam charge collection (measurement of incident protons) and with the target thickness, it was simultaneously measured gamma rays emitted by ongoing nuclear reactions and backscattered protons after suffering Coulomb interaction with a nucleus of the target. Therefore, for each run, i.e. beam energy, an independent analysis has been carried out for each detector: on the one hand, the HPGe detector provided a gamma yield spectra and, on the other hand, the silicon detector provided RBS spectra. Figure 5.2 shows two HPGe energy spectra at 2,6 and 3 MeV beam energies and, for the same two runs, silicon detector spectra are plotted in Figure 5.3. These two compared measurements have the same amount of collected charge. In the first plot, there are also highlighted some photopeaks studied in this work. Afterwards, combining either data analysis, cross sections of the nuclear reactions have been calculated.

[2]We have considered that LISE program does not introduce additional errors, due to the fact that it only converts stoichiometric ratios into thickness. In consequence, the error of the SIMNRA results that is around 2 % has the same magnitude as the error of the LISE results.

USC UNIVERSIDADE DE SANTIAGO DE COMPOSTELA

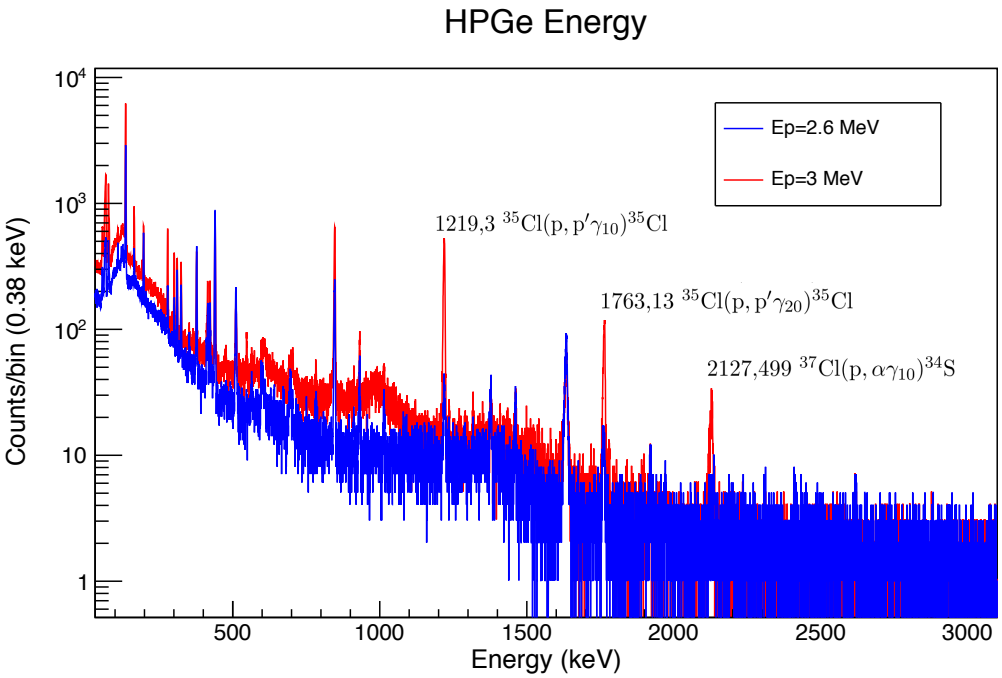

Figure 5.2: Energy spectra of gamma radiation produced by the bombardment of the AgCl target by 2,6 and 3 MeV protons. Some gammas and their reactions studied in this work are highlighted.

USC
UNIVERSIDADE DE SANTIAGO DE COMPOSTELA

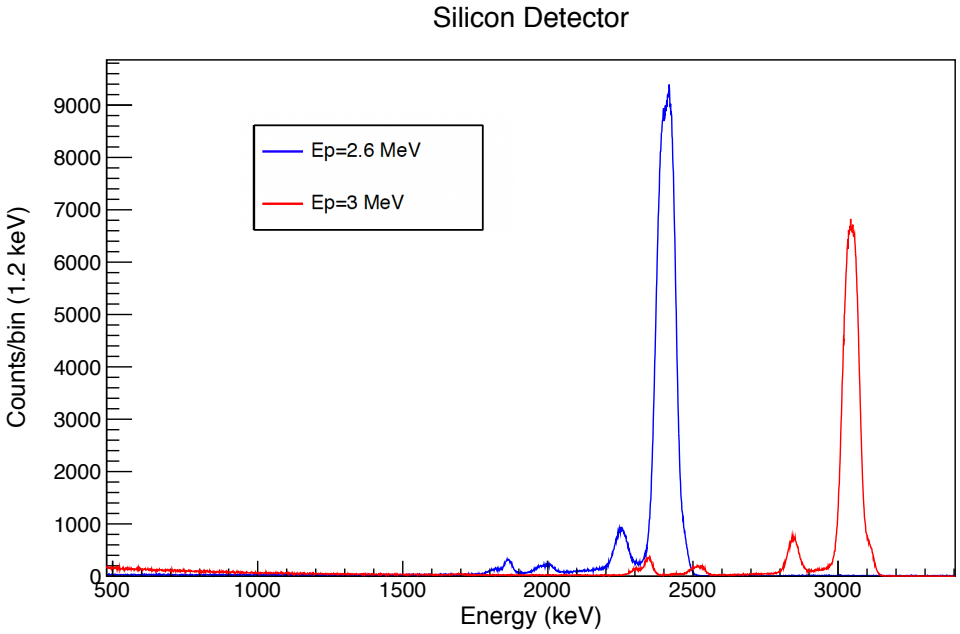

Figure 5.3: Backscattered proton spectra produced by the bombardment of the AgCl target at 2,5 (blue) and 3,2 MeV (red) energies. The peaks that appear are, from right to left, silver, chlorine, carbon build up on the target surface and an unidentified peak.

USC UNIVERSIDADE DE SANTIAGO DE COMPOSTELA

5.1.2.1 RBS Data Analysis from the PIGE Experiment

Backscattered protons spectra (Figures 5.3 and 5.4) reveals that there are diverse nucleus present within AgCl target: the biggest peak on the right are the protons scattered by silver nucleus; on the left of this one there is the chlorine contribution; more to the left side there are two small peaks, one of the remaining peaks is carbon contamination on the target surface (the third peak from the right) and the other structure seems two overlapping peaks of lighter elements that we could not elucidate their compositions and origins. In this case, the tantalum peak does not appear because it overlaps with the silver peak (due to the resolving power of alphas is higher than protons). This result is consistent with the previous SIMNRA target analysis. RBS spectra were analysed by quantifying the Ag and Cl peaks.

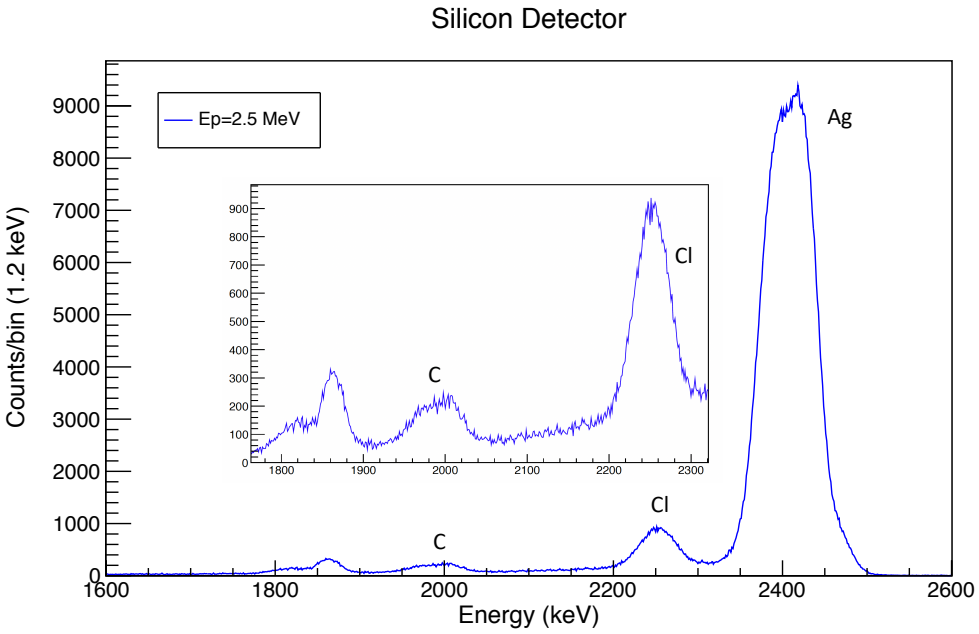

Figure 5.4: Backscattered proton spectrum produced by the bombardment of the AgCl target at 2,5 MeV energy. The peaks that appear are, from right to left, silver, chlorine, carbon build up on the target surface and an unidentified peak corresponding to lower mass elements.

As we stated in theory section, in a standard RBS spectrum two different behaviours could be observed: Rutherford (Figure 5.5) and non-Rutherford (Figure 5.6). Every point of these plots are the result of the Ag or Cl peak integral after removing the background contribution by using a combination of gaussian and linear fits. In the first graph, silver nuclei backscatter protons

USC UNIVERSIDADE DE SANTIAGO DE COMPOSTELA

following Rutherford formula where pure Coulomb interaction dominates. In the second graph, diverse resonance structures appear as a consequence of chlorine nuclear reactions. For this reason, proton RBS spectra were not useful to analyse the target composition because depending on the proton energy the chlorine quantity of each peak varies. On the contrary, silver quantity extracted of proton RBS is a reliable measurement because it only follows the Rutherford formula. In the first plot, it is observable an offset between the first and the second data stage, which is caused by the uncertainty in the collected charge though each point has been normalized at 2 μC, for this reason a cross section calculation independent from beam charge measurement is preferable.

In order to use the normalization procedure when calculating cross sections, the elastic scattered particles by the heavier elements are purely assumed Rutherford, as is the case of the silver scattered protons nature. Moreover, and as expected by the Rutherford cross section formula, they are linearly dependent on the inverse of the square of proton beam energy.

The presented uncertainties of Figure 5.5 are not visible because they are about 0,2 %, while the uncertainties of Figure 5.6 are higher, around 1 %. The main uncertainty source is statistical. In the following Section 5.1.2.3 errors and their origins are more extensively discussed.

USC UNIVERSIDADE DE SANTIAGO DE COMPOSTELA

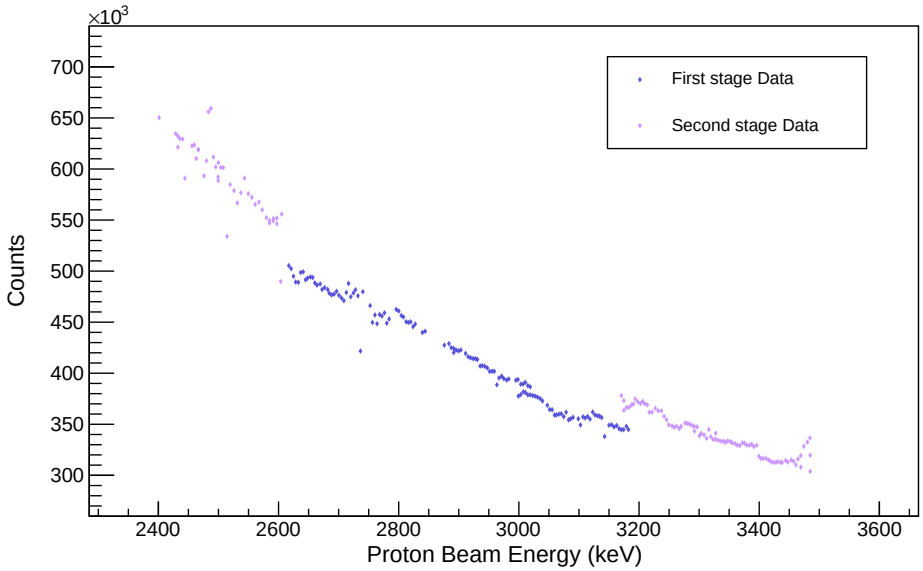

Figure 5.5: Silver backscattered proton contribution. Each point is the integral of the Ag peak at different proton energies where every spectrum has been normalized at 2 μC of collected charge. The statistical error bars are displayed although they are too small to be visible. The two stages of the experiment are shown in distinct purple shades. It follows the Rutherford formula.

USC
UNIVERSIDADE DE SANTIAGO DE COMPOSTELA

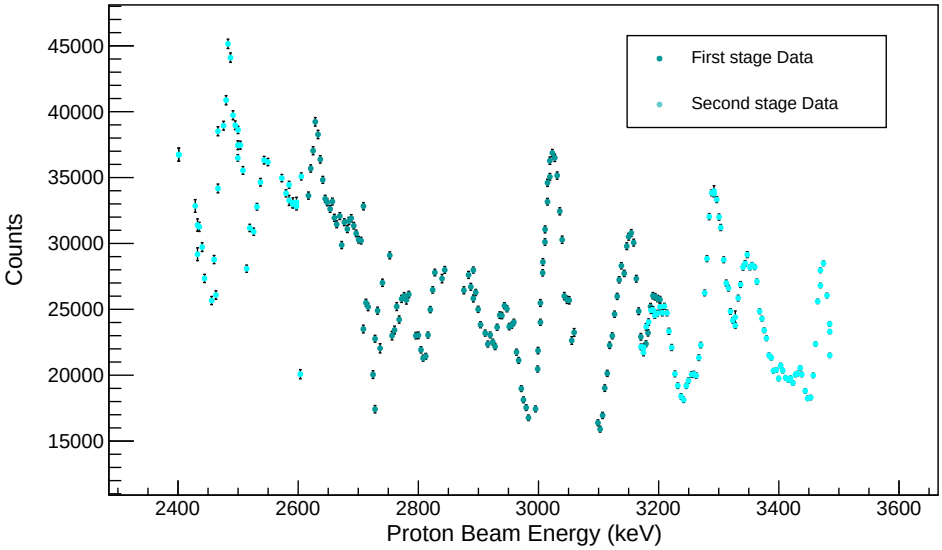

Figure 5.6: Chlorine backscattered proton contribution. Each point is the integral of the Cl peak at different proton energies and where every spectrum has been normalized at 2 μC of collected charge. The error bars are displayed in black, though in some cases are not clearly distinguishable. The two stages of the experiment are shown in distinct blue shades. Diverse resonance structures appear as a consequence of nuclear reactions.

USC UNIVERSIDADE DE SANTIAGO DE COMPOSTELA

5.1.2.2 HPGe Data Analysis

An elemental analysis of the gamma ray spectra have been carried out and the identified peaks are listed in the following Table 5.3, where gamma energies and origins are indicated. The simplified decay schemes of the reactions on both isotopes of chlorine are displayed in Figure 5.7, Figure 5.8 and Figure 5.9. They show the energy values of the reaction as the Q-values, gamma energies, etc. and the photopeaks relevants for the analysis are indicated in blue lines. These reactions proceed mainly through the compound nuclei ^{36}Ar and ^{38}Ar, respectively.

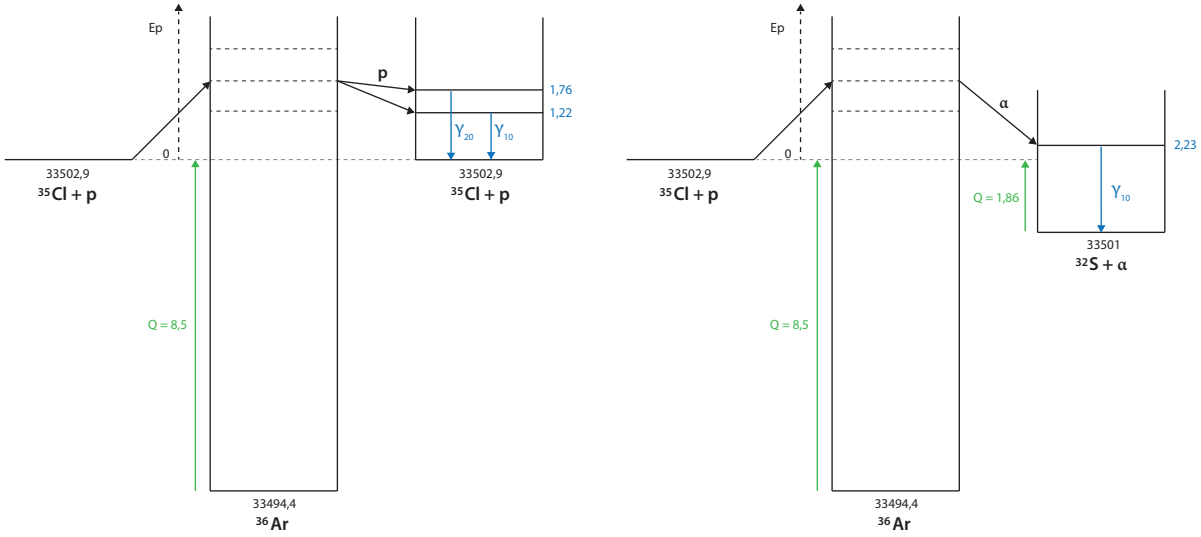

Figure 5.7: Schemes of the proton induced reactions on ^{35}Cl and the opening of two channels: on the left the elastic channel and on the right the alpha channel. Gammas from the de-excitations studied in this work appear in blue. The energy units are in MeV.

In the Table 5.3, gammas coming from environmental background are not indicated, due to an exhaustive analysis was conducted independently and it is explained in Section 5.2. A typical background spectrum of the CTN/IST laboratory is displayed in Figure 5.21 (red line). The background contribution was extracted where necessary in the data analysis.

Doppler broadening effect was not observable (broadening of the peak) in any gamma ray due to the long lifetime of the de-exciting state and the small recoil of the nucleus, making easier the peak identification and avoiding peak overlappings.

The gamma yield corresponding to the de-excitation of the ^{35}Cl first state

USC UNIVERSIDADE DE SANTIAGO DE COMPOSTELA

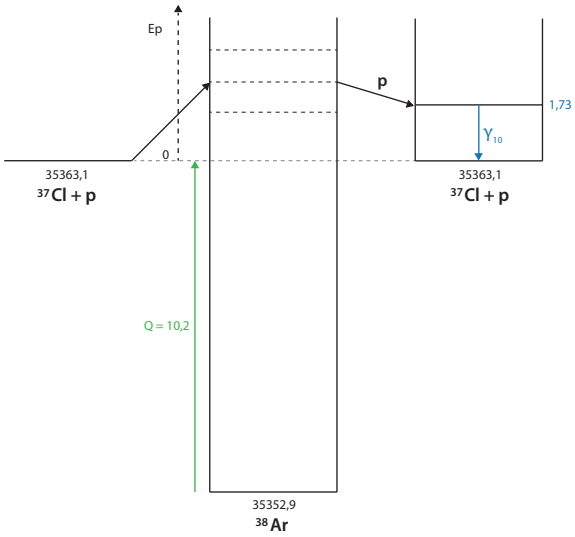

Figure 5.8: Scheme of the proton induced reactions on ^{37}Cl and the opening of the elastic channel. The gamma from the de-excitation studied in this work appears in blue. The energy units are in MeV.

(1219,3 keV) measured in our experiment has a similar shape to the yield curves published by Johnson *et al.* [163] at Ep=2,4-3 MeV (Figure 5.10). However, it should be noted that in our data sets there is a small energy shift of about -2 keV in the first data stage and about $+2$ keV in the second data stage with respect to the Johnson *et al.* paper. They have been calculated by matching the peaks of both spectra. These energy shifts might be an inaccuracy of the CTN/IST Tandem calibration. Besides, some protons of the beam do not follow the exact designed trajectory and small deviations could affect their energies (for example, when a magnetic field is crossed). Another method to calibrate the Tandem accelerator independently should have been used during the experiment, as a calibration based on aluminium resonances. If these energy shifts are corrected in our data, we could observe in Figure 5.11 that all gamma yields agree. Moreover, this correction leads to an overlapping of our both sets of data taken at different stages (see Figure 5.12). The maching between yields, also means that no chlorine was lost during the time interval between measurements and that the target was not damaged in either cases. This sistematic error is taken into account when cross sections are calculated and plotted. It is further discussed in Section 5.1.2.3.

USC UNIVERSIDADE DE SANTIAGO DE COMPOSTELA

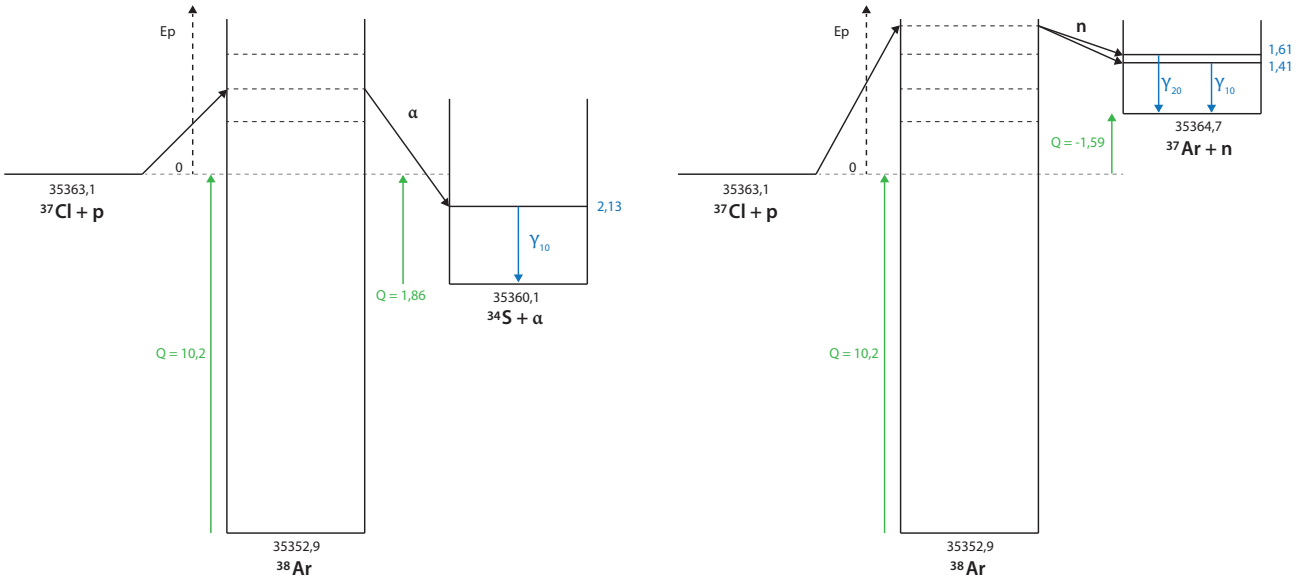

Figure 5.9: Schemes of the proton induced reactions on ^{37}Cl and the opening of two channels on the left the alpha channel and on the right the neutron channel. Gammas from the de-excitations studied in this work appear in blue. The energy units are in MeV.

Table 5.3: Gammas detected from proton induced reactions on natural chlorine in the PIGE experiment. Nuclear data is from NNDC [26].

Gamma Energy (keV)	**Nuclear Reactions**
1219,3(2)	^{35}Cl(p, p$'\gamma_{10}$)^{35}Cl
1763,13(10)	^{35}Cl(p, p$'\gamma_{20}$)^{35}Cl
2230,49(15)	^{35}Cl(p, $\alpha\gamma_{10}$)^{32}S
1726,4(2)	^{37}Cl(p, p$'\gamma_{10}$)^{37}Cl
2127,499(20)	^{37}Cl(p, $\alpha\gamma_{10}$)^{34}S
1409,79(7)	^{37}Cl(p, nγ_{10})^{37}Ar
1611,24(5)	^{37}Cl(p, nγ_{20})^{37}Ar

USC UNIVERSIDADE DE SANTIAGO DE COMPOSTELA

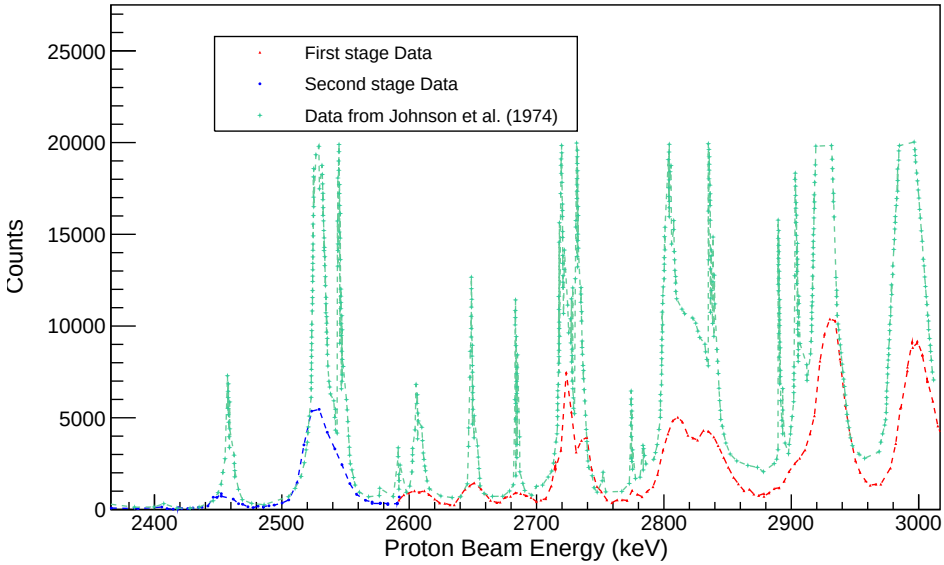

Figure 5.10: Yield curves of the ^{35}Cl first excited state at 1219,3 keV from our work (red line corresponds to the first stage of the experiment and blue line to the second) and from Johnson *et al.* study [163] (green line). A small shift in the proton energy between the two works could be observed, as it is explained in the text.

USC UNIVERSIDADE DE SANTIAGO DE COMPOSTELA

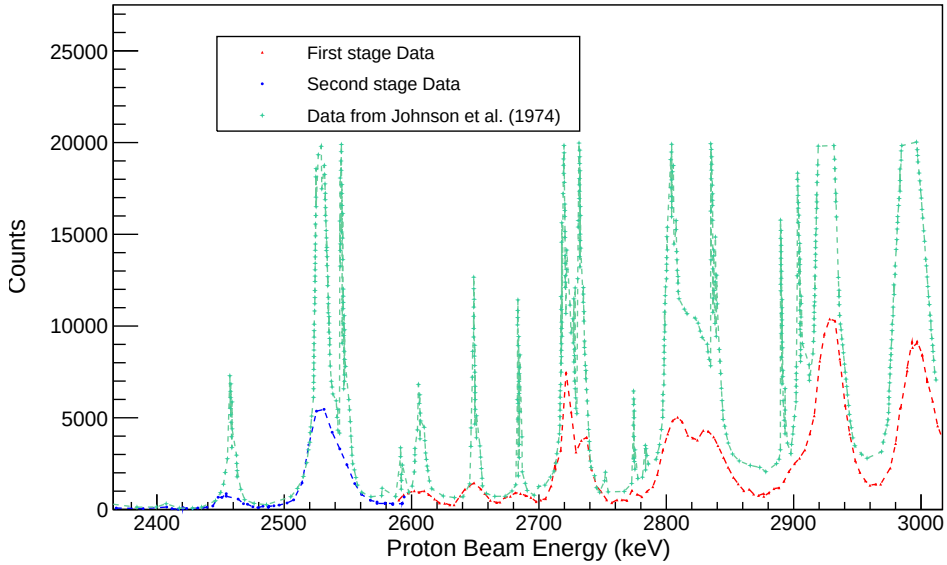

Figure 5.11: Corrected yields curves of the ^{35}Cl first excited state at 1219,3 keV. Data from our experiment has two proton energy corrections: the first stage was corrected by extracting 2 keV (red line) while the second stage adding 2 keV (blue line). The yield from Johnson *et al.* study [163] used as a reference for the corrections is also plotted in green.

USC UNIVERSIDADE DE SANTIAGO DE COMPOSTELA

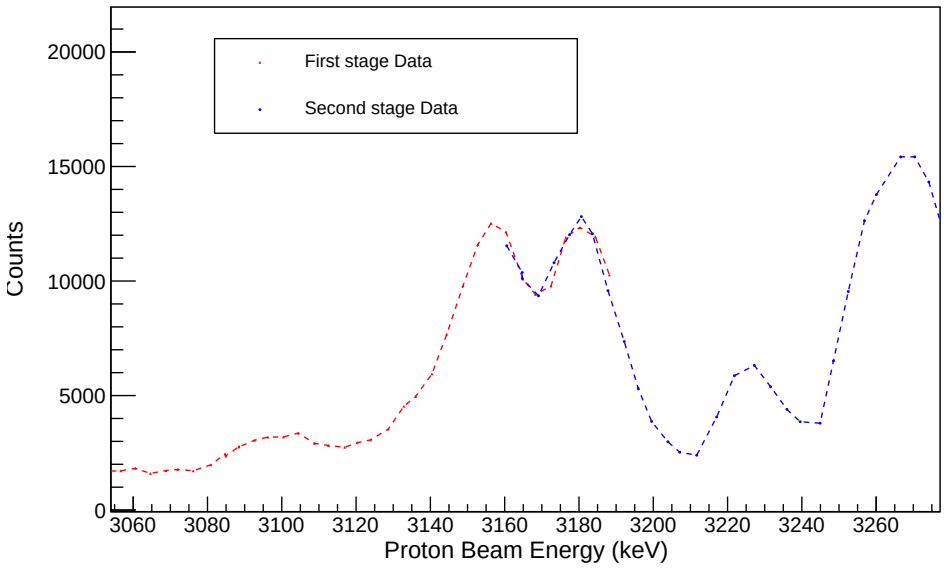

Figure 5.12: Corrected yield curves of the ^{35}Cl first excited state at 1219,3 keV in the proton energy range of 3,06-3,27 MeV. After the corrections, gamma yields from either stages of the experiment match.

USC UNIVERSIDADE DE SANTIAGO DE COMPOSTELA

5.1.2.3 Cross Section Measurements

The differential gamma ray cross section for a standardless analysis using a thin target is displayed in Eq. 3.33. Adapting this equation to our experimental parameters we obtain the following expresion:

$$\left(\frac{d\sigma}{d\Omega}\right)_{\gamma}(E',\theta) = \frac{\varepsilon_p}{r\varepsilon_\gamma} \cdot \frac{Y_\gamma(E',\theta)}{Y_{Ag}(E',\phi)} \cdot \left(\frac{d\sigma}{d\Omega}\right)^{Ag}_{Ruth}, \tag{5.1}$$

where r is the stoichiometric ratio between the number of ^{35}Cl or ^{37}Cl nuclei and Ag atoms in the target determined by RBS analysis in Section 5.1.1; ε_p is the efficiency of the RBS1 particle detector; ε_γ is the HPGe absolute efficiency for each gamma ray determined by simulations; $Y_\gamma(E',\theta)$ is the measured gamma yield at the proton energy E' and θ detection angle; $Y_{Ag}(E',\phi)$ is the yield of backscattered protons from Ag nuclei measured at ϕ angle and energy E'. The energy E' is the incident proton energy E_0 minus the energy loss in the middle of the target and corrected by the energy shift found in the previous section in the laboratory reference system. All cross sections displayed in subsequent sections are at E' energy and denoted as $E_{p,lab}$. Lastly, the silver Rutherford cross section at the same proton energy E' in the center of mass reference system is denoted as $\left(\frac{d\sigma}{d\Omega}\right)^{Ag}_{Ruth}$.

Taking into account that the efficiency of the particle detector is

$$\varepsilon_p = \frac{\Omega_p}{4\pi}\varepsilon_{p,int}, \tag{5.2}$$

where $\Omega_p = 3,65 \times 10^{-3}$ sr is the solid angle of the particle detector determined by H. Silva *et al.* in [164, 165] with 2 % uncertainty [3] and $\varepsilon_{p,int} \sim 100$ % is the particle detector intrinsic efficiency. The final equation for the calculus of the differential cross section is:

$$\left(\frac{d\sigma}{d\Omega}\right)_{\gamma}(E',\theta) = \frac{1}{4\pi}\frac{\Omega_p\varepsilon_{p,int}}{r\varepsilon_\gamma} \cdot \frac{Y_\gamma(E',\theta)}{Y_{Ag}(E',\phi)} \cdot \left(\frac{d\sigma}{d\Omega}\right)^{Ag}_{Ruth}. \tag{5.3}$$

Isotope 35-Chlorine

The measured differential cross sections of the proton induced reactions on ^{35}Cl isotope are shown in the following. Figure 5.13 and 5.14 display the cross sections of the elastic scattering ^{35}Cl(p, p$'\gamma$)^{35}Cl reaction corresponding to the first excited state $E_{\gamma_{10}}$=1219,3 keV and the second excited state

[3] The approximation $\Omega_p \approx \Delta a/d^2$ has been applied for the calculus of the solid angle covered by the detector and is valid only for detectors placed far from the source.

USC UNIVERSIDADE DE SANTIAGO DE COMPOSTELA

$E_{\gamma_{20}}$=1763,13 keV in the range of 2,36 to 3,48 MeV. We could observe that diverse narrow resonant structures appear. In the analysis of the 1763,13 keV photopeak was taken into account the overlapping of the 1764,494 keV gamma coming from the ^{214}Bi decay of the uranium chain.

The other cross section measured in our experiment coming from the same isotope was the $E_{\gamma_{10}}$=2230,49 keV gamma from the ^{35}Cl(p, $\alpha\gamma_{10}$)^{32}S reaction (Figure 5.15). This channel opens at higher energies ($\sim$ 3,35 MeV) and only a broad resonance appears around 3,44 MeV.

As pointed out in the motivation, where a general review of the available cross sections has been done, there is no cross section data published in the literature to benchmark neither of these measurements.

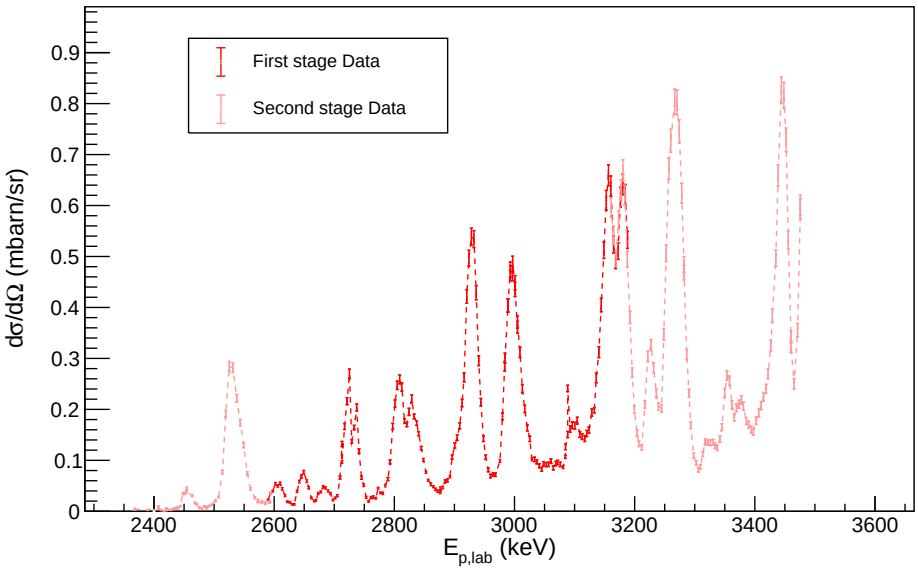

Figure 5.13: Differential cross section of the 1219,3 keV gamma ray from the ^{35}Cl(p, p′γ_{10})^{35}Cl reaction in the energy range of 2,36-3,48 MeV.

USC UNIVERSIDADE DE SANTIAGO DE COMPOSTELA

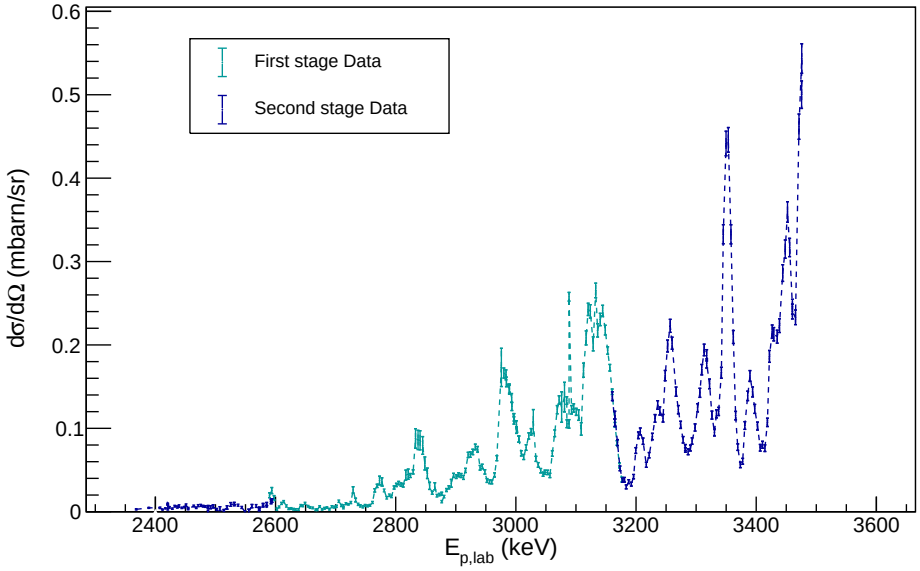

Figure 5.14: Differential cross section of the 1763,13 keV gamma ray from the ^{35}Cl(p, p$'\gamma_{20}$)^{35}Cl reaction in the energy range of 2,36-3,48 MeV.

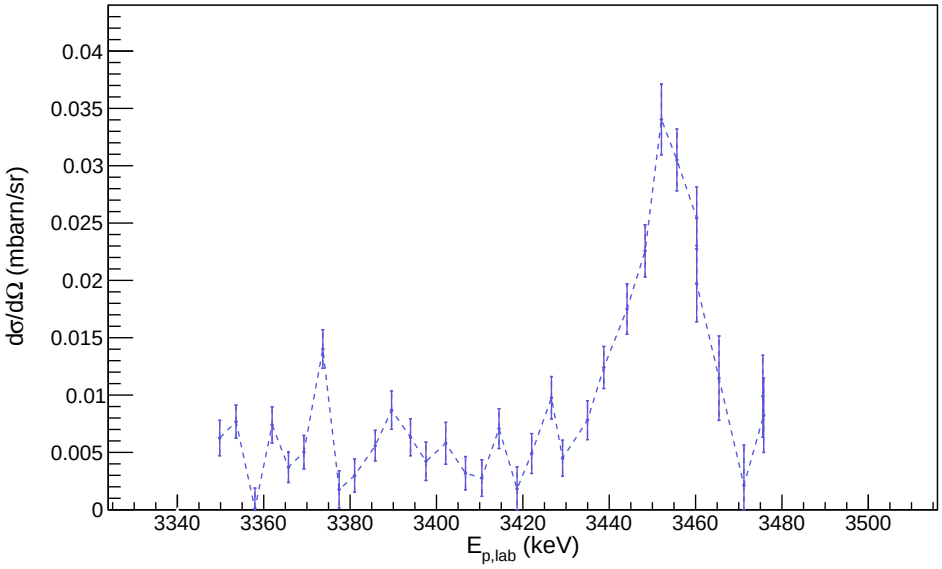

Figure 5.15: Differential cross section of the 2230,49 keV gamma ray from the ^{35}Cl(p, $\alpha\gamma_{10}$)^{32}S reaction in the energy range of 3,35-3,48 MeV.

USC UNIVERSIDADE DE SANTIAGO DE COMPOSTELA

Isotope 37-Chlorine

In this section, there are displayed all measured cross sections coming from proton induced reactions on ^{37}Cl isotope. Figure 5.16 shows the cross section from $E_{\gamma_{10}} = 1726,4$ keV gamma of the ^{37}Cl elastic scattering, where a double resonance appear around 3,25 MeV.

Figure 5.17 presents the alpha channel differential cross section at $E_{\gamma_{10}} = 2127,499$ keV. It opens at lower energies and grows as proton energy increases, appearing more resonant structures at higher energies.

Lastly, we measured two cross sections coming from the neutron channel that opens at $Q = -1596,22$ keV. Figure 5.18 displays the first transition at $E_{\gamma_{10}} = 1409,79$ keV and Figure 5.19 shows the second transition at $E_{\gamma_{20}} = 1611,24$ keV. As we can observe, the cross section of either reactions are not negligible leading to important neutron yield as increasing beam energy.

It can be noted that each channel opens at different energies due to spin-parity rules and angular momenta transmission.

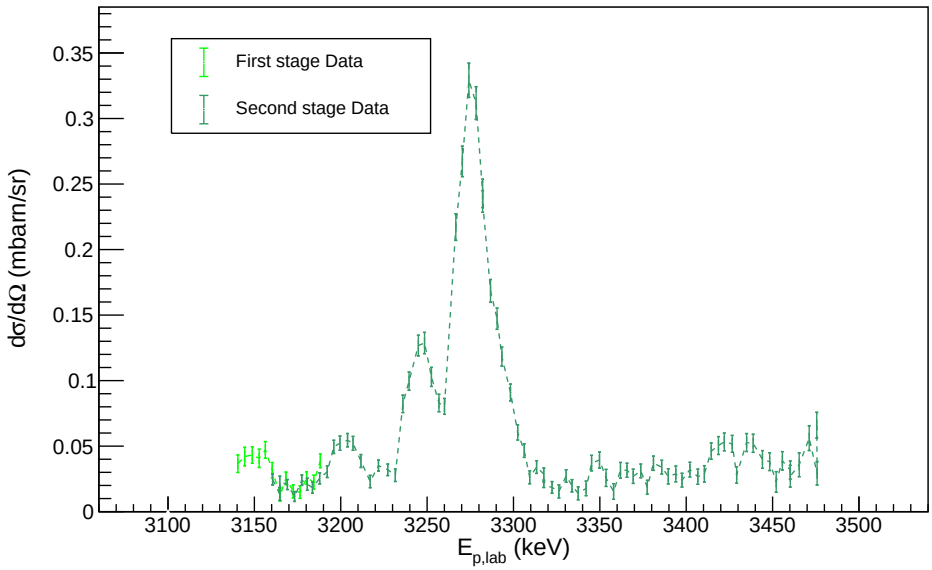

Figure 5.16: Differential cross sections of 1726,4 keV gamma rays from the ^{37}Cl(p, p′γ)^{37}Cl reaction in the range of 3,13 to 3,48 MeV.

USC UNIVERSIDADE DE SANTIAGO DE COMPOSTELA

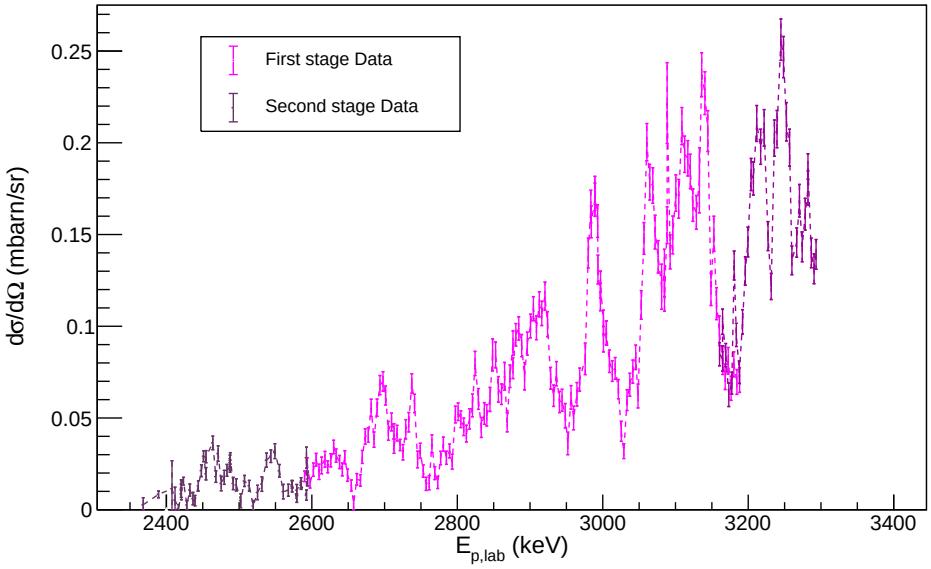

Figure 5.17: Differential cross sections of 2127,499 keV gamma rays from the $^{37}\mathrm{Cl}(\mathrm{p},\alpha\gamma)^{34}\mathrm{S}$ reaction in the energy range of 2,36-3,3 MeV.

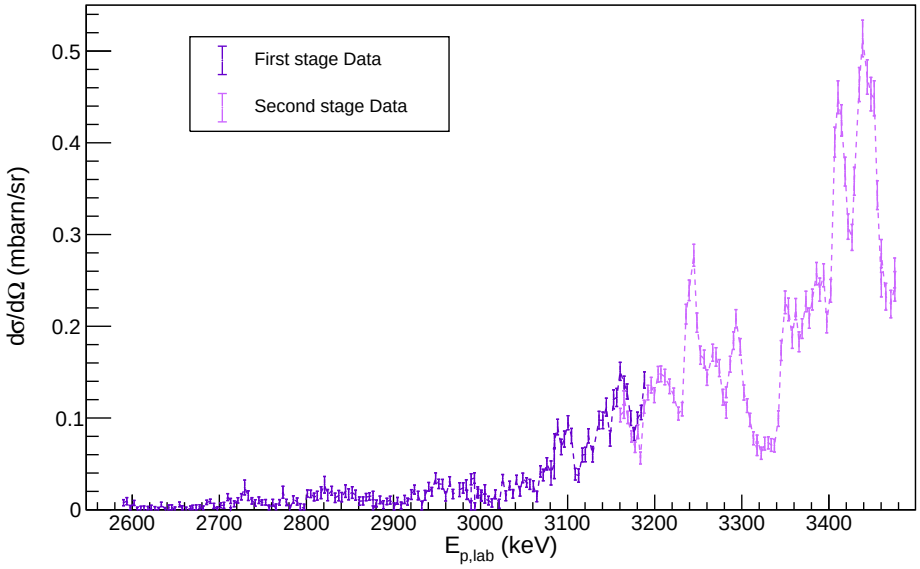

Figure 5.18: Differential cross sections of 1409,79 keV gamma ray from the $^{37}\mathrm{Cl}(\mathrm{p},\mathrm{n}\gamma_{10})^{37}\mathrm{Ar}$ reaction in the energy range of 2,58-3,48 MeV.

USC UNIVERSIDADE DE SANTIAGO DE COMPOSTELA

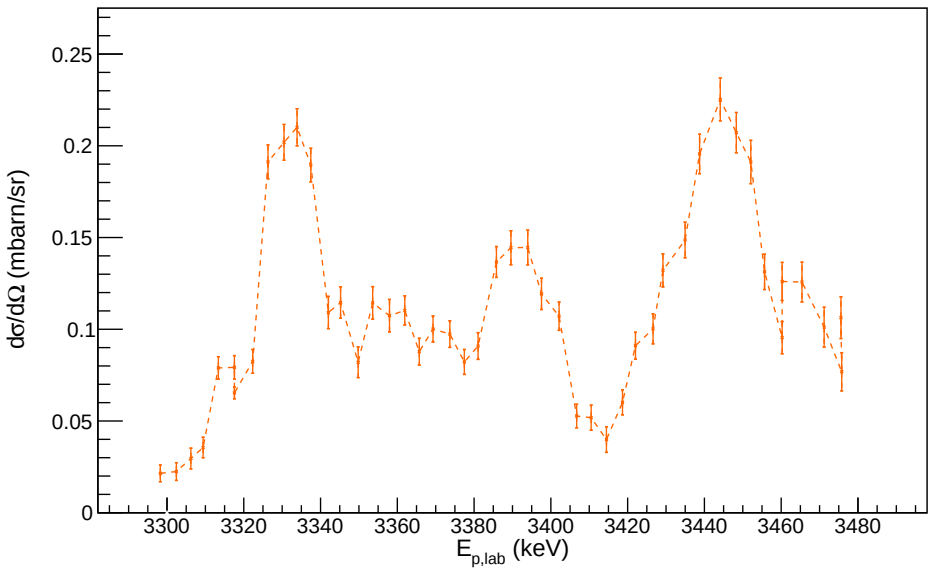

Figure 5.19: Differential cross sections of 1611,24 keV gamma ray from the $^{37}\mathrm{Cl}(\mathrm{p},\mathrm{n}\gamma_{20})^{37}\mathrm{Ar}$ reaction in the energy range of 3,29-3,48 MeV.

USC UNIVERSIDADE DE SANTIAGO DE COMPOSTELA

Uncertainties Discussion

The energy error of the proton beam has two main components: the Tandem accelerator which is a systematic error of around 2 keV and the energy loss in the target before the nuclear reaction is produced. This last component is the dominant because it produces a larger energy variation and there is no way to disentangle the position of the interaction. In order to calculate this error, the physics calculator of the LISE program has been employed to estimate the energy lost by the proton beam through matter at two points: in the middle and at the end of the target. It can be up to 14 keV in the middle for 2,4 MeV protons and up to 11 keV for 3,6 MeV protons. Therefore, the proton energy error ranges from 8 keV to 6 keV considering that the statistics of the energy loss distribution can be approximated by a square function.

In the following Table 5.4 there are listed all the uncertainties that affect the cross section measurements.

Table 5.4: Uncertainty estimations for the measurements.

Statistical mean uncertainties	
Gamma ray peak area (statistics and area determination)	6 %
Ag proton peak area (statistics and area determination)	0,2 %
Systematic uncertainties	
Gamma ray detector efficiency	0,6 %
Particle detector solid angle	2 %
Ratio ^{35}Cl/Ag	2 %
Ratio ^{37}Cl/Ag	2 %
Rutherford cross section	0,05 %

The major uncertainty in the absolute differential cross section value comes from the statistics and area determination of the gamma ray yield, on average, there is an error of 6 %, although, in the worst cases may be as high as 16 %. The other statistical uncertainty is the silver yield, much lower, around 0,2 %.

The sources of the systematic uncertainties were: particle detector solid angle 2 % determined by [164], stochiometric ratios of ^{35}Cl/Ag and ^{37}Cl/Ag have an error estimation of 2 %; Rutherford cross section has an uncertainty of 0,05 % due to the proton beam energy and the particle detector angle; gamma ray detector efficiency 0,6 %, it is worth to mention that thanks to

USC UNIVERSIDADE DE SANTIAGO DE COMPOSTELA

the efficiency simulation determination this value is relatively small compared with a normal process determination (around 7 %). Notice that the efficiency of the particle detector (ε_p) has no error, due to a 100 % of efficiency is considered. In the Appendix G all formulas employed in the error calculation procedure are shown.

We had no difficulties caused by neutrons from open (p,n) channels due to the germanium activation lines are far from the gamma rays energies, as a result, it did not cause additional inaccuracies.

Benchmarking of the Cross Sections

The only published differential cross section of proton induced reactions on both chlorine isotopes is the one shown in Figure 2.4 and published by Weber *et al.* [15].

The benchmarking between the differential cross section obtained in this thesis and the previous graph of the 2127,499 keV gamma ray from the ^{37}Cl(p, $\alpha\gamma$)^{34}S reaction is shown in Figure 5.20. We could observe that both differential cross sections have the same magnitude, together with the measurements of deuteron induced gamma ray emission cross sections on natural chlorine made by Jokar *et al.* [166]. As all chlorine cross sections, they are relatively low in comparison with other cross sections of similar reactions such as the ones displayed in P. Cabanelas *et al.* [86].

Another notable feature of Figure 5.20 is the large energy shift between proton energies which is around ∼1 MeV. The origin of this discrepancy is unknown. If this energy shift were corrected both measurements would agree as indicates the black line of the figure.

In this same study other chlorine cross sections appear, in particular one associated to the neutron channel ^{37}Cl(p, $n\gamma$)^{37}Ar also investigated in the present work, although they do not specify to which gamma transition is associated, as a result it can not be compared with our results.

USC UNIVERSIDADE DE SANTIAGO DE COMPOSTELA

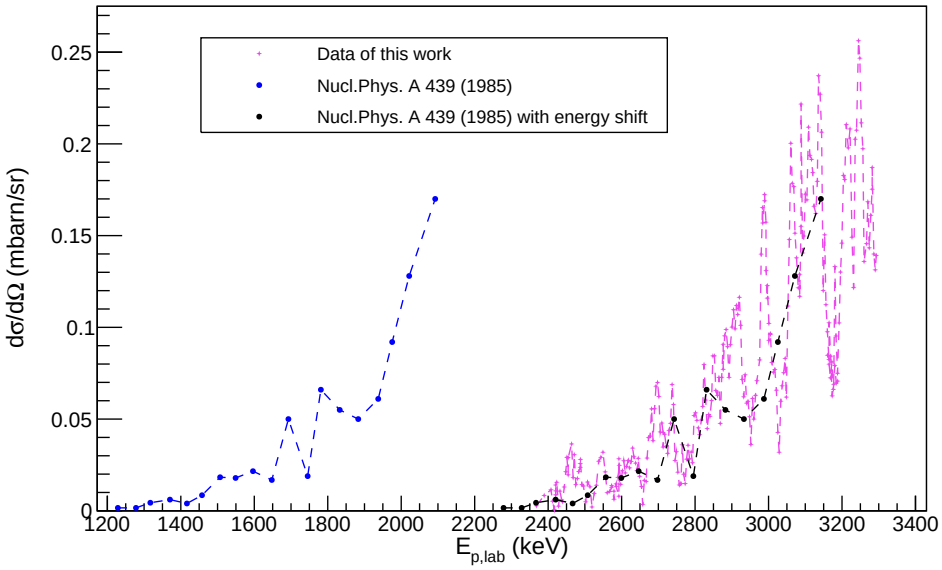

Figure 5.20: Comparison of the differential cross sections of 2127,499 keV gamma ray from the ^{37}Cl(p, $\alpha\gamma$)^{34}S reaction between the experimental results of this thesis (pink) and the Weber *et al.* study [15] (blue). The error of the Weber *et al.* cross section is around 12 %. The black line represents the differential cross section of Weber *et al.* with a proton energy shift around 1 MeV.

5.2 Environmental Radiation Experimental Results

5.2.1 Data Analysis

In this section, an extensive study of the natural gamma radiation measurements is presented. We have analysed environmental background spectra of each location individually and compared these measurements between them in order to identify variations. Moreover, we have been able to distinguish two radioactive series (uranium and thorium) and potassium decay and study their evolution over time.

First, we studied all photopeaks that appear in each spectrum and tried to identify their origins. In Table 5.6 all distinguishable peaks after a measurement of 2 days are listed: energies, intensities, decay modes, half-lifes, parent nuclei, daughter nuclei and series. We could observe that the only visible peaks are the ones with an intensity >1 % and the most prominent peaks do not necessarily have high intensities, it is rather a combination between

USC UNIVERSIDADE DE SANTIAGO DE COMPOSTELA

intensity and amount of material present in the surroundings, for instance, the potassium decay. The annihilation peak at 511 keV also appears in all spectra but it is not mentioned. Moreover, in the CTN/IST spectra there is a peak at 661,657 keV from the ^{137}Cs decay and a possible origin was a calibration source near the detector or attributable to the storage of radioactive material placed in the CTN/IST installation. It should be mentioned that in measurements of 30 min the only visible photopeaks have intensities higher than 5 % [4].

In the following analysis, data from the USC laboratory is not included because the detectors are strongly shielded and the background measurements can not be compared with the other data sets. Nevertheless, USC data has been useful to understand the behaviour of cosmic rays at high energy regime and we could verify that all the photopeaks listed in Table 5.6 are also present in the environmental radiation of the north-west of Iberian peninsula.

5.2.1.1 Environmental Radiation Comparison

A comparison between natural background at CTN/IST laboratory and UBI laboratory sites was conducted. The purpose was to determine natural radiation differences induced by building materials or sub-surface compositions and to detect any variation over time.

This comparison was factible and accurate due to the fact that both detectors are high purity germanium semiconductors and have similar shapes and sizes. A measurement done during 30 minutes at these two locations is shown in Figure 5.21. Clearly, we can observe that the amount of natural radiation in UBI is more than two orders of magnitude greater. This result was expected because of sub-soil composition (see the major soil types of Europe, Figure 2-34 of [109]).

In order to compare specific components of background, a photopeak of reference was chosen for each natural radioactive contribution (Table 5.7). Usually, the most visible peaks are at intermediate-high energies to avoid the bulk of Compton contributions, scatterings and so on, that dominate low energies. As a result, the reference photopeak for the uranium series was taken at 1764,494 keV from ^{214}Bi decay, for thorium series at 2614,533 keV from ^{208}Tl decay and for potassium decay the only gamma is at 1460,849 keV. Unfortunately, the actinium series photopeaks were not visible in any of the cases, therefore this chain could not be tracked by this method. Afterwards,

[4] This information is useful when PIGE spectra are analysed due to PIGE measurements do not last more than this time interval.

USC UNIVERSIDADE DE SANTIAGO DE COMPOSTELA

Table 5.5: Identifiable photopeaks from background spectra measured during two days at CTN/IST, UBI and Laboratorio de Análisis de Radiaciones of USC. Data taken from [167].

Photopeak (keV)	Intensity (%)	Decay mode	Half-life	Parent	Gamma transition in	Series
238,632(2)	43,3(4)	β^-	10,64(1) h	^{212}Pb	^{212}Bi	Thorium
295,224(2)	19,3(2)	β^-	26,8(9) m	^{214}Pb	^{214}Bi	Uranium
338,320(3)	11,27(19)	β^-	6,15(2) h	^{228}Ac	^{228}Th	Thorium
351,932(2)	37,6(4)	β^-	26,8(9) m	^{214}Pb	^{214}Bi	Uranium
463,004(6)	4,40(7)	β^-	6,15(2) h	^{228}Ac	^{228}Th	Thorium
583,191(2)	84,5(7)	β^-	3,053(4) m	^{208}Tl	^{208}Pb	Thorium
609,312(7)	46,1(5)	β^-	19,9(4) m	^{214}Bi	^{214}Po	Uranium
665,453(22)	1,46(3)	β^-	19,9(4) m	^{214}Bi	^{214}Po	Uranium
727,330(9)	6,58(5)	β^-	60,55(6) m	^{212}Bi	^{212}Po	Thorium
768,356(10)	4,94(6)	β^-	19,9(4) m	^{214}Bi	^{214}Po	Uranium
794,947(5)	4,25(7)	β^-	6,15(2) h	^{228}Ac	^{228}Th	Thorium
806,174(18)	1,22(2)	β^-	19,9(4) m	^{214}Bi	^{214}Po	Uranium
835,710(6)	1,61(6)	β^-	6,15(2) h	^{228}Ac	^{228}Th	Thorium
860,564(5)	12,42(10)	β^-	3,053(4) m	^{208}Tl	^{208}Pb	Thorium
911,204(4)	25,8(4)	β^-	6,15(2) h	^{228}Ac	^{228}Th	Thorium
934,061(12)	3,03(4)	β^-	19,9(4) m	^{214}Bi	^{214}Po	Uranium
964,766(10)	4,99(9)	β^-	6,15(2) h	^{228}Ac	^{228}Th	Thorium
968,971(17)	15,8(3)	β^-	6,15(2) h	^{228}Ac	^{228}Th	Thorium
1120,287(10)	15,1(2)	β^-	19,9(4) m	^{214}Bi	^{214}Po	Uranium
1155,19(2)	1,63(2)	β^-	19,9(4) m	^{214}Bi	^{214}Po	Uranium

Table 5.6: Identifiable photopeaks from background spectra measured during two days at CTN/IST, UBI and Laboratorio de Análisis de Radiaciones of USC. Data taken from [167].

Photopeak (keV)	Intensity (%)	Decay mode	Half-life	Parent	Gamma transition in	Series
1238,110(12)	5,79(8)	β^-	19,9(4) m	^{214}Bi	^{214}Po	Uranium
1280,96(2)	1,43(2)	β^-	19,9(4) m	^{214}Bi	^{214}Po	Uranium
1377,669(12)	4,00(6)	β^-	19,9(4) m	^{214}Bi	^{214}Po	Uranium
1401,50(4)	1,27(2)	β^-	19,9(4) m	^{214}Bi	^{214}Po	Uranium
1407,98(4)	2,15(5)	β^-	19,9(4) m	^{214}Bi	^{214}Po	Uranium
1460,849(5)	11	$e + \beta^+$	1,277(8)$\times 10^9$ y	^{40}K	^{40}Ar	Potassium decay
1509,228(15)	2,11(4)	β^-	19,9(4) m	^{214}Bi	^{214}Po	Uranium
1583,22(4)	0,690(15)	β^-	19,9(4) m	^{214}Bi	^{214}Po	Uranium
1588,19(3)	3,22(8)	β^-	6,15(2) h	^{228}Ac	^{228}Th	Thorium
1594,73(8)	0,25(4)	β^-	19,9(4) m	^{214}Bi	^{214}Po	Uranium
1620,50(10)	1,49(3)	β^-	60,55(6) m	^{212}Bi	^{212}Po	Thorium
1630,627(10)	1,51(4)	β^-	6,15(2) h	^{228}Ac	^{228}Th	Thorium
1661,28(6)	1,15(3)	β^-	19,9(4) m	^{214}Bi	^{214}Po	Uranium
1729,595(15)	2,92(4)	β^-	19,9(4) m	^{214}Bi	^{214}Po	Uranium
1764,494(14)	15,4(2)	β^-	19,9(4) m	^{214}Bi	^{214}Po	Uranium
1847,420(25)	2,11(3)	β^-	19,9(4) m	^{214}Bi	^{214}Po	Uranium
2118,55(3)	1,14(3)	β^-	19,9(4) m	^{214}Bi	^{214}Po	Uranium
2204,21(4)	5,08(4)	β^-	19,9(4) m	^{214}Bi	^{214}Po	Uranium
2447,86(10)	1,57(2)	β^-	19,9(4) m	^{214}Bi	^{214}Po	Uranium
2614,533(13)	99	β^-	3,053(4) m	^{208}Tl	^{208}Pb	Thorium

USC UNIVERSIDADE DE SANTIAGO DE COMPOSTELA

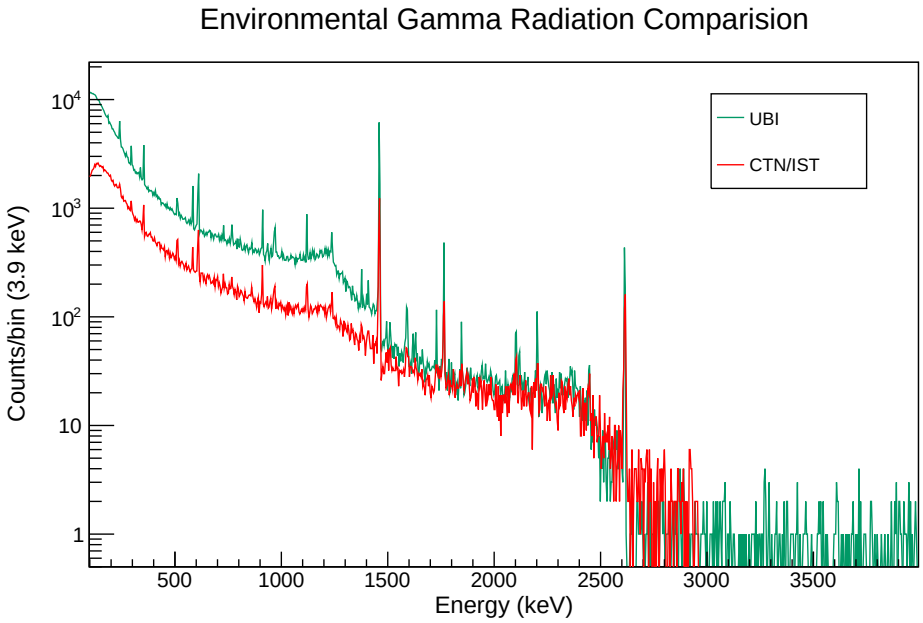

Figure 5.21: Environmental gamma radiation of two laboratories located at CTN/IST (red line) and at Universidade da Beira Interior (green line). Both spectra have been measured with a HPGe detector of similar dimensions during 30 min.

we monitored the amount of counts of each photopeak of reference and considered that this quantity represents the entire series or decay (assuming that there was no chain disruption).

Table 5.7: Photopeaks employed as a reference for each background contribution. Data taken from NNDC [26].

Background component	**Parent nuclei**	**Photopeak of reference (keV)**
Potassium decay	^{40}K	1460,849
Uranium series	^{214}Bi	1764,494
Thorium series	^{208}Tl	2614,533

Temporal Analysis

Temporal statistical analysis allowed us to study natural background behaviour over time. Aiming to observe fluctuations in each background com-

USC UNIVERSIDADE DE SANTIAGO DE COMPOSTELA

ponent, their concentrations were evaluated independently.

Firstly, we analysed diverse data sets of entire days and compared their evolution along weeks. Figures 5.22, 5.23 and 5.24 show the mean value of each component in one day and their error bars are the statistical uncertanties. Fluctuations in every component are similar and follow the same oscillating pattern without any abrupt movement. Uniquely, there is a point in the concentrations of uranium and thorium series at CTN/IST that suddenly drops. Nevertheless, it is still smaller than the standard deviation.

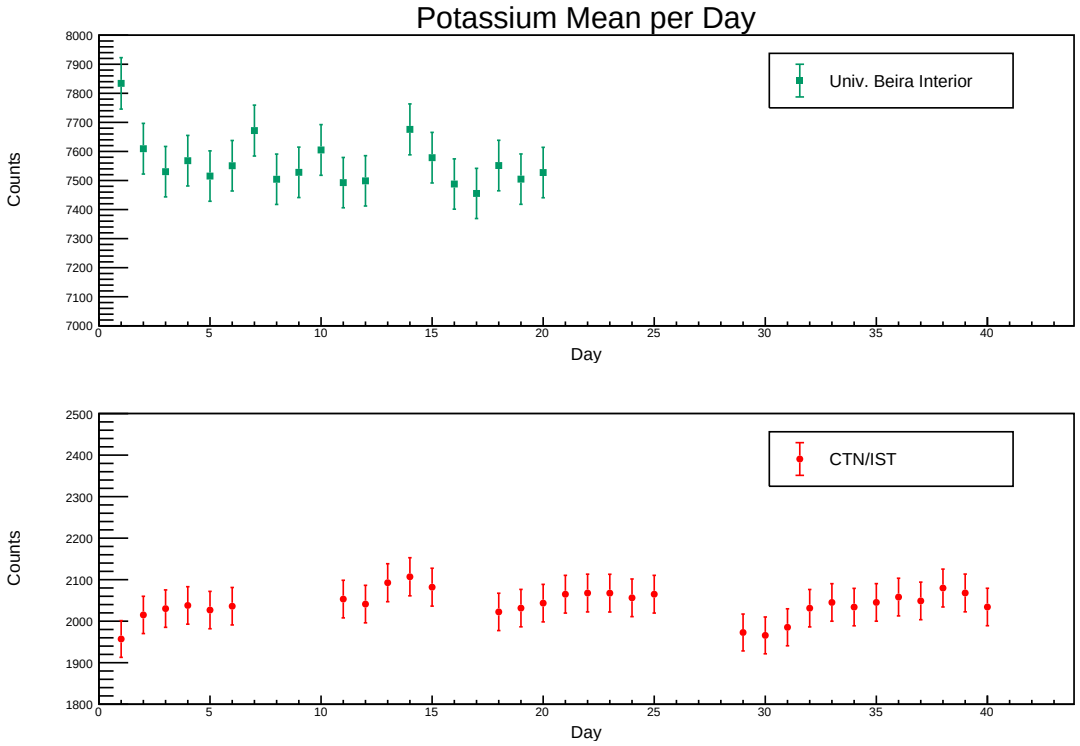

Figure 5.22: Mean of the number of gammas detected per day for the reference photopeak of the potassium decay. The upper pad shows the potassium mean measured at UBI laboratory and the lower pad measured at CTN/IST laboratory. Their uncertainties are statistical deviations.

USC UNIVERSIDADE DE SANTIAGO DE COMPOSTELA

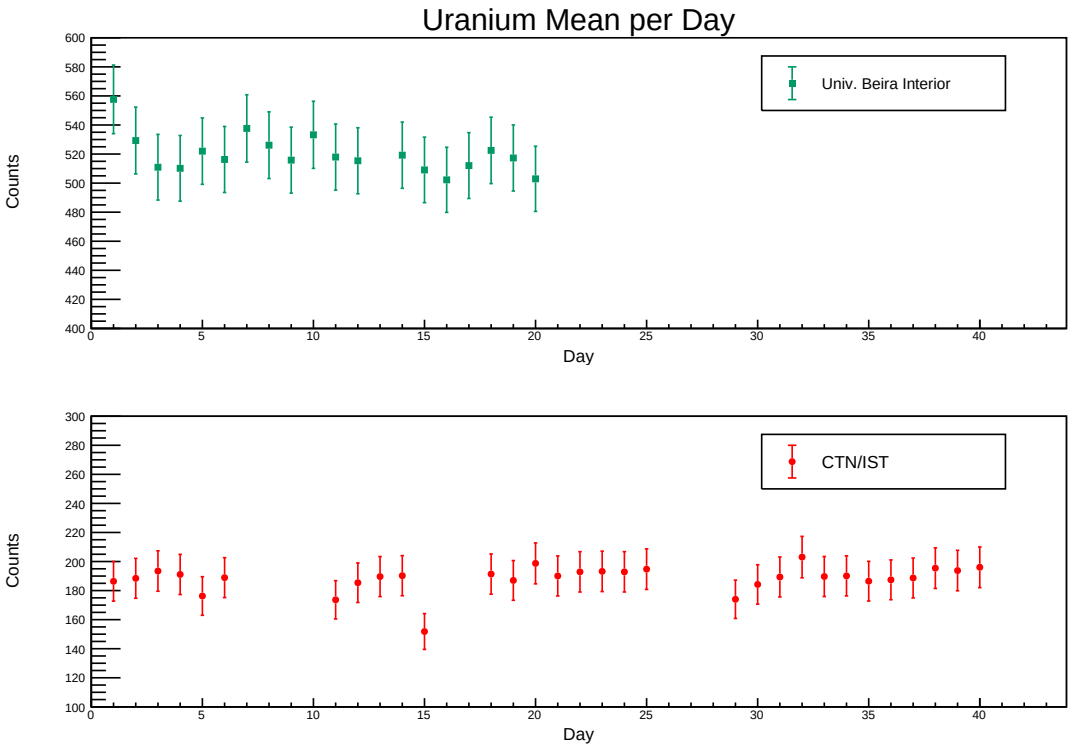

Figure 5.23: Mean of the number of gammas detected per day for the reference photopeak of the uranium series. The upper pad shows the uranium mean measured at UBI laboratory and the lower pad measured at CTN/IST laboratory. Their uncertainties are statistical deviations.

USC
UNIVERSIDADE DE SANTIAGO DE COMPOSTELA

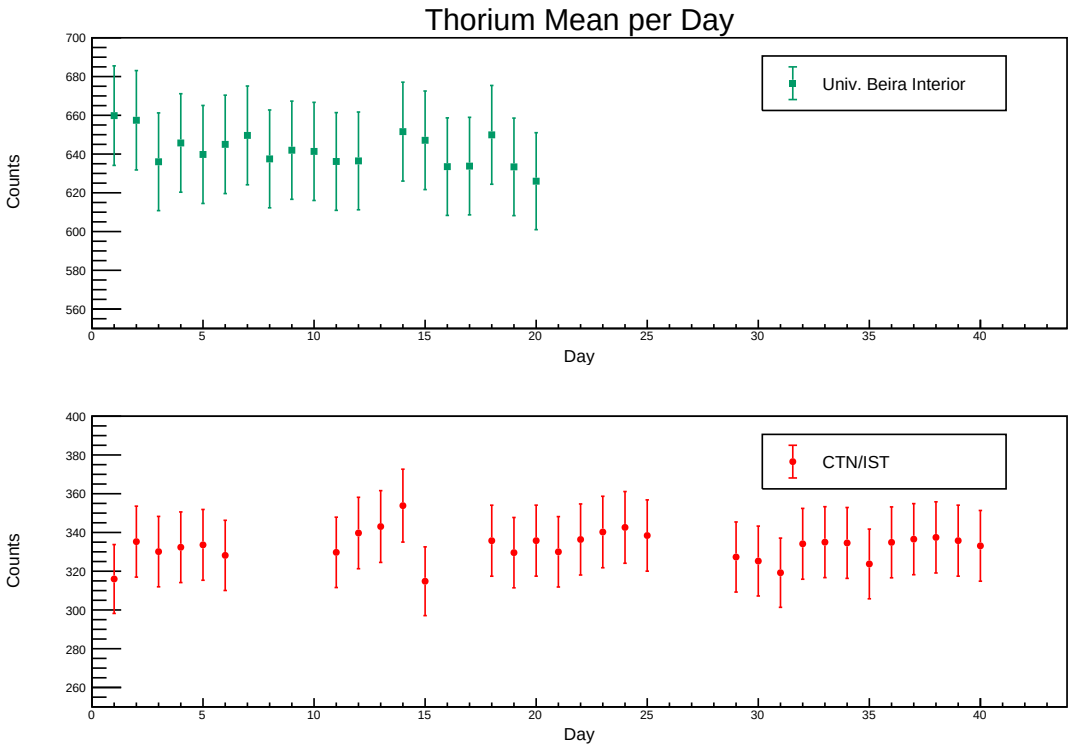

Figure 5.24: Mean of the number of gammas detected per day for the reference photopeak of the thorium series. The upper pad shows the thorium mean measured at UBI laboratory and the lower pad measured at CTN/IST laboratory. Their uncertainties are statistical deviations.

USC UNIVERSIDADE DE SANTIAGO DE COMPOSTELA

Afterwards, we analysed the same data with a different criteria. In order to observe fluctuations along the day, we calculated the mean of each component every hour. The analysis is displayed in Figures 5.25, 5.26 and 5.27. The concentrations over the hours remain steadily with small variations at both laboratories. In the case of UBI data, there is a small increase from 9 to 14 hour observable in all components, although it could be a statistical effect because it is not sufficiently intense. As a result, any pattern related to the hours with higher temperatures or associated with laboratory ventilation could not be concluded.

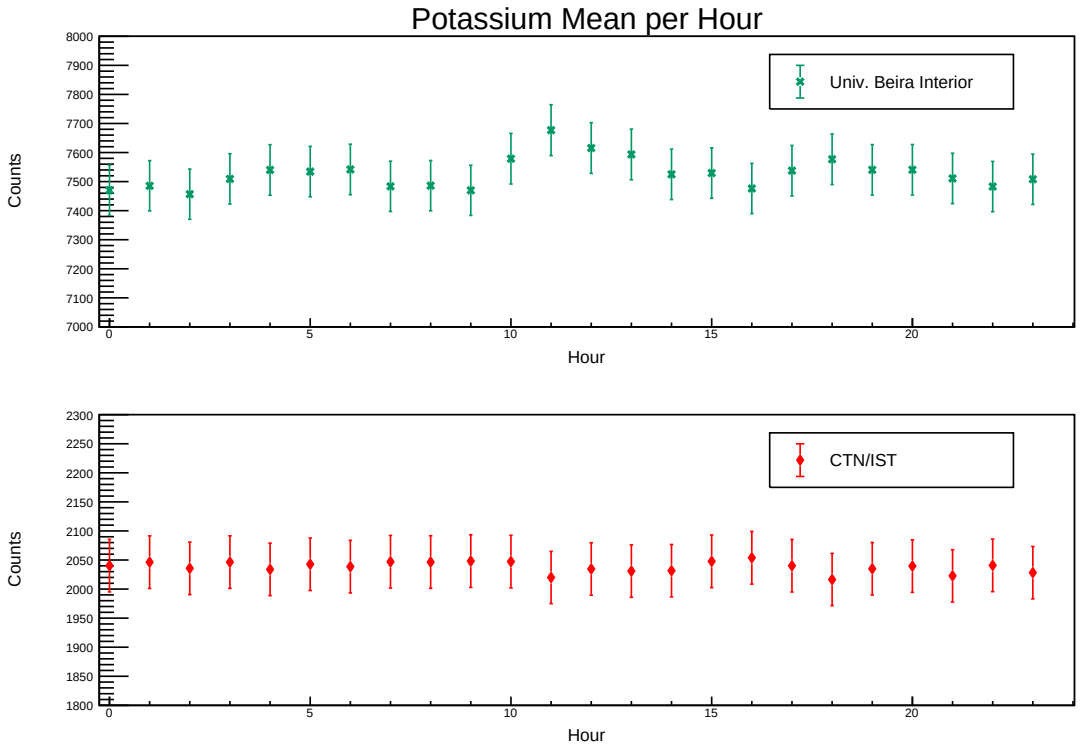

Figure 5.25: Mean of the number of gammas detected per hour for the reference photopeak of the potassium decay. The upper pad shows the potassium mean measured at UBI laboratory and the lower pad measured at CTN/IST laboratory. Their uncertainties are statistical deviations.

Total average rates over all data measured and their ratios are listed in Table 5.8. As we have mentioned before, the concentrations of each component are higher at UBI than at CTN/IST. The most outstanding result is the large amount of potassium present in UBI laboratory's materials, almost four times the potassium component of CTN/IST. It is compulsory to mention that the first detector was nearer from walls than the second one,

USC UNIVERSIDADE DE SANTIAGO DE COMPOSTELA

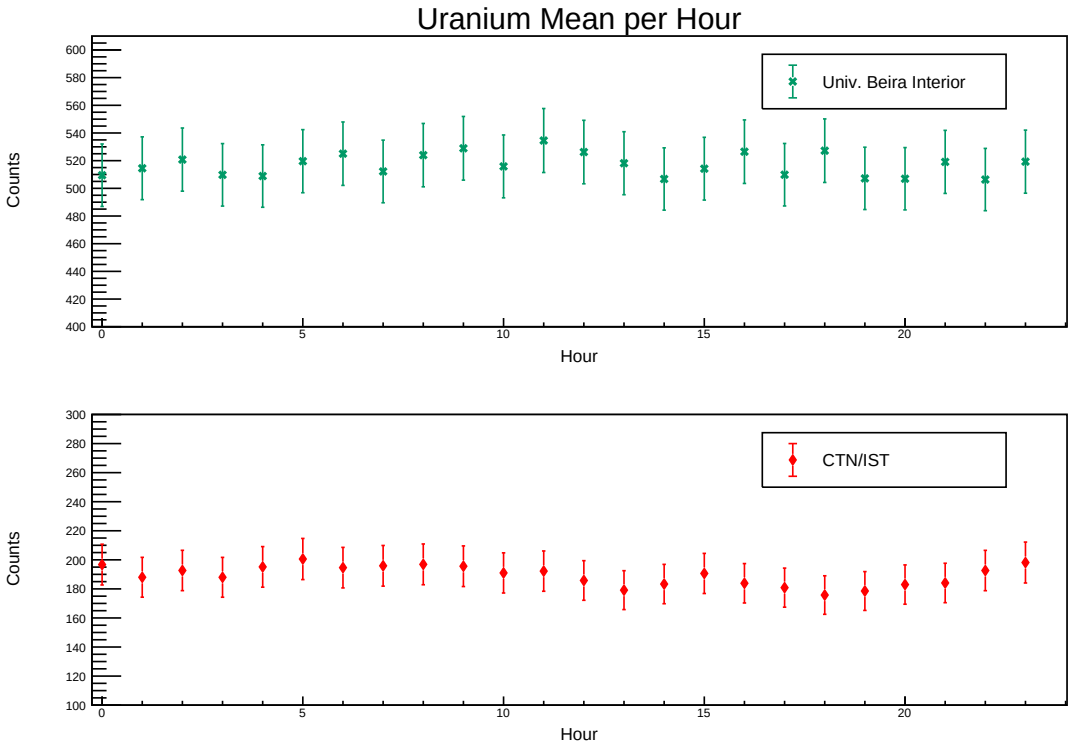

Figure 5.26: Mean of the number of gammas detected per hour for the reference photopeak of the uranium series. The upper pad shows the uranium mean measured at UBI laboratory and the lower pad measured at CTN/IST laboratory. Their uncertainties are statistical deviations.

which is situated in the middle of a large room. With respect to the radioactive series, background coming from thorium chain is more abundant, while uranium chain contribution is less intense in both locations. The quantity of uranium in the UBI laboratory is almost three times the amount of uranium at CTN/IST facility, while the thorium quantity in the UBI laboratory is twice the number of the CTN/IST. Surprisingly, the radiation difference between uranium and thorium are similar in either places, around 120 counts.

USC UNIVERSIDADE DE SANTIAGO DE COMPOSTELA

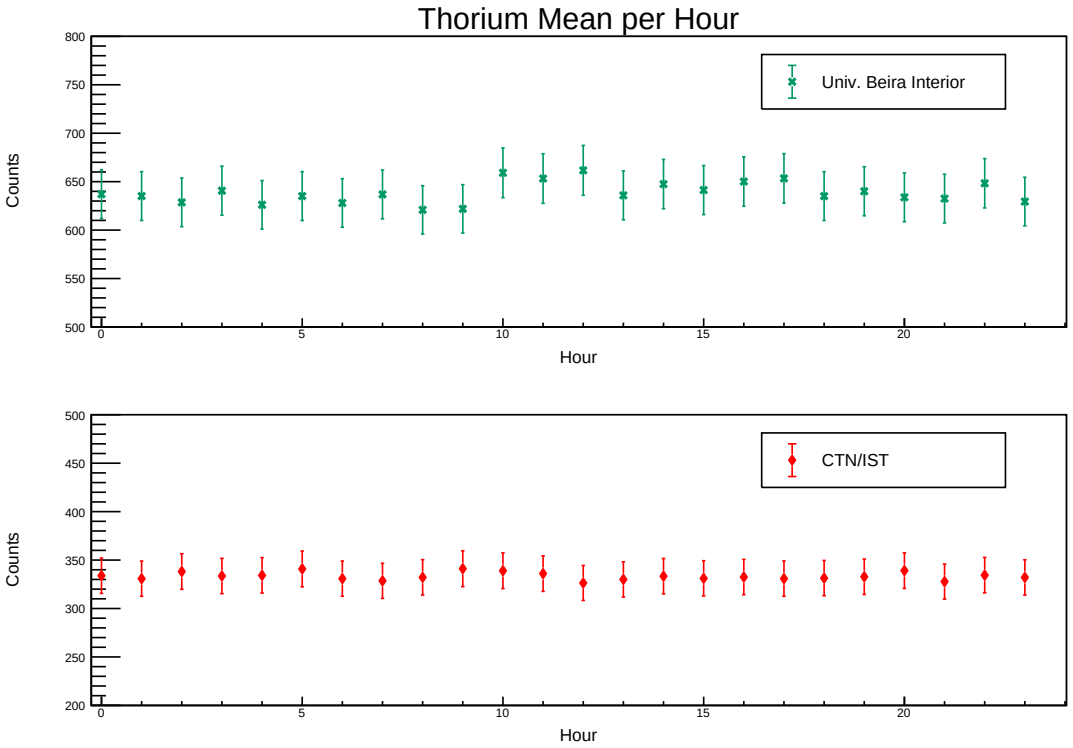

Figure 5.27: Mean of the number of gammas detected per hour for the reference photopeak of the thorium series. The upper pad shows the thorium mean measured at UBI laboratory and the lower pad measured at CTN/IST laboratory. Their uncertainties are statistical deviations.

Table 5.8: Total average rates per day of each environmental component at CTN/IST and at UBI locations. The last column shows the ratios between UBI and CTN/IST components.

Background component	**CTN/IST (counts/day)**	**UBI (counts/day)**	**Ratio**
Uranium series	189(20)	517(28)	2,74
Thorium series	333(20)	640(28)	1,92
Potassium decay	2038(59)	7533(83)	3,70

USC UNIVERSIDADE DE SANTIAGO DE COMPOSTELA

5.2.2 Environmental Radiation Simulations

The radioactive background measurements previously analysed have been studied by comparing them to detailed environmental data simulations. By this procedure, we can also benchmark the validity of the EnsarRoot code developments. Specifically, we have recreated terrestrial and cosmogenic natural ionizing sources. Artificial ionizing radiation was not included in the simulations due to its variability and uncertainty of knowledge.

The simulation of the environmental radioactivity is not straightforward due to the amount of radioisotopes present in nature and diverse factors that could affect them (radionuclides migration, geographical features, etc.). Therefore, aiming to simplify the issue, different assumptions have been pre-established. All radioactive series have been considered not modified chemically and in secular equilibrium, meaning that daughter activity equals parent activity. Moreover, the quantification of the actinium series to the total background was not possible, therefore, we have used the ratio of the uranium and actinium activities as an estimation of this quantity:

$$A_{\text{Actinium}} = 0,0046 \times A_{\text{Uranium}}. \tag{5.4}$$

Lastly, we have considered only gamma emissions coming from transitions with a probability higher than 1 % because, as we have just observed in Table 5.6, they are the only visible photopeaks.

These simulations were done within the EnsarRoot framework using all recreated laboratory setups and the gamma rays generators of the natural series formerly developed, for more information consult Section 4.2 and all gammas included with its probabilities and energies are detailed in Appendixes A, B and C.

The Cosmic ray Shower Library (CRY) [168, 169] was used to reproduce cosmic radiation. CRY software library allows the user to determine some specifications as area, altitude, latitude, date and propagated particles. Afterwards, using these variables, the program provides characteristic primary and secondary cosmic showers. This output is an energy, momentum, direction and angular distribution already prepared into a readable list to use in other transport and detector simulation codes. We have used it as the input of the Cosmic Rays EnsarGenerator [10, 170], a generator previously developed inside EnsarRoot that acts as a particle generator and particle propagator through matter.

5.2.2.1 CTN/IST Data Simulation

As we have just mentioned, CTN/IST terrestrial radiation was simulated by using Radioactive Series EnsarGenerators and Potassium Decay Ensar-

USC UNIVERSIDADE DE SANTIAGO DE COMPOSTELA

Generator. The formers are a number of individual generators and each one emulates the decay of a nucleus of the radioactive series and the posterior de-excitation of its daughter where gamma rays are emitted. Therefore, for each nucleus a simulation with 25×10^6 events was done. Not all simulations produced a signal in the detector, because sometimes there was no particle emission or because gamma rays were scattered or absorbed by surrounding materials before reaching the active volume of the detector.

With the aim of simulating the origin and direction of earth radiation we determined the area of gamma emission as a square of 20 by 20 cm at 30 cm of distance under the detector. These gamma rays were sent in an isotropic distribution but covering only the upper semiesphere for simulation optimization reasons.

The geometry used in these simulations was the CTN/IST standard setup for the potassium decay simulation and including a block of earthy materials of 12,2 cm thickness under the detector for the rest of nuclear decays. This block of earth was specially incorporated in the setup because we observed that photopeaks of lower energies were attenuated before reaching the detector. This additional element was not necessary for the potassium simulation because its gamma rays come mostly from the surrounding walls.

Once the individual processes were finished all simulations belonging to the same chain were gathered in one simulation to treat the whole series as a unit for the posterior analysis, for example, the uranium chain had a total of 125×10^6 events. In addition, we have applied the resolution function of the CTN/IST detector (Figure 4.24) to these simulations in order to reproduce a realistic response.

Figure 5.28 shows separately the simulation of each component along with an experimental background spectrum (black line). We can observe that the shape of the natural background is a convolution among the potassium gamma ray and its characteristic Compton shape (green line) and thorium and uranium series that significantly contribute to the low energy bump (orange and blue lines). On the contrary, the actinium signal is almost imperceptible covering only a short range at low energies (pink line).

In this figure, the simulation of cosmic rays showers is also represented (gray line). This simulation was done firstly configuring CRY library with Lisbon coordinates (at 38° latitude and 0° altitude), the date for the simulation was set on the 20th of January of 2019 (the program also reproduces solar activity fluctuations) and its composition contained muons, photons, neutrons, protons, electrons and positrons. Finally, these particle showers were sent to the CTN/IST simulated setup from top to bottom direction in a cubic box of 1 m length using the Cosmic Ray EnsarGenerator. We can observe in Figure 5.28 that cosmic rays signal overlaps with other background

USC UNIVERSIDADE DE SANTIAGO DE COMPOSTELA

contributions at low-to-intermediate energies and only at high energies is clearly distinguishable.

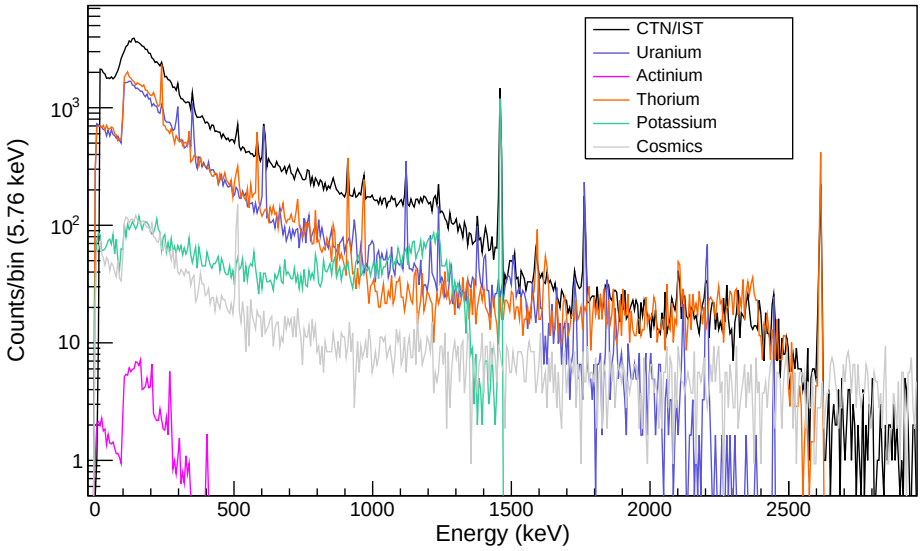

Figure 5.28: Experimental background spectrum of the CTN/IST measured data during an interval of 30 min (black line) and all simulated components weighted as explained in the text.

Once all contributions were simulated separately they had to be weighted by comparing them against real CTN/IST data. For this purpose, we used TMinuit ROOT class which provides to the user several minimization algorithms [171]. We calculated the chi-square between the real data histogram and the simulated inputs given some values of the parameters. The function of TMinuit is to find the numerical values of the parameters to obtain the lowest chi-square value.

Two separate energy regions were defined to fit the simulations: one was at high energies, this is from 2,63 to 3 MeV, and the other was from low to intermediate energies, from 0,1 to 1,5 MeV. The low-to-intermediate energy region is dominated by terrestrial radiation and includes all contributions, while the first region with a smaller gamma yield only contains cosmic rays. In the first step, simulations were minimized at the region of high energies and the parameter which determines the weight of cosmic rays simulation was obtained (Table 5.9). In the second stage, the same methodology was applied to the low-to-intermediate region and the parameters of uranium and thorium chains and potassium decay were resolved (Table 5.9).

USC UNIVERSIDADE DE SANTIAGO DE COMPOSTELA

In Table 5.9 all parameters obtained in the minimisations are shown. The actinium parameter is the result of the multiplication of the uranium parameter by the scalar factor of their activities (Eq. 5.4). We can appreciate that all parameters are around 1, which denotes that there is enough statistics in the simulations to compare it with this particular experimental background spectra. In reference of χ^2 values, in the second region the χ^2 value is a little bit higher than the degrees of freedom (around 8000) due to there are some isolated points where the simulation and the data differ significantly, while in the first region there is not enough statistics to do a correct interpretation. A more detailed residuals comparison is explained hereafter. Figure 5.28 shows all simulated components weighted with their corresponding parameters.

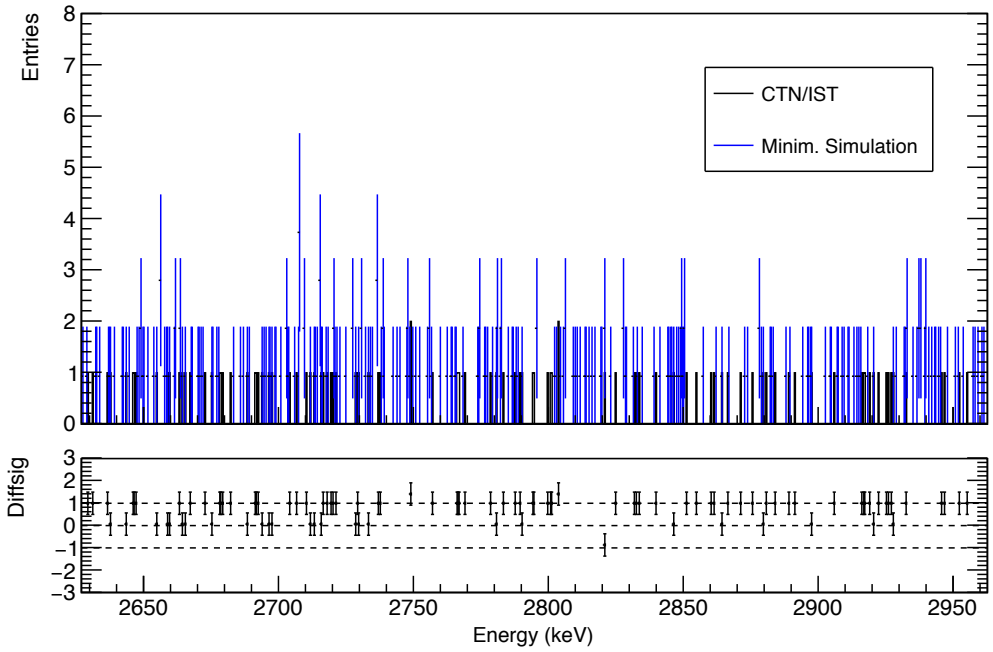

Figure 5.29: In the upper pad it is represented the CTN/IST data (black line) against its simulation at high energy region including only cosmic rays simulation weighted (blue line). In the lower pad it is shown the ratio between the difference of the previous histograms and their uncertainties.

Intending to examine the results of the simulation extensively a method of verification was chosen: the TRatioPlot ROOT class [172]. It accepts two histograms and provides different analysis such as displaying ratios, differences and fitting residuals. We have used the option where both histograms are subtracted and the difference is divided by the uncertainty. Figures 5.29

USC UNIVERSIDADE DE SANTIAGO DE COMPOSTELA

Table 5.9: Numerical values of the weighted parameters after TMinuit fit for the simulations of CTN/IST background. They have been calculated in two steps: the first one determines the cosmic rays parameter at high energy values and in the second stage the rest of the parameters are resolved in the low-to-intermediate energy region.

Energy Region (keV)	**Uranium param**	**Actinium param**	**Thorium param**	**Potassium param**	**Cosmic Rays param**	χ^2	$\chi^2_{reduced}$
2630-3000					0,93(18)	74,94	0,08
100-1500	1,640(17)	754(8)$\times$ 10^{-5}	1,440(15)	1,002(17)		12477,60	3,26

USC UNIVERSIDADE DE SANTIAGO DE COMPOSTELA

and 5.30 show this analysis in the lower pad. The first figure presents the analysis of the cosmic rays contribution at high energies (first step) while in the second there is the final simulation including all weighted components (this plot is splitted into two energy regions to be more clear). Most of the points are inside the interval [-2,2] in the first plot and [-5,5] in the second plot, meaning that the differences between simulation and data are the same order of magnitude as their errors. There is a differentiated region at low energies from 0 to 150 keV where the disagreement is higher due to the simulation does not include neither the X-rays from the surroundings nor some possible contribution from the electronic noise. There is a peak at 238,320 keV from the thorium series that its simulation is overestimated and it is shown in Figure 5.31. In fact, this peak was used for the calculation of the earth block thickness under the detector simulation in order to attenuate the gammas at low energies. However, it is a sensitive parameter and it was not possible to address more accuracy without unbalancing the rest of the chain. The optimization result on the whole is satisfying because the deviations are minimum.

Finally, the sum of all weighted components conforming only one simulation is plotted in Figure 5.32 (blue line) together with CTN/IST data (black line). We can observe that the result of the simulation describes the environmental radiation with a reasonably good precision over a large energy range.

Despite we have calculated the desintegrations per second occurring for each series (D_i) and we also known the scalar factors (parameters of the fit, P_i) we can not convert them into activities because we ignore where are the positions of the emitting radionucleus, in consequence, the efficiency of the detector with respect to these locations is unknown (ε). The simulated activity for any contribution i is expressed as:

$$A_i^s = D_i \cdot P_i \cdot \varepsilon. \tag{5.5}$$

If we assume that the radionuclides from the uranium and thorium series are placed in the same position, hence the geometrical efficiencies would be the same, being the intrinsic efficiencies correctly simulated by the simulation for each energy. Then, we could divide both activities, removing the efficiency from the ratio. Taking the desintegrations/s from the simulation results and the parameters from Table 5.9, the quotient between uranium and thorium activities is:

$$\frac{A_U^s}{A_{Th}^s} = \frac{D_U \cdot P_U \cdot \varepsilon}{D_{Th} \cdot P_{Th} \cdot \varepsilon} = \frac{47539 \cdot 1,640}{57153 \cdot 1,440} = 0,95. \tag{5.6}$$

USC UNIVERSIDADE DE SANTIAGO DE COMPOSTELA

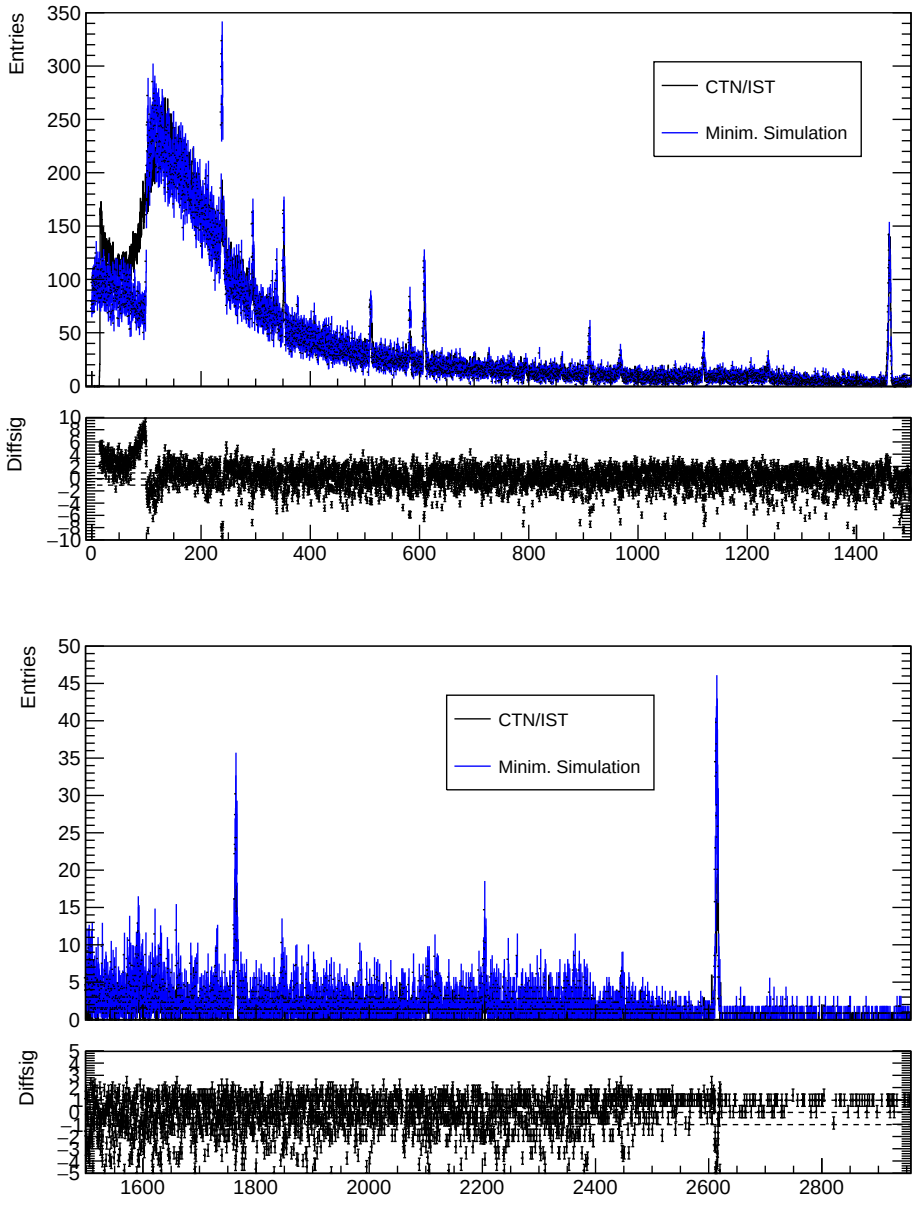

Figure 5.30: In the upper pad it is represented the CTN/IST data (black line) against its simulation including all contributions weighted (blue line). In the lower pad it is shown the ratio between the difference of the previous histograms and their uncertainties. The first plot is displayed in the 0-1500 keV energy region while the second is in the 1500-3000 keV range.

USC UNIVERSIDADE DE SANTIAGO DE COMPOSTELA

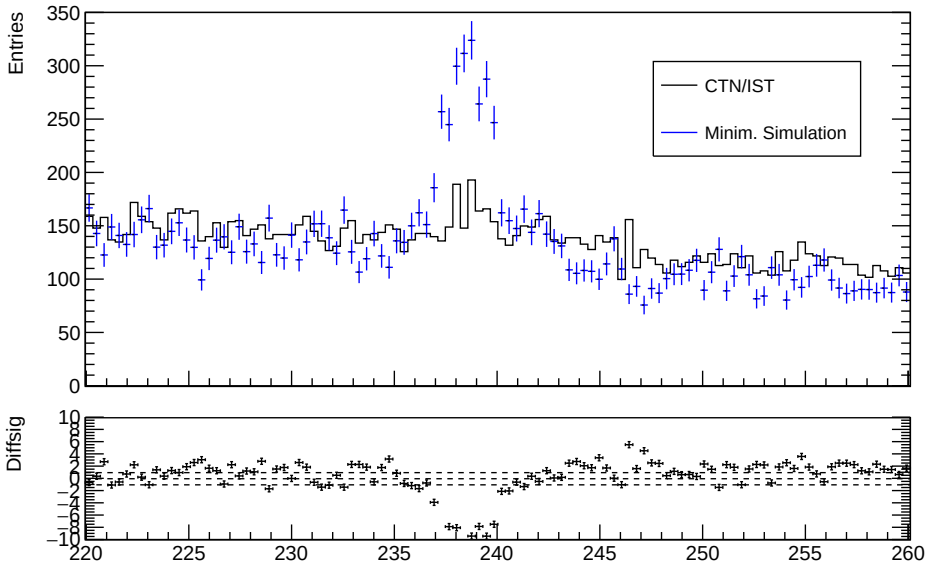

Figure 5.31: Thorium peak at 238,320 keV overestimated by the simulation fit. In the upper pad it is represented the CTN/IST data (black line) against its simulation including all contributions weighted (blue line). In the lower pad it is shown the ratio between the difference of the previous histograms and their uncertainties.

USC UNIVERSIDADE DE SANTIAGO DE COMPOSTELA

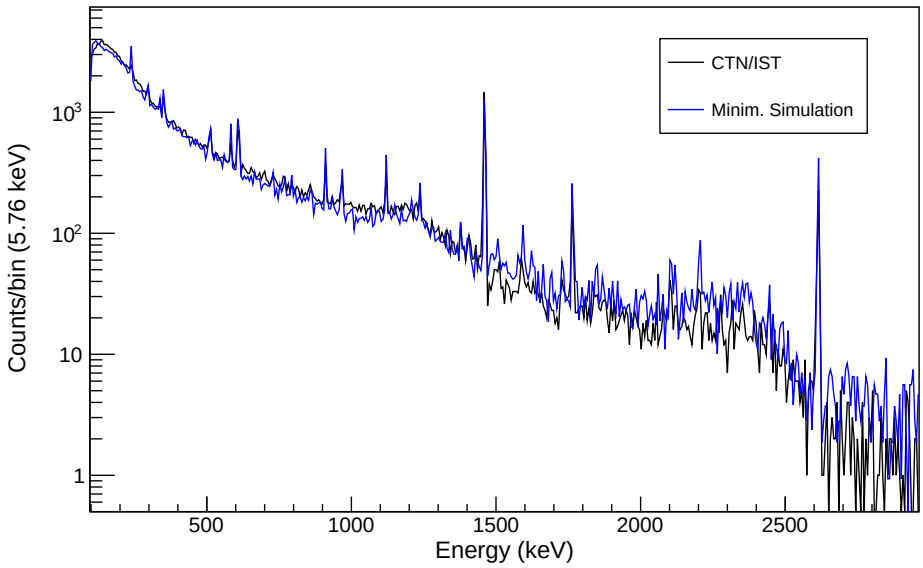

Figure 5.32: Environmental radiation spectra of the CTN/IST laboratory. The black line represents the measured data while the blue line is the minimization of the simulation (weighted).

USC UNIVERSIDADE DE SANTIAGO DE COMPOSTELA

5.2.2.2 UBI Data Simulation

Using the same procedure as in the previous section, we have simulated the environmental radiation measured in the laboratory of Universidade da Beira Interior.

In this case, the geometry only includes an HPGe with a smaller active volume situated vertically. The detector real dimensions were not well known at the moment of the data simulation. As a result, the shape of the potassium Compton and the size relation between this Compton and the potassium photopeak were used as a reference in order to calculate the active volume of this detector. This is possible because the potassium component is predominant and it shapes the final aspect of the spectrum as we can observe in Figure 5.33. Different active volumes were examined until reaching the conclusion that it has a 24 % less active volume compared to the CTN/IST detector. In addition, for the radioactive series a block of earth of 7 cm of thickness was placed below the detector and it was calculated in the same way as in the previous case. Gamma rays have been sent isotropically covering the upper semiesphere from a square area of 20 cm by 20 cm at 30 cm under the detector using the corresponding generators. A number of simulated events were determined for each nuclear decay, for instance, the total amount for the uranium series was $1,35 \times 10^8$ events and 10^8 events for the potassium decay.

Cosmic rays showers were simulated using the same criteria but changing the parameters of the location (40,28106° latitude and 0 m altitude[5]) and date (on the 11th of February of 2019). In this situation, the required number of simulated cosmic rays was lower, 10^7 events, maybe because the upper stores or the roof materials in the laboratory of Universidade da Beira Interior were thicker or made with more absorbent materials.

Once all the simulations were done, we applied the resolution function of the UBI detector (Figure 4.24) in order to reproduce a realistic response.

As we have explained in the previous section, the minimization fit was carried out in two different regions: at high energies where the parameter of the cosmic rays contribution was established and at low-to-intermediate energies where the parameters of the uranium, thorium and potassium were obtained. All these parameters are presented in Table 5.10. In the present case, the χ^2 and $\chi^2_{reduced}$ values are higher than in CTN/IST due to the fact that there are more points of discrepancy between the simulation and the measured data, although Figure 5.34 shows a reasonable agreement between both. As we have just mentioned, the effective size of the UBI detector is in

[5]UBI is placed at Covilhã with an altitude between 450-800 m, however, CRY program has only three altitude options at 0, 2100 and 11300 m. For this reason, we chose 0 m.

USC UNIVERSIDADE DE SANTIAGO DE COMPOSTELA

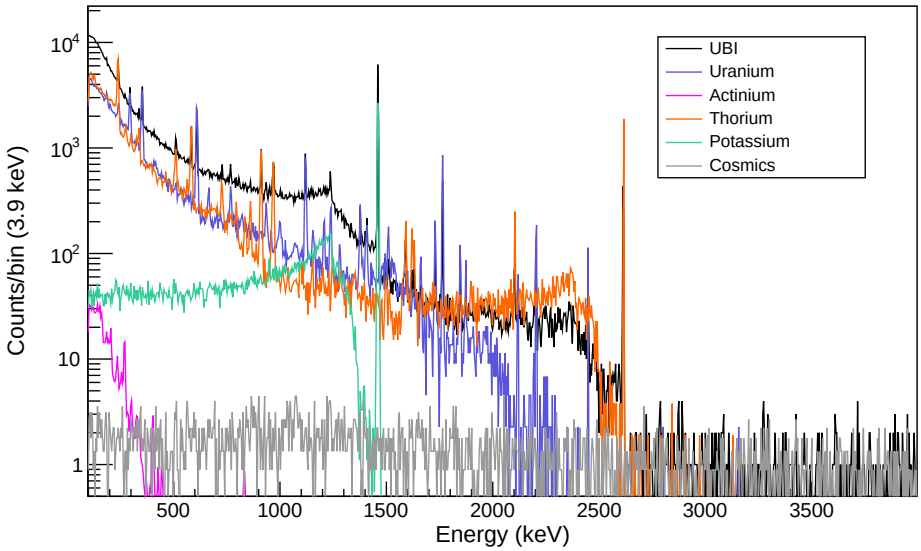

Figure 5.33: Background spectra of the Universidade da Beira Interior, the measured data is highlighted in black and all simulated components already weighted are displayed in different colors.

less control and it affects the simulation results. In Figure 5.33 are plotted the simulated inputs after the application of their associated weights.

The same verification method has been used, TRatioPlot ROOT class, and it is displayed in the lower part of Figures 5.35 and 5.36. It shows the ratio between the difference of the real and simulated data (the residuals) and their uncertainties. Figure 5.35 exposes the results of the first minimization stage at high energies, while Figure 5.36 check the final result of the simulation where are included all weighted components. The majority of the points are around zero in both cases meaning the high degree of agreement, although, in the second case there are some mismatching points mostly at low energies. Diverse adjustments and configurations were tried out in order to reduce such discrepancies, such as applying more weight to some components or modifying the detector's physical appearance. However, these changes led to unfit other regions, for instance if the uranium and thorium chains were fitted at the 200 to 500 keV region the more energetic region (>1000 keV) was completely mismatched.

These discrepancies may have diverse possible origins: although a detailed study about the physical characteristics of the detector was carried out, they were not completely under control and this could be an important cause of mismatching; moreover, the detector resolution in this case was worse than

USC UNIVERSIDADE DE SANTIAGO DE COMPOSTELA

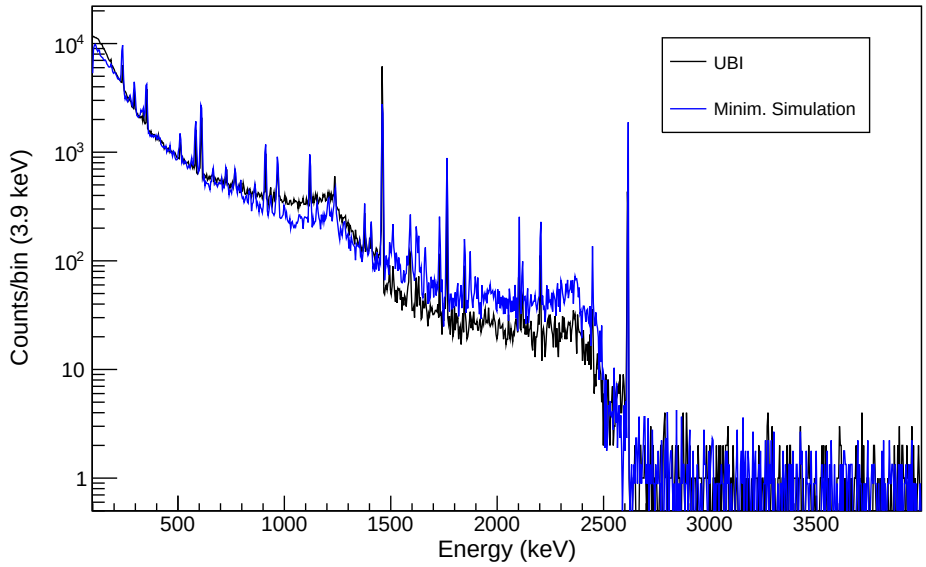

Figure 5.34: Environmental radiation spectra of the Universidade da Beira Interior laboratory. The black line represents the measured data and the blue line the simulation after the minimization procedure (weighted).

in previous case, as a result, it was not possible to reach the same simulation accuracy; another possibility was that the detector was placed next to an element that induce more gamma emissions at low energies (for example, a metallic shielding) and that this element is not included in the geometry setup affecting the simulation results; on the other hand, X-rays from the surrounding materials induced mostly by cosmic rays and electronic noise were not included in the simulation.

As in the previous case, we can not calculate the activities of each radioactive series due to the fact that the exact position of the emitting nucleus is unidentified. However, we can relate the uranium and thorium activities following Eq. 5.6 and assuming that the radionucleus are placed in the same positions. Thus, taking the results of the simulation and the fit parameters of Table 5.10 the quotient of activities is:

$$\frac{A_U^s}{A_{Th}^s} = \frac{D_U \cdot P_U \cdot \varepsilon}{D_{Th} \cdot P_{Th} \cdot \varepsilon} = \frac{120597 \cdot 2,272}{147911 \cdot 1,895} = 0,98. \tag{5.7}$$

The results shown in the activity ratio calculations of both laboratories confirm the conclusion reached in the temporal analysis where the proportions between the uranium and thorium series in the UBI and in the

USC UNIVERSIDADE DE SANTIAGO DE COMPOSTELA

CTN/IST were the quite similar.

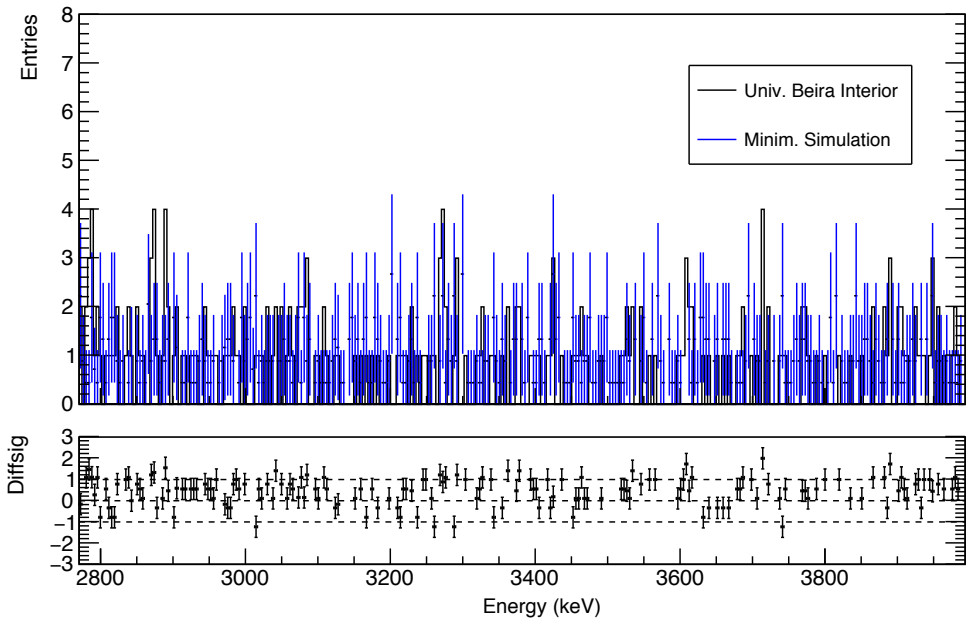

Figure 5.35: In the upper pad it is represented the Universidade da Beira Interior data (black line) against its simulation at high energy region including only cosmic rays simulation weighted (blue line). In the lower pad it is shown the ratio between the difference of the previous histograms and their uncertainties.

USC UNIVERSIDADE DE SANTIAGO DE COMPOSTELA

Table 5.10: Numerical values of the weighted parameters after TMinuit fit for the simulations of the background of Universidade da Beira Interior. They have been calculated in two steps: the first one determines the cosmic rays parameter at high energy values and in the second stage the rest of the parameters are resolved in the low-to-intermediate energy region.

Energy Region (keV)	**Uranium param**	**Actinium param**	**Thorium param**	**Potassium param**	**Cosmic Rays param**	χ^2	$\chi^2_{reduced}$
2630-3000					0,45(4)	110,6	0,3
100-1500	2,272(13)	1044,95(6)$\times$ 10^{-5}	1,895(10)	0,551(6)		33107,3	93,5

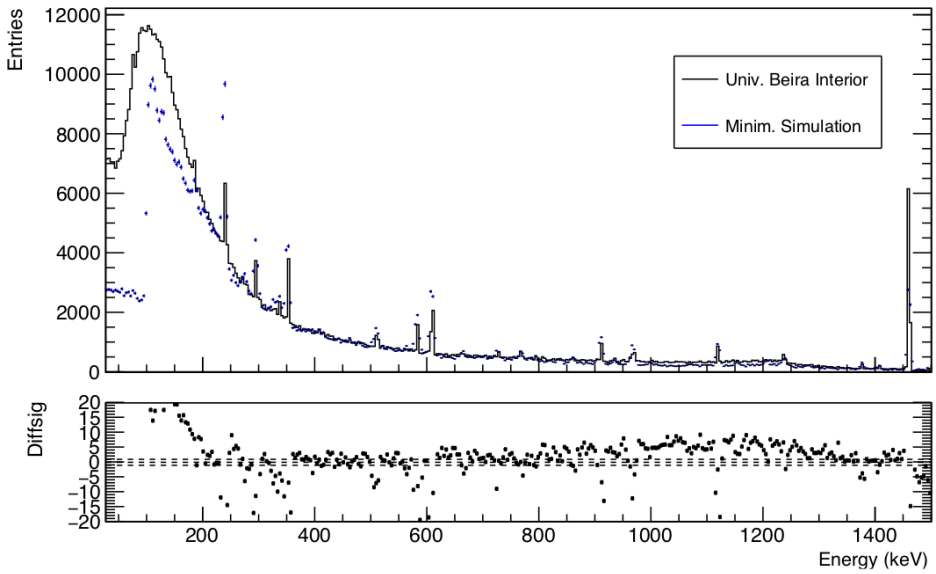

Figure 5.36: In the upper pad it is represented the Universidade da Beira Interior data (black line) against its simulation including all contributions weighted (blue line). In the lower pad it is shown the ratio between the difference of the previous histograms and their uncertainties.

USC UNIVERSIDADE DE SANTIAGO DE COMPOSTELA

Chapter 6

CONCLUSIONS

The present thesis presents a comprehensive work about gamma spectroscopy studies. Motivated by their implementation in the EnsarRoot simulation framework, experiments on two different gamma spectroscopy areas were planned, prepared, executed and analysed, while several simulation and analysis tools were implemented in the EnsarRoot code, allowing for its improvement and expansion. The cornerstone of the program is the possibility to perform accurate simulations from setup and particle generator design, propagation through matter, up to simulated data analysis; as a result, various experiments were conducted and virtually reproduced. Moreover, taking advantage from the fact that the framework treats all data equally, experimental data sets have been analysed using the same analytical tools. This aspect was very useful in order to benchmark simulation results against real findings. The entire work has been centred on gamma spectroscopy using High Purity Germanium semiconductor detectors.

Firstly, gamma emissions coming from low energy ion-induced reactions have been investigated. This is the principle of the PIGE technique, one of the most widely used IBA methods. Data from this technique has been successfully analysed within the EnsarRoot framework and detailed measurements of proton induced gamma emission on stable chlorine isotopes have been performed for the first time. Following the guidelines provided by the IAEA organisation, a standarless analysis has been conducted which implies to carry out two IBA techniques at the same time: RBS and PIGE. With RBS method the backscattered protons by the high-Z nuclei were measured and with PIGE the gamma rays emitted from low-Z nuclei were detected. This procedure allowed to eliminate systematic uncertainties from the measurements.

The experiments were performed at the CTN/IST facility in Lisbon (Portugal), more specifically in the nuclear reaction line of the electrostatic Tan-

USC
UNIVERSIDADE
DE SANTIAGO
DE COMPOSTELA

dem accelerator. The low energy proton interactions between 2,38 and 3,49 MeV on the two stable isotopes of chlorine, ^{35}Cl and ^{37}Cl, were investigated and gamma yields and reaction probabilities were measured for the first time. The differential cross sections measured were:

- E_γ=1219,3 keV from $^{35}\mathrm{Cl}(\mathrm{p},\mathrm{p}'\gamma_{10})^{35}\mathrm{Cl}$;
- E_γ=1763,13 keV from $^{35}\mathrm{Cl}(\mathrm{p},\mathrm{p}'\gamma_{20})^{35}\mathrm{Cl}$;
- E_γ=2230,49 keV from $^{35}\mathrm{Cl}(\mathrm{p},\alpha\gamma_{10})^{32}\mathrm{S}$;
- E_γ=1726,4 keV from $^{37}\mathrm{Cl}(\mathrm{p},\mathrm{p}'\gamma_{10})^{37}\mathrm{Cl}$;
- E_γ=2127,499 keV from $^{37}\mathrm{Cl}(\mathrm{p},\alpha\gamma_{10})^{34}\mathrm{S}$;
- E_γ=1409,79 keV from $^{37}\mathrm{Cl}(\mathrm{p},\mathrm{n}\gamma_{10})^{37}\mathrm{Ar}$;
- E_γ=1611,24 keV from $^{37}\mathrm{Cl}(\mathrm{p},\mathrm{n}\gamma_{20})^{37}\mathrm{Ar}$.

These measurements are of high quality, since they have been carried out with general uncertainties of less than 7 % and they show a great level of detail. Previous data is almost non-existent, and these contributions improve and expand them widening the current database. Only one differential cross section could have been compared with another work and they reasonably agree, although, they are measured at different energy ranges.

Aiming to include the PIGE technique into the EnsarRoot program, the experimental setup was developed and the respective simulations performed. One important parameter obtained from simulation results was the efficiency of the HPGe detector because its accuracy in energy and its uncertainty was reduced. This approach was also within IAEA recommendations. Simulations were also useful to address the real source-to-detector distance.

In order to perform the above-mentioned experiments, natural chlorine targets on a silver backing were produced for the first occasion on the Target Laboratory of FCUL/LIP. Afterwards, they were characterized, analysing their composition and thickness, by RBS technique at the Van der Graff laboratory of CTN/IST. For this evaluation, the widely used SIMNRA program was employed. Their thickness around 0,825 μm were adequate to be considered as thin targets and the chlorine concentration was adequate to have good statistics.

Laboratory measurements have contributed to the ion beam community with new low energy differential cross sections and gamma yields. These breakthrough measurements will also be valuable to address the gaps of

USC UNIVERSIDADE DE SANTIAGO DE COMPOSTELA

knowledge in astrophysical calculations. Further research is needed to investigate the chlorine behaviour in the energy ranges not covered by this work in order to complete the literature and explore other channels.

Complementarily, another line of investigation included in this work was the environmental gamma ray radiation. In order to implement it within the EnsarRoot program, different base classes were developed. Initially, a set of event generators which reproduce the bulk of environmental radiation present on Earth were created: the Environmental Radiation EnsarGenerators simulate the three natural radioactive decay series (^{238}U, ^{235}U and ^{232}Th) and the Potassium Decay EnsarGenerator the potassium decay and de-excitation of its daughter nucleus. It required an exhaustive study on all decays forming part of the natural background and the gamma cascades emitted in each de-excitation. Moreover, taking advantage of the Cosmic Rays EnsarGenerator already developed within the framework, cosmic rays showers were reproduced by creating and propagating the output of the CRY software library.

Experimentally, natural sources of radiation have been studied by measuring environmental background at three locations on the west part of Iberian Peninsula which have diverse subsoil compositions. The selected sites were CTN/IST facility in a near-shore environment in Lisbon (Portugal), UBI installations in a mountainous setting in the central part of Portugal and USC laboratory placed at a valley city in the north of Spain. Natural background spectra of each location was analysed individually and the measurements were compared between them in order to identify variations. These comparisons were possible because the measurements were done with similar germanium detectors. It was observed that the amount of natural radiation in UBI was more than two orders of magnitude greater than in CTN/IST.

Moreover, two radioactive series (uranium and thorium) and potassium decay were distinguishable and their evolution over time was studied. It could not be established any correlation between concentration fluctuations on any series and environmental factors, such as temperature, night-day influence or ventilation patterns. This conclusion agrees with many studies, which also could not establish any connection. Consequently, this research subject is still under investigation and debate.

These background measurements were simulated (and analysed) within the EnsarRoot program. For this purpose, the experimental setups were recreated with great detail. In order to adjust the simulations, different detector parameters were investigated. Moreover, making the adjustments between the simulated radioactive components and the experimental data was a laborious and difficult task, since there were many sensitive variables that were misadjusted at the slightest variation. The final benchmark study

USC UNIVERSIDADE DE SANTIAGO DE COMPOSTELA

between simulations and gathered data showed a great level of agreement. The simulations for the UBI location were less accurate because there were more factors uncontrolled.

Moreover, our findings confirm that the relative activities between uranium and thorium series are similar in both laboratories. This conclusion was obtained in the activity ratio calculations and also in the temporal analysis.

These studies will have a great impact on diverse branches of knowledge. It was the first time that a long term background spectrometry study is carried out at a local level on the western part of the Iberian Peninsula. It is also a pioneering investigation that analyses natural radiation from a simulation perspective, by simulating its emission and its mechanism of detection and posteriorly comparing it with gathered data for these detectors. In particular, the CTN/IST background study was also profitable to interpret PIGE gamma data.

Gamma ray applications have definitely been included in EnsarRoot and data from diverse spectroscopy studies have been analysed and benchmarked with simulated data. This work has prepared the pave for future detailed measurements and open new possibilities.

USC UNIVERSIDADE DE SANTIAGO DE COMPOSTELA

Resumen de la Tesis

Espectroscopía Gamma

La espectroscopía gamma estudia las radiaciones gamma y sus interacciones con la materia y se basa en la medida de la energía y la cuantificación de la intensidad de cada rayo gamma [4]. La espectroscopía gamma juega un papel importante en muchos campos, desde el análisis biológico y de materiales hasta la investigación más avanzada. Una de las principales ventajas de esta técnica analítica es que permite la identificación simultánea de fotopicos provenientes de distintas fuentes radiativas. Esta identificación es posible gracias a que las energías gamma de cada núcleo son únicas. Además, la alta precisión de esta técnica permite estudiar propiedades relevantes de los núcleos.

Este trabajo está basado en estudios de espectroscopía gamma utilizando detectores semiconductores de germanio de alta pureza con unas características similares. En concreto, se abordaron dos líneas de investigación diferentes: por un lado, se investigaron las emisiones gamma provenientes de interacciones de protones a baja energía con los dos isótopos estables de cloro, ^{35}Cl y ^{37}Cl; y la otra línea de investigación de esta tesis es el estudio de la radiación ambiental.

El programa EnsarRoot

Todas las investigaciones anteriores se desarrollaron dentro del programa EnsarRoot [10, 19, 20]. EnsarRoot es un software orientado a objetos que incluye simulaciones, reconstrucciones y análisis de datos experimentales dentro del mismo entorno de trabajo. Una parte importante de esta tesis fue el desarrollo de este código con el fin de implementar las investigaciones anteriores. En dicha expansión se han incluido las simulaciones de los *setups* experimentales y distintos generadores de fuentes gamma. Una gran ventaja de este programa es que todos los datos, independientemente de su

USC
UNIVERSIDADE DE SANTIAGO DE COMPOSTELA

origen, pueden analizarse y manipularse utilizando las mismas herramientas y rutinas, evitando así sesgos adicionales. Como resultado, los datos experimentales se evaluaron y compararon con datos simulados y estos resultados fueron útiles para abordar algunas variables desconocidas.

Secciones Eficaces Diferenciales de los Isótopos ^{35}Cl y ^{37}Cl

Técnicas IBA: PIGE y RBS

La primera línea de investigación está basada en el estudio de la interacción de los dos isótopos estables del cloro y protones a bajas energías mediante mediciones de espectros gamma. Esta técnica analítica se la conece como PIGE (Proton Induced Gamma-ray Emission) y es uno de los métodos IBA (Ion Beam Analysis) [72] más utilizados, ya que permite realizar desde estudios medioambientales hasta analizar piezas arqueológicas. Estas técnicas utilizan haces de iónes que interaccionan con la superficie de la muestra mediante reacciones nucleares o Coulombianas y permiten analizar la composición química de esta hasta cientos de micrómetros. La ventaja es que son no-destructivas y altamente sensibles. Existen diferentes métodos IBA según el método de detección que utilizan.

La técnica PIGE emplea haces de protones, deuterones o partículas alfa a bajas energias (en el rango de los MeV) [5]. El mecanismo básico es la formacion de un núcleo compuesto en un estado excitado y la posterior detección de los gammas emitidos durante el proceso de desexcitación. Las reacciones que se producen son puramente nucleares: escátering elástico y reacciones del tipo (p,$\alpha\gamma$), (p,nγ), etc. La principal limitación de esta técnica es que solo se pueden detectar elementos ligeros con un Z<20, que son aquellos con una barrera Coulombiana poco intensa capaz de ser superada por el haz. El método PIGE permite hacer una diferenciación isotópica además de un análisis multielemental siempre y cuando no se porduzcan solapamientos entre fotopicos.

La otra técnica IBA empleada en este trabajo es la RBS (Rutherford Backscattering Spectrometry) [5]. Este método experimental está basado en la detección de las partículas del haz retrodispersadas por la barrera Coulombiana creada por los propios átomos de la muestra. Al igual que en el caso anterior, se utilizan haces de iones ligeros con energías de pocos MeV, pero en este caso no deben superar la barrera Coulombiana. El sistema de detección es colocado en posición contraria a la dirección del haz.

USC UNIVERSIDADE DE SANTIAGO DE COMPOSTELA

Objetivos y Motivación

El objetivo de este estudio era medir por primera vez los gamma *yields* y las secciones eficaces diferenciales de dichas reacciones. Estas investigaciones son de gran inetrés en diversos campos.

A nivel internacional existe un banco de datos creado, el IBNDL [32], donde se recogen datos de referencia para todas las reacciones estudiadas por la técnica PIGE. Se ha observado que existe un déficit de información en la región de transición Z∼18. En concreto, no existe casi ningún estudio sobre las probabilidades de reacción entre los isótopos estables del cloro, ^{35}Cl y ^{37}Cl, y los protones. La única información disponible son gamma *yields* medidos a ciertas energías puntuales [12, 13, 14] y una sección eficaz del canal alfa del ^{37}Cl medida en el rango 1,25-2,15 MeV [15]. En consecuencia, el estudio y análisis de estas reacciones son de gran interés para la comunidad científica que utiliza PIGE como técnica analítica.

Por otro lado, las reacciones investigadas serán de utilidad en el campo de la astrofísica. Los isótopos del cloro se forman en la fase explosiva de la quema de oxígeno del ciclo CNO, ya que tienen un Z menor que el del hierro [17]. Las secciones eficaces estudiadas permitirán explicar las abundancias isotópicas de estos elementos puesto que son resultado de la competición de diversas reacciones de creación y destrucción de núcleos. En particular, el ^{35}Cl contribuye al ciclo SCl de quema de hidrógeno el cual predomina en el proceso rp a bajas temperaturas [18]. Como resultado, la investigación de estos procesos proporciona información para explicar la evolución de la nucleosíntesis en esta región másica [15]. Desde el punto de vista de la estructura nuclear al estudio del ^{37}Cl resulta interesante porque tiene capa cerrada de 20 neutrones.

Metodología Experimental

Las mediciones experimentales se realizaron en las instalaciones del CTN/IST (Lisboa, Portugal) [23]. Es un centro de investigación avanzada que tiene dos laboratorios dedicados a diversas técnicas IBA: un accelerador Van der Graaf con un voltaje de hasta 2,5 MV y un acelerador electrostático Tándem de hasta 3 MV [151].

En el acelerador Van der Graaf se llevaron a cabo los estudios de los blancos de cloro mediante la técnica RBS. En las mediciones se utilizó un haz de iones $^{4}He^{+}$ con una energía de 2 MeV y un detector semiconductor PIPS (RBS1) situado a +165° con respecto a la dirección del haz.

El experimento de PIGE se llevó a cabo en la línea de reacciones nucleares del accelereador Tandem con un haz de iones H^{+} con una energía

USC UNIVERSIDADE DE SANTIAGO DE COMPOSTELA

de entre 2,36 y 3,48 MeV. Asimismo, durante el experimento se ejecutaron dos técnicas IBA en paralelo: PIGE para medir los gammas emitidos por las reacciones nucleares y RBS para medir los protones retrodispersados del haz. Los espectros gamma se midieron con un detector cilíndrico HPGe con dimensiones 3,75 cm de radio por 6,81 cm de longitud situado dentro de una cápsula de aluminio a una distancia de 4,9 cm del centro de la cámara de reacción y a 130° con respecto de la dirección del haz. La distancia centro-detector fue determinada con certeza gracias a las simulaciones de la eficiencia realizadas con el programa EnsarRoot. El detector de partículas empleado para medir el espectro de protones era un detector de semiconductor PIPS (MOVD) situado a un ángulo de 145° y a una distancia de 8,8(1) cm. Estas medidas se realizaron en dos campañas: una en julio del 2019 y otra en enero del 2020.

En ambos experimentos, los blancos se emplazaron en el centro de las cámaras de reacción perpendiculares al haz y utilizando un goniómetro ajustable desde el exterior.

Producción de Blancos

Para llevar a cabo el experimento anterior, se fabricaron blancos de cloro natural utilizando la técnica de deposición térmica en vacío en el Laboratorio de Blancos de FCUL/LIP (Lisboa) [21, 147]. Al ser la primera vez que este tipo de blancos se fabricaban en estas instalaciones se realizaron diferentes pruebas sobre composiciones químicas, tiempos de evaporación, procedimientos a seguir, etc. hasta que al final se optó por realizar un blanco de cloreto de plata sobre un sustrato de plata. Este blanco tenía que cumplir dos características fundamentales: ser un blanco fino para poder calcular secciones eficaces y tener suficiente cantidad de cloro para tener una buena estadística.

La determinación de sus características físcas se realizó mediante la técnica RBS y el programa SIMNRA [75]. El grosor del blanco empleado en las mediciones fue de 0,825(17) μm y los ratios isotópicos entre el cloro y la plata natural:

$$\text{ratio}(^{35}\text{Cl/Ag}) = 1,42(3),$$
$$\text{ratio}(^{37}\text{Cl/Ag}) = 0,455(9).$$

Asimismo, se pudo determinar que la energía perdida por el protón en el blanco fue de entre 11 y 14 keV, que es la principal fuente de incertidumbre a la hora de determinar la energía del haz (6-8 keV).

USC UNIVERSIDADE DE SANTIAGO DE COMPOSTELA

Análisis de Resultados y Conclusiones

En el análisis de espectros gamma se encontraron diferentes fotopicos correspondientes a las reacciones entre el cloro natural y los protones del haz, detalladas en la Tabla 6.1. Podemos observar que el canal neutrónico del ^{37}Cl se abrió debido a que tiene un valor Q de reacción relativamente bajo ($Q = -1596,22$ keV [26]). También se obervaron las aperturas de los canales alfa para ambos isótopos y, como era de esperar, los escáterings elásticos de los protones. Para cada uno de estos fotopicos se calcularon los *yields* en función de la energía del protón. Para realizar este análisis fue fundamental el estudio de la radiación de fondo realizado en la otra línea de investigación de esta tesis que más adelante explicamos debido a que había solapamiento de fotopicos.

Table 6.1: Gammas medidos en el experimento PIGE donde se han estudiado reacciones entre protones y los dos isótopos estables del cloro. Los datos nucleares están extraídos de la NNDC [26].

Energía Gamma (keV)	**Reacción Nuclear**
1219,3(2)	^{35}Cl(p, p$'\gamma_{10}$)^{35}Cl
1763,13(10)	^{35}Cl(p, p$'\gamma_{20}$)^{35}Cl
2230,49(15)	^{35}Cl(p, $\alpha\gamma_{10}$)^{32}S
1726,4(2)	^{37}Cl(p, p$'\gamma_{10}$)^{37}Cl
2127,499(20)	^{37}Cl(p, $\alpha\gamma_{10}$)^{34}S
1409,79(7)	^{37}Cl(p, nγ_{10})^{37}Ar
1611,24(5)	^{37}Cl(p, nγ_{20})^{37}Ar

Por otro lado, se analizaron los espectros de protones retrodispersados (RBS) y se observaron cuatro picos, de derecha a izquierda: uno de plata, uno de cloro, uno de contaminación por carbono depositado en la superfície y un cuarto pico de origen desconocido. Como los protones retrodispersados por la plata son los únicos que han sufrido una interacción puramente Coulombiana y siguen la ecuación de Rutherford, son los únicos *yields* utilizados en el cálculo de las secciones eficaces.

Las secciones eficaces diferenciales para un blanco fino con la ejecución paralela de dos técnicas IBA se calcularon con la siguiente Ecuación 6.1. Debido a la ejecución simultánea de las técnicas RBS y PIGE las medidas realizadas son independientes de la carga del espectro. Durante todo el pro-

USC UNIVERSIDADE DE SANTIAGO DE COMPOSTELA

cedimiento experimental y de análisis se tuvo en cuenta, dentro de lo posible, las recomendaciones y estándares sugeridos por la IAEA [6].

$$\left(\frac{d\sigma}{d\Omega}\right)_{\gamma}(E',\theta) = \frac{1}{4\pi}\frac{\Omega_p \varepsilon_{p,int}}{r\varepsilon_\gamma} \cdot \frac{Y_\gamma(E',\theta)}{Y_{Ag}(E',\phi)} \cdot \left(\frac{d\sigma}{d\Omega}\right)_{Ruth}^{Ag}. \tag{6.1}$$

Esta expresión ya tiene incorporada los parámetros específicos de nuestro experimento: r es el ratio isotópico entre el número de átomos de ^{35}Cl o ^{37}Cl y el número de átomos de Ag en el blanco determinado mediante un análisis RBS; $\varepsilon_{p,int}$ es la eficiencia interna del detector de protones considerada del 100 %; $\Omega_p = 3,65 \times 10^{-3}$ sr es el ángulo sólido de este mismo detector determinado por H. Silva *et al.* en [164, 165] con un 2 % de incertidumbre; ε_γ es la eficiencia absoluta del detector HPGe para cada gamma determinada por las simulaciones; $Y_\gamma(E',\theta)$ es el gamma *yield* medido a una energía del proton E' y detectado a un ángulo θ; $Y_{Ag}(E',\phi)$ es el *yield* de protones retrodispersados por los átomos de Ag medidos a una energía del protón E' y detectados a un ángulo ϕ; por último, $\left(\frac{d\sigma}{d\Omega}\right)_{Ruth}^{Ag}$ representa la sección eficaz diferencial de Rutherford para la plata a la misma energía del protón E' pero en el sistema de referencia centro de masas. La energía E' es la energía del proton incidente E_0 menos la energía perdida en la parte central del blanco y corregida por un shift de unos ± 2 keV en el sistema de referencia del laboratorio.

Como hemos comentado, la eficiencia del detector de germanio ha sido calculada para cada energía E_γ mediante simulaciones precisas del *setup* experimental y de los gammas emitidos, así como todo el mecanismo de detección y respuesta del detector. En consecuencia, el error estimado de la eficiencia ha disminuido al 0,6 % (cuando generalmente es del 7 %). Este procedimiento es uno de los sugeridos por la IAEA.

Las secciones eficaces diferenciales medidas en este experimento corresponden a los gammas detectados de la Tabla 6.1. Para ejemplificar algunas, en la Figura 6.1 está representada la disperción elástica del ^{35}Cl y en la Figura 6.2 está representado el canal alfa del ^{37}Cl. En todas ellas la energía E' es denotada como $E_{p,lab}$. Las incertidumbres de estas medidas son relativamente bajas, alrededor del 7 % y en el peor de los casos se incrementa hasta el 16 %. En particular, la sección eficaz del gamma 2127,499 keV ha podido ser comparada con otra medida anteriormente hecha por Weber *et al.* [15] donde se ha podido comprobar que coinciden en magnitud aunque en rangos de energía del proton distintos.

En este estudio espectroscópico se han realizado medidas detalladas de los gamma *yields* y se han calculado por primera vez las secciones eficaces difer-

USC UNIVERSIDADE DE SANTIAGO DE COMPOSTELA

enciales de las reacciones nucleares a bajas energías entre un haz de protones y los dos isótopos estables del cloro. Estas medidas son de gran calidad, ya que se han conseguido realizar con unas incertidumbres generales inferiores a un 7 %. Estos datos serán de gran útilidad para la cominudad científica, especialmente, para aquellos que empleen la técnica analítica PIGE.

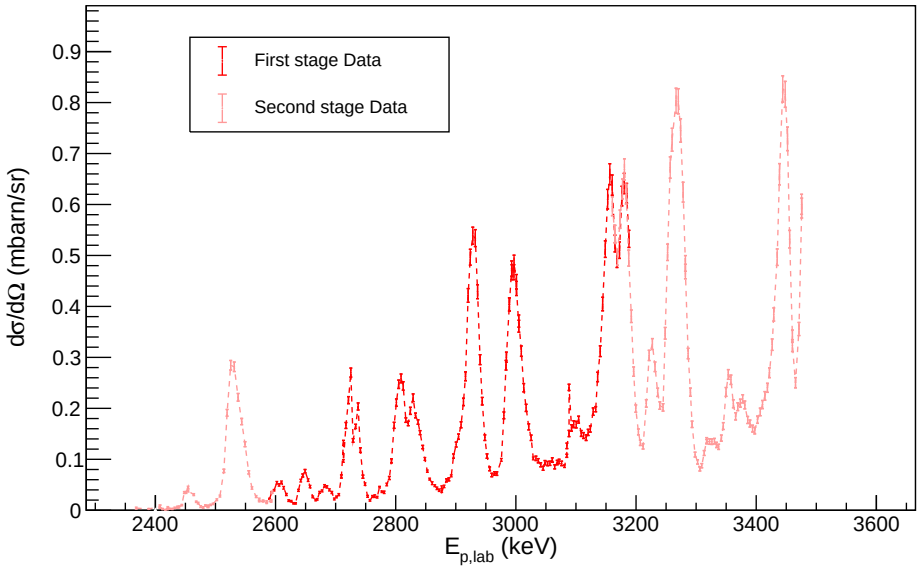

Figure 6.1: Sección eficaz diferencial del gamma 1219,3 keV proveniente de la reacción ^{35}Cl(p, p$'\gamma_{10}$)^{35}Cl en el rango de energías de 2,36-3,48 MeV. Las dos fases del experimento están indicadas en diferentes tonalidades.

USC UNIVERSIDADE DE SANTIAGO DE COMPOSTELA

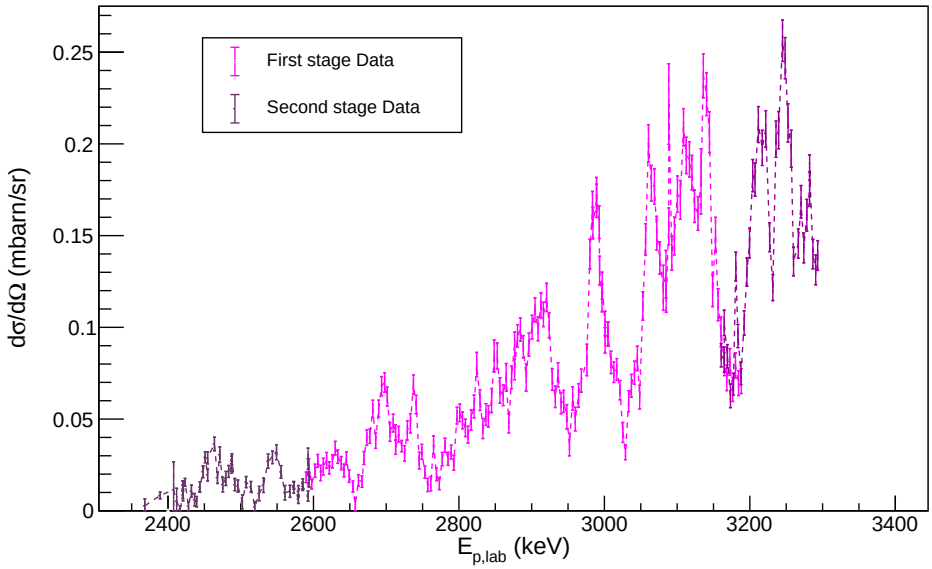

Figure 6.2: Sección eficaz diferencial del gamma 2127,499 keV proveniente de la reacción ^{37}Cl(p, $\alpha\gamma$)^{34}S en el rango de energías de 2,36-3,3 MeV. Las dos fases del experimento están indicadas en diferentes tonalidades.

Estudio de la Radiación Ambiental

La otra línea de investigación de esta tesis es el estudio de la radiación ambiental utilizando espectroscopía gamma, la cual consiste en hacer mediciones de los fotones emitidos por las cadenas de desintegración presentes en la naturaleza y por otras fuentes de radiación natural.

La radiación ionizante natural presente en la Tierra tiene diferentes orígenes: terrestre, que a su vez puede ser primordial (existente desde el origen de los elementos más pesados) o secundaria (derivadas de la desintegración radiactiva de los primordiales) y cosmogénica, creada por la radiación cósmica y su interacción con la materia [112]. Por otro lado, los humanos introdugeron la radiación artificial utilizando técnicas modernas, a esta también se la denomina radiación antropogénica.

Los radionúcleos primordiales que siguen presentes en la Tierra tienen vidas medias, al menos, comparables con la edad del Universo (alrededor de $13,8 \times 10^9$ años [107]). Según el modo de desintegración se clasifican en dos tipos: series o cadenas y desintegraciones individuales.

Una serie radioactiva es un conjunto de radionúcleos inestables generados a partir de la desintegración de un radionúcleo padre y las posteriores

USC UNIVERSIDADE DE SANTIAGO DE COMPOSTELA

desintegraciones de sus núcleos hijos hasta alcanzar un núcleo estable. Las tres cadenas radioactivas todavía presentes en la naturaleza son [26, 112]:

- Serie del torio iniciada por ^{232}Th (vida media de $14,0(1) \times 10^9$ años).
- Serie del uranio iniciada por ^{238}U (vida media de $4,468(3) \times 10^9$ años).
- Serie del actinio iniciada por ^{235}U (vida media de $7,038(5) \times 10^8$ años).

La principal fuente radioactiva que no pertenece a una cadena es el isótopo de potasio ^{40}K que tiene una vida media de $1,248(3) \times 10^9$ años [26]. Este isótopo se desintegra mediante dos modos: β^- y captura electrónica. En este último modo el ^{40}K transmuta a ^{40}Ar emitiendo durante el proceso un gamma de 1460,820(5) keV. Este fotopico y la forma de su dispersión Compton son caracteríticos de cualquier espectro de radiación de fondo.

La otra fuente de radiación natural es la radiación cósmica extraterrestre formada por partículas altamente energéticas [118]. La componente mayoritaria son los radionúcleos cosmogénicos (protones, partículas alfa, iones de carbono, de nitrógeno, etc.) aunque también está compuesta por radiación electromagnética: desde rayos gamma hasta radiofrecuencia, aunque la región de los rayos-X es la más predominante en el espectro. El origen de los rayos cósmicos es extra-galáctico aunque hay una componente que proviene del Sol y que se puede detectar por correlaciones entre ambos. Cuando estos rayos llegan a la atmósfera son aniquilados mediante colisiones con partículas suspendidas creando una cantidad enorme de nuevas partículas másicas, es decir, la energía cinética de los rayos cósmicos primarios es convertida en grandes masas en reposo. Estos productos son conocidos como radiación cósmica secundaria y su principal componente son los piones [112].

Objetivos y Motivación

El principal objetivo de esta parte de la tesis es estudiar estas fuentes radioactivas desde dos aproximaciones: por un lado, hacer mediciones monitorizadas durante largos periodos de tiempo, y, por otro lado, reproducir en simulación estas emisiones y procesos de detección de forma pormenorizada dentro del programa EnsarRoot. Este análisis exhaustivo es de gran relevancia en diferentes ámbitos.

Los seres humanos y otras formas de vida están expuestos a estas radiaciones ionizantes a través de tres formas diferentes: externa, esencialmente de los radionúcleos y los productos de su desintegración (presentes en rocas o en materiales de construcción) y rayos cósmicos; interno, por ingestión de alimentos y agua potable e inhalación de partículas de polvo que contienen

USC UNIVERSIDADE DE SANTIAGO DE COMPOSTELA

productos de la desintegración del uranio (mayoritariamente radón). Estas exposiciones son inevitables y, en altas tasas, pueden causar daños a la salud de los organismos vivos, por ejemplo, la inhalación de radón es la segunda causa de cáncer de pulmón humano [41]. Por consiguiente, cualquier estudio sobre la radiación natural es de gran importancia para la comunidad científica, población y autoridades nacionales.

Desde el punto de vista científico, la radiación natural interfiere en la adquisición de datos de muchos experimentos. En nuestro campo, la espectroscopía gamma, hay un gran número de interferencias espectrales mutuas entre muchos radionúcleos y el gamma *yield* experimental. Este solapamiento, a veces, hace que la diferenciación entre fotopicos sea imposible. En consecuencia, un estudio exhaustivo de la radiación de fondo del laboratorio CTN/IST, donde se llevaron a cabo los experimentos PIGE anteriormente descritos, es de gran utilidad a la hora de analizar los espectros.

Aunque la radiación medioambiental ha sido estudiada en numerosos trabajos [7, 33, 34, 35], no se han encontrado estudios centrados en la monitorización de la radiación en la parte occidental de la Península Ibérica. Además, tampoco se han hallado análisis temporales de las fuentes radioactivas por separado.

Respecto a la simulación de la radiación ambiental, se ha observado un déficit en estudios dónde se simulen las fuentes radioactivas individuales, es decir, reconstruyendo el mecanismo de emisión del gamma y su posterior detección. Igualmente, no se han encontrado trabajos en dónde se comparen mediciones radiológicas y sus correspondientes simulaciones.

Metodología Experimental

Las mediciones experimentales se realizaron en tres enclaves situados sobre regiones con distintas composiciones mineralógicas en la zona oeste de la Península Ibérica. Estas monitorizaciones se realizaron durante largos periodos de tiempo a intervalos de 30 minutos para poder hacer un análisis en función de las variables atmosféricas y horarias. Los detectores empleados en todos los casos eran detectores de germanio con unas características similares.

En Portugal, se realizaron medidas en dos emplazamientos: en las instalaciones del CTN/IST, situadas en un entorno marino cerca de la costa utilizando el mismo detector empleado para las medidas de PIGE, y en el laboratorio de la Universidade da Beira Interior (UBI) [43], ubicado en un entorno montañoso en la parte central del país. En este último laboratorio se empleó un detector de germanio similar en tamaño y forma al anterior. Gracias al estudio realizado con las simulaciones pudimos determinar que el

USC UNIVERSIDADE DE SANTIAGO DE COMPOSTELA

detector de UBI tiene un 24 % menos de volumen activo de detección que el detector del CTN/IST. La electrónica en ambos casos también presentaba unas características similares.

El tercer emplazamiento donde se recogieron medidas fue en el Laboratorio de Análisis de Radiaciones de la Universidad de Santiago de Compostela [44, 45, 162] en la zona noroeste de la Península Ibérica. En este caso, los detectores también eran HPGe (BSI y ORTEC) pero con la particularidad de que estaban recubiertos por un blindaje para evitar interferencias de la radiación de fondo durante su uso diario. Por este motivo, no se pudo realizar un análisis apropiado, ya que muchos fotones, sobre todo de bajas energías, son absorbidos por las paredes del blindaje. Sin embargo, estas medidas nos han permitido entender el comportamiento de la radiación cósmica ya que las medidas se realizaron con las tapas de apertura superiores abiertas.

Simulaciones de la Radiación Ambiental

Como hemos mencionado antes, el *framework* EnsarRoot es la herramienta clave para realizar estos estudios. Este programa ha sido expandido para incluir unos generadores de rayos gamma que reproducen las desintegraciones de los núcleos de las tres cadenas radioactivas y emiten los fotones producidos en las desexcitaciones nucleares. También fue desarrollado un generador que reproduce la desintegración del potasio. Una vez realizadas las simulaciones a nivel individual de cada radionúcleo, todas las simulaciones pertenecientes a la misma cadena fueron juntadas en un único fichero para poder tratar toda la cadena como un conjunto (suponiendo que no hubo ninguna disrupción en la serie). Las diferentes componentes simuladas pueden apreciarse en la Figura 6.3.

Las simulaciones de la radiación cósmica se realizaron en dos etapas: primero con el programa de simulación CRY [168], ampliamente utilizado, se simularon las cascadas de rayos cósmicos utilizando una configuración concreta (latitud, altitud, composición, etc.); y posteriormente, estos datos fueron simulados dentro del programa EnsarRoot mediante un generador que ya había sido previamente desarrollado.

Por otro lado, los *setups* experimentales donde se realizaron las medias fueron simulados con gran detalle. En todos los *setups* simulados se tuvo que incluir un bloque compuesto por un material terroso debajo del detector para atenuar los fotones de las series radioactivas.

USC UNIVERSIDADE DE SANTIAGO DE COMPOSTELA

Análisis de Resultados y Conclusiones

Hemos analizado los espectros ambientales de cada lugar individualmente identificando los fotopicos que aparecen y sus orígenes. Posteriormente, se hizo una comparación entre las distintas medidas para identificar vairaciones. Se pudo observar que la cantidad de radiación ambiental en UBI es dos órdenes de magnitud mayor que la del CTN/IST. Este resultado es coherente con la composición del subsuelo en ambas localidades (consultar Figuras 2-34 de [109]). Además en los espectros hemos podido distinguir dos series radiactivas (la del uranio y la del torio) y el decaimiento del ^{40}K. Desafortunadamente, los fotopicos de la serie de actinio no pudieron ser identificados en ninguno de los casos porque su intensidad es muy baja y porque el fotopico más relevante está situado a bajas energías donde dominan los rayos-X y el ruido producido por la electrónica.

Análisis Temporal

Gracias a que las medidas experimentales se recogieron a intervalos de tiempo cortos, se pudo realizar un análisis temporal. Para poder comparar las concentraciones de las componentes del fondo ambiental por separado, se eligió un fotopico de referencia para cada contribución radioactiva natural (Tabla 6.2). Normalmente, los picos más visibles se encuentran a energías intermedias-altas, ya que se evitan gran parte de las contribuciones Compton, rayos-X, etc. que predominan a bajas energías.

Table 6.2: Fotopicos utilizados como referencia para cada contribución de la radiación ambiental. Los datos nucleares están extraídos de la NNDC [26].

Componente Radiación Ambiental	**Núcleo Padre**	**Fotopico de Referencia (keV)**
Decaimiento del Potasio	^{40}K	1460,849(5)
Cadena del Uranio	^{214}Bi	1764,494(14)
Cadena del Torio	^{208}Tl	2614,533(13)

En primer lugar, se analizaron los datos por días completos y se compararon las evoluciones a lo largo de las semanas. Posteriormente, los mismos datos fueron analizados siguiendo otro criterio, calculando el valor medio por hora para poder identificar algún patrón relacionado con el incremento de temperatura al mediodía, diferenciación día-noche o rutinas de ventilación en el laboratorio. Estos estudios se realizaron para cada componente del fondo

USC UNIVERSIDADE DE SANTIAGO DE COMPOSTELA

radioactivo. En todas las gráficas se pueden observar fluctuaciones, pero no se ha podido establecer ninguna correlación entre estas variaciones y factores ambientales debido a que siguen patrones complejos. Esta conclusión coincide con algunos estudios donde tampoco se pudo establecer ninguna conexión [66, 67].

Por último, se calcularon las tasas promedio totales de cada componente y las relaciones entre ellas. El resultado más destacado es la gran cantidad de potasio presente en los materiales del laboratorio UBI, casi cuatro veces la cantidad de potasio en el CTN/IST. Una posible explicación a este resultado es la proximidad de las paredes al detector de UBI.

Simulaciones de la Radiación Ambiental

Los espectros de radiación de fondo de los laboratorios CTN/IST y UBI fueron simulados dentro del programa EnsarRoot utilizando los generadores de gammas y los *setups* simulados anteriormente explicados.

En la Figura 6.3 se pueden apreciar todas las componentes radioactivas por separado junto con un espectro de fondo ambiental del laboratorio CTN/IST. Podemos observar que la forma del fondo natural es una convolución entre el fotopico del potasio junto con su dispersión Compton (línea verde) y que las series del torio y del uranio contribuyen significativamente a bajas energías (líneas naranja y azul). Por el contrario, la señal del actinio es casi imperceptible (línea rosa). La radiación cósmica es una constante en todo el espectro contribuyendo más a la zona de bajas energías (línea gris). Todas estas componentes fueron ponderadas comparándolas con datos experimentales. Para este fin, se utilizaron varias classes de ROOT: TMinuit para calcular el valor del χ^2 y obtener los valores óptimos de la ponderación y TRatioPlot como método de verificación para comparar la simulación final (incluyendo las componentes pesadas) y los datos medidos experimentalmente.

La Figura 6.3 ya muestra estas componentes pesadas. El espectro final de la simulación (línea azul) junto con los datos reales (línea negra) se muestra en la Figura 6.4. Ambos espectros muestran un elevado grado de concordancia en casi todo el rango energético.

Este mismo estudio se realizó a los datos de radiación ambiental del laboratorio UBI. En este caso, las simulaciones fueron más grandes, ya que la cantidad de radiación ambiental era mayor. Siguiendo los mismos procedimientos que en el caso anterior, se obtuvo una simulación del fondo (recopilando todas las componentes por separado ya pesadas) con un alto nivel de coincidencia con los datos experimentales.

En general, ambas simulaciones son muy precisas y reproducen muy bien

USC UNIVERSIDADE DE SANTIAGO DE COMPOSTELA

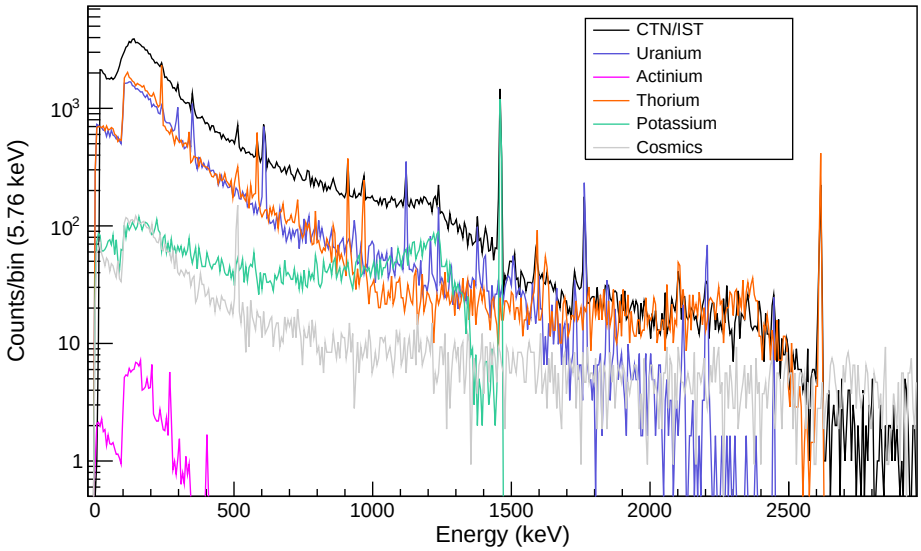

Figure 6.3: Espectro experimental de la radiación ambiental del CTN/IST medido durante un intérvalo de tiempo de 30 minutos (línea negra) y todas sus componentes simuladas y ponderadas.

los espectros de los datos experimentales. Cabe destacar que a bajas energías el nivel de concordancia es menor debido a que no se han incluido rayos-X ni el efecto del ruido electrónico. La simulación de la radiación ambiental del CTN/IST es más definida que la del UBI porque en esta última había más parámetros *a priori* desconocidos, como el volumen activo de detección y puede que algún elemento del *setup* que no se haya incluído en las simulaciones.

Por último, se calcularon las actividades relativas entre las series del uranio y del torio en los dos laboratorios y nuestros resultados confirman que son similares en ambos. Esta conclusión también se obtuvo en el análisis temporal.

En este estudio espectroscópico ambiental se ha realizado un análisis pormenorizado de cada fuente radioactiva, tanto a nivel experimental, analizando sus componentes y su evolución a lo largo del tiempo; como a nivel de simulación, donde se han recreado todas las fuentes que contribuyen a la radiación ambiental y que han sido ajustadas a las mediciones experimentales para analizar su contribución real a este fondo. Además las simulaciones han servido para determinar algunos parámetros imprecisos. Los ajustes entre las componentes simuladas y los datos experimentales han sido una tarea compleja y laboriosa porque había muchas variables sensibles que se desajustaban

USC UNIVERSIDADE DE SANTIAGO DE COMPOSTELA

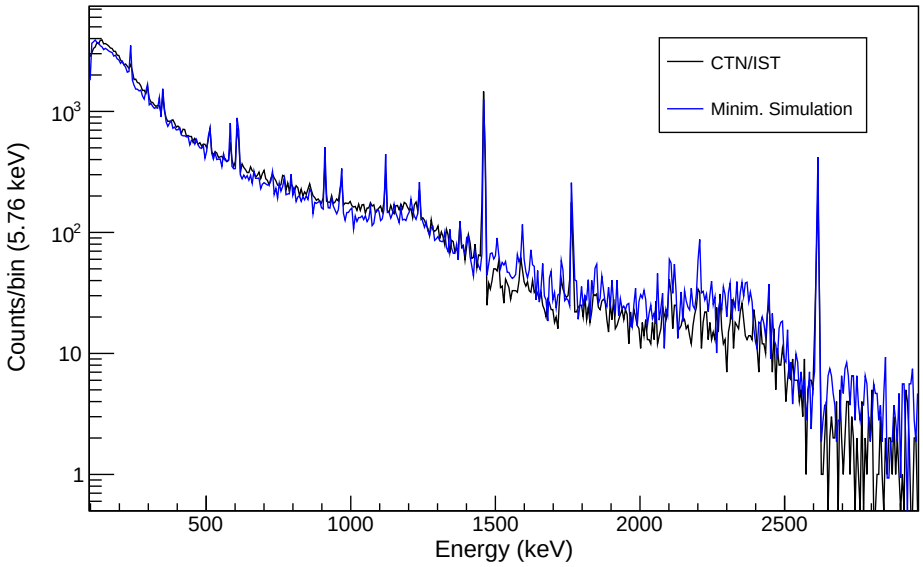

Figure 6.4: Espectro de la radiación ambiental del CTN/IST medido durante un intérvalo de tiempo de 30 minutos (línea negra) y su simulación ponderada (línea azul).

a la mínima variación.

Este análisis también ha resultado útil a la hora de estudiar los espectros de rayos gamma del experimento de PIGE porque nos permitió distinguir solapamientos entre fotopicos e incluso pudimos calibrar el detector a más altas energías mediante los fotopicos ambientales. Asimismo, este estudio puede resultar útil para futuros experimentos realizados en las mismas instalaciones o para otros experimentos con características similares.

USC
UNIVERSIDADE DE SANTIAGO DE COMPOSTELA

Resumo da Tese

A espectroscopia gamma estuda a radiación gamma e as súas interaccións coa materia e baséase na medida da enerxía e na cuantificación de intensidade de cada raio gamma [4]. A espectroscopia gamma xoga un papel importante en moitos campos, desde materiais e análises biolóxicas ata a investigación máis avanzada. Unha das principais vantaxes desta técnica analítica é que permite a identificación simultánea de fotopicos de diferentes fontes radiativas. Esta identificación é posible porque as enerxías gamma de cada núcleo son únicas. Ademais, a alta precisión desta técnica permite estudar propiedades relevantes dos núcleos.

Este traballo baséase en estudos de espectroscopia gamma utilizando detectores de semicondutores de xermanio de alta pureza con características similares. En concreto, abordáronse dúas liñas de investigación diferentes: por unha banda, investigáronse as emisións gamma das interaccións de protóns de baixa enerxía cos dous isótopos estables do cloro, ^{35}Cl y ^{37}Cl; e a outra liña de investigación desta tese é o estudo da radiación ambiental.

O programa EnsarRoot

Todas as investigacións anteriores desenvolvéronse dentro do programa EnsarRoot [10, 19, 20]. EnsarRoot é un software orientado a obxectos que inclúe simulacións, reconstrucións e análise de datos experimentais dentro do mesmo ambiente de traballo. Unha parte importante desta tese foi o desenvolvemento deste código co fin de implementar investigacións previas. Nesta expansión, incluíronse as simulacións dos *setups* experimentais e diferentes xeradores de fontes gamma. Unha gran vantaxe deste programa é que todos os datos, independentemente da súa orixe, poden ser analizados e manipulados utilizando as mesmas ferramentas e rutinas, evitando así sesgos adicionais. Como resultado, os datos experimentais foron avaliados e comparados con datos simulados e estes resultados foron útiles para abordar algunhas variables descoñecidas.

USC
UNIVERSIDADE DE SANTIAGO DE COMPOSTELA

Seccións Efectivas Diferenciais dos Isótopos ^{35}Cl y ^{37}Cl

A primeira liña de investigación baséase no estudo da interacción dos dous isótopos estables do cloro e dos protóns a baixas enerxías mediante medicións espectrales gamma. Esta técnica analítica coñécese como PIGE (Proton Induced Gamma-ray Emission) e é un dos métodos IBA (Ion Beam Analysis) [72] máis utilizado xa que permite realizar a partir de estudos ambientais para analizar pezas arqueolóxicas. Estas técnicas utilizan feixes iónicos que interactúan coa superficie da mostra mediante reaccións nucleares ou de Coulomb e permiten a análise da súa composición química ata centos de micrómetros. A vantaxe é que son non destrutivos e altamente sensibles. Existen diferentes métodos de IBA dependendo do método de detección que utilicen.

A técnica PIGE usa feixes de protóns, deuterones ou partículas alfa a baixas enerxías (no rango MeV) [5]. O mecanismo básico é a formación dun núcleo composto en estado excitado e a posterior detección das gammas emitidas durante o proceso de desexcitación. As reaccións que teñen lugar son puramente nucleares: escátering elástico e reaccións do tipo (p,$\alpha\gamma$), (p,nγ), etc. A principal limitación desta técnica é que só se poden detectar elementos lixeiros cun Z<20, que son aqueles cunha barreira coulombiana de baixa intensidade susceptible de ser superada polo feixe. O método PIGE permite unha diferenciación isotópica así como unha análise multielemental sempre que non haxa solapamentos entre fotopicos.

A outra técnica IBA utilizada neste traballo é RBS (Rutherford Backscattering Spectrometry) [5]. Este método experimental baséase na detección das partículas do feixe retrodispersadas pola barreira de Coulomb creada polos propios átomos da mostra. Como no caso anterior, utilízanse feixes de ións lixeiros con enerxías duns poucos MeV, pero neste caso non deben superar a barreira de Coulomb. O sistema de detección colócase na posición oposta á dirección do feixe.

Obxectivos e Motivación

O obxectivo deste estudo foi medir por primeira vez os gamma *yields* e as seccións efectivas diferenciais destas reaccións. Estas investigacións son de gran interese en diversos campos.

A nivel internacional creouse unha base de datos, a IBNDL [32], onde se recollen datos de referencia de todas as reaccións estudadas pola técnica PIGE. Observouse que existe un déficit de información na rexión de transición Z∼18. En concreto, case non hai estudos sobre as probabilidades de

USC UNIVERSIDADE DE SANTIAGO DE COMPOSTELA

reacción entre os isótopos estables do cloro, ^{35}Cl y ^{37}Cl, e os protóns. A única información dispoñible é os gamma *yields* medidos en determinadas enerxías puntuales [12, 13, 14] e unha sección transversal da canle alfa do ^{37}Cl medido no intervalo de 1,25-2,15 MeV [15]. En consecuencia, o estudo e análise destas reaccións son de grande interese para a comunidade científica que utiliza PIGE como técnica analítica.

Por outra banda, as reaccións investigadas serán útiles no campo da astrofísica. Os isótopos do cloro fórmanse na fase explosiva da combustión do osíxeno do ciclo CNO xa que teñen unha Z inferior á do ferro [17]. As seccións efectivas estudadas permitirán explicar as abundancias isotópicas destes elementos xa que son o resultado da competición de diversas reaccións de creación e destrución de núcleos. En particular, o ^{35}Cl contribúe ao ciclo SCl de combustión do hidróxeno que predomina no proceso rp a baixas temperaturas [18]. Como resultado, a investigación destes procesos proporciona información para explicar a evolución da nucleosíntese nesta rexión de masas [15]. Dende o punto de vista da estrutura nuclear, o estudo do ^{37}Cl é interesante porque ten unha capa pechada de 20 neutróns.

Metodoloxía Experimental

Realizáronse medicións experimentais nas instalacións do CTN/IST (Lisboa, Portugal) [23]. Trátase dun centro de investigación avanzada que conta con dous laboratorios dedicados a diversas técnicas IBA: un acelerador Van der Graaf cunha tensión de ata 2,5 MV e un acelerador electrostático Tandem de ata 3 MV [151].

No acelerador Van der Graaff realizáronse os estudos de brancos de cloro mediante a técnica RBS. Nas medicións, un feixe de $^{4}He^{+}$ ións cunha enerxía de 2 MeV e un detector de semicondutores PIPS (RBS1) situado a +165° con respecto á dirección do feixe.

O experimento PIGE realizouse na liña de reacción nuclear do acelerador Tandem cun feixe de ións H^{+} cunha enerxía entre 2,36 e 3,48 MeV. Así mesmo, durante o experimento executáronse dúas técnicas IBA en paralelo: PIGE para medir os gammas emitidos polas reaccións nucleares e RBS para medir os protóns retrodispersados do feixe. Os espectros gamma foron medidos cun detector de HPGe cilíndrico cunhas dimensións de 3,75 cm de raio por 6,81 cm de lonxitude situado no interior dunha cápsula de aluminio a unha distancia de 4,9 cm do centro da cámara de reacción e a 130° con respecto a a dirección do feixe. A distancia centro-detector non se coñecía con certeza e determinouse grazas ás simulacións de eficiencia realizadas co programa EnsarRoot. O detector de partículas utilizado para medir o espectro de protóns foi un detector de semicondutores PIPS (MOVD) situado nun

USC UNIVERSIDADE DE SANTIAGO DE COMPOSTELA

ángulo de 145° e a unha distancia de 8,8(1) cm. Estas medicións realizáronse en dúas campañas: unha en xullo de 2019 e outra en xaneiro de 2020.

En ambos os experimentos os brancos colocáronse no centro das cámaras de reacción perpendicularmente ao feixe e utilizando un goniómetro axustable externamente.

Produción de Brancos

Para levar a cabo o experimento anterior, fabricáronse brancos de cloro natural mediante a técnica de deposición térmica ao baleiro no Laboratorio de Brancos FCUL/LIP (Lisboa) [21, 147]. Sendo a primeira vez que nestas instalacións se fabricaban este tipo de brancos, realizáronse diferentes probas sobre composicións químicas, tempos de evaporación, procedementos a seguir, etc. ata que ao final se decidiu facer un branco de cloruro de prata sobre un substrato de prata. Este branco tiña que cumprir dúas características fundamentais: ser un branco fino para poder calcular seccións efectivas e ter unha cantidade de cloro suficiente para ter boas estatísticas.

As súas características físicas determináronse mediante a técnica RBS e o programa SIMNRA [75]. O grosor do branco utilizado nas medicións foi de 0,825(17) μm e as relacións isotópicas entre o cloro e a prata natural:

$$\begin{aligned} \text{ratio}(^{35}\text{Cl/Ag}) &= 1,42(3), \\ \text{ratio}(^{37}\text{Cl/Ag}) &= 0,455(9). \end{aligned}$$

Así mesmo, púidose determinar que a enerxía perdida polo protón no branco estaba entre 11 e 14 keV, que é a principal fonte de incerteza á hora de determinar a enerxía do feixe (6-8keV).

Análise de Resultados e Conclusións

Na análise dos espectros gamma, atopáronse diferentes fotopicos correspondentes ás reaccións entre o cloro natural e os protóns do feixe, detallados na Táboa 6.3. Podemos ver que a canle de neutróns de ^{37}Cl abriuse porque ten un valor Q de reacción relativamente baixo ($Q = -1596,22$ keV [26]). Tamén se observaron as aberturas das canles alfa para ambos isótopos e, como era de esperar, as dispersións elásticas dos protóns. Para cada un destes fotopicos, os gamma *yields* calculáronse en función da enerxía do protón. Para realizar esta análise foi fundamental o estudo da radiación de fondo realizado

USC UNIVERSIDADE DE SANTIAGO DE COMPOSTELA

Table 6.3: Gamas medidos no experimento PIGE onde se estudaron as reaccións entre os protóns e os dous isótopos estables do cloro. Os datos nucleares son tomados do NNDC [26].

Enerxía Gamma (keV)	**Reacción Nuclear**
1219,3(2)	^{35}Cl(p, p′γ_{10})^{35}Cl
1763,13(10)	^{35}Cl(p, p′γ_{20})^{35}Cl
2230,49(15)	^{35}Cl(p, $\alpha\gamma_{10}$)^{32}S
1726,4(2)	^{37}Cl(p, p′γ_{10})^{37}Cl
2127,499(20)	^{37}Cl(p, $\alpha\gamma_{10}$)^{34}S
1409,79(7)	^{37}Cl(p, nγ_{10})^{37}Ar
1611,24(5)	^{37}Cl(p, nγ_{20})^{37}Ar

na outra liña de investigación desta tese, que explicaremos máis adiante por haber superposición de fotopicos.

Por outra banda, analizáronse os espectros de protóns retrodispersados (RBS) e observáronse catro picos, de dereita a esquerda: un para a prata, outro para o cloro, outro para a contaminación polo carbono depositado na superficie e o cuarto pico de descoñecido orixe. Como os protóns retrodispersados pola prata son os únicos que sufriron unha interacción puramente coulombiana e seguen a ecuación de Rutherford, son os únicos *yields* utilizados no cálculo das seccións efectivas.

As seccións efectivas diferenciais para un obxectivo fino coa execución paralela de dúas técnicas IBA calculáronse coa seguinte Ecuación 6.2. Debido á execución simultánea das técnicas RBS e PIGE, as medicións realizadas son independentes da carga do espectro. Durante todo o procedemento experimental e de análise, tivéronse en conta, na medida do posible, as recomendacións e estándares suxeridos polo IAEA [6].

$$\left(\frac{d\sigma}{d\Omega}\right)_{\gamma}(E',\theta) = \frac{1}{4\pi}\frac{\Omega_p \varepsilon_{p,int}}{r\varepsilon_{\gamma}} \cdot \frac{Y_{\gamma}(E',\theta)}{Y_{Ag}(E',\phi)} \cdot \left(\frac{d\sigma}{d\Omega}\right)^{Ag}_{Ruth}. \tag{6.2}$$

Esta expresión xa ten incorporados os parámetros específicos do noso experimento: r é a relación isotópica entre o número de átomos de ^{35}Cl ou ^{37}Cl e o número de átomos de Ag no branco determinado por RBS análise; $\varepsilon_{p,int}$ é a eficiencia interna do detector de protóns considerado 100 %; $\Omega_p = 3,65\times10^{-3}$ sr é o ángulo sólido deste mesmo detector determinado por H. Silva *et al.* en

USC UNIVERSIDADE DE SANTIAGO DE COMPOSTELA

[164, 165] con 2 % de incerteza; ε_γ é a eficiencia absoluta do detector HPGe para cada gamma determinada polas simulacións; $Y_\gamma(E', \theta)$ é o gamma *yield* medido coa enerxía de protóns E' e detectado no ángulo θ; $Y_{Ag}(E', \phi)$ é o *yield* de protóns retrodispersados polos átomos de Ag medido a unha enerxía do protón E' e detectado nun ángulo ϕ; finalmente, $\left(\frac{d\sigma}{d\Omega}\right)^{Ag}_{Ruth}$ representa a sección transversal diferencial de Rutherford para a prata á mesma enerxía da protón E' pero no sistema de referencia do centro de masas. A enerxía E' é a enerxía do protón incidente E_0 menos a enerxía perdida na parte central do obxectivo e corrixida por un desprazamento duns ± 2 keV no sistema de referencia de laboratorio.

Como comentamos, a eficiencia do detector de xermanio calculouse para cada enerxía E_γ mediante simulacións precisas da *setup* experimental e das gammas emitidas, así como todo o mecanismo de detección e resposta do detector. En consecuencia, o erro estimado da eficiencia diminuíu a 0,6 % (cando adoita ser de 7 %). Este procedemento é un dos suxeridos polo IAEA.

As seccións efectivas diferenciais medidas neste experimento corresponden ás gammas detectadas na Táboa 6.3. Para exemplificar algúns, na Figura 6.5 represéntase a dispersión elástica de ^{35}Cl e na Figura 6.6 represéntase a canle alfa de ^{37}Cl. En todos eles a enerxía E' denotase como $E_{p,lab}$. As incertezas destas medicións son relativamente baixas arredor dos 7 % e no peor dos casos aumenta ata 16 %. En particular, a sección efectiva da gamma 2127,499 keV puido ser comparada con outra medición realizada previamente por Weber *et al.* [15] onde se puido comprobar que coinciden en magnitude aínda que en diferentes rangos de enerxía do protón.

Neste estudo espectroscópico realizáronse medicións detalladas dos gamma *yields* e calculáronse por primeira vez as seccións transversais diferenciais das reaccións nucleares de baixa enerxía entre un feixe de protóns e os dous isótopos estables do cloro. Estas medicións son de alta calidade xa que se realizaron con incertezas xerais inferiores a 7 %. Estes datos serán moi útiles para a comunidade científica, especialmente, para aqueles que utilicen a técnica analítica PIGE.

USC
UNIVERSIDADE DE SANTIAGO DE COMPOSTELA

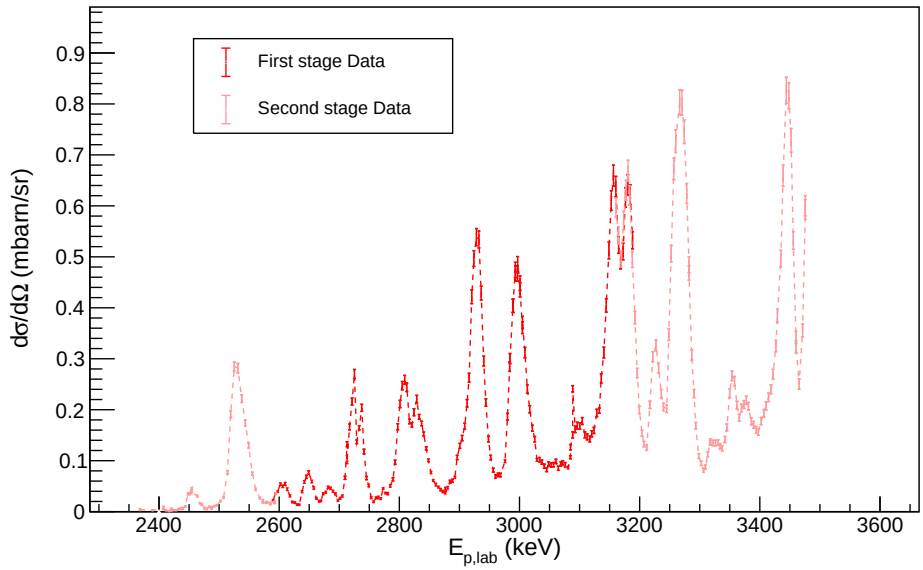

Figure 6.5: Sección efectiva diferencial da gamma 1219,3 keV procedente da reacción $^{35}\mathrm{Cl}(\mathrm{p},\mathrm{p}'\gamma_{10})^{35}\mathrm{Cl}$ no rango de enerxía de 2,36-3,48 MeV. As dúas fases do experimento indícanse en diferentes tonalidades.

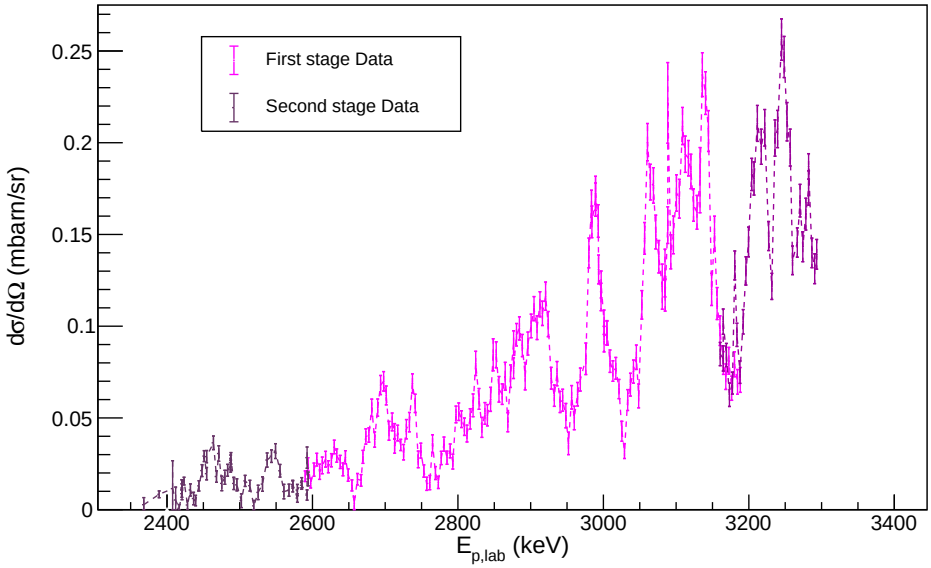

Figure 6.6: Sección efectiva diferencial da gamma 2127,499 keV procedente da reacción $^{37}\mathrm{Cl}(\mathrm{p},\alpha\gamma)^{34}\mathrm{S}$ no rango de enerxía de 2,36-3,3 MeV. As dúas fases do experimento indícanse en diferentes tons.

USC UNIVERSIDADE DE SANTIAGO DE COMPOSTELA

Estudo da Radiación Ambiental

A outra liña de investigación desta tese é o estudo da radiación ambiental mediante espectroscopia gamma, que consiste en realizar medicións dos fotóns emitidos polas cadeas de desintegración presentes na natureza e por outras fontes de radiación natural.

A radiación ionizante natural presente na Terra ten diferentes orixes: terrestre, que á súa vez pode ser primordial (existente da orixe dos elementos máis pesados) ou secundaria (derivada da desintegración radioactiva do primordial) e cosmoxénica, creada pola radiación cósmica e a súa interacción con materia [112]. Por outra banda, os humanos introduciu radiación artificial mediante técnicas modernas, esta tamén se denomina radiación antropoxénica.

Os radionúcleos primixenios que aínda están presentes na Terra teñen vidas medias, en polo menos, comparable á idade do Universo (uns $13,8 \times 10^9$ anos [107]). Segundo o modo de desintegración clasifícanse en dous tipos: series ou cadeas e desintegracións individuais.

Unha serie radioactiva é un conxunto de radionúcleos inestables xerados a partir da desintegración dun radionúcleo proxenitor e a posterior desintegración dos seus núcleos fillos ata chegar a un núcleo estable. As tres cadeas radioactivas aínda presentes na natureza son [26, 112]:

- Serie de torio iniciada por ^{232}Th (vida media de $14,0(1) \times 10^9$ anos).
- Serie de uranio iniciada por ^{238}U (vida media de $4,468(3) \times 10^9$ anos).
- Serie de actinio iniciada por ^{235}U (vida media de $7,038(5) \times 10^8$ anos).

A principal fonte radioactiva non en cadea é o isótopo de potasio ^{40}K que ten unha vida media de $1,248(3) \times 10^9$ anos [26]. Este isótopo decae en dous modos: β^- e captura electrónica. Neste último modo o ^{40}K transmútase a ^{40}Ar emitindo durante o proceso unha gamma de 1460,820(5) keV. Este fotopico e a forma da súa dispersión Compton son característicos de calquera espectro de radiación de fondo.

A outra fonte de radiación natural é a radiación cósmica extraterrestre formada por partículas altamente enerxéticas [118]. O compoñente maioritario son os radionúcleos cosmoxénicos (protóns, partículas alfa, ións carbono, ións nitróxeno, etc.) aínda que tamén está formado por radiación electromagnética: desde raios gamma ata radiofrecuencia, aínda que a rexión dos raios-X é a máis predominante en o espectro. A orixe dos raios cósmicos é extragaláctico aínda que hai un compoñente que procede do Sol e que se

USC UNIVERSIDADE DE SANTIAGO DE COMPOSTELA

pode detectar por correlacións entre ambos. Cando estes raios chegan á atmosfera, son aniquilados por colisións con partículas en suspensión, creando unha enorme cantidade de novas partículas de masa, é dicir, a enerxía cinética dos raios cósmicos primarios convértese en grandes masas en repouso. Estes produtos coñécense como radiación cósmica secundaria e o seu compoñente principal son os pións [112].

Obxectivos e Motivación

O obxectivo principal desta parte da tese é estudar estas fontes radioactivas desde dous enfoques: por unha banda, realizar medicións monitorizadas durante longos períodos de tempo, e por outra banda, reproducir estas emisións e procesos de detección en simulación en detalle dentro do programa EnsarRoot. Esta análise exhaustiva é de gran relevancia en diferentes ámbitos.

O ser humano e outras formas de vida están expostos a esta radiación ionizante, por tres vías diferentes: externas, esencialmente a partir de radionúcleos e os produtos da súa desintegración presentes nas rochas ou nos materiais de construción, e os raios cósmicos; interna, por inxestión de alimentos e auga potable e inhalación de partículas de po que conteñen produtos de desintegración de uranio (principalmente radón). Estas exposicións son inevitables e, en taxas elevadas, poden causar danos á saúde dos organismos vivos, por exemplo, a inhalación de radon é a segunda causa de cancro de pulmón humano [41]. Polo tanto, calquera estudo sobre a radiación natural é de gran importancia para a comunidade científica, a poboación e as autoridades nacionais.

Desde o punto de vista científico, a radiación natural interfire na adquisición de datos en moitos experimentos. No noso campo, a espectroscopia gamma, hai un gran número de interferencias espectrais mutuas entre moitos radionúcleos e o gamma *yield* experimental. Esta superposición ás veces fai imposible a diferenciación entre fotopicos. En consecuencia, un estudo exhaustivo da radiación de fondo do laboratorio CTN/IST, onde se realizaron os experimentos PIGE anteriormente descritos, resulta moi útil á hora de analizar os espectros.

Aínda que a radiación ambiental foi estudada en numerosos traballos [7, 33, 34, 35], ningún estudo centrado no seguimento da radiación na parte alta do oeste da Península Ibérica. Ademais, non se realizaron análises temporais das fontes radioactivas por separado.

En canto á simulación da radiación ambiental, observouse un déficit nos estudos onde se simulan fontes radioactivas individuales, é dicir, reconstruíndo o mecanismo de emisión gamma e a súa posterior detección.

USC UNIVERSIDADE DE SANTIAGO DE COMPOSTELA

Do mesmo xeito, non se atoparon traballos onde se comparen medicións radiolóxicas e as súas correspondentes simulacións.

Metodoloxía Experimental

As medicións experimentais realizáronse en tres enclaves situados en rexións de diferente composición minerais da zona occidental da Península Ibérica. Estes seguimentos realizáronse durante longos períodos de tempo a intervalos de 30 minutos co fin de realizar unha análise a partir de variables atmosféricas e horarias. Os detectores empregados en todos os casos foron detectores de xermanio de similares características.

En Portugal realizáronse medicións en dous lugares: nas instalacións do CTN/IST, situadas nun medio mariño próximo á costa utilizando o mesmo detector que se utiliza para as medicións PIGE, e no laboratorio da Universidade da Beira Interior (UBI) [43], situada nunha contorna montañosa da zona central do país. Neste último laboratorio utilizouse un detector de xermanio similar en tamaño e forma ao anterior. Grazas ao estudo realizado coas simulacións, puidemos determinar que o detector UBI ten 24 % menos de volume de detección activo que o detector CTN/IST. A electrónica en ambos casos tamén presentaba características similares.

O terceiro lugar onde se recolleron as medicións foi no Laboratorio de Análise de Radiación da Universidade de Santiago de Compostela [44, 45, 162] na zona noroeste da Península Ibérica. Neste caso, os detectores tamén eran HPGe (BSI e ORTEC) pero coa particularidade de que estaban cubertos por unha pantalla para evitar interferencias de radiación de fondo durante o uso diario. Por este motivo, non se puido realizar unha análise axeitada xa que moitos fotóns, especialmente de baixas enerxías, son absorbidos polas paredes do escudo. Non obstante, estas medicións permitíronnos comprender o comportamento da radiación cósmica xa que as medicións se fixeron coas tapas das aberturas superiores abertas.

Simulacións de Radiación Ambiental

Como mencionamos antes, o *framework* EnsarRoot é a ferramenta clave para realizar estes estudos. Este programa ampliouse para incluír xeradores de raios gamma que reproducen a desintegración dos núcleos das tres cadeas radioactivas e emiten os fotóns producidos na desexcitación nuclear.

Tamén se desenvolveu un xerador que reproduce a desintegración do potasio. Unha vez realizadas as simulacións a nivel individual de cada radionúclido, todas as simulacións pertencentes a unha mesma cadea reuníronse nun único ficheiro para poder tratar toda a cadea como un todo (supoñendo

USC UNIVERSIDADE DE SANTIAGO DE COMPOSTELA

que non houbese interrupción na serie). Os diferentes compoñentes simulados pódense ver na Figura 6.7.

As simulacións de radiación cósmica realizáronse en dúas etapas: primeiro co programa de simulación CRY [168] simuláronse cascadas de raios cósmicos mediante unha configuración específica (latitud, altitude, composición, etc.); e posteriormente, estes datos foron simulados dentro do programa EnsarRoot mediante un xerador que xa fora desenvolvido previamente.

Por outra banda, simuláronse con moito detalle as *setups* experimentais onde se realizaron as medias. En todas as configuracións simuladas, tivo que incluírse baixo o detector un bloque composto por un material terroso para atenuar os fotóns da serie radioactiva.

Análise de Resultados e Conclusións

Analizamos os espectros ambientais de cada lugar individualmente, identificando os fotopicos que aparecen e as súas orixes. Posteriormente, fíxose unha comparación entre as distintas medidas para identificar variacións. Púidose observar que a cantidade de radiación ambiental no UBI é dúas ordes de magnitude maior que a do CTN/IST. Este resultado é consistente coa composición do subsolo en ambos os lugares (ver as Figuras 2-34 do [109]). Ademais, nos espectros puidemos distinguir dúas series radioactivas (uranio e torio) e a desintegración de ^{40}K. Desafortunadamente, os fotopicos da serie do actinio non se puideron identificar en ningún dos casos porque a súa intensidade é moi baixa e porque o fotopico máis relevante sitúase a baixas enerxías onde dominan os raios-X e o ruído producido pola electrónica.

Análise Temporal

Grazas a que as medicións experimentais foron recollidas en intervalos de tempo curtos, puido realizarse unha análise temporal. Para poder comparar as concentracións dos compoñentes ambientais de fondo por separado, escolleuse un fotopico de referencia para cada contribución radioactiva natural (Táboa 6.4). Normalmente, os picos máis visibles atópanse a enerxías intermedias-altas xa que se evitan gran parte das achegas de Compton, raios-X, etc. que predominan as baixas enerxías.

En primeiro lugar, analizáronse os datos de días completos e comparáronse as evolucións ao longo das semanas. Posteriormente, os mesmos datos foron analizados seguindo outro criterio, calculando o valor medio por hora co fin de identificar un patrón relacionado co aumento da temperatura ao mediodía, diferenciación día-noite ou as rutinas de ventilación no laboratorio. Estes estudos realizáronse para cada compoñente do fondo radioactivo. En todas as

USC UNIVERSIDADE DE SANTIAGO DE COMPOSTELA

Table 6.4: Fotopicos utilizados como referencia para cada contribución de radiación ambiental. Os datos nucleares extráense do NNDC [26].

Compoñente Radiación Ambiental	**Núcleo Proxenitor**	**Fotopico de Referencia (keV)**
Descomposición de Potasio	^{40}K	1460,849(5)
Cadea de Uranio	^{214}Bi	1764,494(14)
Cadea de Torio	^{208}Tl	2614,533(13)

gráficas pódense observar fluctuacións, pero non se estableceu ningunha correlación entre estas variacións e os factores ambientais porque seguen patróns complexos. Esta conclusión é consistente con algúns estudos nos que tampouco se puido establecer ningunha conexión [66, 67].

Por último, calculáronse as taxas medias totais de cada compoñente e as relacións entre elas. O resultado máis salientable é a gran cantidade de potasio presente nos materiais do laboratorio UBI, case catro veces a cantidade de potasio no CTN/IST. Unha posible explicación para este resultado é a proximidade das paredes ao detector de UBI.

Simulacións de Radiación Ambiental

Os espectros de radiación de fondo dos laboratorios CTN/IST e UBI simuláronse dentro do programa EnsarRoot utilizando os xeradores gamma e as *setups* simuladas explicadas anteriormente.

Na Figura 6.7 pódense ver todos os compoñentes radioactivos por separado xunto cun espectro de fondo ambiental do laboratorio CTN/IST. Podemos observar que a forma do fondo natural é unha convolución entre o fotopico de potasio xunto coa súa dispersión Compton (liña verde) e que as series de torio e uranio contribúen significativamente a baixas enerxías (liñas laranxa e azuis). Pola contra, o sinal de actinio é case imperceptible (liña rosa). A radiación cósmica é unha constante en todo o espectro, contribuíndo máis á zona de baixa enerxía (liña gris). Todos estes compoñentes ponderáronse comparándoos con datos experimentais. Para este fin, utilizáronse varias clases ROOT: TMinuit para calcular o valor de χ^2 e obter os valores óptimos da ponderación e TRatioPlot como método de verificación para comparar a simulación final (incluíndo os compoñentes pesados) e os datos medidos experimentalmente.

A Figura 6.7 xa mostra estes compoñentes pesados. O resultado final da simulación (liña azul) xunto cos datos reais (liña negra) móstrase na Figura

USC UNIVERSIDADE DE SANTIAGO DE COMPOSTELA

6.8. Ambos espectros mostran un alto grao de concordancia en case todo o rango de enerxía.

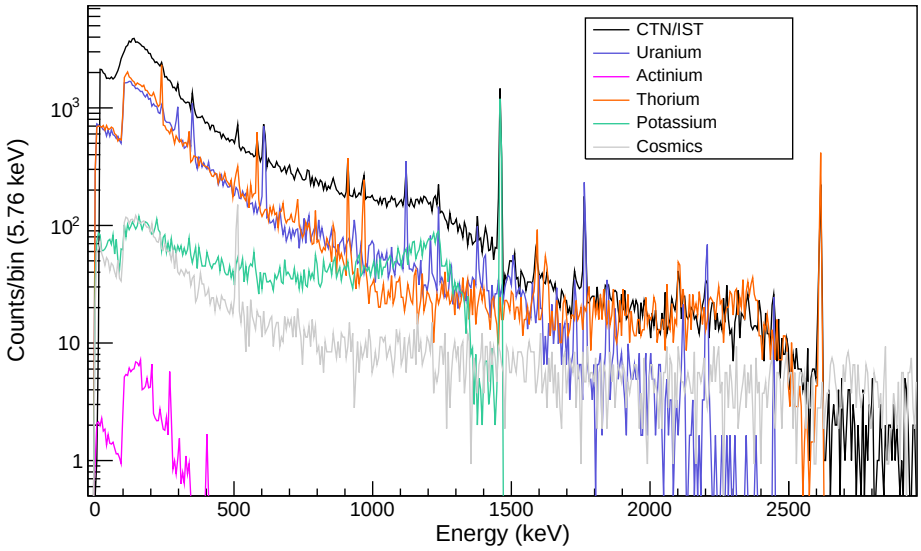

Figure 6.7: Espectro experimental da radiación ambiental do CTN/IST medido durante un intervalo de tempo de 30 minutos (liña negra) e todos os seus compoñentes simulados e ponderados.

Este mesmo estudo realizouse sobre os datos de radiación ambiental do laboratorio da UBI. Neste caso, as simulacións foron maiores xa que a cantidade de radiación ambiental foi maior. Seguindo os mesmos procedementos que no caso anterior, obtívose unha simulación do fondo (compilando todos os compoñentes por separado e xa pesados) cun alto nivel de coincidencia cos datos experimentais.

En xeral, ambas as simulacións son moi precisas e reproducen moi ben os espectros dos datos experimentais. Cómpre sinalar que a baixas enerxías o nivel de concordancia é menor porque non se incluíron os raios-X e o efecto do ruído electrónico. A simulación da radiación ambiental do CTN/IST está máis definida que a do UBI porque neste último había máis parámetros *a priori* descoñecidos, como o volume de detección activo e quizais algún elemento de *setup* que non se incluíu nas simulacións.

Finalmente, nos dous laboratorios calculáronse as actividades relativas entre as series de uranio e torio e os nosos resultados confirman que son similares en ambos. Esta conclusión tamén se obtivo na análise temporal.

Neste estudo espectroscópico ambiental realizouse unha análise detallada de cada fonte radioactiva, tanto a nivel experimental, analizando os seus

USC UNIVERSIDADE DE SANTIAGO DE COMPOSTELA

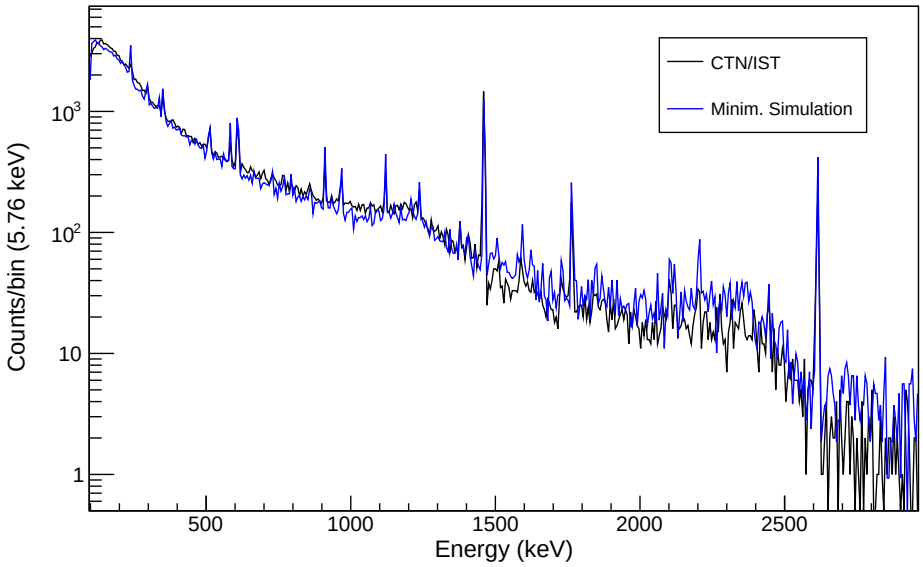

Figure 6.8: Espectro da radiación ambiental do CTN/IST medida durante un intervalo de tempo de 30 minutos (liña negra) e a súa simulación ponderada (liña azul).

compoñentes e a súa evolución no tempo; e a nivel de simulación, onde se recrearon todas as fontes que contribúen á radiación ambiental e se axustaron ás medicións experimentais para analizar a súa contribución real a este fondo. Ademais, as simulacións serviron para determinar algúns parámetros imprecisos. Os axustes entre os compoñentes simulados e os datos experimentais foron unha tarefa complexa e laboriosa porque había moitas variables sensibles que estaban fóra de axuste á mínima variación.

Esta análise tamén foi útil ao estudar os espectros de raios gamma do experimento PIGE porque nos permitiu distinguir solapamentos entre fotopicos e incluso puidemos calibrar o detector a enerxías máis altas a través de fotopicos ambientais. Así mesmo, este estudo pode ser útil para futuros experimentos realizados nas mesmas instalacións ou para outros experimentos de similares características.

USC
UNIVERSIDADE DE SANTIAGO DE COMPOSTELA

Glossary

The acronyms and abbreviations used in this thesis are defined in this section.

BR: Branching Ratio.

CALIFA: CALorimeter for In-Flight detection of gamma-rays and high energy charged pArticles.

CORSIKA: COsmic Ray SImulations for KAscade.

CRY: Cosmic ray Shower Library.

CSN: Consejo de Seguridad Nuclear.

CTN/IST: Campus Tecnológico e Nuclear (CTN) of the Instituto Superior Técnico (IST).

DNA: DeoxyriboNucleic Acid.

ENIAC: Electronic Numerical Integrator And Computer.

ENUSA: Empresa Nacional del Uranio, SA.

ERDA: Elastic Recoil Detection Analysis.

ERYA: Emitted Radiation Yield Analysis.

FAIR: Facility for Antiproton and Ion Research.

FCUL/LIP: Faculdade de Ciências da Universidade de Lisboa and Laboratório de Instrumentação e Física Experimental de Partículas.

USC UNIVERSIDADE DE SANTIAGO DE COMPOSTELA

FORTRAN: FORMula TRANslator.

FWHM: Full Width at Half Maximum.

GEMAS: GEochemical Mapping of Agricultural and grazing land Soil.

HPGe: High-Purity Germanium.

IAEA: International Atomic Energy Agency.

IBA: Ion Beam Analysis.

IBNDL: Ion Beam Analysis Nuclear Data Library.

MARNA: MApa de Radiación gamma Natural en España.

MC: Monte Carlo.

MCA: Multichannel Analyzer.

MOVD: MÓVil Direita.

MOVE: MÓVil Esquerda.

NIST: National Institute of Standards and Technology.

NNDC: National Nuclear Data Center.

NRA: Nuclear Reaction Analysis.

PIGE: Particle Induced Gamma-ray Emission.

PIPS: Passivated Implanted Planar Silicon.

PIXE: Particle Induced X-ray Emission.

RBS: Rutherford Backscattering Spectrometry.

RPC: Resistive Plate Chamber.

USC UNIVERSIDADE DE SANTIAGO DE COMPOSTELA

R3B: Reactions with Relativistic Radioactive Beams.

SATNuRSE: Simulations and Analysis Tools for Nuclear Reactions and Structure in Europe.

SiNuRSE: Simulations for Nuclear Reactions and Structure in Europe.

SRIM: Stopping and Range of Ions in Matter.

TRASGO: TRAck reconStructinG mOdule.

UBI: Universidade da Beira Interior.

USC: Universidad de Santiago de Compostela.

VMC: Virtual Monte Carlo.

WWII: Second World War.

XRF: X-rays Fluorescense.

USC UNIVERSIDADE DE SANTIAGO DE COMPOSTELA

Appendix A

Uranium Series

In this appendix we show the decay information for each nucleus which emmits gamma radiation during the entire transition in the uranium series. This information have been implemented in the EnsarRoot generators. Energy units are expressed in keV and the probabilities for each transition are indicated in decimal fraction. Nuclear data is based on the information provided by the Table of Radioactive Isotopes from The Lund/LBNL Nuclear Data Search [143] and on NNDC data base [26].

Table 5: Decay of ^{238}U.

Parent Nucleus	**Parent $T_{1/2}$**	**Decay Mode**	**Daughter Nucleus**	**I_{decay}**	**Initial Daughter State E_i**
^{238}U	$4,468 \times 10^9$ y	$\alpha : 100\%$	^{234}Th	0,791	**g.s.**
				0,209	49,55

Table 6: De-excitation of ^{234}Th.

Initial Daughter State E_i	**E_γ**	**I_γ**	**Final Daughter State E_f**
49,55	49,55	1	**g.s.**

.

USC UNIVERSIDADE DE SANTIAGO DE COMPOSTELA

Table 7: Decay of ^{234}Th.

Parent Nucleus	Parent $T_{1/2}$	Decay Mode	Daughter Nucleus	I_{decay}	Initial Daughter State E_i
^{234}Th	24,10 d	β^- : 100%	^{234}Pa	0,703	**g.s.**
				0,192	166,3
				0,076	166,72
				0,029	186,73

Table 8: De-excitation of ^{234}Pa. The second excited state of 103,42 keV de-excites to a 73.92+x state with $J^P = 0^-$ and this transition has not been observed experimentally (for more information consult the ENSDF of ^{234}Pa from the NNDC). As a result, we have considered that it de-excited directly to the ground state, but we have preserved the real gamma energy.

Initial Daughter State E_i	E_γ	I_γ	Final Daughter State E_f
73,92	73,92	1	**g.s.**
103,42	*29,49*	*1*	***g.s.***
166,3	62,86	0,0074	103,42
	92,38	0,9926	**g.s.**
166,72	63,29	0,6369	103,42
	92,80	0,3631	**g.s.**
186,73	112,81	0,7564	**g.s.**
	83,30	0,2163	103,42
	20,02	0,20273	166,72

Table 9: Decay of ^{234}Pa.

Parent Nucleus	Parent $T_{1/2}$	Decay Mode	Daughter Nucleus	I_{decay}	Initial Daughter State E_i
^{234}Pa	1,159 m	β^- : 99, 84%	^{234}U	0,9757	**g.s.**
				0,0243	1044,5

USC UNIVERSIDADE DE SANTIAGO DE COMPOSTELA

Table 10: De-excitation of ^{234}U.

Initial Daughter State E_i	**E_γ**	**I_γ**	**Final Daughter State E_f**
43,4981	43,4981	1	**g.s.**
143,352	99,853	1	43,4981
786,288	742,81	0,6329	43,4981
	786,27	0,3671	**g.s.**
809,907	766,38	0,6369	103,42
851,74	41,82	0,0013	809,907
	708,30	0,1620	143,352
	808,20	0,3137	43,4981
	851,70	0,5229	**g.s.**

Table 11: Decay of ^{234}U.

Parent Nucleus	**Parent $T_{1/2}$**	**Decay Mode**	**Daughter Nucleus**	**I_{decay}**	**Initial Daughter State E_i**
^{234}U	2,455×10^5 y	α : 100%	^{230}Th	0,7138	**g.s.**
				0,2842	53,227

Table 12: De-excitation of ^{230}Th.

Initial Daughter State E_i	**E_γ**	**I_γ**	**Final Daughter State E_f**
53,227	52,2	1	**g.s.**

USC UNIVERSIDADE DE SANTIAGO DE COMPOSTELA

Table 13: Decay of ^{230}Th.

Parent Nucleus	Parent $T_{1/2}$	Decay Mode	Daughter Nucleus	I_{decay}	Initial Daughter State E_i
^{230}Th	7,538×10^4 y	α : 100%	^{226}Ra	0,763	**g.s.**
				0,234	67,67

Table 14: De-excitation of ^{226}Ra.

Initial Daughter State E_i	E_γ	I_γ	Final Daughter State E_f
67,67	67,67	1	**g.s.**

Table 15: Decay of ^{226}Ra.

Parent Nucleus	Parent $T_{1/2}$	Decay Mode	Daughter Nucleus	I_{decay}	Initial Daughter State E_i
^{226}Ra	1600 y	α : 100%	^{222}Rn	0,9384	**g.s.**
				0,0616	186,211

Table 16: De-excitation of ^{222}Rn.

Initial Daughter State E_i	E_γ	I_γ	Final Daughter State E_f
186,211	186,211	1	**g.s.**

USC UNIVERSIDADE DE SANTIAGO DE COMPOSTELA

Table 17: Decay of ^{214}Pb.

Parent Nucleus	**Parent $T_{1/2}$**	**Decay Mode**	**Daughter Nucleus**	**I_{decay}**	**Initial Daughter State E_i**
^{214}Pb	26,8 m	β^- : 100%	^{214}Bi	0,11	**g.s.**
				0,402	295,2231
				0,459	351,9324
				0,0104	533,676
				0,0275	839,009

USC UNIVERSIDADE DE SANTIAGO DE COMPOSTELA

Table 18: De-excitation of ^{214}Bi. The NNDC data base has no information about 62,69 keV excited state, as a result, we have filled it with invented data in order to create the generator (it is highlighted in italics).

Initial Daughter State E_i	**E_γ**	**I_γ**	**Final Daughter State E_f**
53,228	53,228	1	**g.s.**
62,69	*62,69*	*1*	***g.s.***
258,87	196,19	0,109	62,69
	205,68	0,0188	53,228
	258,86	0,8722	**g.s.**
295,2231	241,995	0,2824	53,228
	295,2228	0,7176	**g.s.**
351,9324	298,76	0,0007	53,228
	351,9321	0,9993	**g.s.**
377,04	314,33	0,7299	62,69
	323,84	0,2701	53,228
533,676	181,5	0,0012	351,9324
	238,4	0,0179	295,2231
	274,8	0,3986	258,87
	480,432	0,3786	53,228
	533,66	0,2037	**g.s.**
839,009	305,26	0,0113	533,676
	462,02	0,0775	377,04
	487,14	0,1577	351,9324
	543,83	0,016	295,2231
	580,14	0,1351	258,87
	785,96	0,3894	53,228
	839,07	0,213	**g.s.**

USC UNIVERSIDADE DE SANTIAGO DE COMPOSTELA

Table 19: Decay of ^{214}Bi. The intensity of the alpha decay mode is so low that this branch is not included in the generator.

Parent Nucleus	**Parent $T_{1/2}$**	**Decay Mode**	**Daughter Nucleus**	**I_{decay}**	**Initial Daughter State E_i**
^{214}Bi	19,9 m	β^- : 99,979 %	^{214}Po	0,191	**g.s.**
				0,0735	1377,678
				0,0312	1543,372
				0,1757	1729,609
				0,1696	1764,515
				0,0814	1847,443
				0,01588	1890,306
				0,01177	1994,64
				0,01431	2010,83
				0,0245	2017,309
				0,04345	2118,533
				0,056	2204,089
				0,0278	2447,702
				0,08389	2482,468
		α^- : 0,021 %	^{210}Tl	-	-

USC UNIVERSIDADE DE SANTIAGO DE COMPOSTELA

Table 20: De-excitation of ^{214}Po.

Initial Daughter State E_i	E_γ	I_γ	Final Daughter State E_f
609,316	609,32	1	**g.s.**
1015,039	405,72	1	609,316
1274,766	665,447	1	609,316
1377,678	768,36	0,551	609,316
	1377,669	0,449	**g.s.**
1415,495	806,18	1	609,316
1543,372	268,8	0,0048	1274,766
	528	0,0014	1015,039
	934,056	0,9051	609,316
	1543,34	0,0887	**g.s.**
1661,279	1051,96	0,2302	609,316
	1661,274	0,7698	**g.s.**
1712,97	697,93	0,4083	1015,039
	1103,7	0,5917	609,316
1729,609	351,9	0,0041	1377,678
	454,79	0,0161	1274,766
	1120,294	0,8214	609,316
	1729,595	0,1584	**g.s.**
1742,98	1133,66	1	609,316
1764,515	221	0,0002	1543,372
	348,92	0,006	1415,495
	386,78	0,017	1377,678
	1155,21	0,0943	609,316
	1764,491	0,8825	**g.s.**
1847,443	304,2	0,0047	1543,372
	469,77	0,0162	1377,678
	572,78	0,0096	1274,766
	832,36	0,0034	1015,039
	1238,122	0,7172	609,316
	1847,429	0,2489	**g.s.**

USC UNIVERSIDADE DE SANTIAGO DE COMPOSTELA

Table 21: De-excitation of ^{214}Po.

Initial Daughter State E_i	**E_γ**	**I_γ**	**Final Daughter State E_f**
1890,306	615,77	0,0347	1274,766
	1280,976	0,9124	609,316
	1890,32	0,0529	**g.s.**
1994,64	230	0,0031	1764,515
	333,37	0,0505	1661,279
	617,1	0,0265	1377,678
	719,87	0,3042	1274,766
	1385,31	0,6157	609,316
2010,83	595,24	0,012	1415,495
	633,1	0,0385	1377,678
	1401,515	0,9188	609,316
	2010,82	0,0307	**g.s.**
2017,309	252,8	0,0013	1764,515
	356	0,0028	1661,279
	639,62	0,0137	1377,678
	1407,988	0,9822	609,316
2088,44	710,71	0,5747	1377,678
	1479,17	0,4253	609,316
2118,533	388,89	0,0956	1729,609
	703,11	0,1123	1415,495
	740,76	0,0101	1377,678
	1509,2	0,5061	609,316
	2118,5	0,2759	**g.s.**
2147,83	486,7	0,0128	1661,279
	769,7	0,0625	1377,678
	873,06	0,0394	1274,766
	1538,53	0,8558	609,316
	2147,99	0,0295	**g.s.**
2192,537	428,07	0,0131	1764,515
	649,22	0,0665	1543,372
	814,96	0,0452	1377,678
	917,7	0,0049	1274,766
	1583,204	0,821	609,316
	2192,59	0,0493	**g.s.**

USC UNIVERSIDADE DE SANTIAGO DE COMPOSTELA

Table 22: De-excitation of ^{214}Po.

Initial Daughter State E_i	E_γ	I_γ	Final Daughter State E_f
2204,089	461,08	0,0091	1742,98
	474,44	0,0176	1729,609
	542,83	0,0138	1661,279
	660,94	0,0095	1543,372
	788,6	0,0024	1415,495
	8264,5	0,0211	1377,678
	1594,75	0,0475	609,316
	2204,059	0,8790	**g.s.**
2208,69	547,6	0,0095	1661,279
	934,1	0,1292	1274,766
	1599,37	0,8613	609,316
2447,702	452,92	0,0109	1994,64
	683,23	0,029	1764,515
	704,96	0,0164	1742,98
	786,35	0,1093	1661,279
	904,31	0,0268	1543,372
	1032,38	0,0224	1415,495
	1069,96	0,0962	1377,678
	1173	0,0191	1274,766
	1838,36	0,1235	609,316
	2447,7	0,5464	**g.s.**
2482,468	273,8	0,1013	2208,69
	334,78	0,0293	2147,83
	394,05	0,01	2088,44
	487,95	0,0221	1994,64
	634,72	0,005	1847,443
	752,85	0,1017	1729,609
	821,18	0,1274	1661,279
	939,6	0,0139	1543,372
	1104,71	0,0614	1377,678
	1207,68	0,3568	1274,766
	1873,16	0,1695	609,316
	2482,8	0,0016	**g.s.**

USC UNIVERSIDADE DE SANTIAGO DE COMPOSTELA

Table 23: Decay of ^{210}Pb.

Parent Nucleus	**Parent $T_{1/2}$**	**Decay Mode**	**Daughter Nucleus**	**I_{decay}**	**Initial Daughter State E_i**
^{210}Pb	22,20 y	β^- : 100%	^{210}Bi	0,16	**g.s.**
				0,84	46,539

Table 24: De-excitation of ^{210}Bi .

Initial Daughter State E_i	**E_γ**	**I_γ**	**Final Daughter State E_f**
46,539	46,539	1	**g.s.**

USC UNIVERSIDADE DE SANTIAGO DE COMPOSTELA

Appendix B

Actinium Series

In this appendix we show the decay information for each nucleus which emmits gamma radiation during the entire transition in the uranium series. This information have been implemented in the EnsarRoot generators. Energy units are expressed in keV and the probabilities for each transition are indicated in decimal fraction. Nuclear data is based on the information provided by the Table of Radioactive Isotopes from The Lund/LBNL Nuclear Data Search [143] and on NNDC data base [26].

Table 25: Decay of ^{235}U.

Parent Nucleus	**Parent $T_{1/2}$**	**Decay Mode**	**Daughter Nucleus**	**I_{decay}**	**Initial Daughter State E_i**
^{235}U	703,8×10^6 y	α : 100 %	^{231}Th	0,0477	**g.s.**
				0,0382	41,953
				0,0128	96,143
				0,0309	185,7182
				0,5773	205,310
				0,1892	236,906
				0,0352	277,57
				0,0687	387,836

USC UNIVERSIDADE DE SANTIAGO DE COMPOSTELA

Table 26: De-excitation of ^{231}Th .

Initial Daughter State E_i	**E_γ**	**I_γ**	**Final Daughter State E_f**
41,953	41,96	1	**g.s.**
96,143	54,25	0,2481	41,953
	96,09	0,7519	**g.s.**
162,07	120,35	1	41,953
185,7182	143,76	0,1612	41,953
	185,715	0,8388	**g.s.**
205,310	109,197	0,1423	96,143
	163,356	0,4310	41,953
	205,316	0,4267	**g.s.**
236,906	31,6	0,0203	205,310
	51,21	0,0338	185,7182
	74,94	0,0540	162,07
	140,76	0,2162	96,143
	194,94	0,6757	41,953
277,57	41,4	0,1667	236,906
	72,7	0,6666	205,310
	115,45	0,1666	162,07
387,836	150,93	0,0467	236,906
	182,62	0,2136	205,310
	202,12	0,6676	185,7182
	291,65	0,0254	96,143
	345,92	0,0234	41,953
	387,84	0.0233	**g.s.**

USC UNIVERSIDADE DE SANTIAGO DE COMPOSTELA

Table 27: Decay of ^{231}Th.

Parent Nucleus	Parent $T_{1/2}$	Decay Mode	Daughter Nucleus	I_{decay}	Initial Daughter State E_i
^{231}Th	25,52 h	β^- : 100 %	^{231}Pa	0,32	84,2148
				0,4	101,4092
				0,12	102,2692
				0,013	174,161
				0,121	183,4962
				0,026	247,32

USC UNIVERSIDADE DE SANTIAGO DE COMPOSTELA

Table 28: De-excitation of ^{231}Pa .

Initial Daughter State E_i	**E_γ**	**I_γ**	**Final Daughter State E_f**
92,06	9,2	1	**g.s.**
58,56	58,57	1	**g.s.**
77,685	68,5	0,5814	92,06
	77,69	0,4186	**g.s.**
84,2148	25,64	0,68166	58,56
	84,214	0,31834	**g.s.**
101,4092	42,86	1	58,56
102,2692	18,07	0,04322	84,2148
	93,02	0,09248	92,06
	102,27	0,8643	**g.s.**
111,653	10,25	1	101,4092
174,161	72,751	0,1984	101,4092
	89,95	0,7841	84,2148
	115,63	0,0008	258,56
	165	0,0027	92,06
	174,15	0,0140	**g.s.**
183,4962	81,228	0,5817	102,2692
	82,087	0,2693	101,4092
	99,278	0,0849	84,2148
	105,81	0,0051	77,685
	124,914	0,0376	58,56
	183,5	0.0214	**g.s.**
247,32	63,86	0,0778	183,4962
	135,664	0,265	111,653
	145,06	0,0192	102,2692
	145,94	0,1037	101,4092
	163,101	0,5186	84,2148
	169,66	0,0045	77,685
	188,76	0,0112	58,56

USC UNIVERSIDADE DE SANTIAGO DE COMPOSTELA

Table 29: Decay of ^{231}Pa.

Parent Nucleus	**Parent $T_{1/2}$**	**Decay Mode**	**Daughter Nucleus**	**I_{decay}**	**Initial Daughter State E_i**
^{231}Pa	3,276 $\times 10^4$ y	α : 100 %	^{227}Ac	0,11	**g.s.**
				0,025	27,369
				0,2	29,978
				0,254	46,354
				0,014	74,149
				0,228	109,992
				0,03	126,848
				0,014	210,8
				0,084	330,04
				0,01268	354,5
				0,02832	387,2

USC UNIVERSIDADE DE SANTIAGO DE COMPOSTELA

Table 30: De-excitation of ^{227}Ac.

Initial Daughter State E_i	**E_γ**	**I_γ**	**Final Daughter State E_f**
27,369	27,36	1	**g.s.**
29,978	29,97	1	**g.s.**
46,354	16,5	0,2938	29,978
	19,6	0,4593	27,369
	46,35	0,2469	**g.s.**
74,149	44,14	0,7133	29,978
	74,15	0,2867	**g.s.**
84,544	38,2	0,5862	46,354
	54,6	0,2814	29,978
	57,19	0,1324	27,369
109,992	25,48	0,6618	84,544
	35,83	0,09	74,149
	63,64	0,2482	46,354
126,848	52,71	0,4792	74,149
	96,84	0,5208	29,978
187,34	60,5	0,0696	126,848
	77,34	0,7564	109,992
	102,6	0,174	84,544
210,8	23,6	0,1667	187,34
	100,85	0,8333	109,992
273,19	198,89	0,0387	74,149
	226,6	0,0165	46,354
	243,11	0,3079	29,978
	246,04	0,1062	27,369
	273,15	0,5307	**g.s.**
330,04	57,19	0,0015	273,19
	245,6	0,0009	84,544
	255,78	0,0135	74,149
	283,682	0,211	46,354
	300,066	0,3083	29,978
	302,667	0,2912	27,369
	330,055	0,1736	**g.s.**

USC UNIVERSIDADE DE SANTIAGO DE COMPOSTELA

Table 31: De-excitation of ^{227}Ac.

Initial Daughter State E_i	E_γ	I_γ	Final Daughter State E_f
354,5	24,5	0,0358	330,04
	327,14	0,2625	27,369
	354,48	0,7017	**g.s.**
387,2	57,19	0,0032	330,04
	260,19	0,2083	126848
	277,22	0,0779	109,992
	302,667	0,2	84,544
	312,92	0,1152	74,149
	340,71	0,2029	46,354
	357,11	0,1923	29,978
	387	0,0002	**g.s.**

Table 32: Decay of ^{227}Ac.

Parent Nucleus	Parent $T_{1/2}$	Decay Mode	Daughter Nucleus	I_{decay}	Initial Daughter State E_i
^{227}Ac	21,772 y	$\alpha : 1,38$ %	^{223}Fr	0,658	**g.s.**
				0,546	12,882
		$\beta^- : 98,62$ %	^{227}Th	0,54	**g.s.**
				0,35	9,3
				0,11	24,5

Table 33: De-excitation of ^{223}Fr. The 12,90 keV gamma is not included in the generator due to its low energy.

Initial Daughter State E_i	E_γ	I_γ	Final Daughter State E_f
12,882	12,90	1	**g.s.**

USC UNIVERSIDADE DE SANTIAGO DE COMPOSTELA

Table 34: De-excitation of ^{227}Th.

Initial Daughter State E_i	**E_γ**	**I_γ**	**Final Daughter State E_f**
9,3	9,3	1	**g.s.**
24,5	15,1	0,0215	9,3
	24,33	0,9785	**g.s.**

Table 35: Decay of ^{227}Th.

Parent Nucleus	**Parent $T_{1/2}$**	**Decay Mode**	**Daughter Nucleus**	**I_{decay}**	**Initial Daughter State E_i**
^{227}Th	18,68 d	α : 100 %	^{223}Ra	0,242	**g.s.**
				0,029	29,858
				0,235	61,424
				0,03	79,708
				0,0242	174,569
				0,0127	234,858
				0,204	286,087
				0,0489	329,856
				0,083	334,37
				0,0336	342,59
				0,015	350,53
				0,0426	376,296

USC UNIVERSIDADE DE SANTIAGO DE COMPOSTELA

Table 36: De-excitation of ^{223}Ra.

Initial Daughter State E_i	E_γ	I_γ	Final Daughter State E_f
29,858	29,86	1	**g.s.**
50,128	20,25	0,0272	29,858
	50,13	0,9728	**g.s.**
61,424	31,58	0,4318	29,858
	61,441	0,5682	**g.s.**
79,708	29,6	0,0024	50,128
	49,82	0,1832	29,858
	79,69	0,8144	**g.s.**
104,6	43,8	0,6711	61,424
	75,01	0,3289	29,858
123,793	44,22	0,0297	79,708
	62,45	0,1138	61,424
	73,63	0,0076	50,128
	93,88	0,8489	29,858
130,41	6,5	0,0063	123,793
	68,74	0,4051	61,424
	100,27	0,5886	29,858
174,569	44,4	0,0741	130,41
	113,11	0,9259	61,424
234,858	111,05	0,0012	123,793
	155,5	0,0007	79,708
	173,45	0,0263	61,424
	184,65	0,054	50,128
	204,98	0,2429	29,858
	234,76	0,6749	**g.s.**
280,182	150,14	0,0644	130,41
	175,8	0,1223	104,6
	200,5	0,0772	79,708
	218,9	0,6435	61,424
	250,15	0,0521	29,858
	280,7	0,0405	**g.s.**

USC UNIVERSIDADE DE SANTIAGO DE COMPOSTELA

Table 37: De-excitation of ^{223}Ra.

Initial Daughter State E_i	**E_γ**	**I_γ**	**Final Daughter State E_f**
286,087	235,96	0,5959	50,128
	256,23	0,3236	29,858
	286,09	0,0805	**g.s.**
329,856	43,77	0,0345	286,087
	94,97	0,0038	234,858
	206,08	0,0412	123,793
	250,27	0,0738	79,708
	279,8	0,0086	50,128
	299,98	0,3592	29,858
	329,85	0,4789	**g.s.**
334,37	48,3	0,0027	286,087
	54,19	0,0013	280,182
	99,58	0,0052	234,858
	204,14	0,0446	130,41
	210,62	0,2465	123,793
	254,63	0,1405	79,708
	272,91	0,1001	61,424
	284,24	0,0079	50,128
	304,5	0,2268	29,858
	334,37	0,2244	**g.s.**
342,59	56,42	0,0075	286,087
	107,76	0,0063	234,858
	262,87	0,0869	79,708
	281,42	0,1441	61,424
	292,41	0,0535	50,128
	312,69	0,4177	29,858
	342,55	0,284	**g.s.**
342,654	62,45	0,3418	280,182
	107,76	0,0134	234,858
	168,36	0,0254	174,569
	212,7	0,1335	130,41
	218,9	0,1842	123,793
	281,42	0,3017	61,424
350,53	8,15	0,0492	280,182
	64,35	0,169	234,858
	300,5	0,0893	174,569
	350,54	0,6925	130,41

USC UNIVERSIDADE DE SANTIAGO DE COMPOSTELA

Table 38: De-excitation of ^{223}Ra.

Initial Daughter State E_i	**E_γ**	**I_γ**	**Final Daughter State E_f**
376,296	33,39	0,0059	342,654
	41,93	0,0222	334,37
	96,03	0,0519	280,182
	141,42	0,089	234,858
	201,64	0,0178	174,569
	246,12	0,0093	130,41
	252,5	0,0853	123,793
	296,5	0,33	79,708
	314,85	0,3708	61,424
	325,99	0,0048	50,128
	346,45	0,0089	29,858
	376,27	0,0041	**g.s.**

Table 39: Decay of ^{223}Fr. The intensity of the alpha decay mode is so low that this branch is not inclued in the generator. The de-excitations of the ^{223}Ra nucleus are listed in the previous tables.

Parent Nucleus	**Parent $T_{1/2}$**	**Decay Mode**	**Daughter Nucleus**	**I_{decay}**	**Initial Daughter State E_i**
^{223}Fr	22,00 m	$\alpha : 0,006$ %	^{219}At	-	-
		$\beta^- : 99,994$ %	^{223}Ra	0,01	**g.s.**
				0,01	29,858
				0,7	50,128
				0,15	79,708
				0,101	234,585
				0,029	369,361

USC UNIVERSIDADE DE SANTIAGO DE COMPOSTELA

Table 40: Decay of ^{223}Ra.

Parent Nucleus	**Parent $T_{1/2}$**	**Decay Mode**	**Daughter Nucleus**	**I_{decay}**	**Initial Daughter State E_i**
^{223}Ra	11,43 d	α : 100 %	^{219}Rn	0,01	**g.s.**
				0,09	126,77
				0,516	158,64
				0,252	269,48
				0,09	338,27
				0,01	376,26
				0,032	445,03

USC UNIVERSIDADE DE SANTIAGO DE COMPOSTELA

Table 41: De-excitation of ^{219}Rn. In this case, due to the large quantity of states we have labeled them with numbers instead of their corresponding energies

Initial Daughter State E_i	**E_γ**	**I_γ**	**Final Daughter State E_f**
4,47	4,47	1	**g.s.**
14,37	10	0,4536	4,47
	14,4	0,5464	**g.s.**
126,77	122,319	1	4,47
158,64	31,98	0,00001	126,77
	144,235	0,3369	14,37
	154,208	0,591	4,47
	158,635	0,07209	**g.s.**
269,48	110,856	0,0042	158,64
	255,2	0,0038	14,37
	269,463	0,992	**g.s.**
338,27	179,54	0,0214	158,64
	323,871	0,564	14,37
	334,01	0,0141	4,47
	338,282	0,4005	**g.s.**
342,78	328,38	0,4845	14,37
	342,87	0,5155	**g.s.**
376,26	249,3	0,0667	126,77
	362,052	0,0783	14,37
	371,676	0,8333	4,47
	376,1	0,0217	**g.s.**
445,03	102,2	0,0006	342,78
	106,78	0,0172	338,27
	175,65	0,0143	269,48
	430,6	0,0143	14,37
	445,033	0,9536	**g.s.**

USC UNIVERSIDADE DE SANTIAGO DE COMPOSTELA

Table 42: Decay of ^{219}Rn.

Parent Nucleus	**Parent $T_{1/2}$**	**Decay Mode**	**Daughter Nucleus**	**I_{decay}**	**Initial Daughter State E_i**
^{219}Rn	3,96 s	α : 100 %	^{215}Po	0,794	**g.s.**
				0,129	271,228
				0,077	401,812

Table 43: De-excitation of ^{215}Po.

Initial Daughter State E_i	**E_γ**	**I_γ**	**Final Daughter State E_f**
271,228	271,23	1	**g.s.**
401,812	130,6	0,0196	271,228
	401,81	0,9804	**g.s.**

Table 44: Decay of ^{211}Pb.

Parent Nucleus	**Parent $T_{1/2}$**	**Decay Mode**	**Daughter Nucleus**	**I_{decay}**	**Initial Daughter State E_i**
^{211}Pb	36,1 m	β^- : 100 %	^{211}Bi	0,9209	**g.s.**
				0,0163	404,866
				0,0628	831,96

USC UNIVERSIDADE DE SANTIAGO DE COMPOSTELA

Table 45: De-excitation of ^{211}Bi.

Initial Daughter State E_i	E_γ	I_γ	Final Daughter State E_f
404,866	404,853	1	**g.s.**
766,539	362,072	0,0645	404,866
	766,51	0,9355	**g.s.**
831,96	65,42	0,0145	766,539
	427,088	0,3276	404,866
	832,01	0,6579	**g.s.**

Table 46: Decay of ^{211}Bi. The intensity of the beta decay mode is so low that this branch is not inclued in the generator.

Parent Nucleus	Parent $T_{1/2}$	Decay Mode	Daughter Nucleus	I_{decay}	Initial Daughter State E_i
^{211}Bi	2,14 m	$\alpha : 99,724$ %	^{207}Tl	0,8377	**g.s.**
				0,1623	351,06
		$\beta^- : 0,276$ %	^{211}Po	0.276	**g.s.**

Table 47: De-excitation of ^{207}Tl.

Initial Daughter State E_i	E_γ	I_γ	Final Daughter State E_f
351,06	351,07	1	**g.s.**

USC UNIVERSIDADE DE SANTIAGO DE COMPOSTELA

Appendix C

Thorium Series

In this appendix we show the decay information for each nucleus which emmits gamma radiation during the entire transition in the uranium series. This information have been implemented in the EnsarRoot generators. Energy units are expressed in keV and the probabilities for each transition are indicated in decimal fraction. Nuclear data is based on the information provided by the Table of Radioactive Isotopes from The Lund/LBNL Nuclear Data Search [143] and on NNDC data base [26].

Table 48: Decay of ^{232}Th.

Parent Nucleus	**Parent $T_{1/2}$**	**Decay Mode**	**Daughter Nucleus**	**I_{decay}**	**Initial Daughter State E_i**
^{232}Th	$14,0 \times 10^9$ y	$\alpha : 100\%$	^{228}Ra	0,782	**g.s.**
				0,217	63,823

Table 49: De-excitation of ^{228}Ra.

Initial Daughter State E_i	**E_γ**	**I_γ**	**Final Daughter State E_f**
63,823	63,823	1	**g.s.**

USC UNIVERSIDADE DE SANTIAGO DE COMPOSTELA

Table 50: Decay of ^{228}Ra.

Parent Nucleus	Parent $T_{1/2}$	Decay Mode	Daughter Nucleus	I_{decay}	Initial Daughter State E_i
^{228}Ra	5,75 y	β^- : 100%	^{228}Ac	0,3	33,1
				0,2	20,2
				0,4	6,7
				0,1	6,3

Table 51: De-excitation of ^{228}Ac.

Initial Daughter State E_i	E_γ	I_γ	Final Daughter State E_f
6,3	6,28	1	**g.s.**
6,7	6,67	1	**g.s.**
20,2	13,52	1	6,7
33,1	12,75	0,5	20,2
	26,4	0,5	6,7

Table 52: Decay of ^{228}Th.

Parent Nucleus	Parent $T_{1/2}$	Decay Mode	Daughter Nucleus	I_{decay}	Initial Daughter State E_i
^{228}Th	1,9125 y	α : 100%	^{224}Ra	0,734	**g.s.**
				0,26	84,4

Table 53: De-excitation of ^{224}Ra.

Initial Daughter State E_i	E_γ	I_γ	Final Daughter State E_f
84,4	84,373	1	**g.s.**

USC UNIVERSIDADE DE SANTIAGO DE COMPOSTELA

Table 54: Decay of ^{224}Ra.

Parent Nucleus	Parent $T_{1/2}$	Decay Mode	Daughter Nucleus	I_{decay}	Initial Daughter State E_i
^{224}Ra	3,66 d	α : 100%	^{220}Rn	0,9492	**g.s.**
				0,0506	241

Table 55: De-excitation of ^{220}Rn.

Initial Daughter State E_i	E_γ	I_γ	Final Daughter State E_f
241	240,986	1	**g.s.**

Table 56: Decay of ^{212}Pb.

Parent Nucleus	Parent $T_{1/2}$	Decay Mode	Daughter Nucleus	I_{decay}	Initial Daughter State E_i
^{212}Pb	10,622 h	β^- : 100%	^{212}Bi	0,119	**g.s.**
				0,831	238,6
				0,050	415,3

Table 57: De-excitation of ^{212}Bi .

Initial Daughter State E_i	E_γ	I_γ	Final Daughter State E_f
115,2	115,183	1	**g.s.**
238,6	123,5	0,0002	115,2
	238,632	0,9998	**g.s.**
415,3	176,68	0,015686	238.6
	300,087	0,980392	115,2
	415,2	0,003922	**g.s.**

USC UNIVERSIDADE DE SANTIAGO DE COMPOSTELA

Table 58: Decay of ^{212}Bi.

Parent Nucleus	Parent $T_{1/2}$	Decay Mode	Daughter Nucleus	I_{decay}	Initial Daughter State E_i
^{212}Bi	60,55 m	$\alpha : 35,94$ %	^{208}Tl	0,0975	**g.s.**
				0,2513	39,9
^{212}Bi	60,55 m	$\beta^- : 64,06$ %	^{212}Po	0,5537	**g.s.**
				0,0447	727,3
				0,0144	1512,7
				0,186	1620,7

Table 59: De-excitation of ^{208}Tl.

Initial Daughter State E_i	E_γ	I_γ	Final Daughter State E_f
39,9	39,9	1	**g.s.**

Table 60: De-excitation of ^{212}Po.

Initial Daughter State E_i	E_γ	I_γ	Final Daughter State E_f
727,3	727,3	1	**g.s.**
1512,7	785,37	0,79365	727,3
	1512,7	0,20635	**g.s.**
1620,7	893,408	0,2	727,3
	1620,5	0,8	**g.s.**

USC UNIVERSIDADE DE SANTIAGO DE COMPOSTELA

Table 61: Decay of ^{208}Tl.

Parent Nucleus	**Parent $T_{1/2}$**	**Decay Mode**	**Daughter Nucleus**	**I_{decay}**	**Initial Daughter State E_i**
^{208}Tl	3,053 m	β^- : 100%	^{208}Pb	0,0318	3960,93
				0,242	3708,41
				0,222	3475,088
				0,5042	3197,717

Table 62: De-excitation of ^{208}Pb .

IInitial Daughter State E_i	**E_γ**	**I_γ**	**Final Daughter State E_f**
2614,522	2614,511	1	**g.s.**
3197,717	583,187	1	2614,522
3475,088	277,371	0,33687	3197,717
	860,557	0,66313	2614,522
3708,41	233,33	0,01319	3475,088
	510,74	0,96984	3197,717
	1093,95	0,01697	2614,522
3960,93	252,755	0,27202	3708,41
	485,95	0,01776	3475,088
	763,429	0,71022	3197,717

USC UNIVERSIDADE DE SANTIAGO DE COMPOSTELA

Table 63: Decay of ^{228}Ac.

Parent Nucleus	Parent $T_{1/2}$	Decay Mode	Daughter Nucleus	I_{decay}	Initial Daughter State E_i
^{228}Ac	6,15 h	β^- : 100%	^{228}Th	0,0176	1724,299
				0,0243	1688,408
				0,0112	1682,81
				0,0419	1646,003
				0,03	1643,131
				0,0115	1638,284
				0,076	1531,490
				0,012	1431,994
				0,0311	1168,389
				0,058	1153,487
				0,059	1122,959
				0,0311	1022,542
				0,299	968,984
				0,1165	396,094
				0,1808	57,773

USC UNIVERSIDADE DE SANTIAGO DE COMPOSTELA

Table 64: De-excitation of ^{228}Th.

Initial Daughter State E_i	**E_γ**	**I_γ**	**Final Daughter State E_f**
57,773	57,766	1	**g.s.**
186,838	129,065	1	57,773
328,019	270,245	0,53107	57,773
	328,022	0,46893	**g.s.**
378,195	191,349	1	186,838
396,094	338,32	0,74488	57,773
	209,253	0,25475	186,838
	68,08	0,00037	328,019
519,208	141,01	0,09008	378,195
	332,37	0,90992	186,838
695,45	317,2	1	378,195
831,842	503,823	0,75472	328,019
	774,05	0,24151	57,773
	831	0,00377	**g.s.**
874,535	478,4	0,39952	396,094
	546,45	0,35957	328,019
	688,1	0,09988	186,838
	816,62	0,04914	57,773
	874,45	0,09189	**g.s.**
944,205	547,8	0,06859	396,094
	616,21	0,45725	328,019
	886,44	0,01692	57,773
	944,196	0,45725	**g.s.**
968,381	547,8	0,42194	396,094
	640,34	0,16456	328,019
	910,6	0,4135	57,773
968,451	449,23	0,26545	519,208
	572,3	0,45767	396,094
	590,1	0,00686	378,195
	781,9	0,0595	186,838
	910,7	0,21052	57,773

USC UNIVERSIDADE DE SANTIAGO DE COMPOSTELA

Table 65: De-excitation of ^{228}Th.

Initial Daughter State E_i	E_γ	I_γ	Final Daughter State E_f
968,984	782,1405	0,01128	186,838
	911,2044	0,61297	57,773
	968,97417	0,37575	**g.s.**
979,522	583,41	0,34459	396,094
	651,48	0,27912	328,019
	792,74	0,25155	186,838
	921,94	0,04549	57,773
	979,46	0,07925	**g.s.**
1016,386	497	0,16129	519,208
	620,33	0,12724	396,094
	688,11	0,10753	328,019
	829,55	0,12545	186,838
	958,62	0,44803	57,773
	1016,44	0,03046	**g.s.**
1022,542	835,701	0,24869	186,838
	964,777	0,75131	57,773
1059,928	540,68	0,23673	519,208
	663,88	0,3551	396,094
	873,11	0,40817	186,838
1074,80	555,5	0,37175	519,208
	678,6	0,33457	396,094
	697,1	0,05948	378,195
	887,9	0,09665	186,838
	1017	0,13755	57,773
1091,048	571,8	0,01718	519,208
	694,8	0,02166	396,094
	713,1	0,01344	378,195
	904,19	0,74683	186,838
	1033,25	0,20089;	57,773
1122,959	100,41	0,01598	1022,542
	153,962	0,12206	968,984
	178,7	0,01453	944,205
	726,864	0,09881	396,094
	794,948	0,72653	328,019
	1065,19	0,02209	57,773

USC UNIVERSIDADE DE SANTIAGO DE COMPOSTELA

Table 66: De-excitation of ^{228}Th.

Initial Daughter State E_i	**E_γ**	**I_γ**	**Final Daughter State E_f**
1153,487	173,964	0,04648	979,522
	184,54	0,09295	968,984
	278,7	0,21289	874,535
	321,646	0,29985	831,842
	1095,679	0,16492	57,773
	1153,52	0,18291	**g.s.**
1168,389	77,34	0,0075	1091,048
	145,84	0,04588	1022,542
	199,41	0,09189	968,984
	199,8	0,00309	968,451
	224	0,03	944,205
	649,03	0,01037	519,208
	772,29	0,44115	396,094
	840,38	0,27351	328,019
	981,5	0,01323	186,838
	1110,61	0,08338	57,773
1174,515	796,2	0,32432	378,195
	987,7	0,67568	186,838
1175,41	231,42	0,01111	944,205
	779,5	0,03333	396,094
	847,1	0,02778	328,019
	988,45	0,55556	186,838
	1117,56	0,24444	57,773
	1175,33	0,12778	**g.s**
1200,60	178,14	0,05031	1022,542
	231,5	0,22642	968,984
	326,1	0,62893	874,535
	1013,54	0,06918	186,838
	1142,78	0,02516	57,773
1226,580	135,51	0,01999	1091,048
	204,031	0,12346	1022,542
	258,1	0,0241	968,451
	258,1	0,0241	968,381
	707,4	0,16167	519,208
	830,486	0,58789	396,094
	1039,84	0,05879	186,838
1270,08	891,8	1	378,195

USC UNIVERSIDADE DE SANTIAGO DE COMPOSTELA

Table 67: De-excitation of ^{228}Th.

Initial Daughter State E_i	E_γ	I_γ	Final Daughter State E_f
1297,435	206,3	0,34843	1091,048
	602	0,13937	695,45
	778,1	0,18815	519,208
	901,26	0,15679	396,094
	1110,61	0,167265	186,838
1344,142	168,62	0,04355	1175,41
	824,94	0,20906	519,208
	947,98	0,43554	396,094
	1016,44	0,0784	328,019
	1157,14	0,02875	186,838
	1286,27	0,2047	57,773
1416,10	399,8	0,18672	1016,386
	447,8	0,06846	968,451
	471,77	0,20747	944,205
	1019,86	0,13278	396,094
	1088,18	0,03734	328,019
	1229,4	0,18672	186,838
	1358,3	0,18051	57,773
1431,994	134,9	0,00503	1297,435
	161,6	0,00204	1270,08
	231,4	0,02092	1200,60
	257,49	0,00362	1174,515
	263,62	0,00543	1168,389
	278,7	0,00402	1153,487
	340,98	0,04976	1091,048
	357,1	0,00933	1074,80
	372,2	0,00226	1059,928
	409,461	0,24713	1022,542
	415,6	0,01188	1016,386
	452,51	0,00254	979,522
	463,005	0,56551	968,984
	463,3	0,04015	968,451
	557,4	0,01414	874,535
	1053,8	0,0000113	378,195
	1103,41	0,00192	328,019
	1245,16	0,0125	186,838
	1374,24	0,0018087	57,773

USC UNIVERSIDADE DE SANTIAGO DE COMPOSTELA

Table 68: De-excitation of ^{228}Th.

Initial Daughter State E_i	**E_γ**	**I_γ**	**Final Daughter State E_f**
1531,490	99,509	0,44356	1431,994
	356,94	0,00599	1174,515
	377,99	0,00887	1153,487
	440,44	0,04258	1091,048
	508,97	0,17742	1022,542
	562,5	0,31493	968,984
	1135,24	0,00355	396,094
	1344,59	0,0031	186,838
1638,284	470,2	0,01137	1168,389
	515,12	0,04943	1122,959
	1309,71	0,01582	328,019
	1451,4	0,0089	186,838
	1580,53	0,49432	57,773
	1638,28	0,42016	**g.s.**
1643,131	299	0,07176	1344,142
	416,5	0,14801	1226,580
	474,75	0,02063	1168,389
	520,152	0,05606	1122,959
	583,2	0,06907	1059,928
	626,81	0,01256	1016,386
	674,16	0,09419	968,984
	674,7	0,03454	968,381
	698,96	0,03364	944,205
	1247,08	0,44851	396,094
	1315,31	0,01103	328,019

USC UNIVERSIDADE DE SANTIAGO DE COMPOSTELA

Table 69: De-excitation of ^{228}Th. In this case, due to the large quantity of states we have labeled them with numbers instead of their corresponding energies

Initial Daughter State E_i	E_γ	I_γ	Final Daughter State E_f
1646,003	114,54	0,0016	1531,490
	229,9	0,02455	1416,10
	419,4	0,00371	1226,580
	444,9	0,01542	1200,60
	470,6	0,01827	1175,41
	477,5	0,05196	1168,389
	492,3	0,00422	1153,487
	523,132	0,01998	1122,959
	555,1	0,00799	1091,048
	571,1	0,08564	1074,80
	586,2	0,01827	1059,928
	623,48	0,00257	1022,542
	629,4	0,00708	1016,386
	666,47	0,01011	979,522
	677,07	0,01136	968,984
	1249,97	0,01102	396,094
	1459,14	0,13531	186,838
	1588,19	0,57094	57,773
1682,81	660,1	0,00263	1022,542
	1286,3	0,41236	396,094
	1496,03	0,45314	186,838
	1625,06	0,13187	57,773
1688,408	42,46	0,00462	1646,003
	672	0,01286	1016,386
	813,77	0,00348	874,535
	1501,57	0,22244	186,838
	1630,627	0,7566	57,773
1724,299	308,2	0,1041	1416,10
	523,5	0,11767	1200,60
	548,74	0,00996	1175,41
	570,88	0,07785	1153,487
	701,744	0,08192	1022,542
	755,315	0,45259	968,381
	780,2	0,02308	944,205
	849,5	0,02308	874,535
	1537,87	0,01901	186,838
	1666,522	0,0783	57,773
	1724,2	0,01244	**g.s.**

USC UNIVERSIDADE DE SANTIAGO DE COMPOSTELA

Appendix D

EnsarRoot Developments: Gamma Cascades with Angular Correlations EnsarGenerator

This generator was specially developed for the simulations of the CALIFA Testing Experiment. In this investigation, they measured angular correlations of some particular gamma cascades using the two modules of CALIFA detector [142] placed strategically to have an optimum angular coverage.

When two gamma rays are emitted in succession from a nucleus, their emission directions are often correlated due to the physics of the emission process. In particular, when an excited nuclear state decays to the ground state through one or more intermediate states, the characteristics of the states affect the relative angular distribution of the photons emitted in each transition. The relative probability that a photon will be emitted at an angle θ with respect to a previous emitted photon is denoted as [173, 174],

$$W(\theta) = \sum_{i=0,even}^{\infty} A_{ii} P_i(\cos\theta). \tag{3}$$

In the previous equation, A_{ii} coefficients are directly related with the spin-parities J^P of the states involved in the transition, the momentums carried by the emitted gammas (multipole order) and the mixing ratio for each transition, and $P_i(\cos\theta)$ are the Legendre polynomials. The first Legendre polynomials are listed in Table 70. Moreover, the sum in the previous equation only involves even values of i in order to conserve parity rule.

One way of determining the spins of nuclear levels and unknown mixing ratios is studying angular correlations experimentally for instance, the values of A_{ii} coefficients could be measured by fitting experimental data distributions.

In particular, gamma cascades with low spins and low multipolarities are described by the lowest orders of the previous series, as a result, Eq. 3 can be truncated and re-written as

USC
UNIVERSIDADE DE SANTIAGO DE COMPOSTELA

Table 70: The first five Legendre Polynomials where x represents cos(θ).

Legendre Polynomial Order	Form
$P_0(x)$	1
$P_1(x)$	x
$P_2(x)$	$\frac{1}{2}(3x^2-1)$
$P_3(x)$	$\frac{1}{2}(5x^3-3x)$
$P_4(x)$	$\frac{1}{8}(35x^4-30x^2+3)$

$$W(\theta) = A_{00}\big(1 + a_2 P_2(\cos\theta) + a_4 P_4(\cos\theta)]\big), \tag{4}$$

where

$$a_i = A_{ii}/A_{00}. \tag{5}$$

Table 71: Theoretical coefficients a_2 and a_4 for some cascades with diverse nuclear spins. All of them land into a ground state with $J = 0$.

Cascade Nuclear Spins	a_2	a_4
1→2→0	-1/3	0
2→2→0	3/7	0
2→3→0	0	-1/3
2→4→0	1/8	1/24
2→0→0	-3	4
2→1→0	5	-16/3

Figure 9 shows the intensity $W(\theta)$ as a function of the angle θ for some cascades with different nuclear spins. We can observe that angular correlations present diverse degrees of anisotropies. The theoretical coefficients employed are listed on Table 71.

In order to simulate gammas with angular distributions diverse components have been included in the generator: the energy of gammas for each de-excitation, the occupation number of each energy level in the de-excitation scheme and the angular correlations distributions. The first two requirements were easily implemented in the code and data could be obtained from any experimental data source. On the contrary, angular correlations were more complicated to simulate, for this reason, and because the nuclear cascades

USC UNIVERSIDADE DE SANTIAGO DE COMPOSTELA

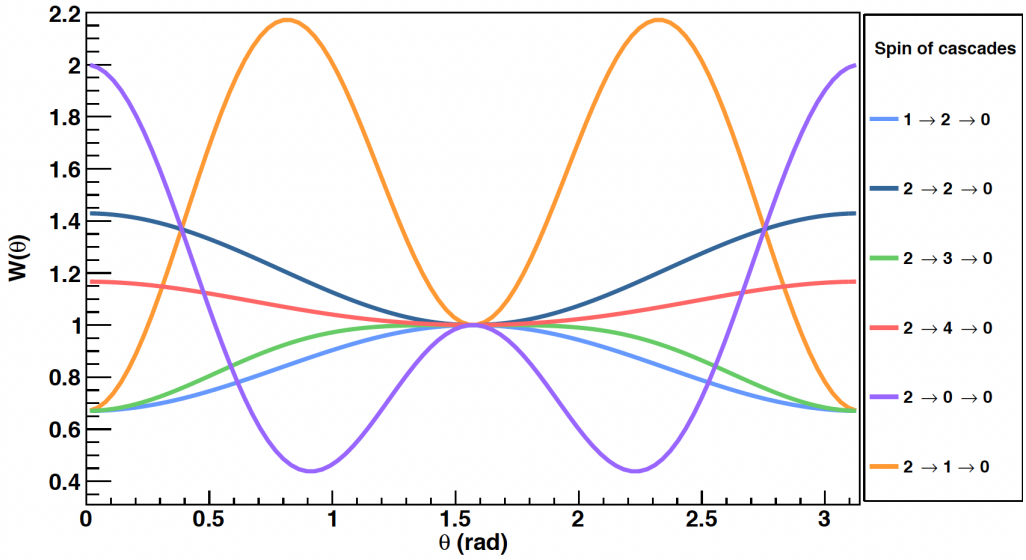

Figure 9: Angular correlations plot for diverse nuclear cascades. On the legend, the spin cascades with different colors are displayed. The theoretical coefficients of each cascade are listed on Table 71.

under analysis have low spins the Eq. 4 was used. Moreover, for simplicity, the generator was restricted to two gamma emissions in a single cascade. These three parameters are the generator's inputs given by the user every time a different cascade is simulated.

The Correlated Gamma Cascade Generator works in two steps. Initially, the first gamma is emitted isotropically in the Laboratory Reference System, from the highest nuclear excited state to a lower energy level. In the second place, the following gamma is emitted from this level to a less energetic level or ground state following an angular correlation distribution in the Reference System of the first gamma ray.

This anisotropy is ruled by θ angle, henceforth, the inverse transform sampling method was used to obtain a random angle θ following $W(\theta)$ distribution. First, we constructed the probability function $p(\theta)$, that is the multiplication of the angular correlations and the term giving the volume differential of spherical coordinates:

$$p(\theta) = W(\theta)\sin(\theta), \qquad where\ \theta\ \in\ [0, \pi]. \tag{6}$$

Afterwards, this function was integrated and normalized as,

USC UNIVERSIDADE DE SANTIAGO DE COMPOSTELA

$$P(\theta) = \frac{1}{N}\int_0^{\pi} W(\theta)\sin(\theta)d\theta \tag{7}$$

$$= \frac{1}{2c}\Big(-\cos(\theta) - a\cos^3(\theta) - b\cos^5(\theta) + c\Big). \tag{8}$$

The coefficients are related such that,

$$a = \frac{a_2}{3}, \quad b = \frac{a_4}{5} \quad and \quad c = 1 + a + b. \tag{9}$$

The application of the inverse transform sampling method requires to find the solutions of the $P(\theta)$ inverse: $P^{-1}(R)$ where R is a random number in the interval [0,1]. However, $P(\theta)$ has no analytical inverse, so we applied an equivalent mathematical calculation to find these solutions. Using a numerical method implemented in Root (BrentRootFinder [175]), we found the zeros of the following equation,

$$0 = P(\theta) - R, \tag{10}$$

that are the solutions of $P^{-1}(R)$. This means that for each random number R we obtain a polar angle θ.

At this point, the angles θ_1, ϕ_1 of the first emitted gamma are isotropically generated in the Laboratory Reference System while the isotropic ϕ_2 and the correlated θ_2 of the second gamma are generated in the Reference System of the first gamma. As a result, gamma's momenta are obtained in different reference systems:

$$p_1 = (p_{1x}, p_{1y}, p_{1z}) \quad and \quad p_2' = (p_{2x}', p_{2y}', p_{2z}'). \tag{11}$$

In terms of simulation, both momenta needed to be in the same Laboratory Reference System, therefore, to change the reference system of p_2' the inverse of rotation matrix using Euler's angles was applied,

$$p_2 = R^{-1}p_2', \tag{12}$$

and

$$R = \begin{pmatrix} \cos\psi & \sin\psi & 0 \\ -\sin\psi & \cos\psi & 0 \\ 0 & 0 & 1 \end{pmatrix} \begin{pmatrix} 1 & 0 & 0 \\ 0 & \cos\phi & \sin\phi \\ 0 & -\sin\phi & \cos\phi \end{pmatrix} \begin{pmatrix} \cos\theta & \sin\theta & 0 \\ -\sin\theta & \cos\theta & 0 \\ 0 & 0 & 1 \end{pmatrix}, \tag{13}$$

where $\psi = 0$, $\phi = -\phi_1 - \pi/2$ and $\theta = \theta_1$.

USC UNIVERSIDADE DE SANTIAGO DE COMPOSTELA

As we have mentioned before, this generator can only emit two angular correlated gamma rays every time, although it is possible to run this generator multiple times in a single simulation to obtain an angular distribution. Due to the fact that the user can control many parameters of the generator (such as energies, coefficients of the angular distribution and occupancy number of each level) it is a flexible and versatile tool that can reproduce almost every nuclear gamma cascade.

EnsarRoot Developments: The CALIFA Testing Experiment Setup

The setup of the CALIFA Testing Experiment was also simulated within EnsarRoot program. The CALIFA Testing Experiment was also located at CTN/IST laboratory, though, in this case, the standard setup of PIGE Line was modified in order to fulfill the experimental requirements. As a result of this change, the simulated setup includes: in the central position a reaction chamber of 27 cm height and 11 cm of diameter made of Al+5083[1] material and filled with vacuum; outside the reaction chamber at 13 cm from its center and at 90° from the beamline the HPGe detector of the CTN/IST laboratory before described is situated; and lastly, there are two sections of CALIFA detector [142] surrounding the reaction chamber (Figure 10).

The EnsarRoot framework includes a part of the CALIFA detector: the CALIFA demonstrator [176]. It is a cylindrical barrel divided in 11 sections and inside each section there are 64 CsI(Tl) scintillator crystals. Using this simulation we have activated two sections of the demonstrator to get the two detectors used at this experiment. In addition, we had to simulate two aluminum boxes where these sections were placed at the moment of the measurement. These boxes, made of Al+5083 material, were carefully recreated including walls of 5 mm thicker and four bars at the corners, upper holes of air and a thin mylar base of 3 μm thicker (see right picture of Figure 10). Therefore, we have simulated two CALIFA sections inside their corresponding boxes which act as two separate detectors working individually. Each unit was translated at a distance of 51,69 cm from the origin and rotated: one section at 90° and the other at 180° with respect to the HPGe detector.

[1]The Al+5083 material was intentionally recreated within EnsarRoot. Its chemical composition is 0,9555 % Al, 0,005 % Cr, 0,04 % Mg and 0,004 % Mn.

USC UNIVERSIDADE DE SANTIAGO DE COMPOSTELA

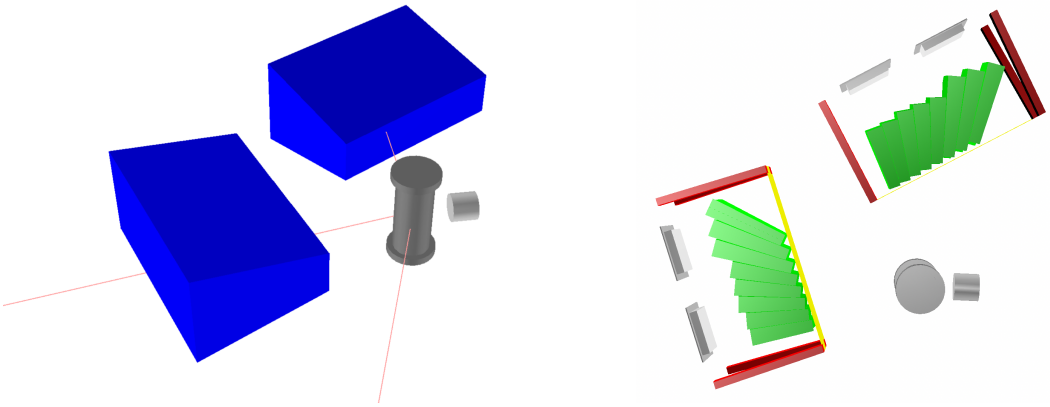

Figure 10: Artistic view of the CALIFA Testing Experiment setup from the event viewer of EnsarRoot. On the side, there are two CALIFA sections (blue boxes), an HPGe detector, the reaction chamber in the central part, and the red lines represent tracks of gamma rays. On the right side, on the ZX plane, there are the same elements showing the inner petal box where the green volumes represent the CsI(Tl) scintillator crystals.

USC UNIVERSIDADE DE SANTIAGO DE COMPOSTELA

Appendix E

R3BRoot Developments: Online Calibration of CALIFA detector

In the same line of the EnsarRoot developments, we expanded the R3BRoot code [11] in order to implement a tool to calibrate CALIFA detector [142]. The R3BRoot program is the simulation and the analysis framework for R3B experiment [177]. It has a similar structure and functionalities than the EnsarRoot code explained in this thesis.

Energy Calibration Parameters

In order to calibrate CALIFA experimental data diverse classes have been developed to obtain and to store the calibration parameters for each crystal of the detector. The classes that were developed are:

- R3BCalifaCrystalCalPar.
- R3BCalifaMapped2CrystalCalPar.
- R3BCalifaContFactory.

The R3BCalifaCrystalCalPar class is the collection of Energy Calibration Parameters and they are calculated by adding a task called R3BCalifaMapped 2CrystalCalPar. The objective of this task is to analyse some spectra (Mapped Data) by fitting known photopeaks determined by the user. Using this information the calibration parameters are determined and they are stored in the R3BCalifaContFactory (a virtual container of parameters). During this process the FairRunTimeDB is also employed. Figure 11 shows schematically the experimental data workflow and the R3BRoot classes involved in the process.

The new task R3BCalifaMapped2CrystalCalPar requires some settings in order to carry on the calculation of these parameters:

USC UNIVERSIDADE DE SANTIAGO DE COMPOSTELA

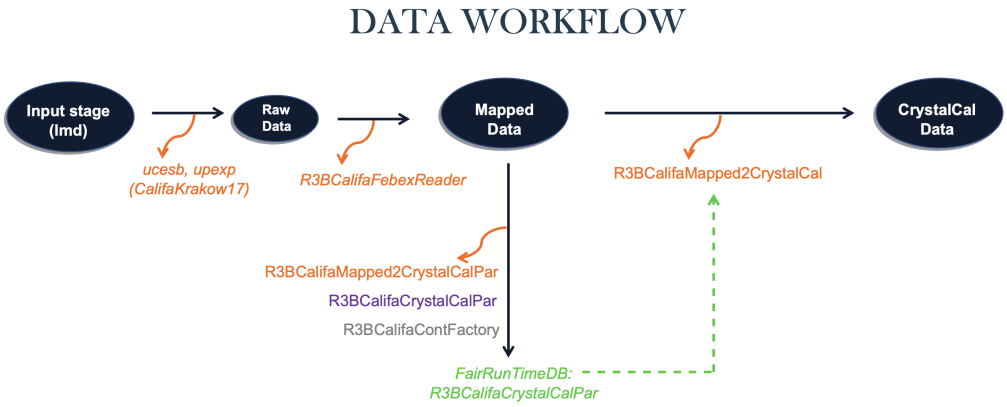

Figure 11: R3BRoot experimental data workflow and the classes involved in the process to convert input stage data (lmd) into calibrated data for each individual crystal (CrystalCal Data).

- Total number of crystals.
- Minimum of statistics.
- Number of fitting parameters: 2 parameters for a 2nd degree polynomial (also defined by default) up to 5 parameters for a 5th degree polynomial.
- Energy range and bins of the histograms that will generate the task.
- Sigma and threshold to search the calibration peaks.
- A pointer to a TArrayF filled with the energies of the peaks that we desire to calibrate (decreasing order in energy).

An example of these settings and the task implementation is displayed on the Figure 12.

USC UNIVERSIDADE DE SANTIAGO DE COMPOSTELA

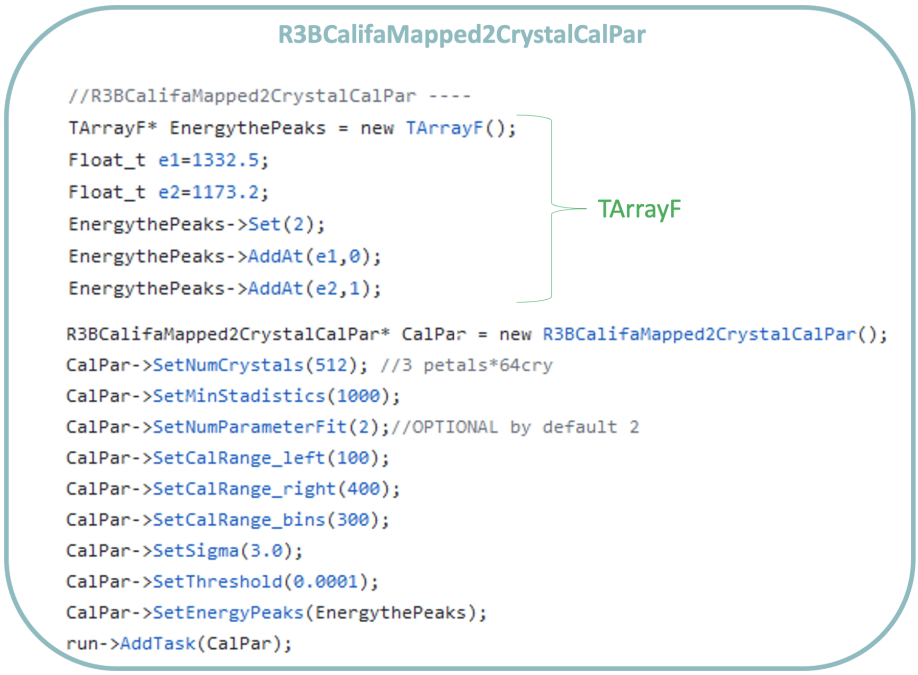

Figure 12: Example of usage of R3BCalifaMapped2CrystalCalPar task with all the required settings. The TArrayF is highlighted in green and filled with data of a ^{60}Co source.

Online Calibration

Once the previous classes were created we developed a class that uses them and allows to visualise and calibrate CALIFA spectra during the course of an experiment, i.e. an online analysis. This task was named R3BOnlineSpectra and is based on a general FairTask. In order to obtain an accurate analysis, we added different settings:

- Total number of petals (a petal is a gathering of 64 crystals).
- CrystalId specific labels for a particular experiment (the CrystalId is the number designated for each individual crystal).
- Histograms information.
- Type of data introduced: it could be Mapped or Cal data.

These settings are basic functions implemented on the header and on the body of the new class and they must be "called" when the task is used. Moreover, each setting requires be filled with data, for example, a boolean or a file name. On the left of the Figure 13 there are displayed the setters of

USC UNIVERSIDADE DE SANTIAGO DE COMPOSTELA

the R3BOnlineSpectra class and, on the left, the same functions when this task is used in a normal macro.

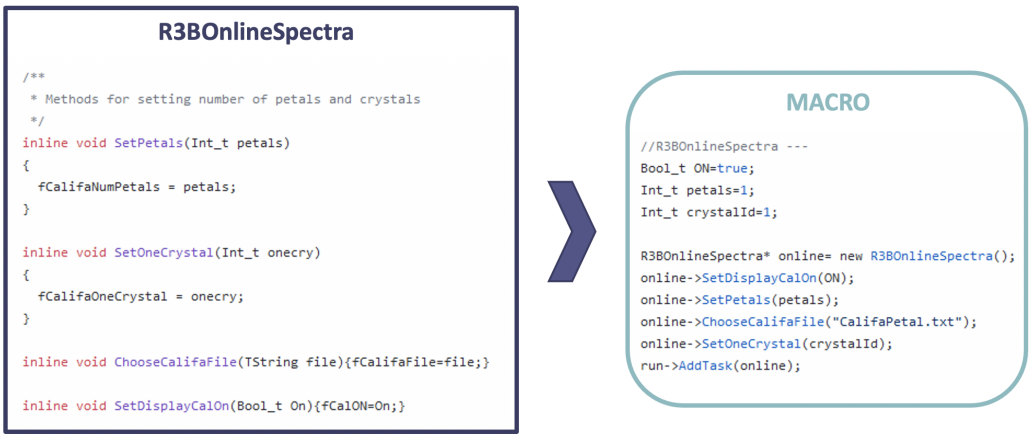

Figure 13: Scheme of the R3BOnlineSpectra settings (on the left) and an example of how to use them on a general macro (on the right).

The histograms obtained with the R3BOnlineSpectra task are shown in the following figures. The Figures 14, 15 and 16 exhibit energy histograms of one crystal with a CrystalId=1, of various crystals and of one CALIFA petal, respectively. Figures 17 and 18 represent bidimensionals histograms of the petal number and the crystal energy versus the CrystalId number.

USC UNIVERSIDADE DE SANTIAGO DE COMPOSTELA

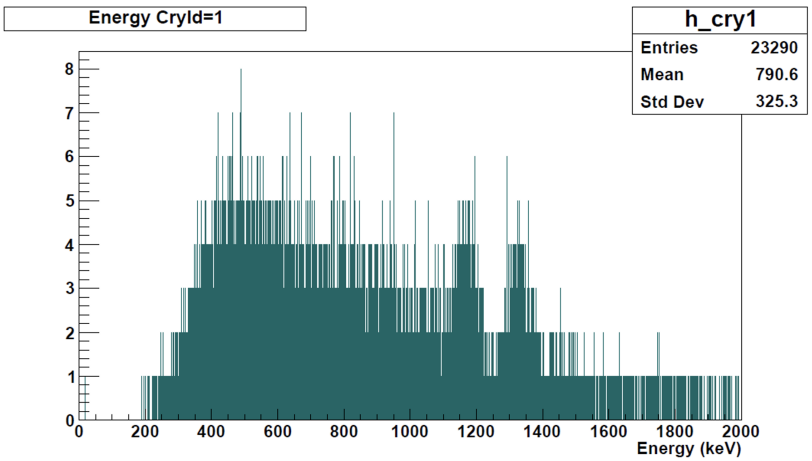

Figure 14: Energy histogram of one CALIFA crystal with a selected CrystalId=1 obtained with the R3BOnlineSpectra task.

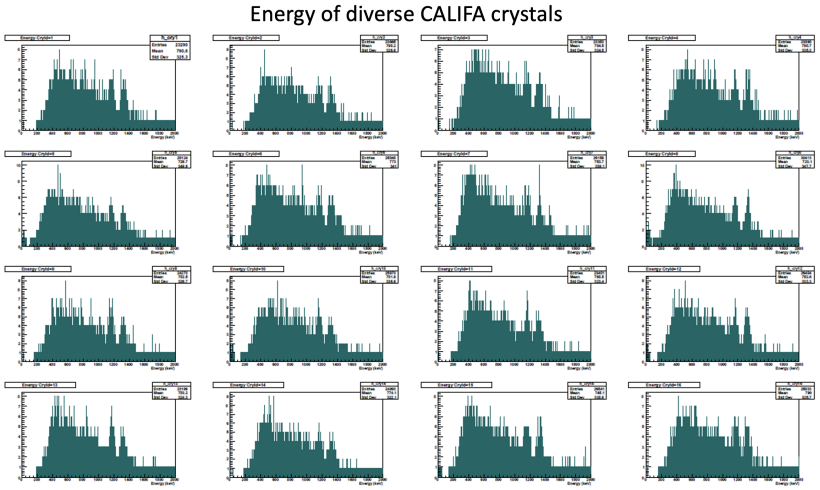

Figure 15: Energy histograms of the CALIFA crystals obtained with the R3BOnlineSpectra task. The x-axis is the energy in keV and the y-axis the number of counts.

USC UNIVERSIDADE DE SANTIAGO DE COMPOSTELA

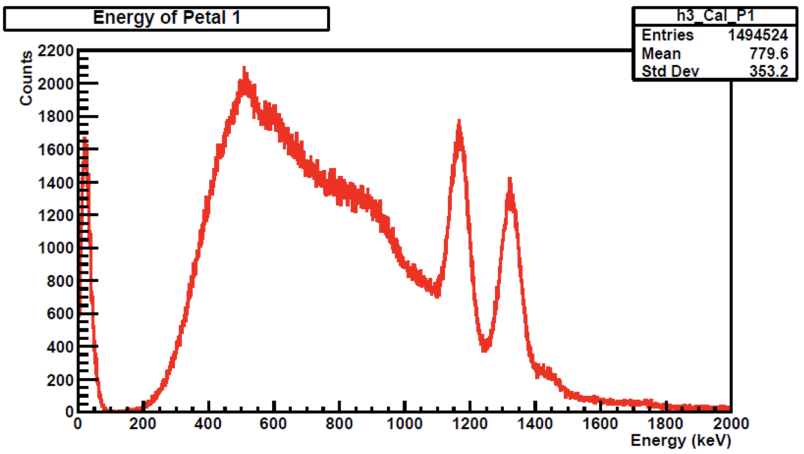

Figure 16: Energy histogram of one CALIFA petal (a gathering 64 crystals) obtained with the R3BOnlineSpectra task.

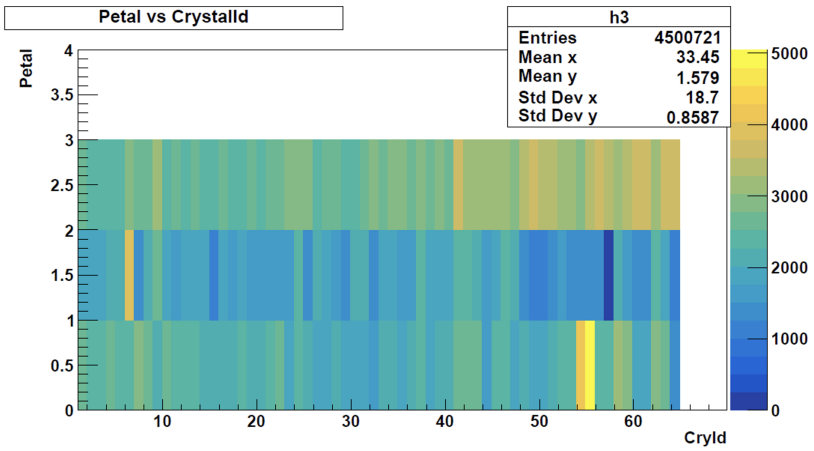

Figure 17: Bidimensional histogram of the CALIFA petal number (1, 2 or 3) versus the CrystalId number obtained with the R3BOnlineSpectra task.

USC UNIVERSIDADE DE SANTIAGO DE COMPOSTELA

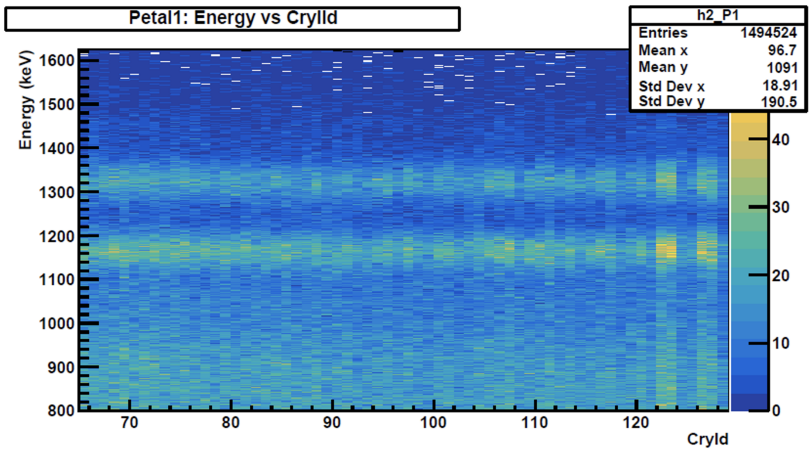

Figure 18: Bidimensional histogram of the crystal energy versus the CrystalId number obtained with the R3BOnlineSpectra task.

USC UNIVERSIDADE DE SANTIAGO DE COMPOSTELA

Appendix F

Efficiency Error Calculation

Photopeak error

Photopeak equation:

$$N_\gamma = N_{Histogram} - N_{background}. \tag{14}$$

Photopeak error equation:

$$\sigma(N_\gamma) = \sqrt{\sigma(N_{Histogram})^2 + \sigma(N_{background})^2}. \tag{15}$$

where $\sigma(N_{Histogram}) = \sqrt{N_{Histogram}}$ and $\sigma(N_{background}) = \sqrt{N_{background}}$ are both the statistical error.

Activity Error

The lifetime of the ^{132}Eu is $T_{1/2} = 13,517 \pm 0,0001$ years.

From the lifetime of the nucleus we can calculate the decay constant as,

$$\lambda = \frac{\ln 2}{T_{1/2}}, \tag{16}$$

and its error,

$$\sigma(\lambda) = \frac{\ln 2 \sigma(T_{1/2})}{T_{1/2}^2}. \tag{17}$$

The activity of the sample at any time t is expressed as,

$$A(t) = A_0 \exp^{-\lambda t}, \tag{18}$$

where the activity at time $t = 0$ s is $A_0 = 382950 \pm 1850$ Bq and its error is:

USC UNIVERSIDADE DE SANTIAGO DE COMPOSTELA

$$\sigma(A(t)) = \sqrt{\left[\exp^{-\lambda t}\,\sigma(A_0)\right]^2 + \left[A_0 t \exp^{-\lambda t}\,\sigma(\lambda)\right]^2}. \tag{19}$$

Number of gamma emissions in all solid angle

The total number of gamma emissions during the time interval Δt of the measurement is:

$$N_i = \mathrm{BR}_i \cdot \Delta t \cdot A(t), \tag{20}$$

where the subindex i refers to each individual gamma, thus its error is:

$$\sigma(N_i) = \sqrt{\left[\Delta t A(t)\sigma(\mathrm{BR}_i)\right]^2 + \left[\mathrm{BR}_i \Delta t \sigma(A(t))\right]^2}. \tag{21}$$

Efficiency

As we have mentioned in Section 4.4.3.1 the absolute efficiency for each gamma ray is determined by:

$$\varepsilon_{abs} = \frac{N_\gamma}{N_{tot}}, \tag{22}$$

hence, its error definition is:

$$\sigma(\varepsilon_{abs}) = \sqrt{\left[\frac{\sigma(N_\gamma)}{N_{tot}}\right]^2 + \left[\frac{N_\gamma \sigma(N_{tot})}{N_{tot}^2}\right]^2}. \tag{23}$$

USC UNIVERSIDADE DE SANTIAGO DE COMPOSTELA

Appendix G

Cross Section Error Calculations

In this appendix there are detailed all formulas employed for error estimation of each magnitud. To propagate errors, dispersion formula has been applied. In all cases, the covariance term has been dismissed due to most variables are independent of each other or there is no clear correlation.

Either gamma ray yield and proton yield follow Poisson statistics, therefore, they have random uncertainties, evaluated from the subtraction of the background to the peak signal:

- Gamma ray yield error:

$$\sigma_{Y_{\gamma,p}} = \sqrt{\sigma^2_{peak} + \sigma^2_{bkg}}, \tag{24}$$

  in particular, the 1763.04 keV peak has suffered an additional subtraction due to the superposition of natural photopeaks at 1764.5 keV from the decay of ^{214}Bi (uranium series).

$$\sigma_{Y_{\gamma,p}} = \sqrt{\sigma^2_{peak} + \sigma^2_{bkg} + \sigma^2_{^{214}Bi\ peak}}. \tag{25}$$

- Backscattered protons by silver nucleus yield error:

$$\sigma_{Y_{p,Ag}} = \sqrt{\sigma^2_{peak} + \sigma^2_{bkg}}, \tag{26}$$

as a consequence, they directly depend on the number of counts in each measurement.

USC UNIVERSIDADE DE SANTIAGO DE COMPOSTELA

Rutherford Cross Section Error

Secondly, there are a series of systematic uncertainties, which do not depend on any statistical process. Rutherford cross section error depends on beam energy error (σ_{E_1}) and backscattering angle error (σ_θ) as follows,

$$\sigma_{\sigma_{Ruth}} = \sqrt{\left[\frac{(\alpha hc Z_1 Z_2)^2}{8E_1^3}\frac{1}{sin^2(\theta/2)}\sigma_{E_1}\right]^2 + \left[\frac{(\alpha hc Z_1 Z_2)^2}{16E_1^2}\frac{cos(\theta/2)}{sin^3(\theta/2)}\sigma_\theta\right]^2}, \tag{27}$$

in turn, σ_θ depends on vertical plane deviation of the beam, denoted as y. Therefore, and taking into account that $\theta = 180 - arctan(y/x)$, where $x = 79.755$ cm is a fixed value that represents the distance between target position and reaction chamber entrance, backscattering angle error is:

$$\sigma_\theta = \frac{1}{y^2/x + x}\sigma_y. \tag{28}$$

Differential Cross Section Error

Finally, the error expression for the differential cross section is:

$$\sigma_\sigma = \left(\left[\frac{\partial\sigma}{\partial Y_{\gamma,p}}\sigma_{Y_{\gamma,p}}\right]^2 + \left[\frac{\partial\sigma}{\partial r}\sigma_r\right]^2 + \left[\frac{\partial\sigma}{\partial\Omega}\sigma_\Omega\right]^2 + \left[\frac{\partial\sigma}{\partial\sigma_{Ruth}}\sigma_{\sigma_{Ruth}}\right]^2 + \right. \tag{29}$$

$$\left. + \left[\frac{\partial\sigma}{\partial Y_{p,Ag}}\sigma_{Y_{p,Ag}}\right]^2 + \left[\frac{\partial\sigma}{\partial\varepsilon_{abs}}\sigma_{\varepsilon_{abs}}\right]^2\right)^{1/2}, \tag{30}$$

where the partial derivatives are,

USC UNIVERSIDADE DE SANTIAGO DE COMPOSTELA

$$\frac{\partial\sigma}{\partial Y_{\gamma,p}} = \frac{\varepsilon_p \Omega \sigma_{Ruth}}{r Y_{p,Ag} \varepsilon_{abs}}, \tag{31}$$

$$\frac{\partial\sigma}{\partial r} = -\frac{Y_{\gamma,p} \varepsilon_p \Omega \sigma_{Ruth}}{Y_{p,Ag} \varepsilon_{abs} r^2}, \tag{32}$$

$$\frac{\partial\sigma}{\partial \Omega} = \frac{Y_{\gamma,p} \varepsilon_p \sigma_{Ruth}}{Y_{p,Ag} \varepsilon_{abs} r}, \tag{33}$$

$$\frac{\partial\sigma}{\partial \sigma_{Ruth}} = \frac{Y_{\gamma,p} \varepsilon_p \Omega}{Y_{p,Ag} \varepsilon_{abs} r}, \tag{34}$$

$$\frac{\partial\sigma}{\partial Y_{p,Ag}} = -\frac{Y_{\gamma,p} \varepsilon_p \Omega \sigma_{Ruth}}{\varepsilon_{abs} r Y_{p,Ag}^2}, \tag{35}$$

$$\frac{\partial\sigma}{\partial \varepsilon_{abs}} = -\frac{Y_{\gamma,p} \varepsilon_p \Omega \sigma_{Ruth}}{Y_{p,Ag} r \varepsilon_{abs}^2}. \tag{36}$$

$$\tag{37}$$

USC UNIVERSIDADE DE SANTIAGO DE COMPOSTELA

Bibliography

[1] Leif Gerward and André Rassat. Paul villard's discovery of gamma rays - a centenary. *Comptes Rendus de l'Académie des Sciences - Series IV - Physics*, 1(7):965–973, 2000.

[2] Sir Ernest Rutherford F.R.S. and E.N. da C. Andrade B.Sc. Ph.D. Xciv. the wave-length of the soft γ rays from radium b. *The London, Edinburgh, and Dublin Philosophical Magazine and Journal of Science*, 27(161):854–868, 1914.

[3] Glenn F. Knoll. *Radiation Detection and Measurement*. Wiley, Fourth Edition edition, 2008.

[4] Gilmore, G., & Hemingway, J.D. . *Practical gamma-ray spectrometry*. United Kingdom: John Wiley and Sons, 1995.

[5] Nuclear Reaction Analysis and Particle-Induced Gamma-Ray Emission. *In: Atomic and Nuclear Analytical Methods*. Springer Berlin Heidelberg, 2007.

[6] *Development of a Reference Database for Particle Induced Gamma Ray Emission (PIGE) Spectroscopy*. Number 1822 in TECDOC Series. INTERNATIONAL ATOMIC ENERGY AGENCY, Vienna, 2017.

[7] Cinelli, G., De Cort, M. & Tollefsen. European Atlas of Natural Radiation, Publication Office of the European Union. *Publication Office of the European Union, Luxembourg*, 2019.

[8] The ENSARRoot Group. ENSARRoot source code. Website, avaliable online at `https://github.com/EnsarRootGroup/EnsarRoot`. last visited on June 2022.

[9] The ENSARRoot Group. ENSARRoot Homepage. Website, avaliable online at `http://igfae.usc.es/satnurse/ensarroot.html`. last visited on June 2022.

USC UNIVERSIDADE DE SANTIAGO DE COMPOSTELA

[10] Pablo Cabanelas, Héctor Álvarez-Pol, Elisabet Galiana, and Yago González-Rozas. Ensarroot: The framework for simulation and data analysis for ensar. *Journal of Physics: Conference Series*, 1024:012038, 05 2018.

[11] Denis Bertini. R3broot, simulation and analysis framework for the r3b experiment at fair. *Journal of Physics: Conference Series*, 331(3):032036, dec 2011.

[12] Arpad Z. Kiss, E. Koltay, B. M. Nyako, E. Somorjai, Asko Anttila, and Jyrki Rasanen. Measurements of relative thick target yields for pige analysis on light elements in the proton energy interval 2.4-4.2 mev. *Journal of Radioanalytical and Nuclear Chemistry*, 89:123–141, 1985.

[13] Hanninen R. & Räisänen J Anttila, A. Proton-induced thick-target gamma-ray yields for the elemental analysis of the z=3-9, 11-21 elements. *Journal of Radioanalytical and Nuclear Chemistry*, 62:293–306, 1981.

[14] J. RÄISÄNEN and T. WITTING and J. KEINONEN. Absolute thick-target γ-ray yields for elemental analysis by 7 and 9 MeV protons. *Nuclear Instruments & Methods in Physics Research. Section B: Beam Interactions with Materials and Atoms*, 28:199–204, 1987.

[15] R.O. Weber, C.I.W. Tingwell, L.W. Mitchell, M.E. Sevior, and D.G. Sargood. Cross sections and thermonuclear reaction rates of proton-induced reactions on 37cl. *Nuclear Physics A*, 439(1):176–188, 1985.

[16] IAEA agency. IBANDL Homepage. Website, available online at `https://www.iaea.org`. last visited on Desember 22 2022.

[17] Christian Iliadis. *Nuclear Physics of Stars*. 2007.

[18] Felix Rembges, Christian Freiburghaus, Thomas Rauscher, Friedrich Thielemann, H. Schatz, and Michael Wiescher. An approximation for the rp-process. *The Astrophysical Journal*, 484, 01 1997.

[19] EnsarRoot Team. EnsarRoot Homepage. Website, available online at `https://igfae.usc.es/satnurse/ensarroot.html`. last visited on Desember 15th 2021.

[20] EnsarRoot Team. EnsarRoot code. Github Website, available online at `https://github.com/EnsarRootGroup/EnsarRoot`. last visited on Desember 15th 2021.

USC UNIVERSIDADE DE SANTIAGO DE COMPOSTELA

[21] Faculdade de Ciencias da Universidade de Lisboa. Homepage. Website, available online at `https://ciencias.ulisboa.pt`. last visited on April 11th 2022.

[22] Laboratório de Instrumentação e Física Experimental de Partículas (LIP). Homepage. Website, available online at `https://www.lip.pt`. last visited on May 9th 2023.

[23] CTN/IST. Homepage. Website, available online at `http://c2tn.tecnico.ulisboa.pt`. last visited on October 20th 2022.

[24] John B. West. Carl wilhelm scheele, the discoverer of oxygen, and a very productive chemist. *American Journal of Physiology-Lung Cellular and Molecular Physiology*, 307(11):L811–L816, 2014. PMID: 25281638.

[25] Meng Wang, W.J. Huang, F.G. Kondev, G. Audi, and S. Naimi. The ame 2020 atomic mass evaluation (ii). tables, graphs and references*. *Chinese Physics C*, 45(3):030003, mar 2021.

[26] National Nuclear Data Center (NNDC). NNDC Homepage. Website, avaliable online at `https://www.nndc.bnl.gov`. last visited on December 1st 2022.

[27] Physical Measurement Laboratory Team. NIST Homepage. Website, available online at `https://physics.nist.gov/cgi-bin/Elements/elInfo.pl?element=17`. last visited on December 20th 2021.

[28] Los Alamos Lab LANL Team. Periodic Table of Elements. Website, avaliable online at `https://periodic.lanl.gov/17.shtml`. last visited on December 20th 2021.

[29] R.T Myers. The Periodicity of Electron Affinity. *Journal of Chemical Education*, 67(4), 04 1990.

[30] Haynes, William M., David R. Lide and Thomas J., Bruno. CRC Handbook of Chemistry and Physics: A Ready-reference Book of Chemical and Physical Data. Boca Raton, Florida, CRC Press, 2016.

[31] Fred Phillips. *Chlorine-36*, pages 299–348. 01 2000.

[32] IAEA agency. IBANDL Homepage. Website, available online at `https://www-nds.iaea.org/exfor/ibandl.htm`. last visited on December 13th 2021.

USC UNIVERSIDADE DE SANTIAGO DE COMPOSTELA

[33] World Health Organization, Available from: http://whqlibdoc.who.int/publications/2009/9789241547673_eng.pdf. *WHO Handbook on Indoor Radon, A Public Health Perspective*, 2009.

[34] Proyecto MARNA. Mapa de Radiacion Natural, Consejo de Seguridad Nuclear. Technical report, CSN, Coleccion Informes Tecnicos 5, 2000.

[35] Batista, M. J., Torres, L., Leote, J., Prazeres, C., Saraiva, J., & Carvalho, J. Carta Radiometrica de Portugal (1: 500 000). Technical report, Laboratorio Nacional de Energia e Geologia, 2013.

[36] Masanao Nakano *et al.* Long-term simulations of the ^{137}Cs dispersion from the Fukushima accident in the world ocean. *Journal of Environmental Radioactivity*, 111:109–115, 2012.

[37] Minsik Kim *et al.* Validity of the source term for the Fukushima Dai-ichi Nuclear Power Station accident estimated using local-scale atmospheric dispersion simulations to reproduce the large-scale atmospheric dispersion of ^{137}Cs. *Journal of Environmental Radioactivity*, 210:10265–931X, 2019.

[38] A.L. Mishev. Contribution of cosmic ray particles to radiation environment at high mountain altitude: Comparison of Monte Carlo simulations with experimental data. *Journal of Environmental Radioactivity*, 153:15–22, 2016.

[39] R. Breier *et al.* Environmental radionuclides as contaminants of HPGe gamma-ray spectrometers: Monte Carlo simulations for Modane underground laboratory. *Journal of Environmental Radioactivity*, 190-191:134–140, 2018.

[40] Mortazavi, SMJ & Mozdarani, Hossein. Non-linear phenomena in biological findings of the residents of high background radiation areas of Ramsar. *International Journal of Radiation Research*, 11:3–9, 2013.

[41] Tarsheen K. Sethi, MD, Moataz N. El-Ghamry, MD, and Goetz H. Kloecker, MD, MSPH. Radon and Lung Cancer. Clinical Advances in Hematology & Oncology Volume 10, Issue 3 March 2012, avaliable online at http://www.hematologyandoncology.net/files/2013/05/ho0312_sethi1.pdf.

[42] Jolyon Hendry, Steven Simon, Andrzej Wojcik, Mehdi Sohrabi, Werner Burkart, Elisabeth Cardis, Dominique Laurier, Margot Tirmarche, and Isamu Hayata. Human exposure to high natural background radiation:

USC UNIVERSIDADE DE SANTIAGO DE COMPOSTELA

What can it teach us about radiation risks? *Journal of radiological protection : official journal of the Society for Radiological Protection*, 29:A29–42, 07 2009.

[43] Universidade da Beira Interior. Homepage. Website, available online at `https://www.ubi.pt`. last visited on May 10th 2022.

[44] Laboratorio de Análisis de Radiaciones (LAR) Team. LAR Homepage. Website, available online at `https://igfae.usc.es/lar/`. last visited on May 10th 2022.

[45] Universidad de Santiago de Compostela. Homepage. Website, available online at `https://www.usc.gal/gl`. last visited on May 10th 2022.

[46] European Comission. European Comission Homepage. Website, available online at `https://commission.europa.eu/index_en`.

[47] Consejo de Seguridad Nacional (CSN). CSN Homepage. Website, available online at `https://www.csn.es/en/home`.

[48] ENUSA INDUSTRIAS AVANZADAS, S.A., S.M.E. (ENUSA). ENUSA Homepage. Website, avaliable online at `https://www.enusa.es`.

[49] *Chemistry of Europe's Agricultural Soils Part A + B (2 Volume set)*. Schweizerbart Science Publishers, Stuttgart, Germany, 04 2014.

[50] Geoportal Energia e Geologia Homepage. Website, available online at `https://geoportal.lneg.pt/mapa/?mapa=CartaRadiometrica`. last visited on October 2022.

[51] Filipa Domingos *et al.* Validation of a database of mean uranium, thorium and potassium concentrations in rock samples of Portuguese geological units, generated of literature data. *Journal of Environmental Radioactivity*, 222(106338), 2020.

[52] F.P. Carvalho *et al.* Radioactivity in the environment around past radium and uranium mining sites of Portugal. *Journal of Environmental Radioactivity*, 96:39–46, 2007.

[53] F.P. Carvalho *et al.* Radionuclides from past uranium mining in rivers of Portugal. *Journal of Environmental Radioactivity*, 98:298–314, 2007.

USC UNIVERSIDADE DE SANTIAGO DE COMPOSTELA

[54] A. Pereira, R. Lamas, M. Miranda, F. Domingos, L. Neves, N. Ferreira, and L. Costa. Estimation of the radon production rate in granite rocks and evaluation of the implications for geogenic radon potential maps: A case study in central portugal. *Journal of Environmental Radioactivity*, 166:270–277, 2017. Special Issue on Geogenic Radiation and its Potential Use for Developing the Geogenic Radon Map.

[55] Fernando *et al.* Carvalho. Radioactivity from fukushima nuclear accident detected in lisbon, portugal. *Journal of Environmental Radioactivity*, 114:152–6, 04 2012.

[56] L.J.P.F. Neves, S.M. Barbosa, and A.J.S.C. Pereira. Indoor radon periodicities and their physical constraints: a study in the coimbra region (central portugal). *Journal of Environmental Radioactivity*, 100(10):896–904, 2009.

[57] Susana Barbosa, Francisco Lopes, A. Correia, Sofia Barbosa, A. Pereira, and L. Neves. Temporal variability of radon in a remediated tailing of uranium ore processing - the case of urgeiriÃ§a (central portugal). *Journal of Environmental Radioactivity*, 142, 01 2015.

[58] D. Cortina-Gil, Ignacio Durán, and J.J. Llerena. Measurements of indoor radon concentrations in the santiago de compostela area. *Journal of environmental radioactivity*, 99:1583–8, 03 2008.

[59] J.J. Llerena, D. Cortina, I. Durán, and R. Sorribas. ^{222}rn concentration in public secondary schools in galicia (spain). *Journal of Environmental Radioactivity*, 101(11):931–936, 2010.

[60] Mose, D. G. *et al.* Seasonal indoor radon variations related to precipitation. *Environmental and molecular mutagenesis*, 17(4):223–30, 1991.

[61] Xi Guo, Jiabin Yan, and Qiangqiang Wang. Monitoring of gamma radiation in aseismic region and its response to seismic events. *Journal of Environmental Radioactivity*, 213:106119, 2020.

[62] Y. W. Tsang and T. N. Narasimhan. Effects of periodic atmospheric pressure variation on radon entry into buildings. *Journal of Geophysical Research: Solid Earth*, 97(B6):9161–9170, 1992.

[63] Allen L. Robinson, Richard G. Sextro, and William J. Riley. Soil-gas entry into houses driven by atmospheric pressure fluctuations:the

USC UNIVERSIDADE DE SANTIAGO DE COMPOSTELA

influence of soil properties. *Atmospheric Environment*, 31(10):1487–1495, 1997.

[64] Susana Barbosa, Johan Alexander Huisman, and Eduardo Brito Azevedo. Meteorological and soil surface effects in gamma radiation time series - implications for assessment of earthquake precursors. *Journal of Environmental Radioactivity*, 195:72–78, 2018.

[65] J Porstendoerfer, G Butterweck, and A Reineking. Daily variation of the radon concentration indoors and outdoors and the influence of meteorological parameters. *Health Physics*, 67(3), 9 1994.

[66] Aumento F. Radon tides on an active volcanic island: Terceira, azores. *Geofísica Internacional*, 41, 10 2002.

[67] C.J. Groves-Kirkby, A.R. Denman, R.G.M. Crockett, P.S. Phillips, and G.K. Gillmore. Identification of tidal and climatic influences within domestic radon time-series from northamptonshire, uk. *Science of The Total Environment*, 367(1):191–202, 2006.

[68] Laboratoire Souterrain de Modane Homepage. Website, available online at `http://www.lsm.in2p3.fr`. last visited on August 10th 2022.

[69] R. Britton, J.L. Burnett, A.V. Davies, and P.H. Regan. Maximising the sensitivity of a γ spectrometer for low-energy, low-activity radionuclides using monte carlo simulations. *Journal of Environmental Radioactivity*, 134:1–5, 2014.

[70] Alexander Mishev and E Hristova. Recent gamma background measurements at high mountain altitude. *Journal of environmental radioactivity*, 113:77–82, 05 2012.

[71] Minsik Kim *et al.* Simulation study of the effects of buildings, trees and paved surfaces on ambient dose equivalent rates outdoors at three suburban sites near fukushima dai-ichi. *Journal of Environmental Radioactivity*, 210, 09 2018.

[72] Copyright. In J.R. Bird and J.S. Williams, editors, *Ion Beams for Materials Analysis*, page iv. Academic Press, San Diego, 1989.

[73] T. Calligaro, J.-C. Dran, and J. Salomon. Chapter 5 ion beam microanalysis. In *Non-Destructive Microanalysis of Cultural Heritage Materials*, volume 42 of *Comprehensive Analytical Chemistry*, pages 227–276. Elsevier, 2004.

USC UNIVERSIDADE DE SANTIAGO DE COMPOSTELA

[74] Professor E. Rutherford F.R.S. Lxxix. the scattering of α and β particles by matter and the structure of the atom. *The London, Edinburgh, and Dublin Philosophical Magazine and Journal of Science*, 21(125):669–688, 1911.

[75] The SIMNRA Team. SIMNRA Homepage. Website, available online at `https://www2.ipp.mpg.de/~mam/`. last visited on July 16th 2022.

[76] The SigmaCalc Team. SigmaCalc Homepage. Website, available online at `http://sigmacalc.iate.obninsk.ru`. last visited on August 6th 2021.

[77] The SRIM Team. SRIM Homepage. Website, available online at `http://www.srim.org`. last visited on March 31st 2022.

[78] The LISE Team. LISE Homepage. Website, available online at `http://lise.nscl.msu.edu/lise.html`. last visited on March 31st 2022.

[79] D. Endisch, H. Sturm, and F. Rauch. Nuclear reaction analysis of hydrogen at levels below 10 at.ppm. *Nuclear Instruments and Methods in Physics Research Section B: Beam Interactions with Materials and Atoms*, 84(3):380–392, 1994.

[80] Markus Wilde and Katsuyuki Fukutani. Hydrogen detection near surfaces and shallow interfaces with resonant nuclear reaction analysis. *Surface Science Reports*, 69(4):196–295, 2014.

[81] Helmut Fritzsche, Jacques Huot, Daniel Fruchart. *Neutron Scattering and Other Nuclear Techniques for Hydrogen in Materials*. Neutron Scattering Applications and Techniques (NEUSCATT). Springer Cham, 1 edition, 2016.

[82] The ERYA Team. ERYA Homepage. Website, available online at `http://www.ctn.tecnico.ulisboa.pt/sec/fis/rn/uk_rn_erya.htm`. last visited on June 18th 2022.

[83] V. Manteigas and J. Cruz and M. Fonseca and A.P. Jesus. ERYA-Profiling: A code for quantitative PIGE analysis of in depth heterogeneous samples. *Nuclear Instruments and Methods in Physics Research Section B: Beam Interactions with Materials and Atoms*, 502:142 149, 2021.

[84] Phillip Womble, Alexander Barzilov, Ivan Novikov, Joseph Howard, and Jason Musser. Evaluation of the doppler-broadening of gamma-ray

USC UNIVERSIDADE DE SANTIAGO DE COMPOSTELA

spectra from neutron inelastic scattering on light nuclei. *AIP Conference Proceedings*, 1099, 03 2009.

[85] H. B.Borner *et al.* Gamma ray induced Doppler broadening and the determination of lifetimes of excited nuclear states. In *Presented at the 7th International Symposium on Capture Gamma-Ray Spectroscopy Asilomar*, California, October 14-19 1990.

[86] P. Cabanelas *et al.* Cross sections for proton induced high energy γ-ray emission (pige) in reaction ^{19}f (p,$\alpha\gamma$) ^{16}o at incident proton energies between 1.5 and 4mev. *Nuclear Instruments and Methods in Physics Research Section B: Beam Interactions with Materials and Atoms*, 381:110–113, 2016.

[87] Krane, Kenneth S. *Introductory nuclear physics.* Wiley, New York, NY, 1988. Chapter 6.

[88] H. Damjantschitsch and M. Weiser and G. Heusser and S. Kalbitzer and H. Mannsperger. An in-beam-line low-level system for nuclear reaction γ-rays. *Nuclear Instruments and Methods in Physics Research*, 218(1):129–140, 1983.

[89] Bird, J.R., Campbell, B.L., & Price, P.B. Prompt nuclear analysis. *Atomic Energy Review*, 12(2):275–345, 1974.

[90] J. R. Tesmer and M. Natasi. *Handbook of Modern Ion Beam Materials Analysis.* Materials Research Society, Pittsburgh, PA.

[91] D. Kuhn, F. Rauch, and H. Baumann. A low-background detection system using a BGO detector for sensitive hydrogen analysis with the ^{1}H(^{15}N,$\alpha\gamma$)^{12}C reaction. *Nuclear Instruments and Methods in Physics Research Section B: Beam Interactions with Materials and Atoms*, 45(1):252–255, 1990.

[92] Jesus, A. and Fonseca, Maria and Luis, Helio and Ribeiro, J. The sensitivity of the PIGE analytical technique. *Nuclear Instruments & Methods in Physics Research Section B-beam Interactions With Materials and Atoms - Nucl. Instrum. Meth. Phys. Res. B*, 264:340–344, 11 2007.

[93] H.W. Choi *et al.* Analysis of chlorine in used oils by external beam pixe-pige. *Nuclear Instruments and Methods in Physics Research Section B: Beam Interactions with Materials and Atoms*, 136-138:1018–1022, 1998. Ion Beam Analysis.

USC UNIVERSIDADE DE SANTIAGO DE COMPOSTELA

[94] D Spemann, E.M Kaidashev, M Lorenz, J Vogt, and T Butz. Ion beam analysis of epitaxial (mg, cd)xzn1-xo and zno:(li, al, ga, sb) thin films grown on c-plane sapphire. *Nuclear Instruments and Methods in Physics Research Section B: Beam Interactions with Materials and Atoms*, 219-220:891–896, 2004. Proceedings of the Sixteenth International Conference on Ion Beam Analysis.

[95] Ch Sastri, Venkatesh Iyengar, Gilbert Blondiaux, Yves Tessier, Hermann Petri, Namik Aras, Vladimir Zaichick, and Hugo Ortner. Fluorine determination in human and animal bones by particle-induced gamma-ray emission. *Fresenius Journal of Analytical Chemistry*, 370:924–929, 08 2001.

[96] H. Yamamoto, Y. Iwami, K. Yagi, M. Hayashi, H. Komatsu, K. Okuyama, Y. Matsuda, and K. Yasuda. Evaluation of caries progression in dentin treated by fluoride-containing materials using an in-air micro-pige and micro-pixe measurement system. *Nuclear Instruments and Methods in Physics Research Section B: Beam Interactions with Materials and Atoms*, 348:152–155, 2015. Proceedings of the 14th International Conference on Nuclear Microprobe Technology & Applications 2014.

[97] K.B. Dasari, S. Chhillar, R. Acharya, D.K. Ray, A. Behera, N. Lakshmana Das, and P.K. Pujari. Simultaneous determination of si, al and na concentrations by particle induced gamma-ray emission and applications to reference materials and ceramic archaeological artifacts. *Nuclear Instruments and Methods in Physics Research Section B: Beam Interactions with Materials and Atoms*, 339:37–41, 2014.

[98] Z. Smit, T. Milavec, H. Fajfar, Th. Rehren, J.W. Lankton, and B. Gratuze. Analysis of glass from the post-roman settlement tonovcov grad (slovenia) by pixe-pige and la-icp-ms. *Nuclear Instruments and Methods in Physics Research Section B: Beam Interactions with Materials and Atoms*, 311:53–59, 2013.

[99] N. Grassi, A. Migliori, P.A. Mando, and H. Calvo del Castillo. Identification of lapis-lazuli pigments in paint layers by pige measurements. *Nuclear Instruments and Methods in Physics Research Section B: Beam Interactions with Materials and Atoms*, 219-220:48–52, 2004. Proceedings of the Sixteenth International Conference on Ion Beam Analysis.

[100] F. Calastrini, P. Del Carmine, F. Lucarelli, P.A. Mando, P. Prati, and A. Zucchiatti. External-beam pige for fluorine determination in atmo-

USC UNIVERSIDADE DE SANTIAGO DE COMPOSTELA

spheric aerosol. *Nuclear Instruments and Methods in Physics Research Section B: Beam Interactions with Materials and Atoms*, 136-138:975–980, 1998. Ion Beam Analysis.

[101] A D'Alessandro, F Lucarelli, P.A Mando, G Marcazzan, S Nava, P Prati, G Valli, R Vecchi, and A Zucchiatti. Hourly elemental composition and sources identification of fine and coarse pm10 particulate matter in four italian towns. *Journal of Aerosol Science*, 34(2):243–259, 2003.

[102] F.J. Ager, M.P. Mata, M.D. Ynsa, M.A. Respaldiza, B. Goffe, and F. Nieto. Nitrogen determination in micas of metamorphic rocks. *Nuclear Instruments and Methods in Physics Research Section B: Beam Interactions with Materials and Atoms*, 249(1):642–645, 2006. Ion Beam Analysis.

[103] Robaye G. Weber G. *et al.* Roelandts, I. Determination of fluorine by proton-induced gamma-ray emission (pige) spectrometry in igneous and metamorphic charnockitic rocks from rogaland (s. w. norway). *Journal of Radioanalytical and Nuclear Chemistry*, Articles 112:453–460, 1987.

[104] Luis Alves, A Jesus, A Faria, and J. Ribeiro. A milliprobe for pixe and pige analysis used for the study of colour-zoned tourmaline. *Physica Scripta*, 2005:237, 02 2006.

[105] M. Fonseca, R. Mateus, C. Santos, J. Cruz, H. Silva, H. Luis, L. Martins, and A.P. Jesus. Quantitative analysis of li by pige technique. *Nuclear Instruments and Methods in Physics Research Section B: Beam Interactions with Materials and Atoms*, 406:144–147, 2017. Proceedings of the 12th European Conference on Accelerators in Applied Research and Technology (ECAART12).

[106] Ferrer Soria, A. *Fisica nuclear y de particulas.* 3a ed. Universitat de Valencia, 2015.

[107] Steve K. Choi *et al.* The atacama cosmology telescope: a measurement of the cosmic microwave background power spectra at 98 and 150 GHz. *Journal of Cosmology and Astroparticle Physics*, 2020(12):045–045, dec 2020.

[108] G. Dalrymple. The age of the earth in the twentieth century: A problem (mostly) solved. *Geological Society, London, Special Publications*, 190:205–221, 01 2001.

USC UNIVERSIDADE DE SANTIAGO DE COMPOSTELA

[109] Giorgia Cinelli, Tore Tollefsen, Peter Bossew, Valeria Gruber, Konstantins Bogucarskis, Luca De Felice, and Marc De Cort. Digital version of the european atlas of natural radiation. *Journal of Environmental Radioactivity*, 196:240–252, 2019.

[110] Schuettmann, W. The discovery of uranium by martin heinrich klaproth 200 years ago. *Kernenergie*, 32(10):416–420, 1989.

[111] NEA/IAEA Group on Uranium. Uranium-resources, production and demand. available at `bit.ly/uranium-2020`.

[112] Gregory Choppin and Jan-Olov Liljenzin and Jan Rydberg and Christian Ekberg. *Radiochemistry and Nuclear Chemistry (Fourth Edition)*. Academic Press, Oxford, Fourth Edition edition, 2013.

[113] William H. Waggoner. Berzelius and the discovery of thorium. *J. Chem. Educ.*, 52, 1:53, 1975.

[114] F. Barthel and H.Tulsidas. Thorium: Geology, occurrence, deposits and resources. IAEA-CN-216 Abstact 164.

[115] Freilich, Mark B. and Petersen, Richard L. and by Staff, Updated. *Potassium Compounds*, chapter , pages 1–35. John Wiley and Sons, Ltd, 2014.

[116] Vasconcelos, P M. K−Ar and (^{40}Ar/^{39}Ar) geochronology of weathering processes. *Annual Review of Earth and Planetary Sciences; Palo Alto*, 27:183, 1999.

[117] Prof. Victor F. Hess. Nobel Prize for Physics. *Nature*, 138:873, 1936.

[118] Gaisser, Thomas K. and Engel, Ralph and Resconi, Elisa. *Frontmatter*, pages i–iv. Cambridge University Press, 2 edition, 2016.

[119] Michael Andree *et al.* 14c dating of plant macrofossils in lake sediment. *Radiocarbon*, 28(2A):411–416, 1986.

[120] Jette Arneborg *et al.* Change of diet of the greenland vikings determined from stable carbon isotope analysis and 14c dating of their bones. *Radiocarbon*, 41(2):157–168, 1999.

[121] Hartmann, Stephan. *The World as a Process*, pages 77–100. Springer Netherlands, Dordrecht, 1996.

USC UNIVERSIDADE DE SANTIAGO DE COMPOSTELA

[122] Paul Humphreys. Computer simulations. *PSA: Proceedings of the Biennial Meeting of the Philosophy of Science Association*, 1990:497–506, 1990.

[123] Duran, Juan M. and Eckhart Arnold. *Computer Simulations and the Changing Face of Scientific Experimentation*. Newcastle upon Tyne: Cambridge Scholars Publishing, 2013.

[124] E. F. Schuster. Buffon Needle Experiment. *The American Mathematical Monthly*, 81(1):26–29, 1974.

[125] Goldsman, David and Nance, Richard and Wilson, James. A brief history of simulation. pages 310–313, 01 2010.

[126] Zachary E Dell and Scott V Franklin. The Buffon-Laplace needle problem in three dimensions. 2009.

[127] Philip Boland. A biographical glimpse of william sealy gosset. *Irish Mathematical Society Newsletter*, 8, 08 1984.

[128] Borrelli, A., Wellmann, J. Computer Simulations Then and Now: an Introduction and Historical Reassessment. pages 407–417, 2019.

[129] Bruce Cameron Reed. *The History and Science of the Manhattan Project*. Springer Berlin, Heidelberg, 2019.

[130] SHARE History Homepage. Website, available online at `https://www.share.org/About/About-Us/History`. last visited on December 2022.

[131] FORTRAN Homepage. Website, available online at `https://fortran-lang.org/en/`. last visited on December 2022.

[132] IBM Homepage. FORTRAN, The Pioneering Programming Language. Website, available online at `https://www.ibm.com/ibm/history/ibm100/us/en/icons/fortran/`. last visited on December 2022.

[133] Simulations and Analysis Tools for Nuclear Reactions and Structure (SATNuRSE). SATNuRSE Homepage. Website, avaliable online at `http://igfae.usc.es/satnurse/index.html`. last visited on June 2022.

[134] The FAIRROOT Group. FAIRROOT source code. Website, avaliable online at `https://github.com/FairRootGroup`. last visited on June 2022.

USC UNIVERSIDADE DE SANTIAGO DE COMPOSTELA

[135] The FAIRROOT Group. FAIRROOT Homepage. Website, avaliable online at `https://fairroot.gsi.de`. last visited on June 2022.

[136] The FAIRSOFT Group. FAIRSOFT source code. Website, avaliable online at `https://github.com/FairRootGroup/FairSoft`. last visited on June 2022.

[137] The Geant4 Group. Geant4 Homepage. Website, avaliable online at `https://geant4.web.cern.ch`. last visited on June 2022.

[138] S. Agostinelli *et al.* Geant4-a simulation toolkit. *Nuclear Instruments and Methods in Physics Research Section A: Accelerators, Spectrometers, Detectors and Associated Equipment*, 506(3):250–303, 2003.

[139] Allison, J. *et al.* Geant4 Developments and Applications. *IEEE Transactions on Nuclear Science*, 53:270–278, 02 2006.

[140] Allison, J. *et al.* Recent developments in Geant4. *Nucl. Instrum. Meth. A*, 835:186–225, 2016.

[141] The ROOT Group. ROOT Homepage. Website, avaliable online at `http://root.cern.ch/drupal/`. last visited on June 2022.

[142] D. Cortina-Gil *et al.* Califa, a dedicated calorimeter for the r3b/fair. *Nuclear Data Sheets*, 120:99–101, 2014.

[143] S.Y.F. Chu, L.P. Ekstrom and R.B. Firestone. The Lund/LBNL Nuclear Data Search Homepage. Website, avaliable online at `http://nucleardata.nuclear.lu.se/toi/`. last visited on May 20th 2022.

[144] The INTDS Society. INDTDS Homepage. Website, available online at `https://www.intds.org`. last visited on April 8th 2022.

[145] Gegier H. and Marsden Ernest. On a diffuse reflection of the α-particles. *Proc. Roy. Soc. A*, 82:495–500, 1909.

[146] P.E. Koehler, H.A. O'Brien, and J.C. Gursky. Radioactive targets for nuclear astrophysics research at lansce. *Nuclear Instruments and Methods in Physics Research Section A: Accelerators, Spectrometers, Detectors and Associated Equipment*, 303(1):182–186, 1991.

[147] Anna Stolarz. Target preparation for research with charged projectiles. *Journal of Radioanalytical and Nuclear Chemistry*, 299, 02 2014.

USC UNIVERSIDADE DE SANTIAGO DE COMPOSTELA

[148] R. Eykens *et al.* Preparation and characterization of ^{35}cl and ^{36}cl samples for (n, p) cross section measurements. *Nuclear Instruments & Methods in Physics Research Section A-accelerators Spectrometers Detectors and Associated Equipment*, 303:152–156, 1991.

[149] Richardson, A. XLIX.-The decomposition of silver chloride by light. *J. Chem. Soc., Trans.*, 59:536–544, 1891.

[150] ST. Homepage. Website, available online at `https://tecnico.ulisboa.pt/pt/`. last visited on October 20th 2022.

[151] Maria Michaela Leal da Fonseca. *Análise de elementos leves por reacções nucleares com produção de radiação gama*. PhD thesis, Lisboa, 2010.

[152] ORTEC Company. Homepage. Website, available online at `https://www.ortec-online.com/products/radiation-detectors/germanium-hpge-radiation-detectors`. last visited on October 20th 2022.

[153] Mayer, M. *SIMNRA User's Guide of SIMNRA Version 7.03*. Max-Planck-Institut fur Plasmaphysik, Garching bei Munchen, Germany, 2020.

[154] N.Q. Huy, D.Q. Binh, and V.X. An. Study on the increase of inactive germanium layer in a high-purity germanium detector after a long time operation applying mcnp code. *Nuclear Instruments and Methods in Physics Research Section A: Accelerators, Spectrometers, Detectors and Associated Equipment*, 573(3):384–388, 2007.

[155] J Rodenas, A Pascual, I Zarza, V Serradell, J Ortiz, and L Ballesteros. Analysis of the influence of germanium dead layer on detector calibration simulation for environmental radioactive samples using the monte carlo method. *Nuclear Instruments and Methods in Physics Research Section A: Accelerators, Spectrometers, Detectors and Associated Equipment*, 496(2):390–399, 2003.

[156] I.O.B Ewa, D Bodizs, Szabolcs Czifrus, and Zs Molnar. Monte carlo determination of full energy peak efficiency for a hpge detector. *Applied radiation and isotopes : including data, instrumentation and methods for use in agriculture, industry and medicine*, 55:103–8, 08 2001.

USC UNIVERSIDADE DE SANTIAGO DE COMPOSTELA

[157] Proceedings of the 3rd Environmental Physics Conference. *Study of Efficiency Calibrations of HPGe Detectors for Radioactivity Measurements of Environmental Samples*, Aswan, Egypt, 19-23 Feb 2008. S. Harb *et al.*

[158] *AIP Conference Proceedings 1584*, volume 1584, 2014. https://doi.org/10.1063/1.4866101.

[159] The Lund/LBNL Nuclear Data Search. Homepage. Website, available online at `http://nucleardata.nuclear.lu.se/toi/`. last visited on November 8th 2022.

[160] Z. Kis *et al.* Comparison of efficiency functions for ge gamma-ray detectors in a wide energy range. *Nuclear Instruments and Methods in Physics Research Section A: Accelerators, Spectrometers, Detectors and Associated Equipment*, 418(2):374–386, 1998.

[161] Instituto Superior Técnico. Homepage. Website, available online at `https://tecnico.ulisboa.pt/pt/`. last visited on May 10th 2022.

[162] Instituto Galego de Física de Altas Enerxías (IGFAE) Team. IGFAE Homepage. Website, available online at `https://igfae.usc.es/igfae/es/`. last visited on May 10th 2022.

[163] A study of the ^{35}cl(p,γ)^{36}ar reaction and the energy levels of ^{36}ar. *Nuclear Physics A*, 218(2):333–354, 1974.

[164] H. Silva, C. Santos, M. Fonseca, H. Luís, L. Martins, V. Manteigas, J. Cruz, and A.P. Jesus. Measurement of gamma-ray production cross sections for nuclear reaction ^{31}p(p,pγ_{1-0})^{31}p. *Nuclear Instruments and Methods in Physics Research Section B: Beam Interactions with Materials and Atoms*, 452:26–29, 2019.

[165] Micaela Fonseca. *Internal Manual: COMPONENTES DO ACELERADOR TANDEM E LINHA DE NRA E PROCEDIMENTOS.* Lisboa, 2011.

[166] A. Jokar, O. Kakuee, and M. Lamehi-Rachti. Measurement of deuteron induced gamma-ray emission differential cross sections on natcl from 1.0 to 2.0mev. *Nuclear Instruments and Methods in Physics Research Section B: Beam Interactions with Materials and Atoms*, 377:37–42, 2016.

USC UNIVERSIDADE DE SANTIAGO DE COMPOSTELA

[167] S.Y.F. Chu, L.P. Ekström and R.B. Firestone. The Lund/LBNL Nuclear Data Search Homepage. Website, available online at `http://nucleardata.nuclear.lu.se/toi/`. last visited on May 20th 2022.

[168] Cosmic-ray Shower Library (CRY). CRY Homepage. Website, available online at `https://nuclear.llnl.gov/simulation/`. last visited on May 24th 2022.

[169] Chris Hagmann, David Lange, and Douglas Wright. Cosmic-ray shower generator (cry) for monte carlo transport codes. volume 2, pages 1143 – 1146, 01 2007.

[170] J.A. Garzón. Trasgos: Towards a new standard for the regular measurement of cosmic rays. *Physics of Atomic Nuclei*, 83:453–462, 2020.

[171] TMinuit Class Reference of ROOT. Homepage. Website, available online at `https://root.cern.ch/doc/master/classTMinuit.html`. last visited on October 3rd 2022.

[172] TRatioPlot Class Reference of ROOT. Homepage. Website, available online at `https://root.cern.ch/doc/v608/classTRatioPlot.html`. last visited on October 3rd 2022.

[173] Goertzel, G. Angular Correlation of Gamma-Rays. *Phys. Rev.*, 70:897–909, Dec 1946.

[174] Gamma angular correlation analysis techniques with the GRIFFIN spectrometer. *Nuclear Instruments and Methods in Physics Research Section A: Accelerators, Spectrometers, Detectors and Associated Equipment*, 922:47–63, 2019.

[175] The ROOT Group. BrentRootFinder Class Reference. Website, avaliable online at `https://root.cern/doc/master/classROOT_1_1Math_1_1BrentRootFinder.html`.

[176] B. Pietras *et al.* First testing of the califa barrel demonstrator. *Nuclear Instruments and Methods in Physics Research, A: Accelerators, Spectrometers, Detectors and Associated Equipment*, 814:56–65, 2016.

[177] GSI Homepage. A next generation experimental setup for studies of Reactions with Relativistic Radioactive Beams. Website, available online at `https://www.gsi.de/en/work/forschung/nustarenna/nustarenna_divisions/kernreaktionen/activities/r3b`. last visited on April 2023.

USC UNIVERSIDADE DE SANTIAGO DE COMPOSTELA

[178] Basic Environmental Observatory Musala Homepage. Website, available online at `https://beo-db.inrne.bas.bg/moussala/index.php`. last visited on August 10th 2022.

[179] I. Bogdanovic *et. al.* Proton elastic scattering from fluorine, chlorine, zinc, selenium and bromine in the energy region from 2.5 to 4.8 mev. *Nuclear Instruments & Methods in Physics Research Section B-beam Interactions With Materials and Atoms*, 79:524–526, 1993.

[180] C. Iliadis, J. Gorres, J.G. Ross, K.W. Scheller, M. Wiescher, R.E. Azuma, G. Roters, H.P. Trautvetter, and H.C. Evans. Explosive hydrogen burning of 35cl. *Nuclear Physics A*, 571(1):132–158, 1994.

[181] M Al-Turany and D Bertini and R Karabowicz and D Kresan and P Malzacher and T Stockmanns and F Uhlig. The FairRoot framework. *Journal of Physics: Conference Series*, 396(2):022001, dec 2012.

[182]

[183] The Ion Beam Analysis DataFurnace Team. IBA DataFurnace Homepage. Website, available online at `https://uknibc.co.uk/WiNDF/`. last visited on July 16th 2021.

[184] Norberto Jose Sobral Catarino. *Van der Graaff, Manual de Operação*, .

[185] K. Gunoglu and S. Arda. Detection efficiency of nai(tl) detector in 511-1332 kev energy range. *Science and Technology of Nuclear Installations*, 2014:1–5, 03 2014.

[186] GammaSpec 2017 Seminar DTU Nutech. *Experimental efficiency calibration for a HPGe gamma-ray detector*, Roskilde, Denmark , October 2017. Roy Pollanen.

USC UNIVERSIDADE DE SANTIAGO DE COMPOSTELA

List of Figures

2.1 SCl cycle diagram. There are represented three types of processes: (p,α) is the black arrow, (p,γ) is the red arrow and (β^+,ν) is the blue arrow. The cycle starts from an even-even nucleus (^{32}S) with two successive proton captures up to ^{34}Ar, then a beta-decay leads to ^{34}Cl, a proton capture reaches ^{35}Ar, a further beta-decay brings down until ^{35}Cl and the closing reaction via (p,α) arrives to the initial ^{32}S nucleus. 6

2.2 Diverse gamma ray yields of ^{35}Cl proton induced reactions. In the first legend there are represented in blue shades the gamma yields of the ^{35}Cl first excited state at 1219,3 keV from the reaction ^{35}Cl(p,p'γ)^{35}Cl determined by Kiss *et al.* [12], Anttila *et al.* [13] and Räisänen *et al.* [14]. In the second legend, there are represented in red shades the gamma yields of the ^{35}Cl second excited state at 1763,04 keV from the reaction ^{35}Cl(p,p'γ)^{35}Cl measured by Kiss *et al.* and Räisänen *et al.*. In the last legend, it is displayed the yield of 2230,49 keV peak from the ^{35}Cl(p,$\alpha\gamma$)^{32}S reaction studied by Räisänen *et al.*. . 9

2.3 Diverse gamma ray yields of ^{37}Cl proton induced reactions. In the first legend there are represented in blue shades the gamma yields of the first and second excited states at 1409,79 keV and 1611,24 keV energies from the neutron channel ^{37}Cl(p,nγ)^{37}Ar measured by Kiss *et al.* [12]. In the second legend, there are represented the gamma ray spectra of 2127,499 keV line from the ^{37}Cl(p,$\alpha\gamma$)^{34}S reaction determined by Kiss *et al.* and Anttila *et al.* [13]. In the last legend, it is displayed the yield of 1726,4 keV peak from the ^{37}Cl(p,p'γ)^{37}Cl reaction studied by Kiss *et al.*. 10

2.4 Cross Section of 2127,499 keV gamma ray from the ^{37}Cl(p,$\alpha\gamma$)^{34}S reaction measured by Weber *et al.* [15] over the range 1,25-2,15 MeV with an associated error of 12 %. 11

USC UNIVERSIDADE DE SANTIAGO DE COMPOSTELA

3.1 Scheme of diverse IBA techniques. On the left the incoming beam is represented by green particles, in the central part, the sample under analysis is placed (purple particles) and surrounding it there are different techniques: ERDA (which measures elastcially-recoild ions depicted by blue particles), NRA (which measures the outcoming particles of a nuclear reaction and these are depicted by red particles), XRF and PIXE (which measure X-rays depicted by pink photons), PIGE (which measures gamma rays depicted by orange photons), and RBS (which measures backscattered ions depicted by green particles). 19

3.2 Schematic view of an interaction between an impinging ion and an atom of the target in the Laboratory Reference System where different parameters are featured: impact parameter (b), distance of closest approach (d), backscattering angle (θ) and recoiling angle (φ). 23

3.3 Principle of the RBS technique: Beam of low-mass ions of 1-3 MeV is made to impinge on the atom's sample which recoils with an angle φ and the particles scattered through angle θ are detected by a particle detector. The scheme is represented in the Laboratory Reference System. 24

3.4 Schematic diagram to illustrate scattering trajectories and energy losses for a thin target (red) and for a thick target (blue), where α is the incident angle, β the exit angle and θ the scattering angle. 27

3.5 Schematic representation of a nuclear reaction dynamics in the Laboratory Reference System. 30

3.6 PIGE Depth Profiling Scheme from IAEA TECDOC Series [6]. It is despicted the scanning of the sample in depth by increasing the energy of the beam and how this produces the movement of the resonance. The material region where the resonance has already passed lies on a low cross section domain emitting quite few gammas. On the left of the figure, it is displayed the resonance on the surface while on the right the resonance has traveled through the material. In the middle, there are plots of the PIGE spectra obtained by gamma measurement and highlighted in red the peak chosen of a certain reaction. On the bottom, it is represented the gamma ray spectra of the previous specific gamma as a function of the beam energy. 33

USC UNIVERSIDADE DE SANTIAGO DE COMPOSTELA

3.7 Potassium decay of the unstable ^{40}K isotope [26]. It decays 89,28 % via beta-minus to ^{40}Ca and 10,72 % via electron capture to ^{40}Ar which, in turn, de-excites emitting a gamma ray of 1460,8 keV. 50

3.8 Uranium radioactive series [26]. It represents the successive decays from the parent nucleus ^{238}U until the stable nucleus ^{206}Pb is reached (black square). The easiest nuclei to detect by gamma spectroscopy, because of their outstanding photopeaks, are highlighted in grey (considering a small-sized germanium detector). 53

3.9 Actinium radioactive series [26]. It represents the successive decays from the parent nucleus ^{235}U until the stable nucleus ^{207}Pb is reached (black square). The easiest nuclei to detect by gamma spectroscopy, because of their outstanding photopeaks, are filled in grey (considering a small-sized germanium detector). 54

3.10 Thorium radioactive series [26]. It represents the successive decays from the parent nucleus ^{232}Th until the stable nucleus ^{208}Pb is reached (black square). The easiest nuclei to detect by gamma spectroscopy, because of their outstanding photopeaks, are highlighted in grey (considering a small-sized germanium detector). 55

4.1 Schematic view of the FairSoft/FairRoot interdependences and their relation to diverse experimental codes; EnsarRoot among them. In the upper part of the scheme, some required system packages needed to construct a complete building environment to compile the FairSoft/FairRoot source code are displayed. In the central part, the FairRoot structure is shown. It contains diverse interrelated components linked by arrows and its own base constituents (Detector List, Event Generator, Analytical Tasks and Magnetic Field) which will be inherited by specific experimental codes, in the lower part of the diagram. 59

4.2 EnsarRoot scheme with the inherited components from FairRoot code: Detector List, Event Generator and Analytical Tasks. Underneath these categories some specific classes inside EnsarRoot are listed. 60

4.3 EnsarRoot data flow. In the upper part, the simulated data flow is shown, while in the bottom part, the real data flow is displayed. 62

USC UNIVERSIDADE DE SANTIAGO DE COMPOSTELA

4.4 Simulation of HPGe detectors, side view. Layers of diverse materials are distinguishable by different colors with the active volume in blue. At left, it is displayed the CTN/IST HPGe detector while, at right, it is exposed the HPGe of the Universidade da Beira Interior laboratory which has 24 % less active volume. 63

4.5 Diverse views of the CTN/IST setup design in the event viewer of the EnsarRoot simulation. It includes a reaction chamber (grey volume) and an HPGe detector (yellow volume). 64

4.6 Frontal and lateral views of the CTN/IST setup with an earth block design in the event viewer of the EnsarRoot simulation. It includes a reaction chamber (grey volume), an HPGe detector (yellow volume) and a block of earth (brown volume). . . . 65

4.7 Vacuum chamber of the Target Laboratory at FCUL/LIP [21, 22]. 69

4.8 View of the inside vacuum chamber. On the left picture there are two boats (one loaded with silver) connected to two electrodes. On the right picture, a boat loaded with silver chloride is shown. 70

4.9 Manual work of releasing targets from the substrate on distilled water. Some targets break at the moment of release due to an excess of release agent. 71

4.10 View of the inside chamber after the silver evaporation. In the middle of the cavity there are two crucibles for resistant heating and on top of it there is placed the target support with substrates. 72

4.11 Silver chloride targets mounted on a thin silver substrate produced in the framework of this thesis work. We can observe that chlorine targets are photosensitive due to its dark pinkish color (on the right), while the silver backing is not (on the left). 73

4.12 View of the inside vacuum chamber while the evaporation was taking place. In the middle of the picture a heated tantalum boat appears in bright orange. 73

4.13 CTN/IST ion beam laboratories and their accelerator schemes. On the left, there is displayed the Van der Graaff accelerator (green), and on the right, there is shown the Tandem accelerator (yellow). 74

USC UNIVERSIDADE DE SANTIAGO DE COMPOSTELA

4.14 Reaction chamber geometry of the RBS Line. The three detectors RBS1, RBS2 and ERD are tagged in their respective positions. The angles with respect to the beam line are also indicated: RBS2 is placed at 140° and ERD and RBS1 are situated at 165° on oposite sides. 76

4.15 Goniometer of the RBS Line. On the left, the sample holder and the three adjustable parameters are shown: z represents the height, θ the inclination and h the screw that fixes the targets. On the right, there is a goniometer vertical sketch with the two manipulable parameters z and θ from outside (once the reaction chamber is closed). 77

4.16 Photography of the Tandem accelerator (blue) and its control room at CTN/IST. 78

4.17 Nuclear reaction line of the Tandem accelerator at CTN/IST. On the left side the switching magnet is displayed. On the center diverse elements of the setup are shown: the HPGe with its cryostat, the reaction chamber and the turbo vacuum pump. In the lower part of the picture the neutron detector used for controlling neutron yields appears (it was only used in order to maintain safety conditions.) 79

4.18 The interior of the reaction chamber of the nuclear reaction line. Diverse elements of the setup appear: HPGe detector, beam entrance, collimator, particle detectors MOVD and MOVE and the beam stopper on the opposite side of the entrance. 81

4.19 Measured (pink) and simulated (violet) photopeak efficiencies of the HPGe by using a ^{152}Eu radioactive source. There are also plotted the simulated efficiencies of the gammas under study in the PIGE experiment (they are highlighted with red circles). There is a point where two peaks almost overlap: the 1408,013 keV from the europium source and the 1409,79 keV from the ^{37}Ar de-excitation. The error bars are also plotted although in most cases are too small to be visible. 85

4.20 Differenced of HPGe photopeak efficiencies (measured minus simulated) from a ^{152}Eu radioactive source. Their error bars are also displayed. 86

USC UNIVERSIDADE DE SANTIAGO DE COMPOSTELA

4.21 Main uncertainty components of the ^{152}Eu radioactive source efficiency. Black line represents the combined uncertainty of the radioactive source efficiency calculated by error propagation (see Appendix F). Orange points represent the photopeak error, a combination of the histogram error (light blue squares) and background errors (dark blue rhombus). Purple stars represent the error of all gammas emitted by the source during the measurement time interval, it also includes the error of the gamma branching ratio (teal crosses) and the error of the source activity that is not included here because it is a constant value of 0,48 %. 88
4.22 HPGe calibration function (red) and experimental points (green) of the second stage of the PIGE experiment. 91
4.23 CTN/IST environmental radiation spectra. The blue line shows a spectrum measured in an interval of 30 min and the red line during a period of 8 hours. 92
4.24 The resolution of all detectors used for the analysis of environmental radiation. It shows the resolution functions (Eq. 4.7) and the experimental points of the CTN/IST detector (red), Universidade da Beira Interior detector (blue), ORTEC of the USC (green) and BSI of the USC (black). The resolutions are plotted with their associated error bars, although some of them are too small to be visible. 93
4.25 Interior of the ORTEC detector with the shielding's lap open from the Laboratorio de Análisis de Radiaciones of the USC. . 95
4.26 Setup of the ORTEC detector from the Laboratorio de Análisis de Radiaciones of the USC. 95
4.27 Environmental radiation spectra of the Laboratorio de Análisis de Radiaciones [44, 45, 162] measured during 2 days. The red line represents the ORTEC detector while the blue line illustrates the BSI detector. In order to compare natural radiation, a spectra of the CTN/IST laboratory measured during the same time interval has been also plotted. 96

5.1 RBS chlorine target spectrum of the RBS1 detector at an angle of $\theta = 165°$, $\beta = 15°$ and $\alpha = 0°$ by using an $^4He^+$ ion beam. It is normalized at 20 μC of collected charge. The experimental points are indicated in red and the SIMNRA fit in blue. 98
5.2 Energy spectra of gamma radiation produced by the bombardment of the AgCl target by 2,6 and 3 MeV protons. Some gammas and their reactions studied in this work are highlighted. 101

USC UNIVERSIDADE DE SANTIAGO DE COMPOSTELA

5.3 Backscattered proton spectra produced by the bombardment of the AgCl target at 2,5 (blue) and 3,2 MeV (red) energies. The peaks that appear are, from right to left, silver, chlorine, carbon build up on the target surface and an unidentified peak. 102

5.4 Backscattered proton spectrum produced by the bombardment of the AgCl target at 2,5 MeV energy. The peaks that appear are, from right to left, silver, chlorine, carbon build up on the target surface and an unidentified peak corresponding to lower mass elements. 103

5.5 Silver backscattered proton contribution. Each point is the integral of the Ag peak at different proton energies where every spectrum has been normalized at 2 μC of collected charge. The statistical error bars are displayed although they are too small to be visible. The two stages of the experiment are shown in distinct purple shades. It follows the Rutherford formula. . . . 105

5.6 Chlorine backscattered proton contribution. Each point is the integral of the Cl peak at different proton energies and where every spectrum has been normalized at 2 μC of collected charge. The error bars are displayed in black, though in some cases are not clearly distinguishable. The two stages of the experiment are shown in distinct blue shades. Diverse resonance structures appear as a consequence of nuclear reactions. 106

5.7 Schemes of the proton induced reactions on ^{35}Cl and the opening of two channels: on the left the elastic channel and on the right the alpha channel. Gammas from the de-excitations studied in this work appear in blue. The energy units are in MeV. 107

5.8 Scheme of the proton induced reactions on ^{37}Cl and the opening of the elastic channel. The gamma from the de-excitation studied in this work appears in blue. The energy units are in MeV. 108

5.9 Schemes of the proton induced reactions on ^{37}Cl and the opening of two channels on the left the alpha channel and on the right the neutron channel. Gammas from the de-excitations studied in this work appear in blue. The energy units are in MeV. 109

USC UNIVERSIDADE DE SANTIAGO DE COMPOSTELA

5.10 Yield curves of the ^{35}Cl first excited state at 1219,3 keV from our work (red line corresponds to the first stage of the experiment and blue line to the second) and from Johnson *et al.* study [163] (green line). A small shift in the proton energy between the two works could be observed, as it is explained in the text. 110
5.11 Corrected yields curves of the ^{35}Cl first excited state at 1219,3 keV. Data from our experiment has two proton energy corrections: the first stage was corrected by extracting 2 keV (red line) while the second stage adding 2 keV (blue line). The yield from Johnson *et al.* study [163] used as a reference for the corrections is also plotted in green. 111
5.12 Corrected yield curves of the ^{35}Cl first excited state at 1219,3 keV in the proton energy range of 3,06-3,27 MeV. After the corrections, gamma yields from either stages of the experiment match. 112
5.13 Differential cross section of the 1219,3 keV gamma ray from the $^{35}\mathrm{Cl}(\mathrm{p},\mathrm{p}'\gamma_{10})^{35}\mathrm{Cl}$ reaction in the energy range of 2,36-3,48 MeV. 114
5.14 Differential cross section of the 1763,13 keV gamma ray from the $^{35}\mathrm{Cl}(\mathrm{p},\mathrm{p}'\gamma_{20})^{35}\mathrm{Cl}$ reaction in the energy range of 2,36-3,48 MeV. 115
5.15 Differential cross section of the 2230,49 keV gamma ray from the $^{35}\mathrm{Cl}(\mathrm{p},\alpha\gamma_{10})^{32}\mathrm{S}$ reaction in the energy range of 3,35-3,48 MeV. 115
5.16 Differential cross sections of 1726,4 keV gamma rays from the $^{37}\mathrm{Cl}(\mathrm{p},\mathrm{p}'\gamma)^{37}\mathrm{Cl}$ reaction in the range of 3,13 to 3,48 MeV. . . . 116
5.17 Differential cross sections of 2127,499 keV gamma rays from the $^{37}\mathrm{Cl}(\mathrm{p},\alpha\gamma)^{34}\mathrm{S}$ reaction in the energy range of 2,36-3,3 MeV. 117
5.18 Differential cross sections of 1409,79 keV gamma ray from the $^{37}\mathrm{Cl}(\mathrm{p},\mathrm{n}\gamma_{10})^{37}\mathrm{Ar}$ reaction in the energy range of 2,58-3,48 MeV. 117
5.19 Differential cross sections of 1611,24 keV gamma ray from the $^{37}\mathrm{Cl}(\mathrm{p},\mathrm{n}\gamma_{20})^{37}\mathrm{Ar}$ reaction in the energy range of 3,29-3,48 MeV. 118
5.20 Comparison of the differential cross sections of 2127,499 keV gamma ray from the $^{37}\mathrm{Cl}(\mathrm{p},\alpha\gamma)^{34}\mathrm{S}$ reaction between the experimental results of this thesis (pink) and the Weber *et al.* study [15] (blue). The error of the Weber *et al.* cross section is around 12 %. The black line represents the differential cross section of Weber *et al.* with a proton energy shift around 1 MeV. 121

USC UNIVERSIDADE DE SANTIAGO DE COMPOSTELA

5.21 Environmental gamma radiation of two laboratories located at CTN/IST (red line) and at Universidade da Beira Interior (green line). Both spectra have been measured with a HPGe detector of similar dimensions during 30 min. 125

5.22 Mean of the number of gammas detected per day for the reference photopeak of the potassium decay. The upper pad shows the potassium mean measured at UBI laboratory and the lower pad measured at CTN/IST laboratory. Their uncertainties are statistical deviations. 126

5.23 Mean of the number of gammas detected per day for the reference photopeak of the uranium series. The upper pad shows the uranium mean measured at UBI laboratory and the lower pad measured at CTN/IST laboratory. Their uncertainties are statistical deviations. 127

5.24 Mean of the number of gammas detected per day for the reference photopeak of the thorium series. The upper pad shows the thorium mean measured at UBI laboratory and the lower pad measured at CTN/IST laboratory. Their uncertainties are statistical deviations. 128

5.25 Mean of the number of gammas detected per hour for the reference photopeak of the potassium decay. The upper pad shows the potassium mean measured at UBI laboratory and the lower pad measured at CTN/IST laboratory. Their uncertainties are statistical deviations. 129

5.26 Mean of the number of gammas detected per hour for the reference photopeak of the uranium series. The upper pad shows the uranium mean measured at UBI laboratory and the lower pad measured at CTN/IST laboratory. Their uncertainties are statistical deviations. 130

5.27 Mean of the number of gammas detected per hour for the reference photopeak of the thorium series. The upper pad shows the thorium mean measured at UBI laboratory and the lower pad measured at CTN/IST laboratory. Their uncertainties are statistical deviations. 131

5.28 Experimental background spectrum of the CTN/IST measured data during an interval of 30 min (black line) and all simulated components weighted as explained in the text. . . . 134

USC UNIVERSIDADE DE SANTIAGO DE COMPOSTELA

5.29 In the upper pad it is represented the CTN/IST data (black line) against its simulation at high energy region including only cosmic rays simulation weighted (blue line). In the lower pad it is shown the ratio between the difference of the previous histograms and their uncertainties. 135

5.30 In the upper pad it is represented the CTN/IST data (black line) against its simulation including all contributions weighted (blue line). In the lower pad it is shown the ratio between the difference of the previous histograms and their uncertainties. The first plot is displayed in the 0-1500 keV energy region while the second is in the 1500-3000 keV range. 138

5.31 Thorium peak at 238,320 keV overestimated by the simulation fit. In the upper pad it is represented the CTN/IST data (black line) against its simulation including all contributions weighted (blue line). In the lower pad it is shown the ratio between the difference of the previous histograms and their uncertainties. 139

5.32 Environmental radiation spectra of the CTN/IST laboratory. The black line represents the measured data while the blue line is the minimization of the simulation (weighted). 140

5.33 Background spectra of the Universidade da Beira Interior, the measured data is highlighted in black and all simulated components already weighted are displayed in different colors. . . . 142

5.34 Environmental radiation spectra of the Universidade da Beira Interior laboratory. The black line represents the measured data and the blue line the simulation after the minimization procedure (weighted). 143

5.35 In the upper pad it is represented the Universidade da Beira Interior data (black line) against its simulation at high energy region including only cosmic rays simulation weighted (blue line). In the lower pad it is shown the ratio between the difference of the previous histograms and their uncertainties. . . 144

5.36 In the upper pad it is represented the Universidade da Beira Interior data (black line) against its simulation including all contributions weighted (blue line). In the lower pad it is shown the ratio between the difference of the previous histograms and their uncertainties. 146

USC UNIVERSIDADE DE SANTIAGO DE COMPOSTELA

6.1 Sección eficaz diferencial del gamma 1219,3 keV proveniente de la reacción ^{35}Cl(p, p′γ_{10})^{35}Cl en el rango de energías de 2,36-3,48 MeV. Las dos fases del experimento están indicadas en diferentes tonalidades. 157

6.2 Sección eficaz diferencial del gamma 2127,499 keV proveniente de la reacción ^{37}Cl(p, $\alpha\gamma$)^{34}S en el rango de energías de 2,36-3,3 MeV. Las dos fases del experimento están indicadas en diferentes tonalidades. 158

6.3 Espectro experimental de la radiación ambiental del CTN/IST medido durante un intérvalo de tiempo de 30 minutos (línea negra) y todas sus componentes simuladas y ponderadas. . . . 164

6.4 Espectro de la radiación ambiental del CTN/IST medido durante un intérvalo de tiempo de 30 minutos (línea negra) y su simulación ponderada (línea azul). 165

6.5 Sección efectiva diferencial da gamma 1219,3 keV procedente da reacción ^{35}Cl(p, p′γ_{10})^{35}Cl no rango de enerxía de 2,36-3,48 MeV. As dúas fases do experimento indícanse en diferentes tonalidades. 172

6.6 Sección efectiva diferencial da gamma 2127,499 keV procedente da reacción ^{37}Cl(p, $\alpha\gamma$)^{34}S no rango de enerxía de 2,36-3,3 MeV. As dúas fases do experimento indícanse en diferentes tons. 172

6.7 Espectro experimental da radiación ambiental do CTN/IST medido durante un intervalo de tempo de 30 minutos (liña negra) e todos os seus compoñentes simulados e ponderados. . 178

6.8 Espectro da radiación ambiental do CTN/IST medida durante un intervalo de tempo de 30 minutos (liña negra) e a súa simulación ponderada (liña azul). 179

9 Angular correlations plot for diverse nuclear cascades. On the legend, the spin cascades with different colors are displayed. The theoretical coefficients of each cascade are listed on Table 71. 223

10 Artistic view of the CALIFA Testing Experiment setup from the event viewer of EnsarRoot. On the side, there are two CALIFA sections (blue boxes), an HPGe detector, the reaction chamber in the central part, and the red lines represent tracks of gamma rays. On the right side, on the ZX plane, there are the same elements showing the inner petal box where the green volumes represent the CsI(Tl) scintillator crystals. . . . 226

USC UNIVERSIDADE DE SANTIAGO DE COMPOSTELA

11 R3BRoot experimental data workflow and the classes involved in the process to convert input stage data (lmd) into calibrated data for each individual crystal (CrystalCal Data). 228
12 Example of usage of R3BCalifaMapped2CrystalCalPar task with all the required settings. The TArrayF is highlighted in green and filled with data of a ^{60}Co source. 229
13 Scheme of the R3BOnlineSpectra settings (on the left) and an example of how to use them on a general macro (on the right). 230
14 Energy histogram of one CALIFA crystal with a selected CrystalId=1 obtained with the R3BOnlineSpectra task. 231
15 Energy histograms of the CALIFA crystals obtained with the R3BOnlineSpectra task. The x-axis is the energy in keV and the y-axis the number of counts. 231
16 Energy histogram of one CALIFA petal (a gathering 64 crystals) obtained with the R3BOnlineSpectra task. 232
17 Bidimensional histogram of the CALIFA petal number (1, 2 or 3) versus the CrystalId number obtained with the R3BOnlineSpectra task. 232
18 Bidimensional histogram of the crystal energy versus the CrystalId number obtained with the R3BOnlineSpectra task. . . . 233

USC UNIVERSIDADE DE SANTIAGO DE COMPOSTELA

List of Tables

4.1 Decay of ^{40}K. Energy units are expressed in keV and the probabilities for each transition are indicated in decimal fraction. The nuclear data is extracted from NNDC [26]. 66

4.2 Technical characteristics of the RBS1, RBS2 and ERD detectors placed in the RBS Line. 75

4.3 Gammas from ^{152}Eu decay with a BR$>$ 5%. Data extracted from the NNDC database [26]. 87

4.4 Resolution of CTN/IST HPGe detector at different energies. The origin of the photopeaks is environmental radiation. . . . 89

4.5 Experimental points from ^{60}Co and ^{137}Cs sources and two natural background photopeaks used for the calibration of the HPGe detector in the second experimental phase [26]. 90

5.1 Layers and their parameters introduced in the SIMNRA program to reproduce the RBS chlorine target spectrum. 99

5.2 Experimental setup parameters introduced in the SIMNRA program. 99

5.3 Gammas detected from proton induced reactions on natural chlorine in the PIGE experiment. Nuclear data is from NNDC [26]. 109

5.4 Uncertainty estimations for the measurements. 119

5.5 Identifiable photopeaks from background spectra measured during two days at CTN/IST, UBI and Laboratorio de Análisis de Radiaciones of USC. Data taken from [167]. 123

5.6 Identifiable photopeaks from background spectra measured during two days at CTN/IST, UBI and Laboratorio de Análisis de Radiaciones of USC. Data taken from [167]. 124

5.7 Photopeaks employed as a reference for each background contribution. Data taken from NNDC [26]. 125

USC UNIVERSIDADE DE SANTIAGO DE COMPOSTELA

5.8 Total average rates per day of each environmental component at CTN/IST and at UBI locations. The last column shows the ratios between UBI and CTN/IST components. 131
5.9 Numerical values of the weighted parameters after TMinuit fit for the simulations of CTN/IST background. They have been calculated in two steps: the first one determines the cosmic rays parameter at high energy values and in the second stage the rest of the parameters are resolved in the low-to-intermediate energy region. 136
5.10 Numerical values of the weighted parameters after TMinuit fit for the simulations of the background of Universidade da Beira Interior. They have been calculated in two steps: the first one determines the cosmic rays parameter at high energy values and in the second stage the rest of the parameters are resolved in the low-to-intermediate energy region. 145

6.1 Gammas medidos en el experimento PIGE donde se han estudiado reacciones entre protones y los dos isótopos estables del cloro. Los datos nucleares están extraídos de la NNDC [26]. . 155
6.2 Fotopicos utilizados como referencia para cada contribución de la radiación ambiental. Los datos nucleares están extraídos de la NNDC [26]. 162
6.3 Gamas medidos no experimento PIGE onde se estudaron as reaccións entre os protóns e os dous isótopos estables do cloro. Os datos nucleares son tomados do NNDC [26]. 170
6.4 Fotopicos utilizados como referencia para cada contribución de radiación ambiental. Os datos nucleares extráense do NNDC [26]. 177
5 Decay of ^{238}U. 183
6 De-excitation of ^{234}Th. 183
7 Decay of ^{234}Th. 184
8 De-excitation of ^{234}Pa. The second excited state of 103,42 keV de-excites to a 73.92+x state with $J^P = 0^-$ and this transition has not been observed experimentally (for more information consult the ENSDF of ^{234}Pa from the NNDC). As a result, we have considered that it de-excited directly to the ground state, but we have preserved the real gamma energy. 184
9 Decay of ^{234}Pa. 184
10 De-excitation of ^{234}U. 185
11 Decay of ^{234}U. 185
12 De-excitation of ^{230}Th. 185

USC UNIVERSIDADE DE SANTIAGO DE COMPOSTELA

13 Decay of ^{230}Th. . . . 186
14 De-excitation of ^{226}Ra. . . . 186
15 Decay of ^{226}Ra. . . . 186
16 De-excitation of ^{222}Rn. . . . 186
17 Decay of ^{214}Pb. . . . 187
18 De-excitation of ^{214}Bi. The NNDC data base has no information about 62,69 keV excited state, as a result, we have filled it with invented data in order to create the generator (it is highlighted in italics). . . . 188
19 Decay of ^{214}Bi. The intensity of the alpha decay mode is so low that this branch is not included in the generator. . . . 189
20 De-excitation of ^{214}Po. . . . 190
21 De-excitation of ^{214}Po. . . . 191
22 De-excitation of ^{214}Po. . . . 192
23 Decay of ^{210}Pb. . . . 193
24 De-excitation of ^{210}Bi . . . 193
25 Decay of ^{235}U. . . . 194
26 De-excitation of ^{231}Th . . . 195
27 Decay of ^{231}Th. . . . 196
28 De-excitation of ^{231}Pa . . . 197
29 Decay of ^{231}Pa. . . . 198
30 De-excitation of ^{227}Ac. . . . 199
31 De-excitation of ^{227}Ac. . . . 200
32 Decay of ^{227}Ac. . . . 200
33 De-excitation of ^{223}Fr. The 12,90 keV gamma is not included in the generator due to its low energy. . . . 200
34 De-excitation of ^{227}Th. . . . 201
35 Decay of ^{227}Th. . . . 201
36 De-excitation of ^{223}Ra. . . . 202
37 De-excitation of ^{223}Ra. . . . 203
38 De-excitation of ^{223}Ra. . . . 204
39 Decay of ^{223}Fr. The intensity of the alpha decay mode is so low that this branch is not inclued in the generator. The de-excitations of the ^{223}Ra nucleus are listed in the previous tables. 204
40 Decay of ^{223}Ra. . . . 205
41 De-excitation of ^{219}Rn. In this case, due to the large quantity of states we have labeled them with numbers instead of their corresponding energies . . . 206
42 Decay of ^{219}Rn. . . . 207
43 De-excitation of ^{215}Po. . . . 207
44 Decay of ^{211}Pb. . . . 207

USC UNIVERSIDADE DE SANTIAGO DE COMPOSTELA

45 De-excitation of ^{211}Bi. . . . 208
46 Decay of ^{211}Bi. The intensity of the beta decay mode is so low that this branch is not inclued in the generator. . . . 208
47 De-excitation of ^{207}Tl. . . . 208
48 Decay of ^{232}Th. . . . 209
49 De-excitation of ^{228}Ra. . . . 209
50 Decay of ^{228}Ra. . . . 210
51 De-excitation of ^{228}Ac. . . . 210
52 Decay of ^{228}Th. . . . 210
53 De-excitation of ^{224}Ra. . . . 210
54 Decay of ^{224}Ra. . . . 211
55 De-excitation of ^{220}Rn. . . . 211
56 Decay of ^{212}Pb. . . . 211
57 De-excitation of ^{212}Bi . . . 211
58 Decay of ^{212}Bi. . . . 212
59 De-excitation of ^{208}Tl. . . . 212
60 De-excitation of ^{212}Po. . . . 212
61 Decay of ^{208}Tl. . . . 213
62 De-excitation of ^{208}Pb . . . 213
63 Decay of ^{228}Ac. . . . 214
64 De-excitation of ^{228}Th. . . . 215
65 De-excitation of ^{228}Th. . . . 216
66 De-excitation of ^{228}Th. . . . 217
67 De-excitation of ^{228}Th. . . . 218
68 De-excitation of ^{228}Th. . . . 219
69 De-excitation of ^{228}Th. In this case, due to the large quantity of states we have labeled them with numbers instead of their corresponding energies . . . 220
70 The first five Legendre Polynomials where x represents $\cos(\theta)$. 222
71 Theoretical coefficients a_2 and a_4 for some cascades with diverse nuclear spins. All of them land into a ground state with $J = 0$. . . . 222

USC UNIVERSIDADE DE SANTIAGO DE COMPOSTELA

USC
UNIVERSIDADE
DE SANTIAGO
DE COMPOSTELA

The present thesis is focused on gamma spectroscopy studies using germanium semiconductor detectors. In particular, two different lines of research were addressed. On one hand, gamma emissions coming from low energy proton interactions on the two stable isotopes of chlorine, ^{35}Cl and ^{37}Cl, via elastic scattering and (p,α) and (p,n) channels were investigated with the purpose of measuring, for the first time, detailed gamma yields and differential cross sections. The other branch of research was the study of environmental gamma radiation. Natural sources of radiation have been investigated by measuring and analysing the background at three locations. The EnsarRoot program was the cornerstone of these investigations, because it provided a general framework where data analysis and simulations were conducted.